

# VICERRECTORIA DE INVESTIGACIÓN Y POSTGRADO DIRECCIÓN DE POSTGRADOS Y POSTITULOS

### FACULTAD DE CIENCIAS DEPARTAMENTO DE ASTRONOMÍA

### SEARCH AND CHARACTERIZATION OF STAR-FORMING DWARF GALAXIES IN THE ABELL 370 DEEP FIELD

BÚSQUEDA Y CARACTERIZACIÓN DE GALAXIAS ENANAS CON FORMACIÓN ESTELAR EN EL CAMPO PROFUNDO ABELL 370

> Tesis presentada para optar al Grado Académico de Magíster en Astronomía.

AUTOR: SEBASTIÁN ANDRÉS SUÁREZ ULLOA PROFESOR PATROCINANTE: RICARDO OSCAR AMORÍN BARBIERI

LA SERENA, CHILE, OCTUBRE DE 2024

### CONSTANCIA

Don/Doña
(Indicar nombre completo del Director(a) de la Tesis)
Que el trabajo correspondiente a la presente Tesis de Magíster, titulada "
, ha sido realizada por Don/Doña
, bajo mi dirección.
Para que conste y en cumplimiento de las normativas vigentes de la Universidad de La
Serena, Chile, firmo el presente documento en La Serena, Chile, OCTUBRE DE 2024.

### TESIS PARA OPTAR AL GRADO DE MAGISTER EN ASTRONOMÍA

TITULO	:	BÚSQUEDA Y CARACTERIZACIÓN DE GALAXIAS ENANAS CON FORMACIÓN ES- TELAR EN EL CAMPO PROFUNDO ABELL 370
PRESENTADO POR	:	SEBASTIÁN ANDRÉS SUÁREZ ULLOA
DIRECTOR DE TESIS	:	RICARDO OSCAR AMORÍN BARBIERI
TRIBUNAL CALIFIC		
PRESIDENTE:		
MIEMBROS DEL TRIE	3UN	AL:
ACUERDAN OTORGAF	RLE	LA CALIFICACIÓN DE:

La Serena, Chile, octubre de  $2024\,$ 

"We suffer more often in imagination than in reality." -Seneca

### Agradecimientos

Quiero hacer un agradecimiento especial a mis padres, Wille y Viviana, por haberme ayudado a llegar hasta aquí. Su apoyo en todo momento ha sido un pilar fundamental en esta gran experiencia, y a pesar de que durante el curso de este postgrado hemos estado separados por la distancia, su cariño y afecto nunca ha faltado. Agradezco también a mis hermanas, Yael y María, por su cariño e igualmente grande apoyo a lo largo de este tiempo. Si bien estamos repartidos por distintas ciudades, hemos sabido sobrellevar esa barrera física y hemos podido mantener el contacto en todo momento. Quiero dedicar también unas líneas de agradecimiento a mis compañeros de postgrado; es bien sabido que las carreras científicas están asociadas a grandes desafíos y también a grandes sacrificios en términos de salud mental, pero los amigos siempre están para prestar oído, o quizá para ayudarnos a distraernos de los problemas y dificultades a los que nos enfrentamos de cara a nuestro trabajo. Finalmente quiero dar un especial agradecimiento a mi director de tesis, Ricardo Amorín, por su incomparable trabajo como guía en este proyecto; los contenidos que he aprendido durante todo este tiempo que he trabajado bajo su dirección han fomentado en gran manera las áreas en las que deseo enfocarme en un futuro. Si bien tuvimos que ajustarnos a la modalidad virtual durante la última parte del proyecto, no hubo diferencia en cuanto a la comunicación para seguir adelante. Valoro cada consejo y sugerencia, así como cada buena charla que tuvimos durante el magíster.

# Contents

	List	of Figures	V
	List	of Tables	i
$\mathbf{R}$	esum	en :	1
A	bstra	ct :	3
1	Intr	roduction	5
	1.1	Galaxy Evolution: The big picture	5
	1.2	Chemical enrichment and galaxy growth	7
	1.3	Global properties of galaxies from photometric data	9
	1.4	Studying nebular properties of galaxies from spectroscopy	1
	1.5	The secrets behind the emission lines of galaxies	4
		1.5.1 Electron temperature	4
		1.5.2 Electron density	6
		1.5.3 Metallicity	7
	1.6	Star formation rates	8
	1.7	Scaling relations	9
		1.7.1 Evolution with redshift	2
	1.8	Motivation and aims of this work	5
2	Obs	ervations 28	8
	2.1	Spatially-resolved spectroscopy	8
		2.1.1 Datacube reduction	9
		2.1.2 Background subtraction: Zurich Atmosphere Purge	0
		2.1.3 Modifications to the main datacubes	1
	2.2	Photometric data and multiwavelength catalogs	2
		2.2.1 HFF-DEEPSPACE	2
		2.2.2 ASTRODEEP	6
3	San	aple selection and line measurements  3'	7
	3.1	Criteria for selecting galaxies	7
	3.2	Selection of emission-line galaxies	7
	3.3	Spectral extraction of galaxies	9

		3.3.1 Importance of segmentation maps for the extraction of spectra	40
	3.4	Line measurements with LiMe	41
		3.4.1 $$ Advantages of incorporating LiMe into line measurement analysis	46
	3.5	The case of a lensed galaxy identified twice: ID 8 & 20	47
4	Der	ivation of physical properties	<b>50</b>
	4.1	Nebular dust extinction	50
	4.2	Ionization source from classic emission-line diagnostics	57
	4.3	Physical properties from Spectral Energy Distribution (SED) fitting	58
		4.3.1 About the Stellar Population Synthesis (SPS)	59
		4.3.2 About the Star Formation History	60
		4.3.3 Parameters fitted and details on the sample	60
	4.4	Magnification correction	61
	4.5	Star formation rates from Balmer lines	63
	4.6	Metallicity diagnostics	64
		4.6.1 Oxygen abundance from the direct method	65
		4.6.2 Gas-phase metallicity from strong-line methods	69
	4.7	Review of results	75
5	Disc	cussion	<b>78</b>
	5.1	The relation between Star Formation Rate and Stellar Mass	78
	5.2	The stellar mass and metallicity relationship	80
	5.3	The dependence of metallicity on stellar mass and SFR	81
	5.4	The Fundamental Metallicity Relation	82
	5.5	The Mass-Metallicity Relation for galaxies with detection of [O III] $4363$	85
	5.6	The serendipitous discovery of a dwarf galaxy group at $z=0.84$	88
6	Con	nclusions and outlook	91
${f A}_{f J}$	ppen	dices	94
Δ	Ext	racted spectra and LiMe Gaussian fits	95
<b></b>			96
		A370 N CUT 2	
		A370 N CUT 3	
		A370 S CUT 1	
		A370 S CUT 2	
		A370 S CUT 3	
R	HS	$\Gamma$ , HAWK-I and Spitzer photometry 1	41
ע		A370 N CUT 1	
	B.2	A370 N CUT 2	
			166

### CONTENTS

Bibliog	raphy			197
B.6	A370 S CUT 3	 	 	185
B.5	$\rm A370~S~CUT~2$	 	 	177
B.4	$\rm A370~S~CUT~1$	 	 	173

# List of Figures

1.1	Representation of the cosmic timeline, after the formation of the Cosmic	
	Microwave Background (CMB). Image taken from Wise (2019)	6
1.2	History of cosmic star formation, from Far-UV+IR measurements. The	
	black curve is the best-fit star formation density. Image taken from Madau	
	& Dickinson (2014)	7
1.3	Cartoon representation of the circumgalactic medium (CGM). The different	
	elements involved in the process of chemical enrichment are shown with	
	different colors. Image taken from Tumlinson et al. (2017)	8
1.4	Analysis of a subsample of star-forming dwarf galaxies (blue dots) from	
	Calabrò et al. (2017), comparing metallicity with the gas fraction $f_{\rm gas}$ . The	
	red, blue and green curves represent a closed-box model, an open-box model	
	with outflows and inflows, and an open-box model with outflows only, re-	
	spectively	9
1.5	Overview of the Stellar Population Synthesis (SPS). The main ingredients	
	necessary for the creation of a SSP (isochrones, stellar spectra, and ini-	
	tial mass function) are displayed in the three top figures, with the SSP	
	represented in the center figure. The star formation history and chemical	
	evolution are displayed in the middle left figures, and the dust component is	
	represented in the middle right figure. These properties compose the CSP,	
	represented with and without the contribution of dust attenuation in the	
	bottom figure. Image taken from Conroy (2013)	11
1.6	Examples of the spectra of different types of galaxies. Top left: Spectrum	
	from an Spiral galaxy. Top right: Spectrum from an Irregular galaxy. Bot-	
		12
1.7	Ionization and recombination events	
1.8	Example of the results of the models in the BPT diagram	15

1.9	Similar to Fig. 1.8 but from a Neistein et al. (2006) sample. Upper left:	
	theoretical grids with different values for metallicity and ionization parame-	
	ter. Upper right: Variations for the mean star-forming abundance sequence	
	(i.e., the region covered by H II galaxies from lower ionization to higher	
	ionization). Lower: Variations for the ionization parameter and its effect	
	on the position of the star-forming abundance sequence. Image taken from	
	Kewley et al. (2019)	16
1.10	Mass-Metallicity Relation from Tremonti et al. (2004), using theoretical	
	models to derive metallicity. Black diamonds are the median in 0.1 dex	
	bins in mass, each with at least 100 data points. The black lines represent	
	the contours enclosing 68% and 95% of the SDSS-DR4 data, at $0.005 < z <$	
	0.25, and the red line represents a polynomial fit	20
1.11	Comparison between the MZR with abundances derived with direct method	
	vs. derived with a strong-line method based on photoionization models. $\ .$ .	21
1.12	Results from the FMR. Image taken from Mannucci et al. (2010)	22
1.13	Mass-metallcity relation from an SDSS sample presented in Mannucci et al.	
	(2010). The colored curves represent median metallicities for a given value	
	of SFR. The gray shaded regions are the same contours enclosing the $68\%$	
	and 95% of d the SDSS-DR4 data obtained in Tremonti et al. (2004) (see	
	Fig. 1.10)	23
1.14	BPT diagram from samples at $z\sim 0$ and $z\sim 2$ , taken from Garg et al.	
	(2022) Black hex bins represent local SDSS-DR8 galaxies. The blue points	
	are from a sample of KBSS galaxies from Strom et al. (2017). The green and	
	red curves represent the polynomial fits for the local and high- $z$ galaxies,	
	respectively, and the blue-shaded region is the intrinsic scatter relative to	
	the red best-fit curve.	24
1.15	MZR for local and high-redshift galaxies. Image taken from Sanders et al.	
	$(2021) \ldots \ldots$	25
1.16	Color image of Abell 370 from $HST$ , in different filters	26
2.1	Cartoon representing how Integral Field Spectrographs operate. It consists	
	of a microlens array that guides the light from a small sky area and sends it	
	on to the spectrograph (illustrated inside the dotted box) to later be con-	
	verted into an individual spectrum, and combine each spectra to generate	
	a datacube, with two physical dimensions plus the spectral information of	
	the target. Image taken from ESO	29

2.2	Exposure-time map of the mosaic covering Abell 370, taken from Lagattuta	
	et al. (2019). The longest exposure times are those from the central region	
	of the galaxy cluster due to its higher lensing properties. The outer regions	
	correspond to 28° rotation exposures in order to cover the most of the <i>HST</i>	
	WFC3 footprint, and the area where multiple images of background galaxies	
	are expected is be represented with the black thick line (see Lagattuta et al.	
	(2019) for a detailed analysis)	30
2.3	Left: Reduction cascade for N input files and n observations. 'pst' marks	
	the pixel-table products of muse_scipost. The final product is the deep	
	combined datacube (dpc). Right: Reduction cascade for N input files and	
	n observations, with M SKY observations available. Pictures taken from	
	the ESO Phase 3 Data Release Description	31
2.4	Abell 370 datacube before (top panel) and after (bottom panel) applying	
	the ZAP code	32
2.5	Top: Abell 370 separated into two main datacubes. Bottom: Abell 370	
	divided into two regions with three cuts each. From top to bottom and	
	from left to right, the datacubes are labeled A370 N CUT 1, A370 N CUT	
	2, A370 N CUT 3, A370 S CUT 1, A370 S CUT 2, A370 S CUT 3	33
3.1	Redshift distribution for the sample. The orange band around the bin	
	represents the cluster members, in the redshift range $0.35 < z < 0.40$	38
3.2	Comparison of traditional spectra found in the sample. Top: Spectrum of	
	galaxy DEEPSPACE ID = 5741, at $z = 0.8413$ . The upper plot is a general	
	view of the spectrum, and the lower plot is the same spectrum limited to	
	3000 flux units, in order to perceive in more detail the weaker lines. The	
	boxes are zoom-ins of relevant emission lines. The vertical dashed lines	
	mark the main emission lines of the spectrum. This is one of the most	
	intense spectra, showing faint lines such as the Mg II] $\lambda\lambda 2795,2802$ doublet.	
	Bottom: Spectrum of galaxy DEEPSPACE ID = 3684, at $z = 0.2068$ . The	
	upper plot represents a general view of the spectrum, and the lower plot is	
	the same spectrum limited to 1300 flux units. The inside boxes are zoom-	
	ins of relevant emission lines. Due to its redshift, lines beyond 4000 $\hbox{Å}$ are	
	displaced beyond the detection range of the instrument, rendering the [O	
	II] doublet at 3726 and 3729 Å impossible to measure	42
3.3	Flow chart of the process of extraction of a galaxy. After the segmentation	
	map is created (A), the original datacube is multiplied by the segmentation	
	map to isolate the galaxy (B)	43
3.4	Different views for a selected galaxy	44

3.5	Single line fitting of the [Ar III] $\lambda$ 7135 for galaxy ID 19 provided by LiMe. The top panel presents the line fit and the bottom panel shows the residuals	
	of the fit. The pink areas represent the wavelength range of the continuum	
	surrounding the line; the yellow area represents the wavelength range of the	
	emission line. The solid blue line is the Gaussian fit. The orange-dashed	
	line represents the continuum of the spectrum.	45
3.6	Double line fitting of the $[O II]\lambda 3726,3729$ doublet for galaxy ID 16. The top	
	panel is the line fit. The pink areas represent the wavelength range of the continuum surrounding the line; the yellow area represents the wavelength	
	range of the emission line. The green-dashed lines are the independent fits	
	for the blended lines, and the blue line is the total Gaussian fit. The bottom	
	panel represents the residuals of the fit.	46
3.7	Gaussian fit around ${\rm H}\beta$ in galaxy ID 35, showing the underlying stellar	
	contribution fitted by LiMe. The bottom panel shows the residuals of the	
2.0	fit. The colors represent the same as in the previous Figures	47
3.8	HST F814W field of A370 showing the lensed galaxy identified as two	
	separated systems (DEEPSPACE ID 3342 and ID 3392). The image is $10.5'' \times 10.5''$ , and is centered at R.A.=2:39:52.29, Dec.=-1:34:35.69. The	
	magenta boxes represent the area selected for the cutouts of both galaxies.	48
3.9	$5'' \times 5''$ separate cutouts made for the galaxies in our sample, with $HST$ and	
	MUSE images, and the extracted spectra for DEESPACE ID 3342 and 3392 $$	49
4.1	Histogram distribution of $c(H\beta)$ . The mean value is represented with a	
	vertical dashed line	52
4.2	Diagnostic diagrams to identify the ionization mechanism for our sample.	
	We compare the traditional BPT diagram in the top left (Fig. 4.2a), the S2-BPT in the top right (Fig. 4.2b), the O2-BPT diagram in the lower left	
	(Fig. 4.2c), and the $O_{32}$ vs. $R_{23}$ diagram in the lower right, comparing the	
	tracers of ionization parameter $(O_{32})$ and metallicity $(R_{23})$ (Fig. 4.2d)	59
4.3	Left: $[O III]\lambda 5007$ equivalent width plotted against $log(O_{32})$ . Diamonds and	
	squares represent foreground and background galaxies, respectively. Stars	
	represent cluster galaxies. We include a sample of extreme-emission line	
	galaxies (EELGs), from Pérez-Montero et al. (2021), to compare the range	
	covered Right: Histogram distribution of EW[O III] $\lambda$ 5007. The mean value	60
4.4	is represented with a vertical dashed line	60
1.1	z = 0.5478. The top panel shows the reconstruction of the photometric	
	points (blue). The data are from the <i>HST</i> , HAWK-I and Spitzer observa-	
	tions (see Table 2.1). The uncertainty range is also visible for the posterior	
	photometry (orange). The lower panel shows the corner plots for the dif-	
	ferent posteriors of the physical parameters obtained from the SED fittings.	62

4.5	Histogram distribution of $\log(M_{\star})$ . The mean value is represented with the red vertical line.	63
4.6	Left: Histogram distribution of $\log(SFR)$ . The mean value is represented with the red vertical line. Right: SFR comparison between SED-based SFR and SFR from extinction-corrected H $\alpha$ luminosity. The diamonds, stars and squares represent foreground, cluster and background galaxies, respectively. The black line shows the one-to-one relation.	64
4.7	Histogram distribution of log(sSFR). The mean value is represented with a red vertical line	65
4.8	Monte Carlo simulation example for galaxy ID 8. The abundance derived for this galaxy was 8.244. The red vertical dashed lines represent the cut in the 16th and 84th percentiles	71
4.9	Monte Carlo simulation example for galaxy ID 1. The abundance derived for this galaxy was 7.870. We made a cut in order to keep the values close to this abundance. The red vertical dashed lines indicate the same as in	
4.10	Fig. 4.8	71
4.11	the works of Bian et al. (2018), and Pérez-Montero et al. (2021), respectively. Comparison between the direct method and strong-line method for the metallicity derivation. The arrows represent lower limits. The diagonal	73
4.12	line represents a one-to-one relation	74
4.13	et al. (2022) and Maiolino et al. (2008), respectively. The black line represents a $\Delta(\log(O/H)=0$ Histogram of metallicities for the different methods. Left: metallicities derived using the strong-line method. Right: metallicities derived using the	74
	direct method. The red continuous line represent the mean metallicity, and vertical dashed lines represent $1\sigma$ uncertainty	75

5.1	Galaxy stellar mass vs. SFR diagram for our sample. The green dots repre-	
	sent the VUDS SFDGs from Calabrò et al. (2017), and the pink pentagons	
	are the sample of [O III] $\lambda 4363$ -non-detected galaxies. Cluster galaxies are	
	defined to be those within the redshift range $0.35 < z < 0.40$ , following	
	Lagattuta et al. (2022). Foreground galaxies are those below this range	
	(z < 0.35), and background galaxies those above it $(z > 0.40)$ . The color	
	map represents the logarithm of the [O $\scriptstyle\rm III$ ]5007 EW. The dashed lines are	
	continuous sSFR values, starting at $10^{-7}$ yr <sup>-1</sup> , and down to $10^{-10}$ yr <sup>-1</sup> .	
	The red line is the fit of the Main Sequence from Whitaker et al. (2014),	
	with its extrapolation towards stellar masses lower than $10^8~{\rm M_{\star}~yr^{-1}}$ as the	
	red-dashed line	0
5.2	Galaxy stellar mass vs. sSFR diagram for the sample. The symbols and	
	colorbar are the same as in the previous Figure	1
5.3	Mass-metallicity relation (MZR) for the galaxies in our sample. The blue	
	curve and its offset represent the fit suggested by Andrews & Martini (2013),	
	with the dashed lines the $1\sigma$ uncertainty. The symbols and color bar are	
	the same as in Fig. 5.1	2
5.4	Diagram of metallicity vs. sSFR for the sample. The symbols are the same	
	as Fig. 5.1. The color bar represents the [O III]5007 EW 83	3
5.5	Cartoon model of the sSFR-Z relation based on local galaxies from Lara-	
	Lopez et al. (2013). The blue ellipse corresponds to low-mass galaxies, and	
	the red ellipse to high-mass galaxies	3
5.6	Diagram of metallicity vs. sSFR for the sample. Symbols are the same as	
	in Fig. 5.4. Here we present the same axis as in the previous figure, but	
	they are inverted, in order to match the description presented in Lara-Lopez	
	et al. (2013). The color bar represents the stellar mass. The dashed line	
	represents the turnover at $log(sSFR) = -9.9.$	4
5.7	Diagram showing the relation between the FMR and the metallicity from	
	the strong-line method. The red curve represents the polynomial fit of the	
	FMR, described in Sanders et al. (2021). Diamonds are foreground galaxies,	
	the stars are cluster galaxies, and squares are background galaxies. The	
	color bar applied to the sample represents the logarithm of the [O III]5007	
	EW	
5.8	Comparison between the $\mu_{0.60}$ parameter and $\Delta FMR = \log(O/H) - \log(O/H)_{FMR}$	•
	The expression for the abundance in terms of the FMR is defined in Eq.	
	5.3, and is dependent on SFR and $M_*$ . The markers are the same as in Fig.	
	5.7 The red line represents a $\Delta FMR = 0$	റ

5.9	MZR for galaxies with detection of [O III]4363. The diamonds are fore-	
	ground galaxies, the stars are cluster galaxies, and the squares are back-	
	ground galaxies. Green circles are VUDS SFDGs from Calabrò et al. (2017).	
	The blue curve and its offset represent the fit suggested by Andrews & Mar-	
	tini (2013), with the dashed lines the $1\sigma$ uncertainty	87
5.10	Diagram showing sSFR vs. Metallicity for the sample with detection of [O	
	III]4363. The symbols are the same as in the previous Figure	87
5.11	Dwarf galaxy association formed by galaxies 14, 16 and 17. The image	
	presents the MUSE image with a narrowband filter for [O $\mbox{\sc iii}]\lambda5007$ plus a	
	continuum subtraction of a region including the three main members (green	
	circles), and also considering the smaller system around galaxies 16 and 17	
	(orange circle). The cutouts are false color $HST$ stamps using the F275W,	
	F814W and F160W filters showing the main members of the group, with	
	their spectroscopic redshifts and names included	90
A =	Mark the Country of t	0.0
A.1	Main emission lines fitted for DEEPSPACE ID 4112	
A.2	Main emission lines fitted for DEEPSPACE ID 3628	
A.3	Main emission lines fitted for DEEPSPACE ID 4225	
A.4	Main emission lines fitted for DEEPSPACE ID 4178	
A.5	Main emission lines fitted for DEEPSPACE ID 3806	
A.6	Main emission lines fitted for DEEPSPACE ID 3595	
A.7	Main emission lines fitted for DEEPSPACE ID 3529	
A.8	Main emission lines fitted for DEEPSPACE ID 3342	
A.9	Main emission lines fitted for DEEPSPACE ID 3826	
	Main emission lines fitted for DEEPSPACE ID 3440	
	Main emission lines fitted for DEEPSPACE ID 3633	
	Main emission lines fitted for DEEPSPACE ID 4070	
	Main emission lines fitted for DEEPSPACE ID 4266	
	Main emission lines fitted for DEEPSPACE ID 5165	
	Main emission lines fitted for DEEPSPACE ID 5455	
	Main emission lines fitted for DEEPSPACE ID 5741	
	Main emission lines fitted for DEEPSPACE ID 5522	
	Main emission lines fitted for DEEPSPACE ID 3910	
	Main emission lines fitted for DEEPSPACE ID 3684	
	Main emission lines fitted for DEEPSPACE ID 3392	
	Main emission lines fitted for DEEPSPACE ID 5407	
	Main emission lines fitted for DEEPSPACE ID 5271	
	3 Main emission lines fitted for DEEPSPACE ID 4912	
	Main emission lines fitted for DEEPSPACE ID 5041	
A.25	Main emission lines fitted for DEEPSPACE ID 4284	120
A.26	Main emission lines fitted for DEEPSPACE ID 4031	121

### LIST OF FIGURES

A.27	Main	emission	lines	fitted	for	DEEP	SPACI	E ID	4321.					 	122
		emission													
A.29	Main	emission	lines	fitted	for	DEEP	SPACI	E ID	3923.					 	124
A.30	Main	emission	lines	fitted	for	DEEP	SPACI	E ID	5915.					 	125
A.31	Main	emission	lines	fitted	for	DEEP	SPACI	E ID	3906.					 	126
A.32	Main	emission	lines	fitted	for	DEEP	SPACI	E ID	1602.					 	127
A.33	Main	emission	lines	fitted	for	DEEP	SPACI	E ID	2807.					 	128
A.34	Main	emission	lines	fitted	for	DEEP	SPACI	E ID	2002.					 	129
		emission													
		emission													
		emission													
		emission													
		emission													
		emission													
		emission													
		emission													
		emission													
		emission													
A.45	Main	emission	lines	fitted	for	DEEP	SPACI	E ID	3187.					 	140
B.1	HST,	HAWK-I	and	Spitzer	r in	nages c	of DEE	PSP	ACE I	D 4	112.			 	142
B.2	HST,	HAWK-I	and	Spitzer	r in	nages c	of DEE	PSP	ACE I	D 3	682.			 	143
B.3	HST,	HAWK-I	and	Spitzer	r in	nages c	of DEE	PSP	ACE I	D 4	225.			 	144
B.4	HST,	HAWK-I	and	Spitzer	r in	nages c	of DEE	PSP	ACE I	D 4	178.			 	145
B.5	HST,	HAWK-I	and	Spitzer	r in	nages o	of DEE	PSP	ACE I	D 3	806.			 	146
B.6	HST,	HAWK-I	and	Spitzer	r in	nages o	of DEE	PSP	ACE I	D 3	595.			 	147
B.7	HST,	HAWK-J	and	Spitzer	r in	nages o	of DEE	PSP	ACE I	D 3	529.			 	148
B.8	HST,	HAWK-I	and	Spitzer	r in	nages o	of DEE	PSP	ACE I	D 3	342.			 	149
B.9	HST,	HAWK-I	and	Spitzer	r in	nages o	of DEE	PSP	ACE I	D 3	826.			 	150
B.10	HST,	HAWK-I	and	Spitzer	r in	nages o	of DEE	PSP	ACE I	D 3	3440.			 	151
B.11	HST,	HAWK-I	and	Spitzer	r in	nages o	of DEE	PSP	ACE I	D 3	633.			 	152
B.12	HST,	HAWK-I	and	Spitzer	r in	nages o	of DEE	PSP	ACE I	D 4	070.			 	153
		HAWK-I		•		0									
B.14	HST,	HAWK-I	and	Spitzer	r in	nages o	of DEE	PSP	ACE I	D 5	165.			 	155
B.15	HST,	HAWK-I	and	Spitzer	r in	nages o	of DEE	PSP	ACE I	D 5	455.			 	156
B.16	HST,	HAWK-I	and	Spitzer	r in	nages o	of DEE	PSP	ACE I	D 5	741.			 	157
		HAWK-I		-											
		HAWK-I													
		HAWK-I		-											
B.20	HST,	HAWK-I	and	Spitzer	r in	nages o	of DEE	PSP	ACE I	D 3	392.			 	161
B.21	HST	HAWK-1	and	Spitzer	r in	nages c	of DEE	PSP	ACE I	D 5	407	_	_		162

### LIST OF FIGURES

B.22 HST, HAWK-I and Spitzer images of DEEPSPACE ID 5271	. 163
B.23 HST, HAWK-I and Spitzer images of DEEPSPACE ID 4912	. 164
B.24 HST, HAWK-I and Spitzer images of DEEPSPACE ID 5041	. 165
B.25 HST, HAWK-I and Spitzer images of DEEPSPACE ID 4284	. 166
B.26 HST, HAWK-I and Spitzer images of DEEPSPACE ID 4031	. 167
B.27 HST, HAWK-I and Spitzer images of DEEPSPACE ID 4321	. 168
B.28 HST, HAWK-I and Spitzer images of DEEPSPACE ID 5199	. 169
B.29 HST, HAWK-I and Spitzer images of DEEPSPACE ID 3923	. 170
B.30 HST, HAWK-I and Spitzer images of DEEPSPACE ID 5915	. 171
B.31 HST, HAWK-I and Spitzer images of DEEPSPACE ID 3906	. 172
B.32 HST, HAWK-I and Spitzer images of DEEPSPACE ID 1602	. 173
B.33 HST, HAWK-I and Spitzer images of DEEPSPACE ID 2807	. 174
B.34 HST, HAWK-I and Spitzer images of DEEPSPACE ID 2002	. 175
B.35 HST, HAWK-I and Spitzer images of DEEPSPACE ID 2441	. 176
B.36 HST, HAWK-I and Spitzer images of DEEPSPACE ID 998	. 177
B.37 HST, HAWK-I and Spitzer images of DEEPSPACE ID 1247	. 178
B.38 HST, HAWK-I and Spitzer images of DEEPSPACE ID 1989	. 179
B.39 HST, HAWK-I and Spitzer images of DEEPSPACE ID 1666	. 180
B.40 HST, HAWK-I and Spitzer images of DEEPSPACE ID 1857	. 181
B.41 HST, HAWK-I and Spitzer images of DEEPSPACE ID 2753	. 182
B.42 HST, HAWK-I and Spitzer images of DEEPSPACE ID 1227	. 183
B.43 HST, HAWK-I and Spitzer images of DEEPSPACE ID 3060	. 184
B.44 HST, HAWK-I and Spitzer images of DEEPSPACE ID 2935	. 185
B.45 HST, HAWK-I and Spitzer images of DEEPSPACE ID 3187.	186

## List of Tables

2.1	Image sources used for the photometric analysis. The columns represent:						
	(1) The name of the filter, (2) Wavelength range of the filter, in Å, (3) The						
	telescope and instrument employed for obtaining the images, (4) Survey or						
	Program ID, (5) Date of observation, considering the beggining and end of						
	observations (identical dates for each period represent an observation on the						
	same day), (6) Total exposure time considering the final processed images,						
	(7) Number of images combined to create the final processed image	35					
3.1	Basic information about the galaxies in the North zone of the cluster	40					
3.2	Basic information about the galaxies in the South zone of the cluster	41					
3.3	Main emission lines fitted. Air wavelengths indicated in rest-frame	43					
4.1	Main emission line fluxes up until the ${\rm H}\beta$ line derived for the galaxies of						
	the North (N) zone of the MUSE observations. The row below the emission						
	line names displays the value of the reddening curve. For each galaxy,						
	we present the ID, the extinction coefficient, and the observed flux and						
	extinction-corrected intensity, both relative to $F(H\beta) = I(H\beta) = 1000$ . For						
	galaxies with negative extinction coefficients, the values of the observed flux						
	are the same as the intensity. In the last two columns, we display the EW[O						
	III] and the observed flux of the H $\beta$ line (the flux units are $10^{-20} {\rm erg~cm}^{-2}$						
	$s^{-1}$ )	53					
4.2	Main emission line fluxes up until H $\beta$ derived for the galaxies of the South	00					
4.2							
	(S) zone of the MUSE observations. The row below the emission line names						
	displays the value of the reddening curve. For each galaxy, we present						
	the ID, the extinction coefficient, and the observed flux and extinction-						
	corrected intensity, both relative to $F(H\beta) = I(H\beta) = 1000$ . For galaxies						
	with negative extinction coefficients, the values of the observed flux are the						
	same as the intensity. In the last two columns, we display the $\mathrm{EW}[\mathrm{O}\ \textsc{iii}]$						
	and the observed flux of the H $\beta$ line (the flux units are $10^{-20} {\rm erg~cm^{-2}~s^{-1}}$ ).	54					

4.3	Main emission line fluxes ranging from [O III]4959 up until [S II]6730, derived	
	for the galaxies of the North (N) zone of the MUSE observations. The row	
	below the emission line names displays the value of the reddening curve. For	
	each galaxy, we present the ID, the extincion coefficient, and the observed	
	flux and extincion-corrected intensity, both relative to $F(H\beta) = I(H\beta) =$	
	1000. For galaxies with negative extinction coefficients, the values of the	
	observed flux are the same as the intensity. The final column displays the	
	observed flux of the H $\beta$ line (the flux units are $10^{-20} \text{erg cm}^{-2} \text{ s}^{-1}$ )	55
4.4	Main emission line fluxes ranging from [O III]4959 up until [S II]6730, derived	
	for the galaxies of the South (S) zone of the MUSE observations. The row	
	below the emission line names displays the value of the reddening curve. For	
	each galaxy, we present the ID, the extinction coefficient, and the observed	
	flux and extinction-corrected intensity, both relative to $F(H\beta) = I(H\beta) =$	
	1000. For galaxies with negative extinction coefficients, the values of the	
	observed flux are the same as the intensity. The final column displays the	
	observed flux of the H $\beta$ line (the flux units are $10^{-20} \text{erg cm}^{-2} \text{ s}^{-1}$ )	56
4.5	Main intensities and derived parameters for galaxies with detection of [O	
	III]4363	68
4.6	Calibrations for the Strong-line method shown in Sanders et al. (2021)	70
4.7	Comparison of the averages of metallicity calibrations. We show: (1) The	
	sources of the calibrations employed, i.e., Maiolino et al. (2008); Curti et al.	
	(2020); Sanders et al. (2021) and Nakajima et al. (2022), (2) The weighted	
	mean and standard deviation of each calibration, (3) The mean differences	
	between the metallicity according to the strong-line method and the direct-	
	method	72
4.8	Comparison of the metallicity calibrations from Maiolino et al. (2008); Curti	
	et al. (2020); Sanders et al. (2021) and Nakajima et al. (2022) for the galax-	
	ies in our sample. We derive the uncertainties in the same way described	
	in Sect. 4.6.2	<b>7</b> 6
4.9	Main physical parameters derived for the North zone of A370. The value of	
	the magnification effect due to the galaxy cluster is presented in the third	
	column. The values of SFR are based on the measurements of the ${\rm H}\alpha$ line,	
	following the expression from Kennicutt (1998). The oxygen abundance	
	values are obtained following the strong-line method	77

## Resumen

El estudio de las galaxias y la evolución de sus propiedades físicas desde las primeras épocas cosmológicas hasta el presente sigue siendo uno de los más grandes desafíos en la astrofísica moderna. En particular, hay un gran interés en caracterizar la formación estelar y el enriquecimiento químico de las galaxias más pequeñas y menos masivas, conocidas en el Universo local como galaxias enanas, debido a sus propiedades únicas, similares a las galaxias más distantes y primitivas del Universo. Sin embargo, el estudio de sus propiedades se ve limitado por su débil brillo y pequeño tamaño angular, problema que se exacerba conforme aumenta el redshift de las galaxias.

En esta tesis reportamos los resultados de un estudio observacional enfocado en la búsqueda de galaxias enanas con formación estelar en el rango  $z \sim 0.2-0.9$ , por medio de espectroscopía e imágenes de gran profundidad. El análisis se centra en el campo cosmológico del cúmulo masivo de galaxias Abell 370, aprovechando la riqueza de datos públicos disponibles gracias a la iniciativa Hubble Frontier Fields, así como los efectos de lensado gravitacional del cúmulo para detectar galaxias en el extremo de baja luminosidad. La caracterización de propiedades físicas globales considera la masa estelar, extinción por polvo, metalicidad del gas ionizado, y tasa de formación estelar, entre otras. Derivamos estas propiedades utilizando una combinación de indicadores espectroscópicos, calibraciones empíricas, y el ajuste de la distribución espectral de energía de las galaxias. Los resultados se discuten por medio de las relaciones de escala fundamentales, posicionando a la muestra en un contexto más global y comparándola con una muestra similar estudiada previamente. También analizamos los procesos físicos principales ocurriendo en la muestra, y su relación con los procesos de feedback, y finalmente determinamos la fracción de galaxias con propiedades más extremas, que son de gran interés para entender los brotes de formación estelar, y cómo estos afectan al medio interestelar en forma análoga a sus contrapartes a mayor redshift. Los resultados revelan que estas galaxias presentan las características distintivas de las galaxias jóvenes, generalmente con masas estelares bajas, bajas abundancias de oxígeno, y siguiendo las relaciones entre masa estelar, metalicidad, y tasa de formación estelar, donde los sistemas más masivos son más ricos en metales, al igual que presentan un mayor ritmo de formación estelar. Identificamos 11 galaxias con emisión de la línea auroral de  $[O III]\lambda 4363$  no reportadas anteriormente en la literatura, permitiendo una determinación de la temperatura electrónica del gas ionizado y su metalicidad, que resulta similar a la de las galaxias enanas locales, con masas y tasas de formación estelar igualmente similares. Estos valores de metalicidad sugieren un medio interestelar pobre en metales, presentando valores subsolares (7.5 < 12 + log(O/H) < 8.3;  $0.1 \lesssim {\rm Z/Z_{\odot}} \lesssim 0.4$ ). Concluimos que nuestra muestra incluye galaxias que son relativamente jóvenes, o bien que han experimentado un episodio reciente de formación estelar, donde las galaxias que presentan menor contenido de metales son las menos evolucionadas químicamente, y con propiedades comparables a aquellas identificadas a z > 4-10 con el James Webb Space Telescope (JWST), sugiriendo que las propiedades del medio ionizado en el entorno de las regiones de formación estelar podrían compartir una física con propiedades promedio similares en este tipo de galaxias. Nuestro trabajo abre la posibilidad de extender este tipo de análisis hacia otros campos lensados, donde se dispone de datos de alta calidad, que combinan espectroscopía e imágenes profundas, via telescopios terrestres y espaciales, incluyendo el Hubble Space Telescope HST y JWST, y aumentando así la significancia de nuestros resultados.

## Abstract

The study of galaxies and the evolution of their physical properties from the earliest cosmological epochs to the present remains one of the greatest challenges in modern astrophysics. In particular, there is great interest in characterizing the properties of the smallest, least massive galaxies, known in the local Universe as dwarf galaxies, due to their unique properties, akin to the most distant and primeval galaxies. However, the study of their properties is limited due to their weak brightness and small angular size, a problem that aggravates as the redshift of galaxies increases.

In this thesis we report the results of an observational study focused on searching star-forming dwarf galaxies at  $z \sim 0.2 - 0.9$ , through deep spectroscopy and imaging. The analysis is centered on the cosmological field of the Abell 370 massive galaxy cluster, harnessing the richness of available public data thanks to the Hubble Frontier Fields initiative, as well as the effects of gravitational lensing of the cluster to detect galaxies in the low-luminosity end. The characterization of global physical properties considers stellar mass, dust extinction, ionized gas metallicity, and star formation rate, among others. We derive these properties utilizing a combination of spectroscopic indicators, empirical calibrations, and the fitting of the spectral energy distribution of the galaxies. The results are discussed through the main scaling relations, placing the sample in a more global context and comparing it with a similar sample previously studied. We also analyze the main physical processes taking place in the sample, and their relation with feedback processes, and finally we determined the fraction of galaxies with more extreme properties, of great interest to understand starbursts, and their effect on their interstellar medium, similar to their higher redshift counterparts. The results reveal that these galaxies represent the distinctive features of young galaxies, generally with low stellar masses, low oxygen abundances, and that follow the relations between stellar mass, metallicity, and star formation rate, in which more massive systems are more metal-rich, with a faster rate of star formation. We identify 11 galaxies with the emission of the  $[O III]\lambda 4363$  auroral line not reported previously in the literature, which allowed us to determine the electron temperature of the ionized gas and their metallicity, which turned out similar to that of local dwarf galaxies, with equally similar masses and star formation rates. These values of metallicity suggest a metal-poor interstellar medium, showing subsolar values  $(7.5 < 12 + \log(\mathrm{O/H}) < 8.3; 0.1 \lesssim \mathrm{Z/Z_{\odot}} \lesssim 0.4)$ . We conclude that our sample includes galaxies that are relatively young, or that have experienced a recent starburst episode, where galaxies with less metal content are the least chemically evolved, with properties equivalent to those identified at z>4-10 with the James Webb Space Telescope (JWST), suggesting that the properties of the ionized medium in the environment of star forming regions could share physics with similar mean physical properties in this type of galaxies. Our work opens the possibility to extend this type of analysis towards other lensed fields, with high-quality data that combines deep spectroscopy and imaging, using ground-based and spacial telescopes, including the Hubble Space Telescope (HST) and JWST, and thus increasing the significance of our results.

## 1 | Introduction

### 1.1 Galaxy Evolution: The big picture

Galaxy formation and evolution is still one of the most challenging topics of investigation in contemporary astrophysics. One of the main goals in several fields regarding the study of young galaxies is understanding how they formed and what processes were involved. Observational astrophysics has dedicated a considerable amount of resources to study high redshift galaxies, formed after a period known as the Dark Ages, where the Universe was in a neutral state, at  $z \geq 20$  (Robertson, 2022). This posterior epoch is defined by the transition of intergalactic neutral hydrogen gas from a cold, neutral state to a hotter, ionized one, defined as the Reionization Epoch, at z > 6 (Wise, 2019). Figure 1.1 describes a timeline of the process of reionization, from the formation of the first stars to the current state of the Intergalactic Medium (IGM). One of the pieces of research that has been deeply investigated is the evolution of the shape of the star-formation rate (SFR) through cosmic time. In the review of Madau & Dickinson (2014), special attention is drawn to this matter, stating that up until  $z \sim 2$ , the SFR activity reached its peak, only to begin to decrease until  $z \sim 0$ , as seen in Fig. 1.2.

Nowadays new technologies and scientific development allow us to study the Universe in ways never seen before; the James Webb Space Telescope (JWST, Gardner et al., 2023) has pushed the redshift barrier, providing spectroscopically confirmed sources in the  $z\gtrsim 7$  vicinity (Finkelstein et al., 2022; Trump et al., 2023; Donnan et al., 2023; Arrabal Haro et al., 2023; Oesch et al., 2023; Duan et al., 2024; Finkelstein et al., 2024; Roberts-Borsani et al., 2024; Harikane et al., 2024), and with many more candidates at even higher redshifts. These early results seem to challenge the  $\Lambda$  Cold Dark Matter (CDM) model, suggesting constraints on ultraviolet (UV) luminosity, stellar mass, and SFR (Naidu et al., 2022; Niemiec et al., 2023), and have also provided with some of the most primitive emission line galaxies (Álvarez-Márquez et al., 2023). This, however, is not an easy task: galaxies at such distances are extremely faint and therefore difficult to detect, so a detailed study of such a population of early galaxies demands challenging observations, even for the JWST.

On the other hand, cosmology has offered frameworks to understand galaxy formation, in an effort to reconcile the theory and observations. The most accepted currently is the  $\Lambda$ CDM Universe, in which low-mass halos collapse first, undergoing episodes of merging over cosmic time until they become larger systems (White & Rees, 1978; Blumenthal et al.,

#### Reionization and Galaxies 15-20 ~30 Redshift 950 Myr 100 Myr-200-300 Myr -13.8 Gyr Time First Stars First Galaxies Cosmic Reionization Reionization Pre-overlap Overlap Post-overlap Highly ionized stages John H. Wise (Georgia Tech)

**Figure 1.1:** Representation of the cosmic timeline, after the formation of the Cosmic Microwave Background (CMB). Image taken from Wise (2019).

1985; Cole et al., 2000; Madau & Dickinson, 2014). This is known as the 'hierarchical' model, also called 'bottom-up' formation. Efforts to better understand these processes have been invested in the creation of cosmological simulations, that aim to replicate the dynamical conditions that drive dark matter halos to collapse and form galaxies, as well as to do a follow-up on their posterior evolution (see Vogelsberger et al., 2020 for a detailed description). Simulating the conditions of the dark matter is not enough; the astrophysical processes associated with a galaxy must also be taken into consideration, such as feedback, star-formation via cold gas collapsing, or interactions with the environment (e.g., Cole et al., 2000; Agertz et al., 2013). This is a challenge in and of itself: many of these complex physical parameters are bound to degeneracies that must be treated carefully.

Another view for the galaxy formation is the one proposed in the 'downsizing' model, first suggested by Cowie et al. (1996). This model suggests that higher-mass systems reach their peak SFR earlier, while low-mass systems form stars at later cosmic epochs (Mouri & Taniguchi, 2006; Spitoni et al., 2020). This approach is particularly interesting because it proposes that low-mass galaxies reach their peak SFR at low redshift, which could be capitalized on through the study local galaxies, in part solving the difficulty of gaining information about these young systems.

These models, however, may appear paradoxical: the first proposes that small-mass systems form earlier, followed by bigger galaxies, as suggested by the formation of dark-matter halos. In contrast, the second model claims the opposite, as inferred from the analysis of the main scaling-relations of galaxies (Spitoni et al., 2020). However, some authors claim that this is not necessarily the case, as it is only a matter of how 'formation' is defined (Neistein et al., 2006).

In the context of the evolutionary phases of galaxies, it is of great importance to study local star-forming dwarf galaxies. In the literature, these low-mass systems have been cataloged as dwarf irregulars (Kunth & Östlin, 2000), and a smaller fraction of low-mass starbursting systems have been denominated blue compact dwarfs (BCD, Searle & Sargent, 1972; Thuan & Martin, 1981; Papaderos et al., 1996; Cairós et al., 2001; Amorín et al., 2009), H II galaxies (Terlevich et al., 1991), and Green pea galaxies (Cardamone et al.,

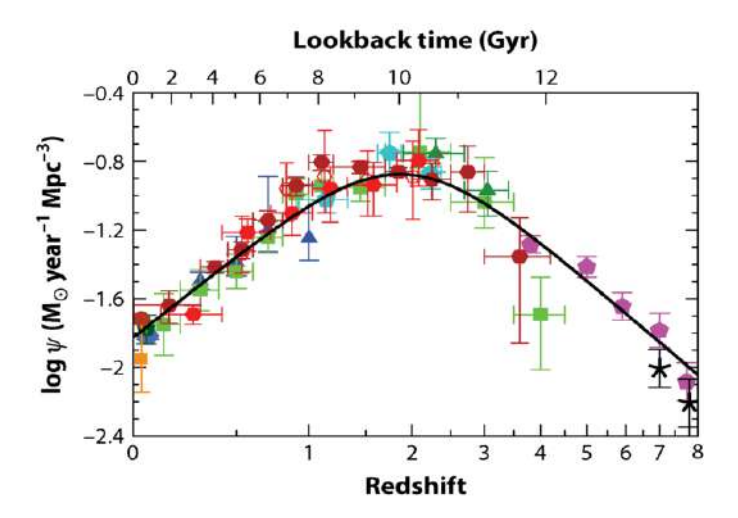


Figure 1.2: History of cosmic star formation, from Far-UV+IR measurements. The black curve is the best-fit star formation density. Image taken from Madau & Dickinson (2014).

2009; Amorín et al., 2010, 2012). The difference in the classification mostly depends on the selection criteria, photometric or spectroscopic, respectively. They are characterized by their compact optical size, extremely low metallicity, and low luminosity, as well as their intense starburst episodes, lasting 5-10 Myr (McQuinn et al., 2010), in which they produce up to 20% of their stellar mass. Because of their extreme properties, they are considered excellent local analogs to the first galaxies (Izotov et al., 2016).

### 1.2 Chemical enrichment and galaxy growth

A fundamental part of the evolution of galaxies is the cycle in which they interact with the IGM, by means of expelling, accreting, and recycling materials (Tumlinson et al., 2017). This happens because stars, at the end of their lives, expel previously enriched materials via nucleosynthesis in the form of stellar winds, and in the case of the more massive ones, when they explode as supernovae (SNe) (Kunth & Östlin, 2000). This injects new content into the interstellar medium (ISM), which can then be re-utilized, but in the form of diffuse gas, due to the mix of previously ejected gas with pristine (metal-free) gas, as seen in Fig. 1.3.

As this cycle (generally referred to as the 'baryon cycle') repeats, it is expected that galaxies experience an overall increase in their abundance of metals, so it is of great interest to know the phases in which these abundances are at their lowest. As the modeling methods to study the baryon cycle are perfected, different approaches to simulate it have been developed. The simplest ones consider parameters such as the accreted gas, the gas fraction that has turned into stars, the amount of metals ejected from the galaxy, and the amount of lost gas (Tortora et al., 2021). In a **closed-box** model, there is no exchange of metals between those produced by a galaxy and the external gas from the circumgalactic medium (CGM), so every new generation of stars supposes an increase in

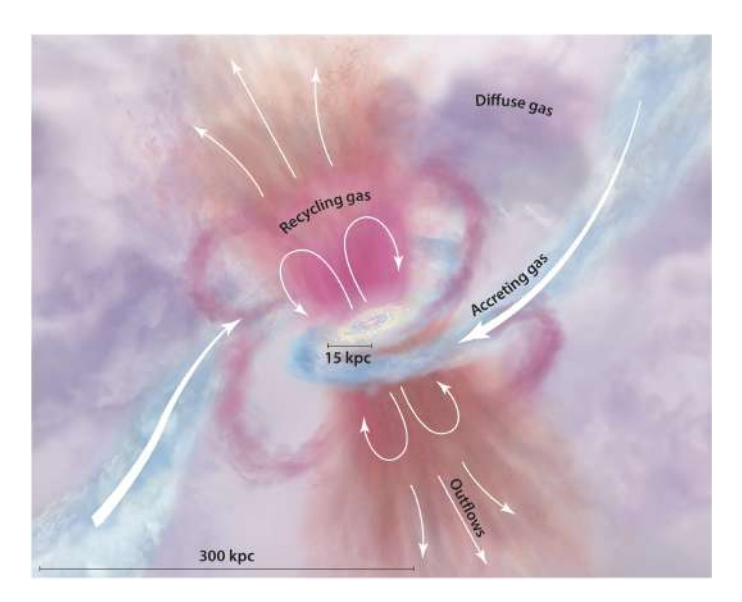


Figure 1.3: Cartoon representation of the circumgalactic medium (CGM). The different elements involved in the process of chemical enrichment are shown with different colors. Image taken from Tumlinson et al. (2017).

the metal abundance (Kewley et al., 2019). Other models consider an **open-box** approach, in which there is an exchange of materials, but can be modified, such that the parameters allow for outflows only or outflows combined with inflows of pristine gas from the IGM. This allows for a better understanding of the fundamental properties regarding the gas content of a galaxy, such as metallicity or gas fraction, which are strongly connected with the process of galaxy growth. Fig. 1.4 shows an example of this, displaying the gas fraction versus oxygen abundance, while comparing an open-box model with outflows (green curve), an open-box model with outflows and inflows (blue curve), and a closed-box model (red curve), from a subsample of star-forming dwarf galaxies (SFDGs) analyzed in (Calabrò et al., 2017, blue dots).

In this context, the study of the different paths at which galaxies grow and evolve through cosmic time is mostly focused on the physical properties that can be extracted from different types of data, either photometric (e.g., stellar masses (M\*), ages, star formation histories), or spectroscopic (e.g., SFRs, metallicities, electron densities). With this in mind, several photometric and spectroscopic surveys have been harnessed to detect and characterize star-forming galaxies (SFGs) in the local universe, spanning different parts of the electromagnetic spectrum, such as the optical with the Sloan Digital Sky Survey (SDSS, Abazajian et al., 2003), the UV with the Galaxy Evolution Explorer (GALEX, Martin et al., 2005), or the infrared (IR) with the Wide-field Infrared Survey Explorer (WISE, Wright et al., 2010). For intermediate and high redshift, deep surveys from ground-based telescopes have provided with great richness of spectroscopic data, with some examples from the Very-Large Telescope (VLT) being the zCOSMOS survey (Scoville et al., 2007), the VIMOS Ultra-Deep Survey (VUDS, Le Fèvre et al., 2015), and the VANDELS survey (McLure et al., 2018). In the photometric side there are also some rele-

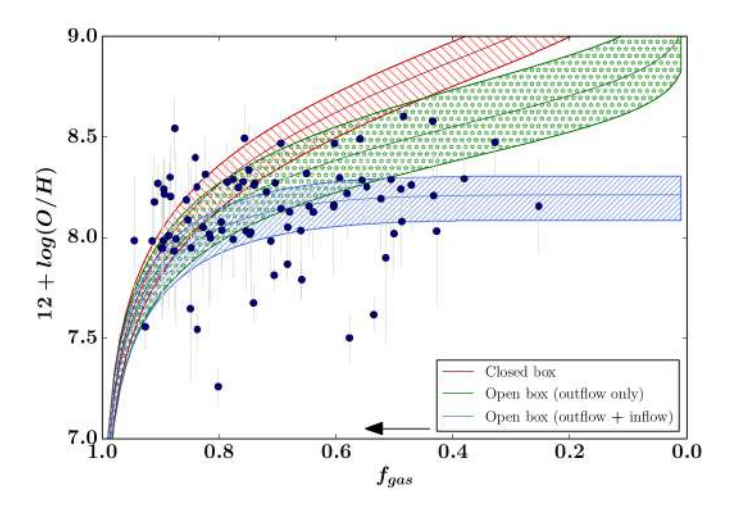


Figure 1.4: Analysis of a subsample of star-forming dwarf galaxies (blue dots) from Calabrò et al. (2017), comparing metallicity with the gas fraction  $f_{\rm gas}$ . The red, blue and green curves represent a closed-box model, an open-box model with outflows and inflows, and an open-box model with outflows only, respectively.

vant examples, like the COSMOS survey (Scoville et al., 2007), and the CANDELS survey (Koekemoer et al., 2011) with the Hubble Space Telescope (HST). On the same note, this decade has provided with great tools to further analyze primeval galaxies in ways never expected, with the James Webb Telescope Advanced Deep Extragalactic Survey (JADES, Eisenstein et al., 2023), centered on obtaining deep photometric and spectroscopic data from high-z galaxies, or the CEERS survey (Finkelstein et al., 2023), setting the stage for even more detailed catalogs in the near future (e.g., Dickinson et al., 2024).

With this taken into consideration, the main focus of our work is to gain insight into the evolution of galaxies with star formation activity, and to explore some of the techniques employed to study them. The main part of this task is marked by the detailed analysis of our spectroscopic data, so a proper understanding of the physical and chemical processes behind is fundamental.

### 1.3 Global properties of galaxies from photometric data

One of the most efficient tools for studying the global properties of galaxies is the modeling of their multiwavelength spectral energy distribution (SED) from photometric data. Through this method, it is possible to obtain rough estimates of the redshift, and once this redshift is fixed, it can provide simultaneously multiple physical parameters during the fitting process. Moreover, due to the spectral coverage -from UV to far infrared (FIR)-this method allows us to recognize different physical processes dominating at each domain (Walcher et al., 2010). To extract all this information and accurately describe properly the SED of a galaxy, the implementation of models to the observed photometric data is of the essence. Here, we give a brief description of the main ingredients generally considered, although a more in-depth review can be found in Conroy (2013).

To characterize a set of photometric data, the following elements are crucial for a successful SED fitting:

- Simple stellar populations (SSP), consisting mainly of:
  - isochrones (covering a stellar mass range)
  - spectral libraries (theoretical or empirical)
  - an initial mass function (IMF)
- Dust, consisting of:
  - attenuation (dust grains, polycyclic aromatic hydrocarbons (PAHs), ice)
  - emission (IR range)
- Composite stellar population (CSP), containing stars covering a range in ages and metallicities.
- Star formation history (SFH), which could be based on analytic or nonparametric functions.
- Nebular emission, separated in:
  - continuum emission (two-photon, free-bound, free-free)
  - recombination line emission, and collisionally excited emission

Several photometric surveys have been generated, covering a wide spectral range, with the determination of physical properties via SED fitting as one of their main purposes. To perform this important task, over the years, multiple codes have been developed, such as STARBURST99 (Leitherer et al., 1999), CIGALE (Boquien et al., 2019), or BAGPIPES (Carnall et al., 2018). These codes consider a range of input parameters, along with a large number of combinations of physical properties, and compare them with libraries of preexisting templates, following different methods to provide a best fit, e.g., nested sampling, grids, or Markov Chain Monte Carlo. From the resulting SED of a galaxy, we can gain information about its most fundamental properties, such as the SFH, the stellar IMF, total stellar mass, the amount of gas and dust, or the SFR. An overview of the stellar population synthesis technique is displayed in Fig. 1.5. The isochrones, IMF, and stellar spectra are in the three top figures, corresponding to the components of the SSP, present in the centermost figure. The chemical evolution and star formation history are displayed in the middle left figure, and the dust component is in the middle right figure. The bottom figure is the combination of these components as the CSP.

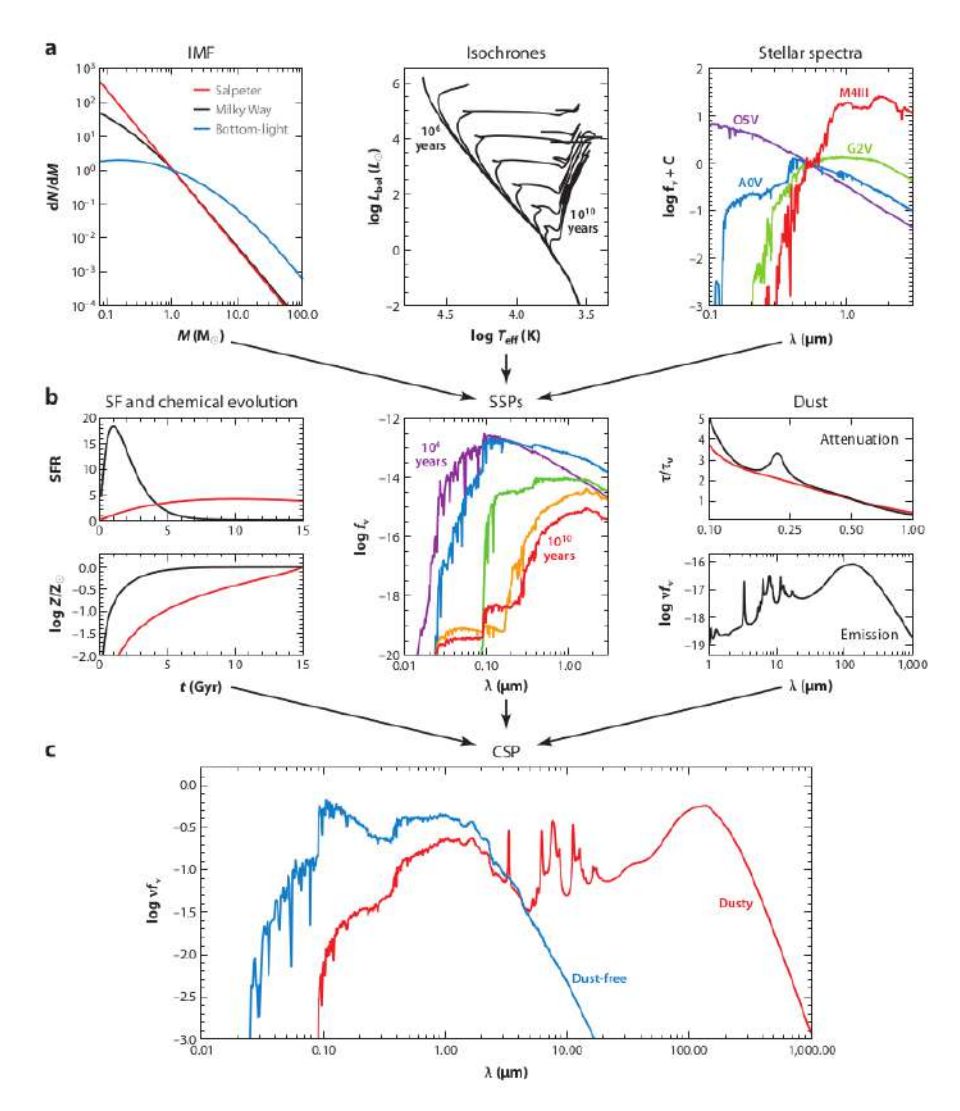


**Figure 1.5:** Overview of the Stellar Population Synthesis (SPS). The main ingredients necessary for the creation of a SSP (isochrones, stellar spectra, and initial mass function) are displayed in the three top figures, with the SSP represented in the center figure. The star formation history and chemical evolution are displayed in the middle left figures, and the dust component is represented in the middle right figure. These properties compose the CSP, represented with and without the contribution of dust attenuation in the bottom figure. Image taken from Conroy (2013).

## 1.4 Studying nebular properties of galaxies from spectroscopy

The optical spectrum of a galaxy is the result of the combination of the spectra of both young and old stellar populations and the nebular spectrum of their ISM (Osterbrock & Ferland, 2006). When a galaxy presents absorption lines, these are caused by atoms and molecules in stellar atmospheres, which absorb the radiation emitted at certain wavelengths (Brutti et al., 2005). This is indicative of older stellar populations, and such spectra are commonly found in elliptical galaxies, as well as in the bulge of spiral galaxies. Spiral galaxies can present absorption and emission components, due to the mix of young and old stellar populations in different parts of the disk. In the case of irregular galaxies (e.g., BCDs), the dominance of young O and B stars ionizing gas clouds is noticeable

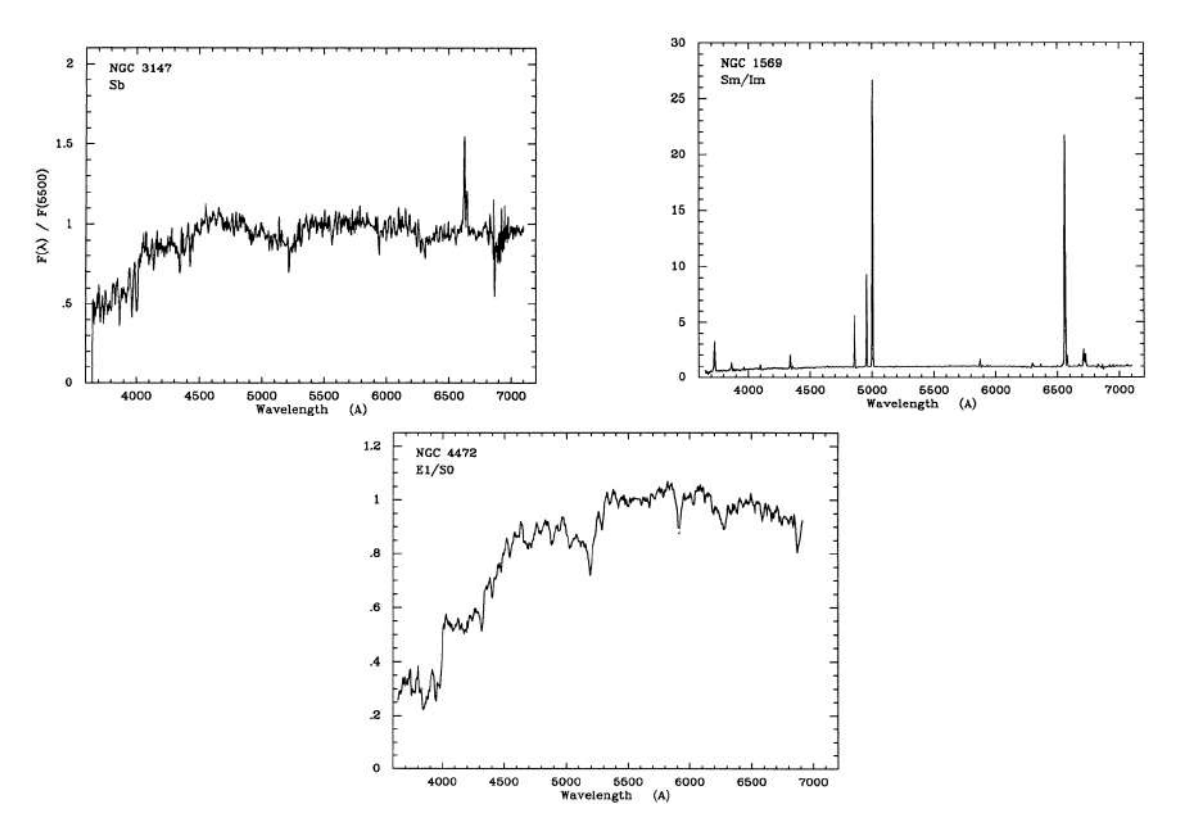


**Figure 1.6:** Examples of the spectra of different types of galaxies. Top left: Spectrum from an Spiral galaxy. Top right: Spectrum from an Irregular galaxy. Bottom: Spectrum from an Elliptical galaxy. Taken from Kennicutt (1992).

through the weak continuum and intense emission lines of the spectra. Fig. 1.6 provides examples of the spectra of these three types of galaxies.

In irregular galaxies the emission is caused by the photoionization from highly energetic photons, mostly in the UV range, coming directly from young O and B stars into gas clouds. The energy of these photons is enough to ionize the hydrogen atoms (E  $\geq$  13.6 eV), which frees their electrons, and when they recombine with another hydrogen nucleus, they cascade to the ground state, contributing with the emission of recombination lines (e.g., H $\alpha$   $\lambda$ 6563, H $\beta$   $\lambda$ 4861, H $\gamma$   $\lambda$ 4340, etc.). Both processes are visually represented in Figure 1.7.

Since gas clouds are not entirely composed of hydrogen, some other atoms can be ionized as well. Even though they are not as abundant, elements such as O, C, N, and others, can interact with the photons, or even with other atoms, in a process called collisional excitation. After an atom is excited either by a photon or by a collision with another atom, it can emit photons in forbidden lines when it relaxes to its lower-energy state (e.g., [O II] $\lambda\lambda 3727, 3729$ , [O III] $\lambda\lambda 4959, 5007$ , [N II] $\lambda\lambda 6548, 6583$ ). The generated photons may or may not escape, continuing the process of photoionization/recombination with other atoms. There are two cases for understanding this: Case A Recombination, where the gas cloud is optically thin, and ionizing photons can easily escape, and Case B Recombination, where the cloud is optically thick, so ionizing photons produced are absorbed for

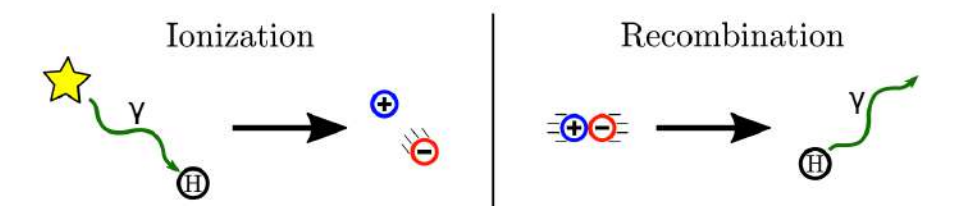


**Figure 1.7:** Ionization and recombination events. The left image represents the interaction between a photon and a neutral hydrogen atom, releasing its electron. The right image depicts the union of a free electron with an hydrogen nucleus, reforming it and in the way emitting a photon with energy of 13.6 eV, plus the excess kinetic energy from the particle. Image taken from Wise (2019).

other photoionizations (Peimbert et al., 2017). The latter is the most commonly used to interpret the different behaviors in spectra, along with some assumptions in temperature (T =  $10^4$  K), electron density ( $n_e = 100$  cm<sup>-3</sup>), and a theoretical ratio between H $\alpha$  and H $\beta$  (H $\alpha$ /H $\beta$  = 2.86, Osterbrock & Ferland, 2006).

In this thesis, we study star-forming galaxies, from which we can obtain valuable information from their intense emission lines, such as spectroscopic redshift. This is a fundamental parameter, as it helps to avoid inconsistencies when performing the SED fitting, by fixating the redshift parameter, instead of being a variable. We derive spectroscopic redshift by detecting distinctive spectral features, such as emission lines, and comparing them with rest-frame values (see Sect. 3.2 for more details). Dust extinction, metallicity, electron temperature and density, ionization conditions, and the ongoing star formation rate are also key properties that we derive. Originally thought as young objects, further investigation of BCD galaxies revealed that they are in reality chemically unevolved systems, with an old underlying population, that are currently undergoing a starburst episode (Amorín et al., 2007, 2009; Cairós et al., 2010).

# Sources of ionization: Diagnostic diagrams from optical emission line ratios

Previously, we commented on the ionization mechanism produced by very hot, young O and B stars (stellar photoionization). However, some galaxies can host active galactic nuclei (AGN), which can also emit great amounts of ionizing radiation. Another important ionization source is shocks, produced by different causes, such as interactions between galaxies, galactic outflows, or jets. All of these phenomena can considerably affect the shape of the optical spectra.

A problem that arose was the classification of these objects. At the beginning of the 1980s, AGNs (e.g., Seyfert galaxies, quasi-stellar objects (QSO), radio galaxies, etc.) were cataloged based on arbitrary properties such as morphology, or line width. This issue was addressed by Baldwin et al. (1981), and they proposed a quantitative, more global parameter, namely the ionization mechanism. Comparing two intense line ratios, they used the combination of  $[O III]\lambda 5007/H\beta$  vs.  $[N II]\lambda 6584/H\alpha$ , primarily because

of their low sensitivity to reddening and the distinct separation they provide between emission-line galaxies and QSOs based on their primary excitation mechanisms. This combination of emission-line intensity ratios is now known as the 'BPT diagram'. Later, other combinations were added, focused on a more proper classification between 'H II galaxies' and specific types of AGNs, such as low-ionization nuclear regions (LINERs), or Seyfert galaxies. One example is the work of Kennicutt & Keel (1984), where they include the ratio [S II] $\lambda\lambda$ 6717, 6731/H $\alpha$ , a ratio sensitive to the hardness of the ionization radiation. The work of Veilleux & Osterbrock (1987) put together all these diagnostics, as well as adding the line ratio between [O I] $\lambda$ 6300 and H $\alpha$ , and including an analysis of photoionization models to create a theoretical classification.

#### Incorporation of theoretical models

Kewley et al. (2001) proposed a theoretical approach to study these systems, using photoionization models. Comparing two stellar population synthesis codes (PEGASE v2.0, Fioc & Rocca-Volmerange, 1997; STARBURST99, Leitherer et al., 1999). The results obtained were presented in the form of BPT diagrams, including different theoretical grids and varying expressions such as the ionization parameter q, or metallicity Z. It is key to point out that there will be considerable differences in the output theoretical grids depending on the photoionization source; if the code of interest allows for binarity (e.g., the Binary Population and Spectral Synthesis code, BPASS, Eldridge et al., 2017), the resulting ionizing spectrum will be harder, shifting the models towards more extreme line ratios. There will also be differences with redshift, with more distant galaxies presenting more extreme ISM conditions, with the electron density, ionization parameter or metal abundances playing an important role in the displacement of the theoretical grids (Kewley et al., 2013). Fig. 1.8 and Fig. 1.9 (from Kewley et al., 2019), provide some examples of these results.

### 1.5 The secrets behind the emission lines of galaxies

As mentioned before, there is a wealth of important information hidden behind the emission lines of a galaxy spectrum. In this thesis, we focus on three key properties essential to characterize the ISM of a galaxy: electron density, electron temperature, and ion abundance. Using a set of relevant emission lines can give hints of these processes, as some lines trace different regions of the cloud. We review some of the classical definitions of these properties.

#### 1.5.1 Electron temperature

The electron temperature (T<sub>e</sub>) of oxygen is measurable by means of the auroral lines, whose excitation is highly sensitive to temperature. It is a key property, as it allows for the derivation of the abundance of oxygen, and electron density. In optical spectra,

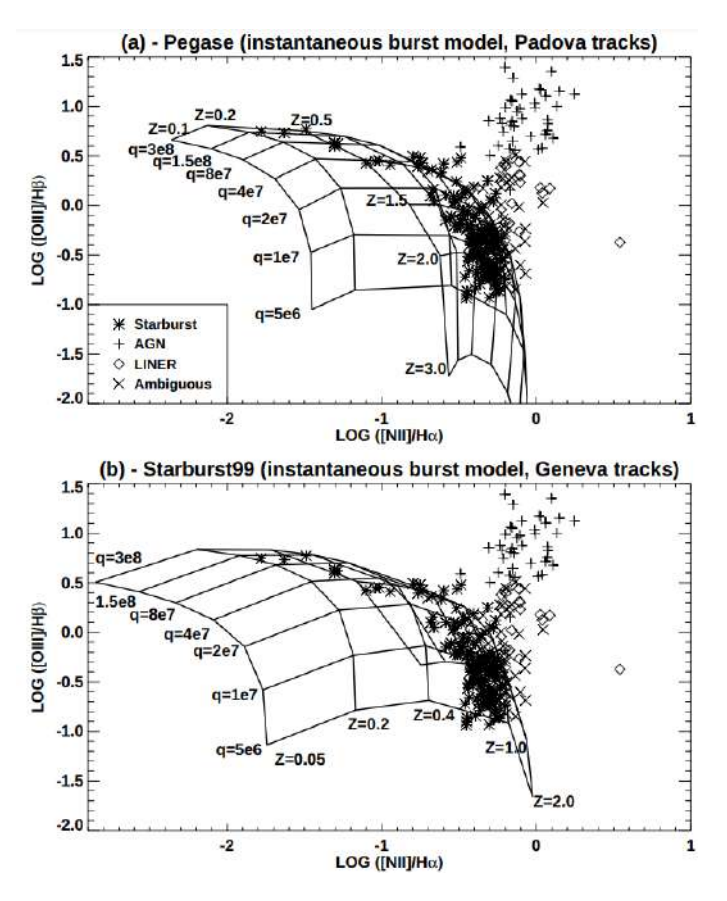


Figure 1.8: Example of the results of the models in the BPT diagram. The upper diagram is from the models of PEGASE, and the lower diagram from the STARBURST99 models. Both models consider different theoretical stellar tracks: PEGASE considers the Padova stellar tracks (Bressan et al., 1993), while STARBURST99 adopts the Geneva stellar tracks (Schaller et al., 1992). The theoretical grids represent the ionization parameter and the metallicity for various values. The crosses represent a population of AGNs, which fall outside of the allowed region for the combination of ionization parameter and metallicity, which could only imply some additional ionization mechanism. Image taken from Kewley et al. (2001).

the most used emission line is  $[O III]\lambda4363$ , in combination with the  $[O III]\lambda\lambda4959,5007$  doublet ([O III]4959,5007/[O III]4363). Additionally, the electron temperature of the  $[O II]\lambda\lambda3727,3729$  doublet is also useful; it traces the low ionization zone of a gas cloud, as opposed to the high excitation zone, traced by the electron temperature of [O III] (Garnett, 1992), and can be determined using the ratio between the  $[O II]\lambda\lambda3727,3729$  and  $[O II]\lambda\lambda7319,7330$  doublets. However, through photoionization models, an appropriate value can be derived from the electron temperature of [O III] (Pérez-Montero, 2017).

The difficulty of deriving electron temperature with this method lies in the faintness of the auroral  $[O\ III]\lambda4363$  line; this is an obstacle when investigating high-z galaxies, and can even be a problem for local galaxies. To overcome this issue, and derive expressions for abundance, empirical calibrations were designed, based only on line ratios between collisionally excited lines and recombination lines, the so-called "strong-line method". We review this issue in the following sections of this thesis.

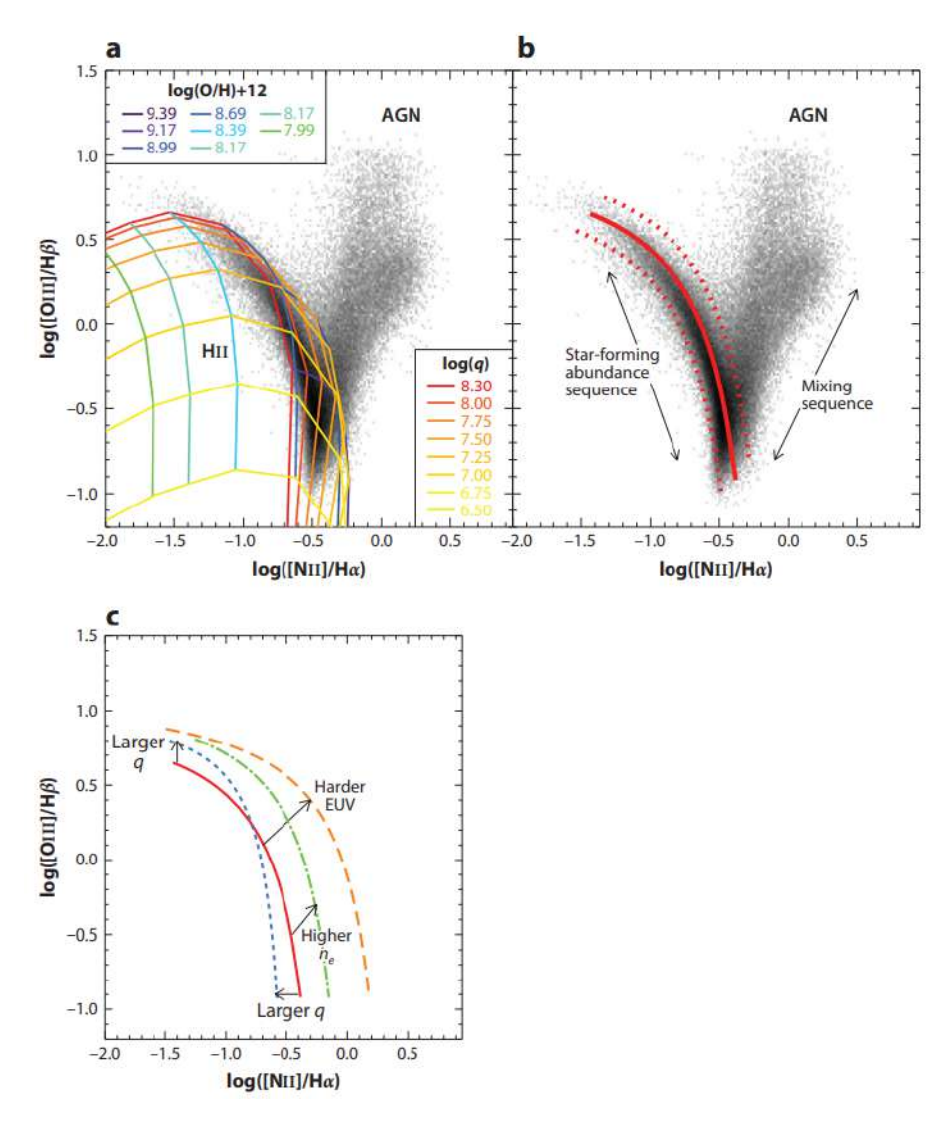


Figure 1.9: Similar to Fig. 1.8 but from a Neistein et al. (2006) sample. Upper left: theoretical grids with different values for metallicity and ionization parameter. Upper right: Variations for the mean star-forming abundance sequence (i.e., the region covered by H II galaxies from lower ionization to higher ionization). Lower: Variations for the ionization parameter and its effect on the position of the star-forming abundance sequence. Image taken from Kewley et al. (2019).

### 1.5.2 Electron density

In order to calculate the electron density  $(n_e)$ , we can use the line ratio of two lines from the same ion, emitted from different energy levels, and that count with similar excitation energies (Osterbrock & Ferland, 2006). Commonly used lines include the [O II] $\lambda\lambda$ 3727, 3729 [S II] $\lambda\lambda$ 6716, 6730 doublets. This is a very useful tool, because of the distance in wavelength between the doublets; if the [S II] doublet falls out of the spectral range, it is possible to use the [O II] doublet to try to derive the electron density. Nowadays the calculations for electron density and electron temperature can be made simultaneously when the necessary emission lines are present using computer programs like IRAF (Tody, 1986) or PyNeb (Luridiana et al., 2015), which take into consideration the atomic physics

behind the emission lines and find the best values (see Pérez-Montero, 2017 for a detailed description). Commonly adopted values of electron density and temperature for photoionized nebulae are in the order of 10<sup>2</sup> cm<sup>-3</sup> and 10<sup>4</sup> K, respectively (Osterbrock & Ferland, 2006), but they may vary more than a factor of 2 within galaxies.

#### 1.5.3 Metallicity

We review one of the key aspects of the study of galaxy evolution, as it can give insight about the star formation taking place in galaxies. To calculate the abundance we can use the ratio between certain emission lines and a recombination line. The abundance of oxygen (defined as  $12 + \log(O/H)$ , with the solar oxygen abundance adopted as  $12 + \log(O/H) = 8.69$ , Asplund et al., 2021) is commonly the most used in the literature, because it is the most abundant metal element, and its emission lines are very intense in the optical spectrum.

#### Direct method

The most reliable way to infer the oxygen abundance is by means of the electron temperature, as well as considering the value of the electron density. The line ratios [O II] $\lambda\lambda$ 3727, 3729/H $\beta$  and [O III] $\lambda\lambda$ 4959, 5007/H $\beta$  are used to calculate the abundance of ionized oxygen and doubly ionized oxygen, respectively, which are summed to obtain the total oxygen abundance (see Sect. 4.6.2 for specific equations). However, the main issue with this method is the extreme faintness of the [O III] $\lambda$ 4363 auroral line, being 10-100 times fainter than Balmer lines.

#### Strong-line method

As mentioned before, auroral lines are very faint lines, being very weak at low nebular temperatures or with poor signal-to-noise (S/N). To overcome this, empirical calibrations were designed, based on the comparison of ratios of more intense lines with metallicities derived following the direct method, as well as comparison with photoionization models (Pagel et al., 1979). We list some of the most used line ratios here:

- R23 =  $\frac{I(3727)+I(4959,5007)}{I(H\beta)}$  (Pagel et al., 1979)
- N2 =  $\log \left( \frac{I(6584)}{I(H\alpha)} \right)$  (Storchi-Bergmann et al., 1994)
- O3N2 =  $\log \left( \frac{I(5007)}{H\beta} \cdot \frac{I(H\alpha)}{I(6584)} \right)$  (Pagel et al., 1979)
- S23 =  $\frac{I(6716,6730)+I(9099,9532)}{I(H\beta)}$  (Vilchez & Esteban, 1996)
- R2 = log  $\left(\frac{\text{I}(3727)}{\text{H}\beta}\right)$  (Maiolino & Mannucci, 2019)
- R3 =  $\log \left(\frac{I(5007)}{H\beta}\right)$  (Maiolino & Mannucci, 2019)

- Ne3O2 =  $\log \left( \frac{I(3869)}{I(3727)} \right)$  (Nagao et al., 2006)
- N2O2 =  $\log \left( \frac{I(6584)}{I(3727)} \right)$  (Kewley & Dopita, 2002)

There are additional line ratios that can be used (see Kewley & Dopita, 2002; Pérez-Montero, 2017; Dopita et al., 2013; Maiolino & Mannucci, 2019), useful to derive not only oxygen abundances, but also nitrogen, neon, or sulfur. When calculating these properties, metallicity uncertainties are about 0.2 dex, corresponding to the dispersion in the calibrations. Additional systematic errors arise since some indicators are highly dependent on properties like the ionization parameter U (e.g., O32, R2, R3), dust extinction, or flux calibration. The methodology implemented to derive the metallicity also highly affects the resultant uncertainties too, either being calibrations based on the direct method or based on predictions from photoionization models (e.g., Bresolin et al., 2004; Garnett et al., 2004). This can result in offsets of more than 0.5 dex in metallicity, even for the same index (Kewley & Ellison, 2008), and can affect most importantly the calibrations which are dependent on other relative abundances, such as with the case of the N2 index and the N/O ratio (see Amorín et al., 2010 for a specific case). Possible solutions contemplate the combination of diverse indexes, aiming to minimize the uncertainties, either by means of calibrations consistent with the direct method (e.g., Curti et al., 2020; Sanders et al., 2021; Nakajima et al., 2022), or by combining the use of photoionization models and calibrations with the direct method, relying on a large coverage on physical parameters, and a model grid with priors that control the index dependencies (e.g., HII-CHI-MISTRY, Pérez-Montero, 2014, IZI, Blanc et al., 2015). Another important caveat when working with these calibrations is that each calibration is applicable only within specific metallicity ranges, thus special care is needed when selecting a calibration relation (e.g., Kewley & Dopita, 2002). Some ratios can also present positive properties, such as independence from extinction or flux calibration. This is the case of the N2 ratio, due to the small wavelength distance between [N II] $\lambda$ 6584 and H $\alpha$ . This feature can be used to solve the double-value problem of line ratios such as R23.

#### 1.6 Star formation rates

As with the case of metallicity, knowing the amount of gas being turned into stars is a crucial aspect of the study of galaxy evolution. This property is represented by the star formation rate (SFR). Currently, there are several methods to derive the SFR, with some methods tracing shorter timescales than others (Kennicutt, 1998). These tracers can be measured using the integrated light in the UV, the IR, or with recombination lines, along with synthesis models which assume a known IMF (see specific descriptions in Kennicutt, 1998 or Calzetti, 2012). The reasoning behind this is that the fluxes from these specific regions can trace the emission from high-mass stellar populations (Figueira et al., 2022). Some SFR tracers commonly used are:

- the UV continuum luminosity,  $L_{UV}$  ( $\lambda < 3000$  Å): can trace star formation on timescales of  $\approx 100-300$  Myr, coming from very luminous O and B stars. Observations from space telescopes, such as GALEX or HST can cover this wavelength range, which can be problematic due to its high sensitivity to dust extinction. The use of UV continuum luminosity can be combined with IR luminosity, which comes from re-emitted UV flux between  $5-1000~\mu m$  (Calzetti, 2012).
- Recombination lines: in the optical range the extinction-corrected luminosity of H $\alpha$  recombination line can trace star formation on timescales of  $\lesssim 20$  Myr due to ionizing photons from H II regions.
- the Far-infrared (FIR) continuum luminosity,  $L_{FIR}$  (10  $\mu m < \lambda < 1000 \ \mu m$ ): due to dust that has been heated by the flux of the young stars, reprocesses it in longer wavelengths, tracing high-mass stars in timescales of  $\sim 1$  Gyr.

## 1.7 Scaling relations

As has been established before, galaxies present a baryon cycle, in which gas is accreted from the ISM, stars are formed, and when they die, expel metals, contributing to the enrichment of the medium. The key aspect of this cycle is to understand how galaxies change their physical properties, and evolve through time. One of the tools that have been implemented to analyze this process is through the comparison of observed properties, in particular those described in previous Sections. We briefly review the logic behind the main scaling relations for SFGs.

#### Mass-metallicity relation

Relating the stellar mass of a galaxy with its metallicity is a powerful tool for understanding how the baryon cycle operates. The mass-metallicity relation (MZR) pictures efficiently the amount of gas converted into stars by means of the stellar mass and, at the same time, relates this stellar mass to the abundance of the galaxy (Lequeux et al., 1979; Tremonti et al., 2004; Zahid et al., 2014). This helps to understand how the metals are processed by stars, and puts constraints on the properties when making theoretical models. With the advent of large photometric surveys, better resolution spectra, and the possibility of obtaining more precise stellar masses from SED fittings, remarkable progress was made in the study of baryonic processes, their impact on the internals of galaxies, and the effects using the MZR. In particular, Tremonti et al. (2004) provided some of these new results, analyzing a sample of 0.005 < z < 0.25 SDSS galaxies. They found a very tight correlation, and implemented chemical evolutionary models to attempt an explanation of this. They suggested the presence of outflows, produced by the most massive stars, able to expel these metals due to the shallowness of their potential wells, but did not reject the possibility of secondary processes. Fig. 1.10 shows the MZR found with their SDSS data.

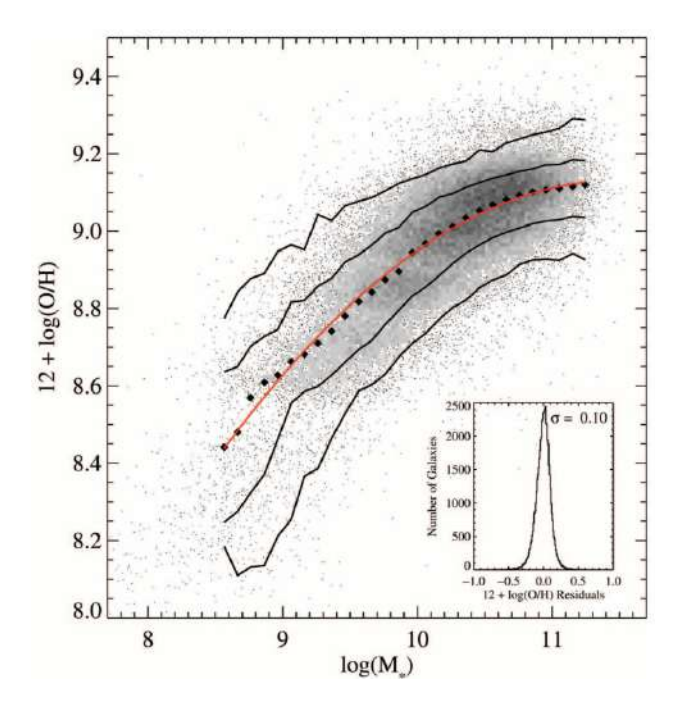


Figure 1.10: Mass-Metallicity Relation from Tremonti et al. (2004), using theoretical models to derive metallicity. Black diamonds are the median in 0.1 dex bins in mass, each with at least 100 data points. The black lines represent the contours enclosing 68% and 95% of the SDSS-DR4 data, at 0.005 < z < 0.25, and the red line represents a polynomial fit.

Another key part of their results was the fact that the MZR appeared to flatten for high stellar masses. Taking this into account, for the Milky Way galaxy, with  $\log(M_{\star}/M_{\odot}) \sim 12$  (Bobylev & Baykova, 2023), it would imply that for this normalization of the MZR, derived from photoionization models, it has a metallicity  $12 + \log(O/H) \gtrsim 9.0$ , higher than the solar value,  $12 + \log(O/H) = 8.69$ . The issue of the flattening of the MZR at high stellar mass was addressed in later investigations, such as Andrews & Martini (2013), where after a similar analysis, they found that the MZR flattens and becomes independent of stellar mass at  $M_{\star} \sim 10^{10.5} M_{\odot}$ . One caveat about their method is that it considers the stacking of SDSS spectra in order to detect the [O III] $\lambda 4363$  line, and in this way apply the direct method with their sample. This can cause a shift in the normalization  $\sim 0.3$  dex towards lower metallicities compared to the theoretical calibration, although maintaining the overall shape of the MZR. In the following years, further advances were made in the modeling of the processes seen in SFGs, which were confirmed with more observational data (see Maiolino & Mannucci, 2019 for an in-depth review).

#### Different MZRs with different methods

It is important to point out one of the main issues with defining a MZR: according to the method employed to derive the metallicity, the curve that is generated when comparing it with stellar mass will vary. Indeed, this result can be seen in Fig. 1.11, from a work from Andrews & Martini (2013).

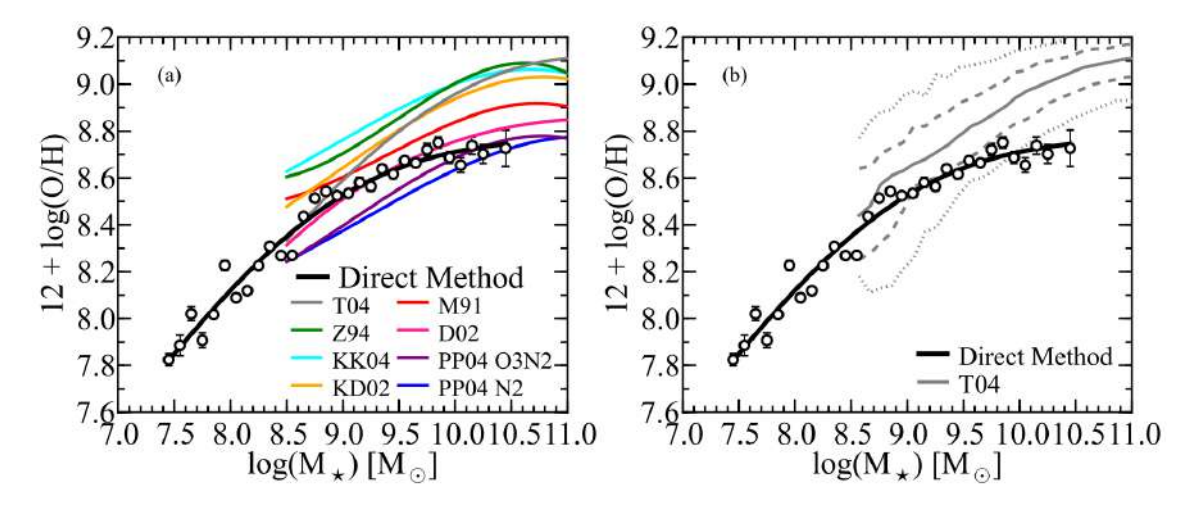


Figure 1.11: Left: MZR from abundances from theoretical and empirical calibrations from several authors compared with the MZR following the direct method after stacking SDSS spectra (black). Right: Same MZR with direct method (black) compared with the contours from the MZR derived using theoretical calibrations from Tremonti et al. (2004). The direct method MZR is  $\sim 0.3$  dex displaced towards lower metallicities, while keeping the overall shape of the curve. Image taken from Andrews & Martini (2013).

#### The Fundamental Metallicity Relation

Another physical property that has been related to the MZR is the SFR. In works such as Ellison et al. (2008), the stellar mass is compared to metallicity, but with bins defined by the specific star formation rate (sSFR = SFR/ $M_{\star}$ ). It was found that there is an anti-correlation between sSFR and low metallicity for a given stellar mass. Following this discovery, Mannucci et al. (2010), using a sample of local and high-z galaxies from SDSS, AMAZE and from previous results, considered that SFR should have a connection with metallicity, pointing the importance of the cycle of gas infall and recycling, affecting the rate in which stars are formed. They named this parameter space the fundamental metallicity relation (FMR), defining

$$\mu_{\alpha} = \log(M_{\star}/M_{\odot}) - \alpha \log(SFR/M_{\odot} \text{ yr}^{-1}),$$

with  $\alpha$  being 0.32, based on the quantity that minimizes the scatter when comparing  $\mu_{\alpha}$  with metallicity, as seen in Fig. 1.12. Using empirical calibrations to derive metallicities, and considering the emission of H $\alpha$  as a proxy for deriving the SFR, they find that their MZR shares many similarities with that of Tremonti et al. (2004). Fig. 1.13 shows the results, where the same flattening of the curve is visible at  $\log M_{\star} \sim 10.9$ . When including SFR as a third parameter, it is clear that SFR decreases as metallicity increases, and vice versa, for a given stellar mass. This can be explained considering that the stellar mass observed in a galaxy is the result of the gas that has turned into stars (SFR), while the proxy of the star formation history is metallicity, describing the past generations of stars (Lara-Lopez et al., 2013).

In Lara-López et al. (2010), using multiple samples at redshfits  $z \sim 0.1, z \sim 0.8$ ,

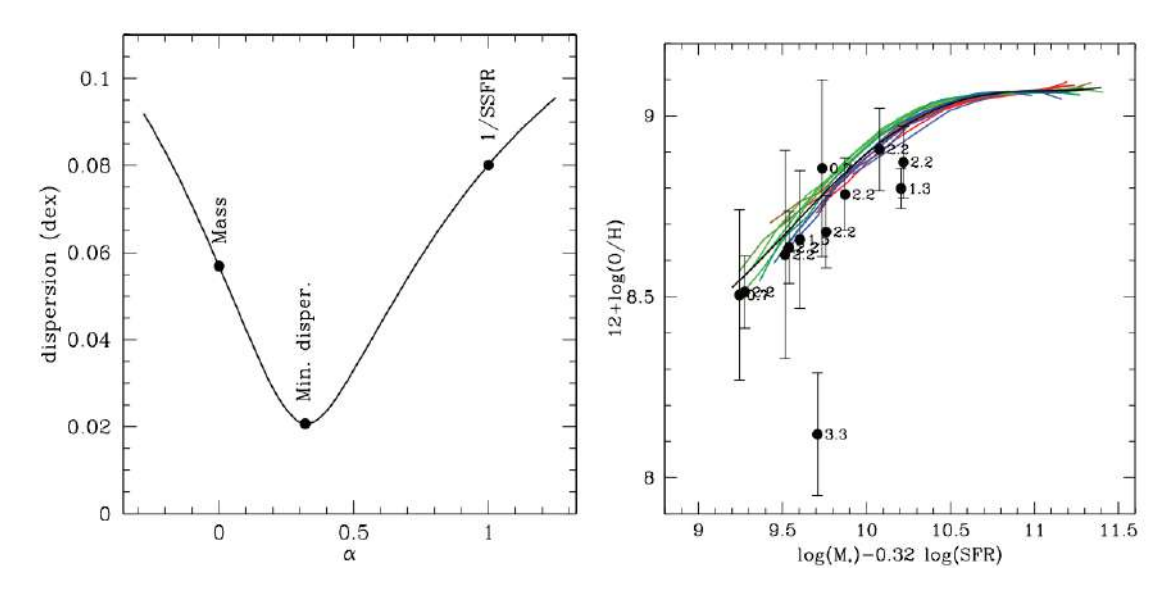


Figure 1.12: Results from the FMR. Left: Minimal scatter of the parameter  $\alpha$ , located at 0.32. Also is visible the value of FMR for  $\alpha = 0$  and  $\alpha = 1$ , being  $\log M_{\star}$  and  $-\log(sSFR/yr^{-1})$ , respectively. Right: FMR plotted against metallicity, with the high-redshifts of the sample plotted with black dots. The polynomial fit is also plotted in black, while SDSS galaxies are plotted as colored lines. Image taken from Mannucci et al. (2010).

 $z \sim 2.2$  and  $z \sim 3.3$ , a fundamental plane is designed, relating the contributions from metallicity and SFR, in the form of a linear function:  $\log (M_{\star}/M_{\odot}) = \alpha(12 + \log(O/H)) + \beta(\log(SFR/M_{\odot} \text{ yr}^{-1})) + \gamma$ . With this definition, they suggest that stellar mass could be derived from SFR and metallicity in star-forming galaxies.

There are some caveats that must be taken into consideration when comparing these observables. Mainly, the shape of the FMR is dependent on the selection of the method to derive SFR, stellar mass and metallicity. In particular, Andrews & Martini (2013), using the direct method to derive abundances, found an  $\alpha$  parameter of 0.66, much higher than those previously reported (e.g., Mannucci et al., 2010 reported an  $\alpha$  of 0.32, following the strong-line method). They argue that these differences might be related to some dependencies coming from the strong-line method on the physical properties that correlate with SFR. In general, there is a dispersion of  $\sim 0.2$  dex in this relation, with an increase towards lower masses ( $\log(\mathrm{M_{\star}/M_{\odot}}) < 10$ ).

#### 1.7.1 Evolution with redshift

With the advent of new surveys and the expansion of the redshift range for observations, new studies could be performed, particularly focusing on the comparison between local and high-z galaxies. The results provided evidence pointing towards an apparent evolution of the main physical parameters with redshift in the BPT diagram, such as Fig. 1.14, where a sample of  $z \sim 2$  galaxies from Garg et al. (2022) is compared with local SDSS galaxies. This further motivated the investigation of samples at z > 1 and beyond, to investigate the possible explanations for this behavior (e.g., Kewley et al., 2013; Steidel et al., 2014).

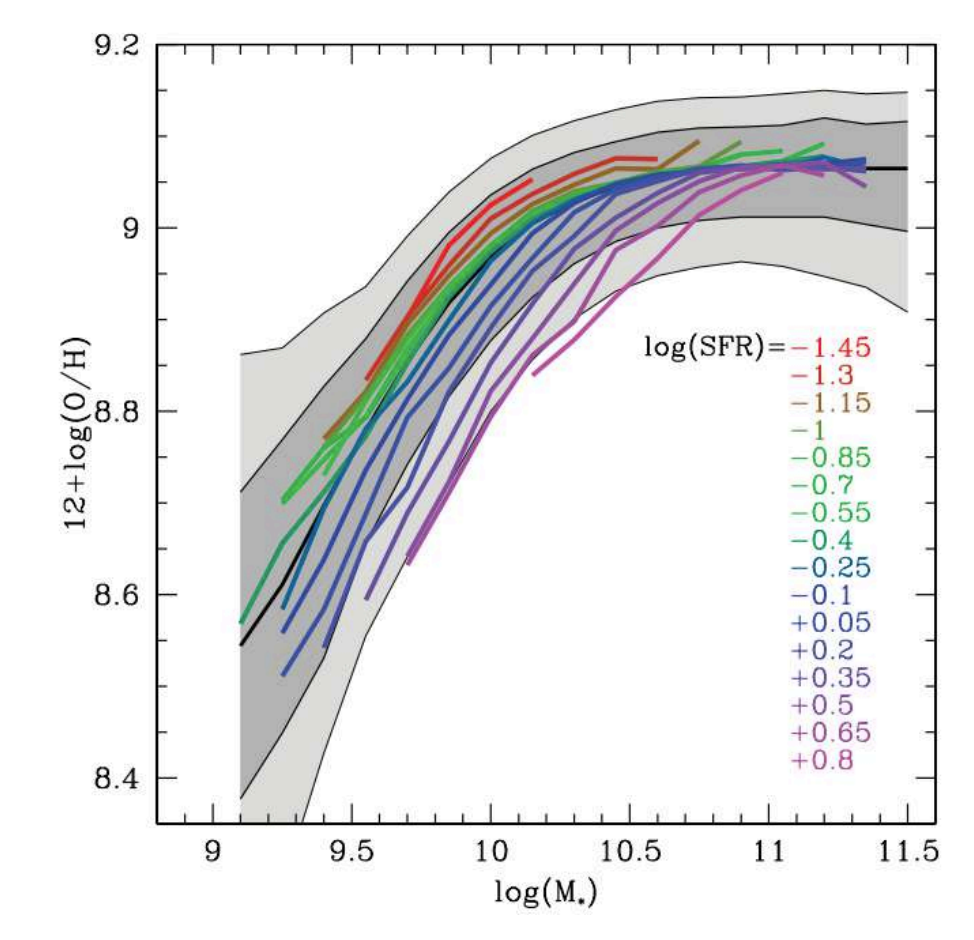


**Figure 1.13:** Mass-metallicity relation from an SDSS sample presented in Mannucci et al. (2010). The colored curves represent median metallicities for a given value of SFR. The gray shaded regions are the same contours enclosing the 68% and 95% ofd the SDSS-DR4 data obtained in Tremonti et al. (2004) (see Fig. 1.10).

The position of high-z galaxies appeared displaced from local galaxies, leading to suggest that these type of galaxies might present more intense ionization parameters, contribution from extreme ultraviolet (EUV) radiation, and higher star formation activity.

This behavior is also seen in the MZR, with reports of a trend similar to that of local galaxies up to  $z \gtrsim 2.5$ , with an invariant slope (Erb et al., 2006; Mannucci et al., 2010; Sanders et al., 2021), but also with higher redshift galaxies being less metal-rich. An example of this is presented in Fig. 1.15, where the high-z sample does not reach the flattening point as the  $z \sim 0$  galaxies, but clearly has less metal content. At higher redshifts, the work of Curti et al. (2024) showed that for a sample of SFGs at z = 3 - 10 the MZR presents a different slope compared to the  $z \sim 0$  MZR, which would suggest a difference in the feedback mechanisms depending on the redshift. These brand-new results allow for the constrain of cosmological simulations and chemical evolution models, providing with more insight of the processes which regulate the growth of early galaxies.

Lara-Lopez et al. (2013) suggested that there is an equilibrium between SFR and the metallicity, so at higher redshifts it is expected to get galaxies with higher SFR, which implies less metal content, due to the less enriched gas; in the local Universe we see that

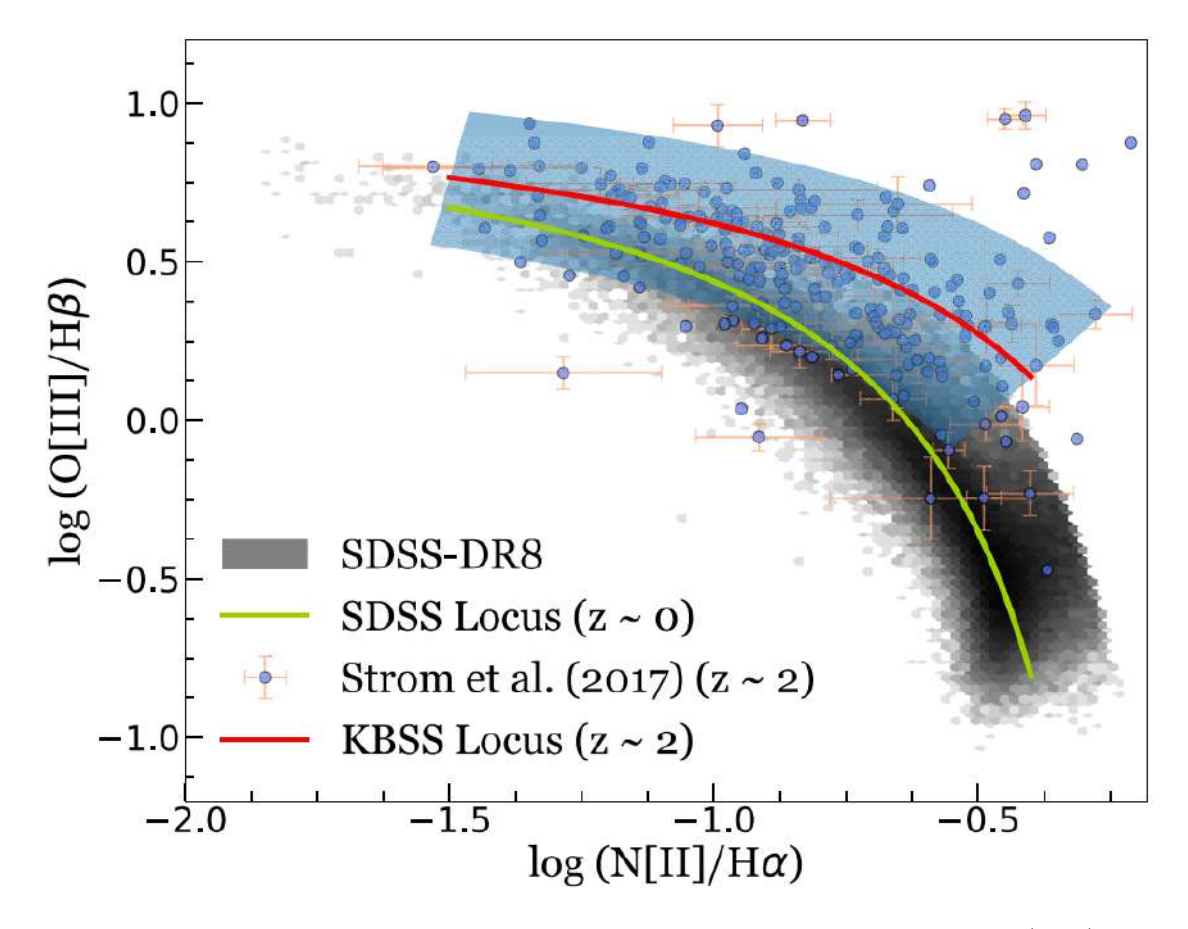
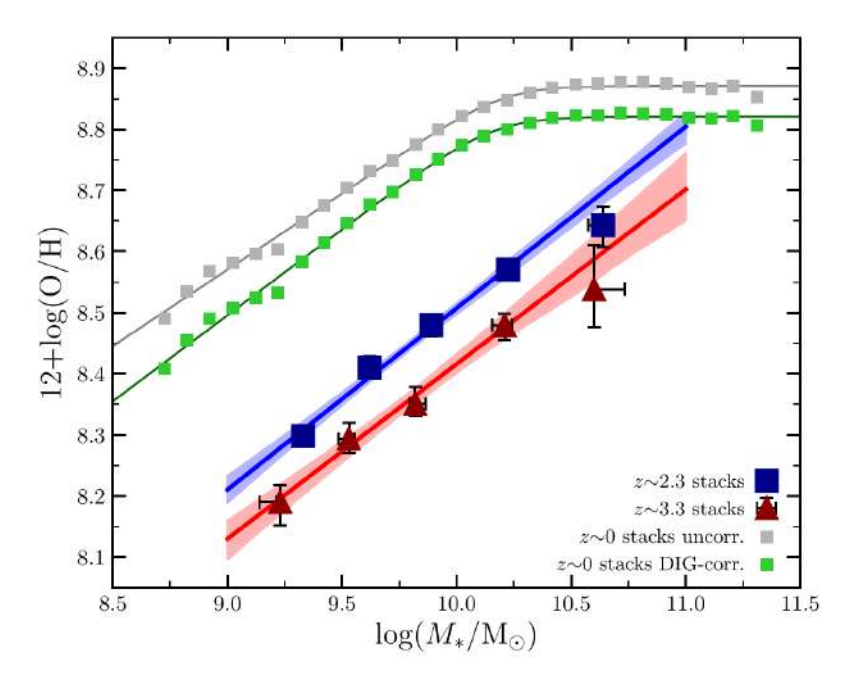


Figure 1.14: BPT diagram from samples at  $z \sim 0$  and  $z \sim 2$ , taken from Garg et al. (2022) Black hex bins represent local SDSS-DR8 galaxies. The blue points are from a sample of KBSS galaxies from Strom et al. (2017). The green and red curves represent the polynomial fits for the local and high-z galaxies, respectively, and the blue-shaded region is the intrinsic scatter relative to the red best-fit curve.

this situation flips over and stars formed by later generations present higher metal content, resulting in lower star-forming activity (lower SFRs).

Finally, the FMR has been target of study for this same purpose, with reports of a non-evolutionary trend with metallicity (Mannucci et al., 2010), at least up to  $z\sim 3$  (Sanders et al., 2021). After an extensive chemical analysis, they concluded that this happens because the gas fraction and the mass-loading factor do not evolve with z either, suggesting that this might be because the metal loading factor must equal the outflow mass loading factor. For a higher-z sample, at  $z\sim 3.4$ , Troncoso et al. (2014) found a deviation from the FMR, reporting metallicities  $\sim 0.34$  dex lower than local galaxies, but with no evidence of a correlation between this and the dynamical properties of the galaxies, or with interactions. Similar results are reported in Curti et al. (2024), for a sample of deep JWST/NIRSpec galaxies at 3 < z < 10, from the JADES program.



**Figure 1.15:** MZR for a sample of local SDSS (green (diffuse ionized gas-corrected) and gray (diffuse ionized gas-uncorrected) squares),  $z \sim 2.3$  and  $z \sim 3.3$  galaxy bins. The solid lines represent the polynomial fits of each group. Image taken from Sanders et al. (2021).

#### 1.8 Motivation and aims of this work

In the previous sections, we briefly reviewed the main concepts on relevant aspects of galaxy formation and evolution that will be addressed in this thesis. Several key questions regarding the main properties of galaxies beyond the local universe remain unanswered, which are key for studying their cosmic evolution.

There is a particular interest in studying the evolution of dwarf galaxies at z < 1, in order to understand until when in the cosmic time galaxies keep forming. However, these low-mass systems can be extremely hard to detect and even harder to analyze due to their faintness. For this reason, the use of deep spectrophotometric data can be an especially useful tool in this important task. However, despite existing previous works using wide spectroscopic and photometric surveys, they are severely incomplete in the low-mass range  $(M_{\star} < 10^9 M_{\odot})$ , turning the study of the ISM properties into a major challenge for low-luminosity systems.

We define our scientific objective to be the characterization of the low-mass population of galaxies from z 0.2 to z 1, spanning a range of more than 6 billion years of evolution. To achieve this, we study one of the deepest HST cosmological fields, specifically the one containing the massive cluster of galaxies, Abell 370 (A370, Fig. 1.16). This is a massive cluster ( $M_{200} = 2.2 \times 10^{15} M_{\odot}$ ; Niemiec et al., 2023), located at redshift z = 0.375 (Lagattuta et al., 2022), in the constellation Cetus. Due to its strong lensing properties, essential to our objectives and widely studied in literature (e.g., Soucail et al., 1987; Richard et al., 2010; Lotz et al., 2017; Lagattuta et al., 2022; Niemiec et al., 2023),

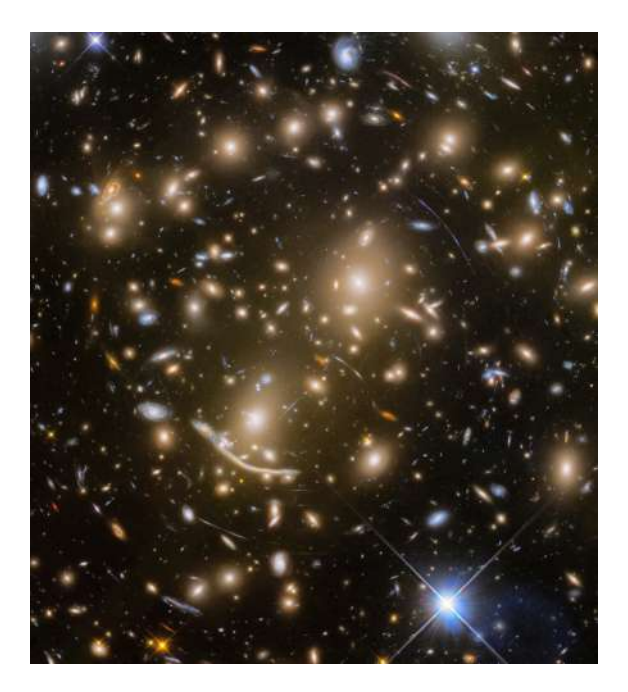


**Figure 1.16:** Color image of Abell 370, using the *HST* F606W, F435W, F814W, F105W, F125W, F140W, and F160W filters. Image taken from https://esahubble.org/images/heic1711a/

this cluster has been selected to perform our search of low-mass dwarf galaxies, as we will be able to detect systems located in the background that would otherwise be too faint to detect and study, in addition to galaxies in the foreground, and also cluster members.

The main scientific questions that this thesis addresses can be summarized as follows:

- 1. What are the least luminous dwarf galaxies that we can find and study spectroscopically in the redshift range 0.2-0.9? What are their SFRs, stellar masses, and nebular properties?
- 2. What are the trends followed by galaxies in the low-mass/luminosity end of scaling relations of mass, SFR, and metallicity?
- 3. What is the relation that exists between the physical processes that affect star formation and feedback of dwarf galaxies?
- 4. Can we find galaxies with particularly extreme properties, such as extremely young, metal-poor systems, which could serve as probes for the early stages of chemical evolution?

As specific objectives, we propose to tackle the following specific goals:

 Define a sample of emission line galaxies, based on the detailed inspection of a datacube centered on the galaxy cluster Abell 370, and focus on detecting the intense emission lines of these characteristic objects.

- Study the main integrated physical properties, i.e., SFR; stellar masses; metallicities, from this sample of young dwarf galaxies, performing a spectrophotometric data analysis using available data from publicly available observational data.
- Make use of the uniquely available ultra deep spectra to measure the most intense emission lines using a novel line measuring tool and derive the main nebular properties of the sample based on measured emission line ratios, such as dust extinction, ionization conditions, and gas-phase metallicity. This also contemplates the identification of low-metallicity galaxies with detections of the [O III] $\lambda 4363$  auroral line when possible, aiming to employ the direct method to derive properties such as electron density or electron temperature.
- Attempt to explore the low-mass end of the fundamental scaling relations, such as the stellar mass-metallicity relation, and its apparent dependance with star formation rate, while discussing our results in the context of previous works.

## 2 | Observations

## 2.1 Spatially-resolved spectroscopy

MUSE (Multi Unit Spectroscopic Explorer) is a panoramic integral-field spectrograph (IFS), located at the UT4 at the 8m Very Large Telescope (VLT) at the Paranal Observatory of the European Southern Observatory (ESO). It possesses a spatial sampling of 0.2 arcsec/pixel, with a wavelength coverage primarily in the optical range, ranging from 4750 to 9351 Å, a 1 arcmin<sup>2</sup> field of view, a mean spectral resolution of  $\approx 100 \text{ km s}^{-1}$ , and a spectral sampling of 1.25 Å/pixel (Bacon et al., 2010).

MUSE also has a throughput focused on the detection of very faint sources, implying very long integrations, which poses a challenge to the stability and calibration of the instrument. Figure 2.1 shows a cartoon illustrating how an Integrated Field Unit (IFU) operates: it receives the signal in each pixel and sends it to the spectrograph, where it generates a single spectrum for each individual pixel, and generates a datacube with two axes representing the 2D field, and a third spectral axis representing the spectral dimension.

The datacube was retrieved from the ESO Science Archive<sup>1</sup> Phase 3, based on programme 096.A-0710(A) (PI: Bauer) presented in Lagattuta et al. (2019), which was a follow-up of a work presented in Lagattuta et al. (2017), programme 096.A-0115(A) (PI: Richard). It is composed of a large mosaic that covers  $\sim 4 \text{ arcmin}^2$ , totaling 18 h of on-source exposure, reaching an AB magnitude at  $5\sigma$  of 25.74. This is significantly deeper than the usual AB magnitudes for the normal observations (22.7 for the R band, with (S/N) equal to 10).

MUSE was used in Wide-Field Mode (WFM), without considering adaptive optics (AO), and with individual exposures of up to 30 min. The observations were performed between November 20, 2014, and June 28, 2016, with a median airmass and seeing of 1.17 and 0.68 arcsec, respectively. Fig. 2.2 shows the total area covered by MUSE compared to an *HST* image, while also describing the exposure times of the different zones. The area where multiple images of background galaxies are expected to be represented is outlined with the black thick line. The final datacube includes the central area of the galaxy cluster, where the lensing effects are higher, and is complemented with 28° rotation exposures to cover the outer regions of the cluster. This datacube was later divided into two regions, North (N) and South (S), divided along the separation between the two centermost datacubes

<sup>1</sup>http://archive.eso.org/cms.html

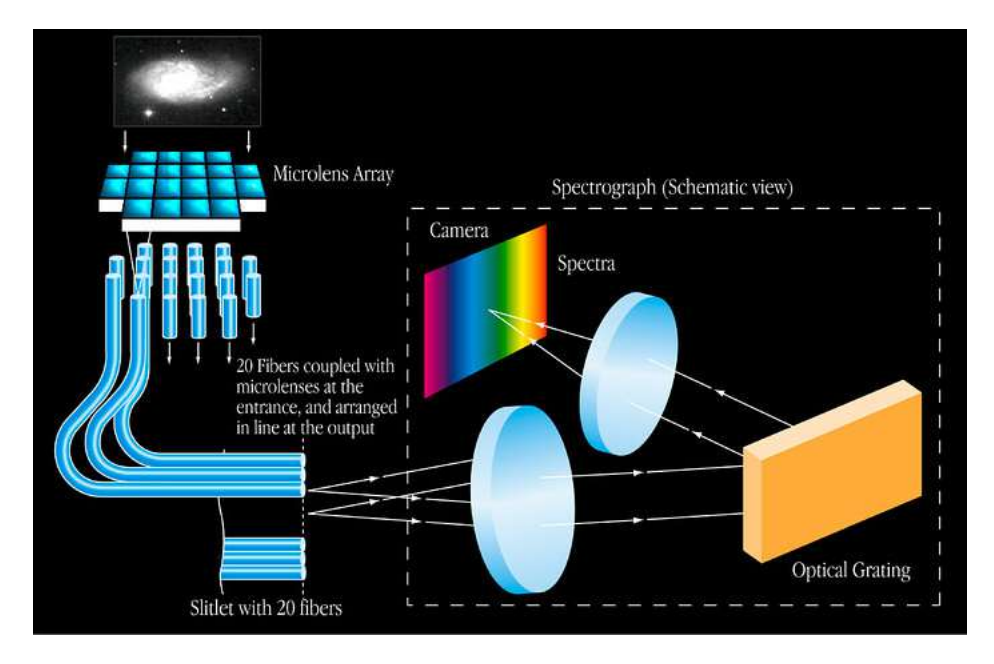


**Figure 2.1:** Cartoon representing how Integral Field Spectrographs operate. It consists of a microlens array that guides the light from a small sky area and sends it on to the spectrograph (illustrated inside the dotted box) to later be converted into an individual spectrum, and combine each spectra to generate a datacube, with two physical dimensions plus the spectral information of the target. Image taken from ESO.

from the mosaic. This leaves each region with approximately three individual datacubes.

#### 2.1.1 Datacube reduction

The MUSE-DEEP initiative involves combined observations across observation blocks (OB), conducting multiple visits to the same target, with the ultimate goal of merging the input files to achieve high-depth observations. In the deepest datacubes, an integration time of more than 30 hours is reached. The data were processed using the MUSE pipeline, version muse-1.6.1 and later. The main pipeline, which compares the fundamental steps and differences with the standard MUSE reduction pipeline (Weilbacher et al., 2012, 2014), is detailed in the ESO Phase 3 Data Release Description<sup>2</sup>. We provide a concise summary of the steps involved.

First, individual raw files are preprocessed, following the routine muse\_scibasic and the sky product files (if available) are processed with muse\_create\_sky, in order to create files for sky subtraction. After this, pixel tables are created and an alignment step is performed. Then, the combination is performed, making sure of measuring the relative alignment of the input data. When the datacube is combined, the routine muse\_exp\_align creates a coordinate offset table for automatic exposure alignment, correcting the instrumental alignment errors, which are more likely when there is more than one observation. Fig. 2.3 shows this procedure, for a reduction without and with a SKY observation. The final MUSE-DEEP science data product offers two 3D image extensions:

<sup>&</sup>lt;sup>2</sup>https://www.eso.org/rm/api/v1/public/releaseDescriptions/102

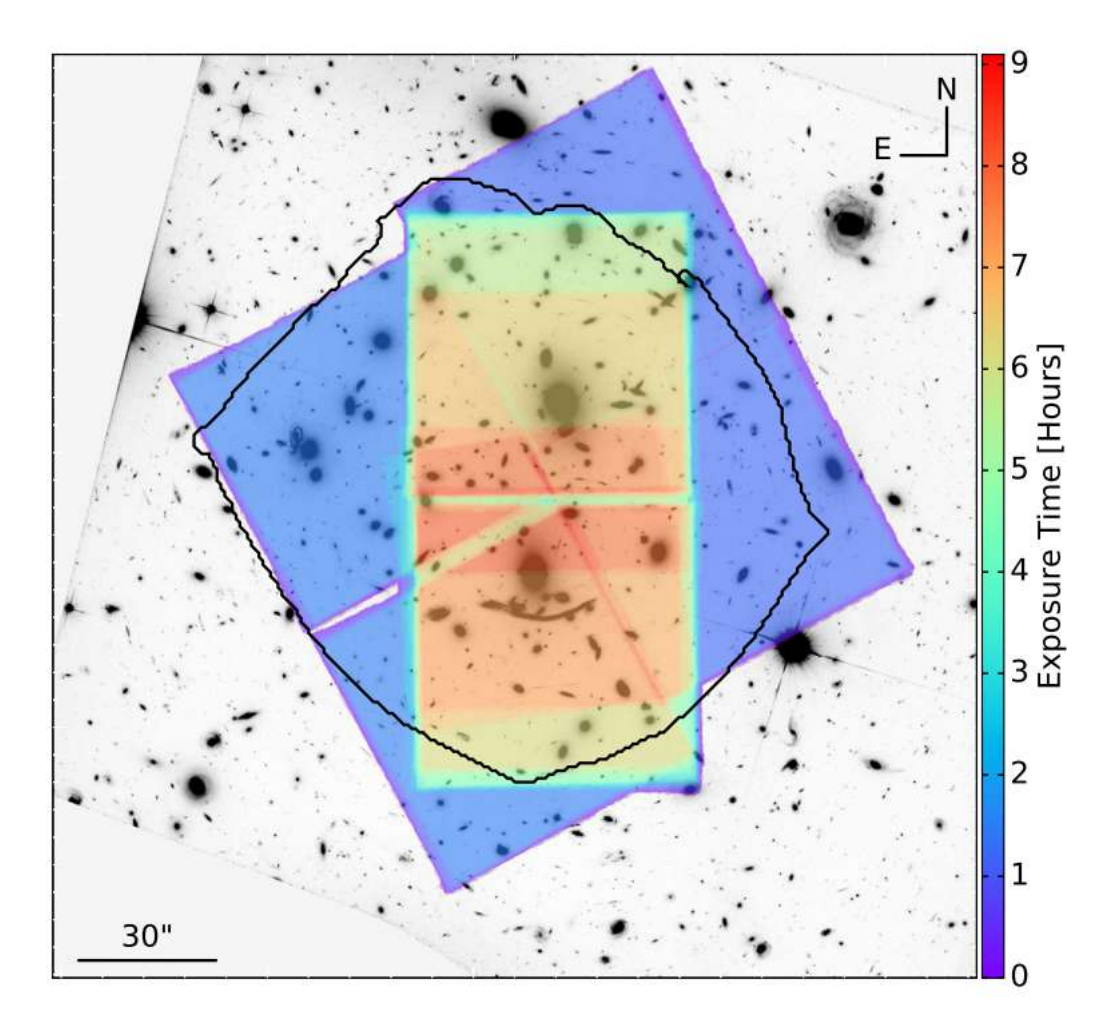
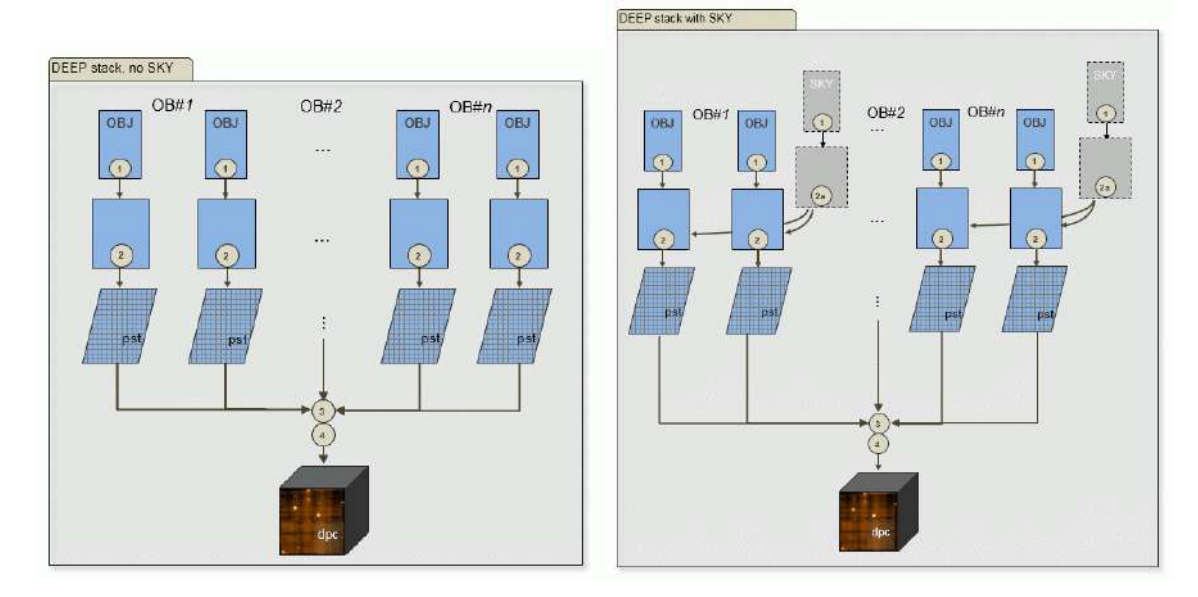


Figure 2.2: Exposure-time map of the mosaic covering Abell 370, taken from Lagattuta et al. (2019). The longest exposure times are those from the central region of the galaxy cluster due to its higher lensing properties. The outer regions correspond to 28° rotation exposures in order to cover the most of the *HST* WFC3 footprint, and the area where multiple images of background galaxies are expected is be represented with the black thick line (see Lagattuta et al. (2019) for a detailed analysis).

- 1. a 3D datacube with two spatial dimensions and one wavelength axis, with fluxcalibrated spatial pixels
- 2. a 3D datacube with the errors (variance)

### 2.1.2 Background subtraction: Zurich Atmosphere Purge

ZAP (Zurich Atmosphere Purge, Soto et al., 2016) is a tool developed specifically for MUSE, utilizing principal component analysis (PCA). It effectively reduces sky emission residuals while leaving astronomical sources unaltered. ZAP employs a different approach compared to the standard pipeline, which relies on a sky-subtraction algorithm dependent on the line spread function (LSF) and an accurate wavelength solution. The original cluster datacube is presented in the top panel of Fig. 2.4. We reprocessed the MUSE datacube



**Figure 2.3:** Left: Reduction cascade for N input files and n observations. 'pst' marks the pixel-table products of muse\_scipost. The final product is the deep combined datacube (dpc). Right: Reduction cascade for N input files and n observations, with M SKY observations available. Pictures taken from the ESO Phase 3 Data Release Description.

resulting in a smoother image, making it more suitable for detecting faint sources, aligning with the goals of the MUSE-DEEP initiative. The final cluster image after applying ZAP is shown in the bottom panel of Fig. 2.4.

#### 2.1.3 Modifications to the main datacubes

Before selecting the sample of galaxies for this work, we performed a previous step involving a crop of the two main datacubes (N and S, top panel of Fig. 2.5), this was because, due to their large dimensions (750x520 voxels, approx.), manipulating them was highly RAM consuming. We divided the area into three regions, resulting in a total of six smaller datacubes: three from the northern zone and three from the southern zone. This allows us to categorize the galaxy sample based on both the region (1,2,3) and the zone (N,S). It is important to point out that all the information regarding the third dimension (wavelength) is always maintained, without any interpolation or manipulation, only that they are split into more manageable pieces for the analysis. The bottom panel of Figure 2.5 shows the final result of this operation. The rest of the processes taken to work with the resulting datacubes were performed using python scripts.

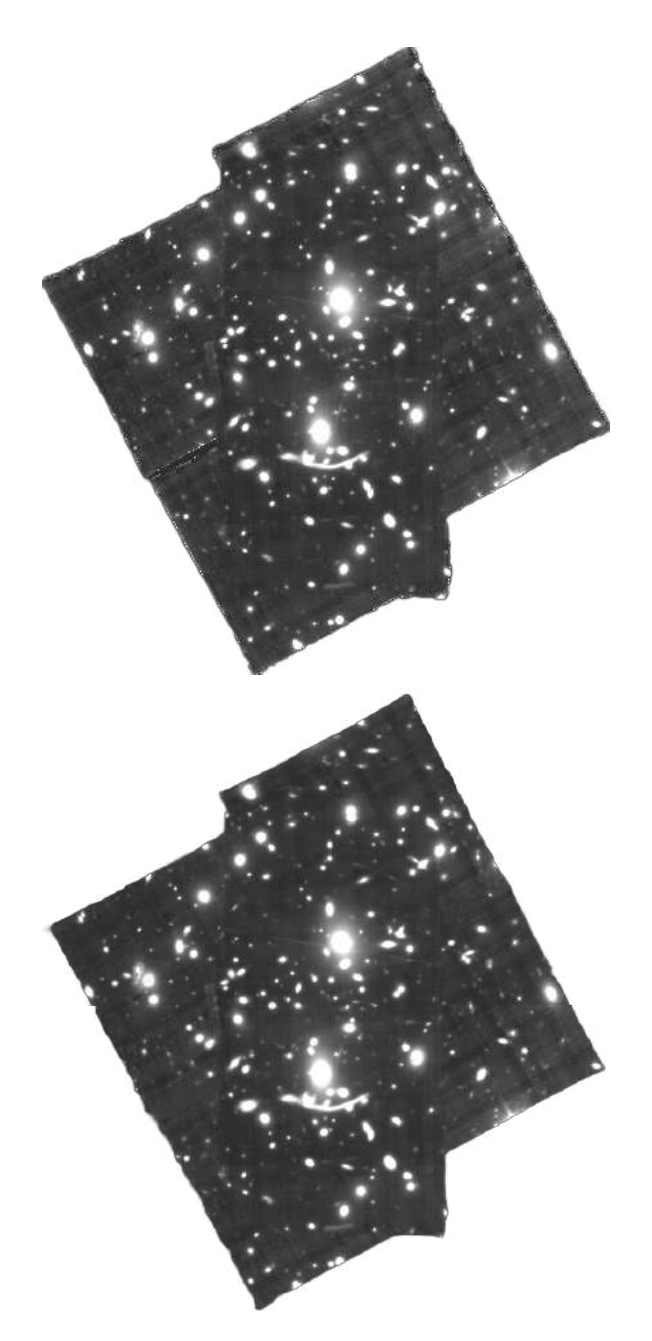
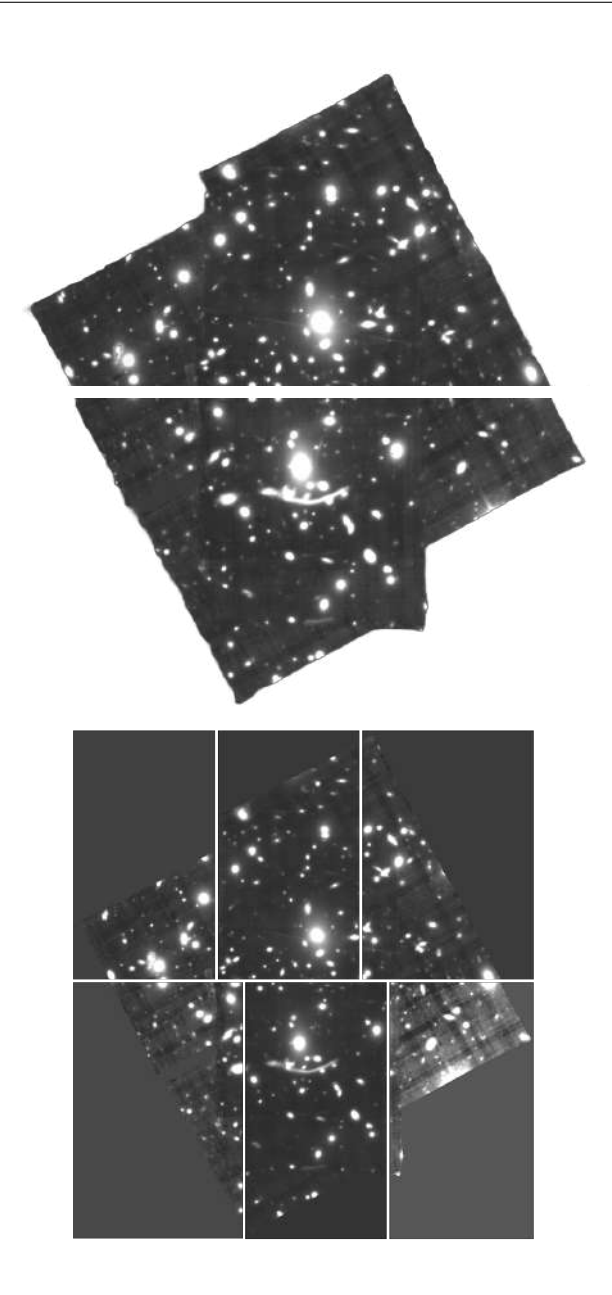


Figure 2.4: Abell 370 datacube before (top panel) and after (bottom panel) applying the ZAP code.

## 2.2 Photometric data and multiwavelength catalogs

#### 2.2.1 HFF-DEEPSPACE

Recently the HST Frontier Fields (HFF) program has been conducted (Lotz et al., 2017). The program is centered on mapping six fields around galaxy clusters exhibiting strong lensing, in the redshift range between 0.3 < z < 0.55. Its primary goal is to detect extremely faint galaxies at z > 5, contributing to the characterization and enhanced understanding of SFGs. In addition to this, Spitzer also dedicated observation time to



**Figure 2.5:** Top: Abell 370 separated into two main datacubes. Bottom: Abell 370 divided into two regions with three cuts each. From top to bottom and from left to right, the datacubes are labeled A370 N CUT 1, A370 N CUT 2, A370 N CUT 3, A370 S CUT 1, A370 S CUT 2, A370 S CUT 3.

observe the HFF fields at 3.6 and 4.5  $\mu$ m, using the Infrared Array Camera (IRAC). Abell 370 is one of the six galaxy clusters included in this initiative, as it possesses the necessary properties looked for by the program: high lensing strength; observability in HST, Spitzer and JWST; and ancillary and ground-based data availability.

One of the greatest challenges for programs of this kind is extracting a substantial amount of information regarding objects situated within and behind galaxy clusters without being affected by the intense light emitted from the clusters themselves. This is one of the main motivations behind the initiative HFF-DEEPSPACE (Shipley et al., 2018), focused

on creating photometric catalogs of the six fields of HFF, incorporating models of the brightest cluster galaxies, and also accounting for the contribution of intracluster light, due to stars not linked to a specific galaxy, but nevertheless bound within the gravitational well of the cluster (de Oliveira et al., 2022). The data used for the project were obtained from different sources. Observations in the near-infrared (NIR) originated from four broadband filters implemented for HFF, with the WFC3 instrument, onboard the HST: F105W, F125W, F140W, and F160W. Images from the Infrared Array Camera (IRAC), equipped on the Spitzer Telescope were also incorporated to complement the NIR data from HFF, with the 3.6  $\mu$ m, 4.5  $\mu$ m (PI: Egami) and 5.8  $\mu$ m and 8.0  $\mu$ m (PID: Fazio), as well as images from the F110W filter (PI: Kneib). Observations in the  $K_S$  band were also utilized, derived from the 'K-band Imaging of the Frontier Fields' (KIFF) project, described in Brammer et al. (2016). In the optical range, three broadband filters from HFF were employed, using the ACS instrument, also onboard the HST: F435W, F606W, and F814W. Additionally, images from the F475W and F625W filters were utilized. Finally, deep UV data (PI: Siana), from the WFC3/UVIS expand the coverage of the project, adding the filters F275W and F336W. Table 2.1 summarizes the image sources, including the wavelength range covered and the survey they were taken from.

Filters	Wavelength range (Å)	Telescope/Instrument	Survey	Date o	of obs.	T. exp. time	Images per filter
(1)	(2)	(3)	(4)	Beginning	End	(6)	(7)
F275W	2300-3100	HST/UVIS	DID: 14000	2016-08-20	2016-08-21	22240	8
F336W	3000-3700	HST'/UVIS	PID: 14209	2016-09-16		22240	8
F435W	3700-4800	HST/ACS	$_{ m HFF}$	2015-12-19	2016-02-17	51400	40
F475W	4000-5600	HST/ACS	PID: 11507	2009-07-16	2009-07-17	9030	9
F606W	4800-7200	HST/ACS	$_{ m HFF}$	2016-01-13	2016 - 01 - 25	25316	20
F625W	5400-7200	HST/ACS	PID: 11507	2009-07-16	2009-07-17	2040	6
F814W	7000-9400	HST/ACS	$_{ m HFF}$	2015-12-19	2016-02-17	117203	106
F105W	9000-12000	HST/WFC3	$_{ m HFF}$	2016-07-27	2016-09-06	67240	60
F110W	9000-14000	HST/WFC3	PID: 11591	2010-	12-19	6088	13
F125W	11000-14000	HST/WFC3	$_{ m HFF}$	2016-07-29	2016-09-11	32770	24
F140W	12000-14000	HST/WFC3	$_{ m HFF}$	2009-09-28	2016-09-10	34740	48
F160W	14000-17000	HST/WFC3	$_{ m HFF}$	2010-12-19	2016-09-06	75787	64
Ks	19000-24000	VLT/HAWK-I	KIFF	2015-07-27	2016-01-29	101952	1062
Channel 1	30000-40000	Spitzer/IRAC	DID: 60024	2010 02 24	100	1	
Channel 2	40000-50000	Spitzer/IRAC	PID: 60034	2010-03-24		100	1
Channel 3	50000-64000	Spitzer/IRAC	DID. 197	2006 02 04	100	1	
Channel 4	64000-94000	Spitzer/IRAC	PID: 137	2006-02-04		50	2

#### 2.2.2 ASTRODEEP

Using the multiwavelength catalogs from the original HFF initiative, the ASTRODEEP³ initiative explores a different approach for measuring photometry, photometric redshifts, and stellar properties from the six HST Frontier Fields. While a detailed description of these analyzes can be found, for instance, in Merlin et al. (2015, 2016); Castellano et al. (2016), their wide scientific scope includes analysis of the luminosity and mass functions, and part of the work is dedicated to create photometric and redshift catalogs and validate these results with spectroscopic subsamples, obtaining overall fairly good agreement between the two methods. Another key part of the project was to detect new high-redshift galaxies, with interest in confirming z > 6 galaxies. ASTRODEEP has published catalogs for Abell 370 (Bradač et al., 2019). However, since their photometric catalog includes a smaller number of HST filters, particularly lacking UV filters which are essential for constraining the bluest part of the SED in our galaxies, we prefer to use the DEEPSPACE catalog as the primary one and use the ASTRODEEP catalog by Bradač et al. (2019) for only three galaxies of our sample, for which the photometric data provided by DEEPSPACE was flagged as problematic (see Section 4.3.3 for details).

<sup>3</sup>http://www.astrodeep.eu/

# 3 | Sample selection and line measurements

## 3.1 Criteria for selecting galaxies

We select galaxies within the redshift range 0.2 < z < 0.85, focused on covering a wavelength range that included the [O III] $\lambda\lambda4959,5007$  doublet, in the high-z galaxies, and the [O II] $\lambda\lambda3727,3729$  doublet, for the low-z galaxies. This ensures the possibility of working with at least one useful line ratio for chemical abundance derivation. We also refrain from selecting galaxies exhibiting a combination of emission lines and a markedly red continuum, centering more on galaxies with a flatter continuum. We include a threshold for all the lines measured, defining a S/N > 3, ensuring a reliable line fitting and therefore reliable values of the line ratios.

## 3.2 Selection of emission-line galaxies

We load the data cubes into the FITS file viewer software QFitsView<sup>1</sup> (Ott, 2012), which allows us to inspect the 2D image of the cube, as well as the spectrum of the selected region. We perform a scan throughout the image, looking for emission lines, and in particular those in the 4850-5020 Å rest-frame range, to detect the spectral pattern of H $\beta$  up to [O III] $\lambda$ 5007. When we get confirmation of the existence of the latter line -owing to its characteristic structure, accompanied by [O III]4959 and H $\beta$  - we create a narrowband filter, leaving space just for [O III]5007. In this way we can get an idea of the general aspect of the galaxy.

This filter includes the full width of the line, plus some 2 or 3 Å to isolate the galaxy in the 2D images. The information on this wavelength range is stored in a file denominated "range". When the galaxy is well identified, the coordinates of an approximate center are registered, to extract subcubes from the main datacube. To obtain a spectroscopic redshift, we use the expression

$$z = \frac{\lambda_{\text{obs}} - \lambda_0}{\lambda_0},\tag{3.1}$$

https://www.mpe.mpg.de/~ott/dpuser/qfitsview.html

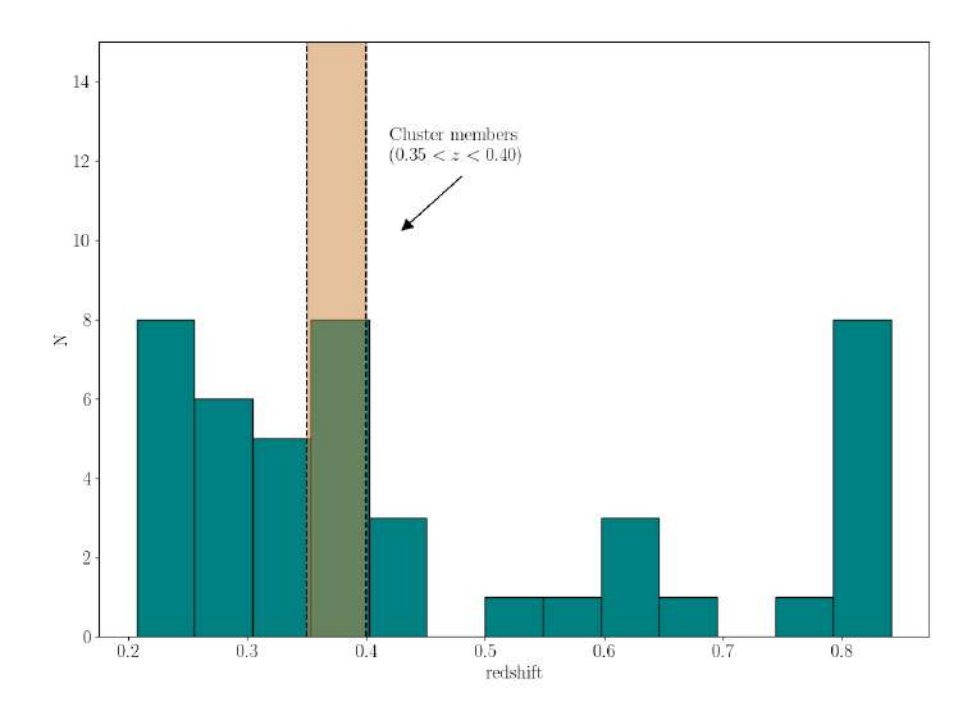


**Figure 3.1:** Redshift distribution for the sample. The orange band around the bin represents the cluster members, in the redshift range 0.35 < z < 0.40.

where  $\lambda_{\rm obs}$  and  $\lambda_0$  are the observed wavelength and rest-frame wavelength, respectively. For increased precision, we calculate three different redshifts from distinct emission lines, adjusting them according to the wavelength range covered by each galaxy. Common combinations included the [O II] $\lambda$ 3727,3729 doublet; H $\beta$ ; the [O III] $\lambda$ 4959,5007 doublet; and H $\alpha$  lines. After surveying the cluster's northern (N) and southern (S) zones, our sample comprises 45 galaxies with detected emission lines. We perform a crossmatch with the photometric catalog from DEEPSPACE using the software TOPCAT<sup>2</sup> (Taylor, 2005), however, due to the methodologies applied in producing the catalogs and segmentation maps (see Sect. 3.3 of Shipley et al., 2018), one of our emission line galaxies is close to an elliptical galaxy listed in the photometric catalog. This proximity complicates effective SED fitting. Unfortunately, the ASTRODEEP catalog does not include the emission line galaxy in the final dataset, making this galaxy unable to analyze photometrically.

We based the redshift range 0.35 < z < 0.40 for cluster membership, following Lagattuta et al. (2022), who also performed a spectroscopic analysis based on MUSE-based data, centered on A370 as well. We define all galaxies with redshift below 0.35 as foreground galaxies and those with redshift above 0.40 as background galaxies. We find that 19 galaxies, or 42% of our sample correspond to foreground galaxies; 8 galaxies, or 18% are cluster members; and 18 galaxies, or 40% of the sample are background galaxies. We present the distribution of the redshift of the final sample in Figure 3.1, and Tables 3.1 and 3.2 show the redshift values and coordinates of the sample.

We use the MUSE Python Data Analysis Framework (MPDAF) package (Bacon

<sup>2</sup>https://www.star.bris.ac.uk/~mbt/topcat/

et al., 2016), specialized in datacube manipulation. Utilizing the tools for extracting a subcube (mdpaf.Cube.cube), we center the datacube on the previously defined center coordinates and extract  $30 \times 30$  pixels cutouts. This process retains the information contained in the original header, as well as the third dimension of the cubes (spectral). Our next step involves applying the same method to our variance spectra. Given that their format is also in the form of a datacube, it is straightforward to execute the previous step to obtain the new  $30 \times 30$  pix datacube cutouts, retaining their spectral dimension.

## 3.3 Spectral extraction of galaxies

To extract the maximum number of pixels comprising a galaxy, excluding background elements that contribute to the noise, and increasing the signal-to-noise, we generate segmentation maps. These maps assign a value of 1 to pixels corresponding to the galaxy, and a value of 0 to anything else. We use the software SEXTRACTOR (Bertin & Arnouts, 1996) in the following configuration.

We define the region of interest from the six available regions. The script created for this purpose generates segmentation maps for all galaxies within this region. We modify relevant parameters of the configuration file of SEXTRACTOR, such as MINAREA, DETECT\_THRESH, and in particular CHECKIMAGE\_TYPE, setting it to SEGMENTATION, to obtain as output the segmentation maps of each galaxy. It is important to point out that the first two parameters are different for each galaxy. In order to run SEXTRACTOR, we need to have a 2D image, so we collapse each datacube using the mdpaf tools, along the wavelength range previously defined around [O III]5007, thus reducing the dimensions to only two. This range is usually 5 to 8 Å. These collapsed 2D images were also stored.

After obtaining these two files, we run SEXTRACTOR. During this step, a visual inspection is necessary to assess the quality of the segmentation maps, identifying any inconsistencies or errors. It was common to discover that the segmentation map did not encompass the entire galaxy. As a result, it was necessary to modify the parameters in the configuration file, followed by a rerun of SEXTRACTOR. This step was particularly critical because of the significance of preserving the morphological properties of the galaxies while simultaneously reducing the number of background pixels. This process entails multiple iterations, adjusting the parameters until generating satisfactory maps. When we were satisfied with the result of the segmentation map, we multiply the original datacube by the segmentation map to obtain the final datacube, retaining only the information of importance. Once the galaxies are isolated, we return to the use of mpdaf, this time to extract the galaxy spectrum employing the tool mpdaf.Cube.sum(axis = (1,2)). We present two examples of typical spectra obtained for the galaxies of our sample in Figure 3.2. A visual representation of the complete process process is shown in Fig. 3.3.

Table 3.1: Basic information about the galaxies in the North zone of the cluster

$\begin{array}{c ccccccccccccccccccccccccccccccccccc$	
$\begin{array}{cccccccccccccccccccccccccccccccccccc$	gion
$\begin{array}{cccccccccccccccccccccccccccccccccccc$	
3       2       39       56.801       -1       34       28.251       4225       0.4216         4       2       39       57.696       -1       34       12.925       4178       0.6050       1         5       2       39       55.208       -1       34       23.475       3806       0.2313         6       2       39       55.649       -1       34       29.020       3595       0.3922         7       2       39       57.262       -1       34       29.294       3529       0.3650         8       2       39       52.094       -1       34       36.886       3342       0.8041         9a       2       39       53.298       -1       34       28.191        0.2557         10       2       39       54.310       -1       34       33.750       3440       0.8041         11       2       39       54.924       -1       34       13.796       3633       0.3263         12       2       39       55.040       -1       34       11.750       4266       0.6246         14       2       39       53.600	
$\begin{array}{cccccccccccccccccccccccccccccccccccc$	
5       2 39 55.208       -1 34 23.475       3806       0.2313         6       2 39 55.649       -1 34 29.020       3595       0.3922         7       2 39 57.262       -1 34 29.294       3529       0.3650         8       2 39 52.094       -1 34 36.886       3342       0.8041         9a       2 39 53.298       -1 34 28.191        0.2557         10       2 39 54.310       -1 34 33.750       3440       0.8041         11       2 39 54.924       -1 34 31.796       3633       0.3263         12       2 39 55.040       -1 34 14.725       4070       0.2559         13       2 39 52.522       -1 34 11.750       4266       0.6246         14       2 39 53.700       -1 33 43.100       5165       0.8415         15       2 39 53.600       -1 33 37.300       5455       0.7830	1
6       2 39 55.649       -1 34 29.020       3595       0.3922         7       2 39 57.262       -1 34 29.294       3529       0.3650         8       2 39 52.094       -1 34 36.886       3342       0.8041         9a       2 39 53.298       -1 34 28.191        0.2557         10       2 39 54.310       -1 34 33.750       3440       0.8041         11       2 39 54.924       -1 34 31.796       3633       0.3263         12       2 39 55.040       -1 34 14.725       4070       0.2559         13       2 39 52.522       -1 34 11.750       4266       0.6246         14       2 39 53.700       -1 33 43.100       5165       0.8415         15       2 39 53.600       -1 33 37.300       5455       0.7830	L
$\begin{array}{cccccccccccccccccccccccccccccccccccc$	
$\begin{array}{cccccccccccccccccccccccccccccccccccc$	
$\begin{array}{cccccccccccccccccccccccccccccccccccc$	
10       2 39 54.310       -1 34 33.750       3440       0.8041         11       2 39 54.924       -1 34 31.796       3633       0.3263         12       2 39 55.040       -1 34 14.725       4070       0.2559         13       2 39 52.522       -1 34 11.750       4266       0.6246         14       2 39 53.700       -1 33 43.100       5165       0.8415         15       2 39 53.600       -1 33 37.300       5455       0.7830	
11       2 39 54.924       -1 34 31.796       3633       0.3263         12       2 39 55.040       -1 34 14.725       4070       0.2559         13       2 39 52.522       -1 34 11.750       4266       0.6246         14       2 39 53.700       -1 33 43.100       5165       0.8415         15       2 39 53.600       -1 33 37.300       5455       0.7830	
12       2 39 55.040       -1 34 14.725       4070       0.2559         13       2 39 52.522       -1 34 11.750       4266       0.6246         14       2 39 53.700       -1 33 43.100       5165       0.8415         15       2 39 53.600       -1 33 37.300       5455       0.7830	
13       2 39 52.522       -1 34 11.750       4266       0.6246         14       2 39 53.700       -1 33 43.100       5165       0.8415         15       2 39 53.600       -1 33 37.300       5455       0.7830	
14       2 39 53.700       -1 33 43.100       5165       0.8415         15       2 39 53.600       -1 33 37.300       5455       0.7830	
15 2 39 53.600 -1 33 37.300 5455 0.7830	
16 2 39 52.684 -1 33 25.587 5741 0.8413	2
17 2 39 52.343 -1 33 29.069 5522 0.8413	
18 2 39 54.997 -1 34 17.200 3910 0.2069	
19 2 39 54.928 -1 34 30.144 3684 0.2068	
20 2 39 52.467 -1 34 35.753 3392 0.8041	
21 2 39 53.082 -1 33 34.822 5407 0.2515	
22 2 39 54.233 -1 33 40.295 5271 0.3272	
23 2 39 51.941 -1 33 50.620 4912 0.3296	
24 2 39 54.795 -1 33 45.020 5041 0.3829	
25 2 39 51.093 -1 34 09.861 4284 0.6802	
26 2 39 50.300 -1 34 21.890 4031 0.2071	
27 2 39 49.410 -1 34 13.324 4321 0.5478	
28 2 39 50.506 -1 33 43.192 5199 0.2557	3
29 2 39 50.415 -1 34 23.176 3923 0.2251	
30 2 39 51.434 -1 33 17.517 5915 0.6030	
31 2 39 50.788 -1 34 20.808 3906 0.2257	

<sup>&</sup>lt;sup>a</sup> Although this galaxy is reported, in the DEEPSPACE catalogs it describes the photometry of an elliptical galaxy superimposed, probably part of the galaxy cluster. For this reason, we were unable to derive physical properties from SED fitting, but the properties obtained from the spectroscopic information (abundances, SFR  $(H\alpha)$ , etc.) are effectively representative of the galaxy we are interested in.

#### 3.3.1 Importance of segmentation maps for the extraction of spectra

The crucial aspect of extracting a galaxy through a segmentation map is to prevent the inclusion of emission from other sources, such as another selected galaxy, or a part of an elliptical galaxy within the cluster. A particularly illustrative example of this is presented

ID	R.A.	Dec.	DEEPSPACE	~	Dogion
Ш	(h m s)	(d m s)	ID	$z_{ m spec}$	Region
32	2 39 54.466	-1 35 27.700	1602	0.4226	
33	$2\ 39\ 55.235$	-1 34 47.820	2807	0.256	1
34	$2\ 39\ 55.686$	-1 35 14.574	2002	0.3864	1
35	$2\ 39\ 54.830$	-1 35 02.190	2441	0.3605	
36	2 39 53.220	-1 35 50.674	998	0.3238	
37	$2\ 39\ 53.761$	-1 35 40.341	1247	0.3746	
38	$2\ 39\ 52.523$	-1 35 13.548	1989	0.5802	
39	$2\ 39\ 52.109$	-1 35 23.923	1666	0.8040	2
40	$2\ 39\ 51.297$	-1 35 17.605	1857	0.8049	4
41	$2\ 39\ 53.930$	-1 34 47.846	2753	0.3737	
42	$2\ 39\ 52.124$	-1 35 40.587	1227	0.242	
43	$2\ 39\ 53.622$	-1 34 48.049	3060	0.4100	
44	2 39 50.685	-1 34 45.634	2935	0.3663	3
45	$2\ 39\ 49.479$	-1 34 45.185	3187	0.3264	3

**Table 3.2:** Basic information about the galaxies in the South zone of the cluster

in Figure 3.4. Here, the selected galaxy (DEEPSPACE ID 4178) is very close to an elliptical galaxy, which affected the spectrum obtained when using a circular aperture, and ultimately would affect the line measurements. An extra step involved performing the previous operation (multiplying the cube by the segmentation map) for our variance spectra. After this step, we effectively have the information of the isolated galaxies in datacubes plus the information of the variance spectra.

#### 3.4 Line measurements with LiMe

The LiMe (**Line Me**asuring, Fernández et al. 2024)<sup>3</sup> library is designed to fit Gaussian profiles to emission lines in astronomical spectra. It provides the necessary tools for masking, detecting, profile fitting, and storing the results. In order to fit emission lines, we considered the largest number of emission lines inside of the wavelength range covered by each galaxy, according to its redshift, but it can be reduced to the lines presented in Table 3.3.

The rationale behind this selection lies in the fact that the oxygen abundance estimators, both those based on intense emission lines and the direct method, utilize combinations of these lines. The [S II] lines are also considered for deriving expressions for electron density  $(n_e)$ , when available.

We loaded a spectrum to perform the fitting, specifying the following parameters, available in the spectrum header:

- The step between pixels  $(\Delta \lambda)$
- The minimum wavelength of the spectrum (4750 Å)

<sup>&</sup>lt;sup>3</sup>https://lime-stable.readthedocs.io/en/latest/index.html

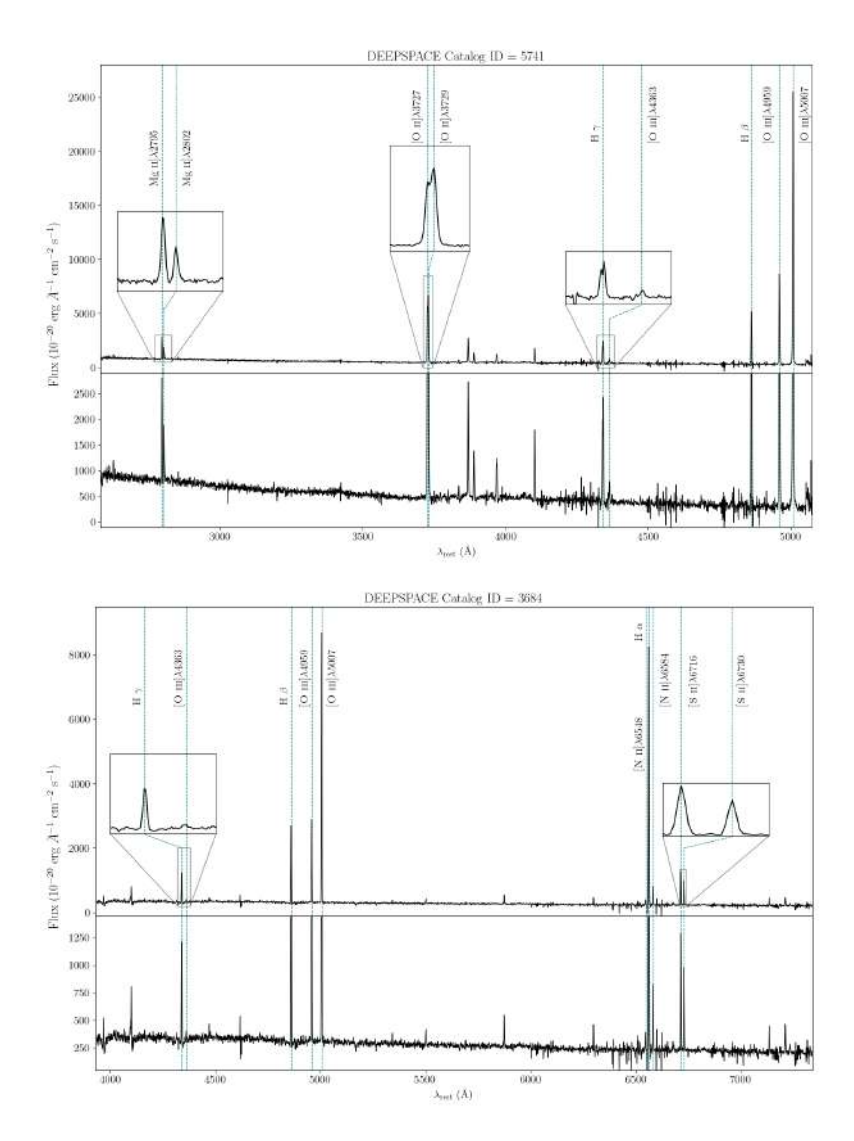
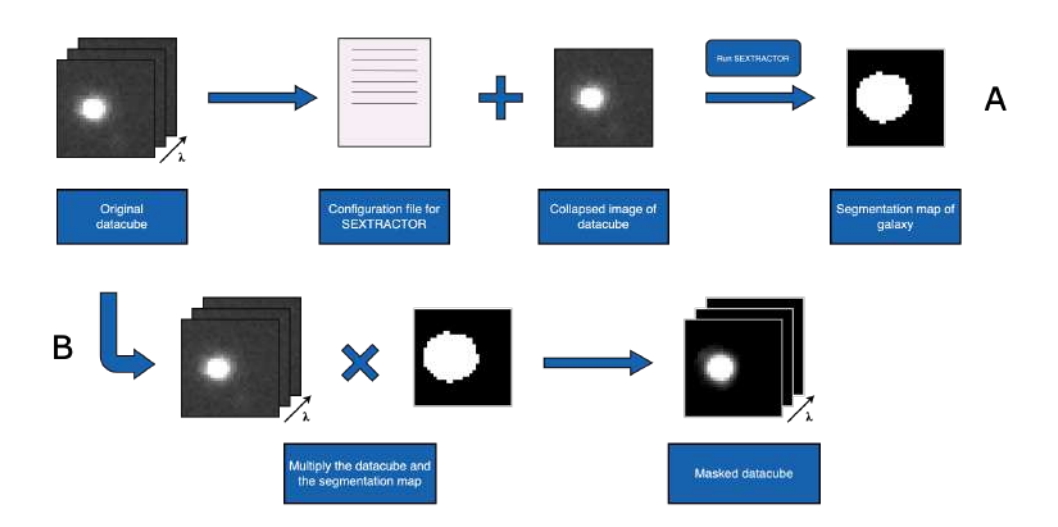


Figure 3.2: Comparison of traditional spectra found in the sample. Top: Spectrum of galaxy DEEPSPACE ID = 5741, at z=0.8413. The upper plot is a general view of the spectrum, and the lower plot is the same spectrum limited to 3000 flux units, in order to perceive in more detail the weaker lines. The boxes are zoom-ins of relevant emission lines. The vertical dashed lines mark the main emission lines of the spectrum. This is one of the most intense spectra, showing faint lines such as the Mg II] $\lambda\lambda2795,2802$  doublet. Bottom: Spectrum of galaxy DEEPSPACE ID = 3684, at z=0.2068. The upper plot represents a general view of the spectrum, and the lower plot is the same spectrum limited to 1300 flux units. The inside boxes are zoom-ins of relevant emission lines. Due to its redshift, lines beyond 4000 Å are displaced beyond the detection range of the instrument, rendering the [O II] doublet at 3726 and 3729 Å impossible to measure.

• The number of pixels composing the spectrum (3682 pix.)

Besides this, we need two extra files, containing key parameters for the line fitting:

• A configuration file, specifying the width of the Gaussian curve in units of the spectrum wavelength (denoted as sigma), and the amplitude of the Gaussian relative to the continuum, measured in the spectrum's units (denoted as amp). Additionally, one can specify the center of the Gaussian (denoted as center). All these param-



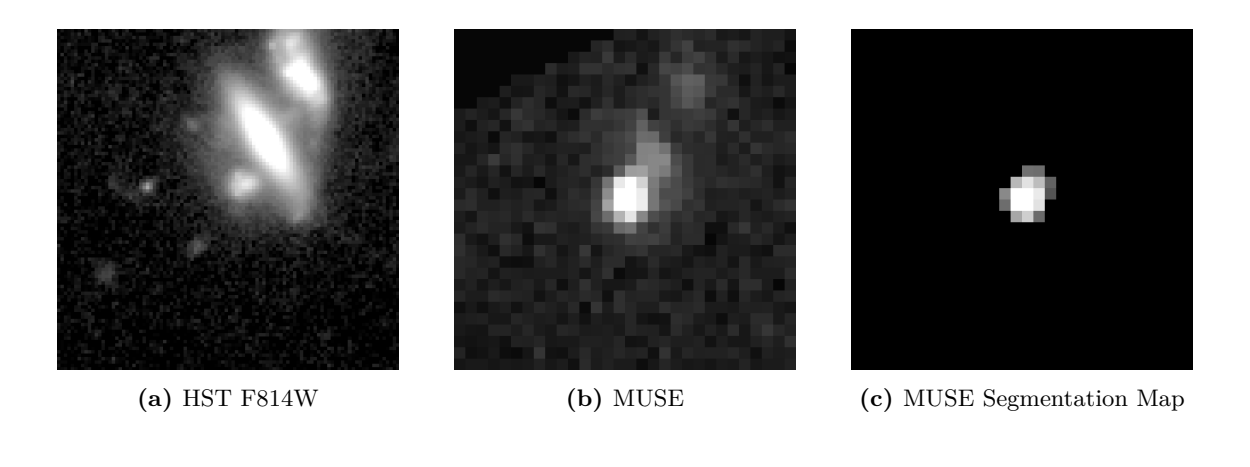
**Figure 3.3:** Flow chart of the process of extraction of a galaxy. After the segmentation map is created (A), the original datacube is multiplied by the segmentation map to isolate the galaxy (B).

Table 3.3: Main emission lines fitted. Air wavelengths indicated in rest-frame.

λ (Å)	Line
3726.032	[O II]
3728.815	[O II]
3868.760	[Ne III]
4363.210	[O]
4861.333	$_{\mathrm{H}\beta}$
4959.911	[O]
5006.843	[O III]
6562.819	$H\alpha$
6583.460	[N II]
6716.440	[S 11]
6730.810	[S II]

eters can be fixed using the command 'vary: False'. There is also an option to mask specific areas within the region of interest, excluding damaged spectrum zones from the fitting, by using mask. Finally, the kinematic information of one ion can be translated into a similar one (e.g., [Ne III] and [O III]) using the command kinem.

• A text file with seven columns, named mask file. The first column contains the line label, and the remaining columns provide the rest-frame wavelength values, indicating the position of the line, along with two additional adjacent bands. These values are arranged in ascending order based on wavelength.



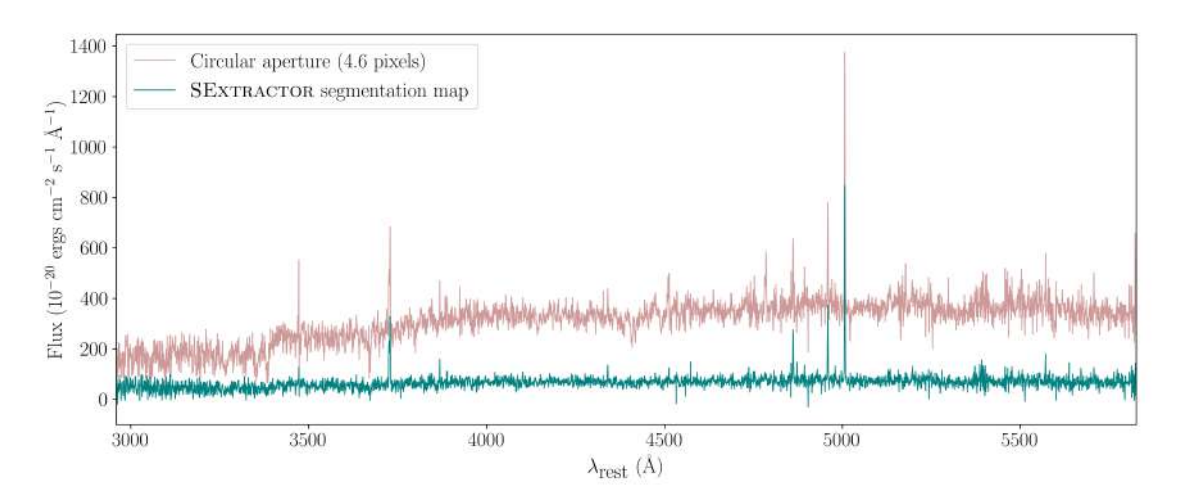


Figure 3.4: Different views for a selected galaxy. Top left: HST image of galaxy ID 4 in the F814W filter. The elongated galaxy towards the top-right corner of the cutout is an elliptical galaxy, while the small, rounded shape at the left side of the elliptical is the galaxy of interest. Top middle: MUSE datacube centered on the  $[O\ III]\lambda5007$  emission line. Here, the galaxy clearly distinguishes from the elliptical galaxy, allowing a more precise extraction. Top right: MUSE segmentation map after applying the SEXTRACTOR method, described in Section 3.3. We conserve only the parts related to the galaxy, while converting external spaxels to zero. Bottom: Comparison between extractions performed in two different approaches. The purple spectrum is from an extraction considering a circular aperture, with a radius of 4.6 pixels. Contamination from the elliptical galaxy is prominent, contributing part of its continuum to the characteristic weak continuum and strong emission lines from the SFGs. The green spectrum corresponds to the extraction using the SEXTRACTOR method. The continuum from the elliptical galaxy is not perceivable, leaving only the weak continuum with the emission lines mostly unaltered.

#### Fitting multiple curves

Another relevant component is the modularity of the line labels. It informs LiMe whether to fit one or more Gaussian curves.

#### • Single line

This parameter is interpreted as an emission or absorption feature, capable of being fitted with a single Gaussian curve.

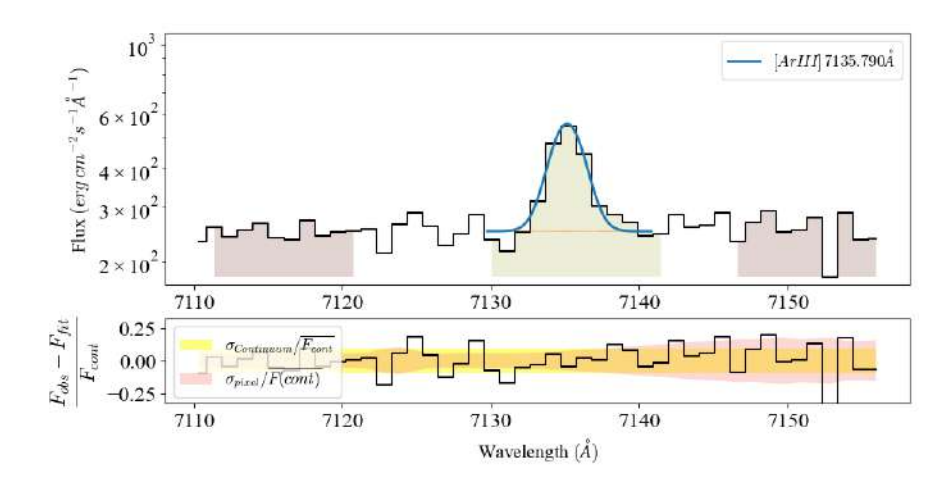


Figure 3.5: Single line fitting of the [Ar III] $\lambda$ 7135 for galaxy ID 19 provided by LiMe. The top panel presents the line fit and the bottom panel shows the residuals of the fit. The pink areas represent the wavelength range of the continuum surrounding the line; the yellow area represents the wavelength range of the emission line. The solid blue line is the Gaussian fit. The orange-dashed line represents the continuum of the spectrum.

Figure 3.5 shows an example of this mode, where the top panel presents the line fit and the bottom panel shows the residuals of the fit considering the error spectrum (pink strip) and the observed continuum (yellow strip). The pink areas represent the wavelength range of the continuum surrounding the line; the yellow area represents the wavelength range of the emission line, both mentioned in the mask file of the galaxy. The blue line is the Gaussian fit considering the parameters contained in the configuration file, which will provide the value of the flux of the line measured, and the orange-dashed is the continuum at the wavelength range. This color scheme will remain consistent for all the following Gaussian fits.

In Figure 3.5 we present an example of a single line fit for  $[Ariii]\lambda7139$  in galaxy ID 19. The configuration file for this fit is represented by

```
#Ar3_7135A
Ar3_7135.790A = Ar3_7135.790A
Ar3_7135.790A_sigma = min:0.5,max:1.7
Ar3_7135.790A_amp = value:50
```

#### Blended line

This parameter is represented with the suffix '\_b' after the label of the line. It represents multiple transitions and/or kinematic components. LiMe interprets this parameter and fits a Gaussian curve to each component described in the configuration file. This is particularly important for transitions that are too close to each other, granting the possibility of separating them and obtaining information independently.

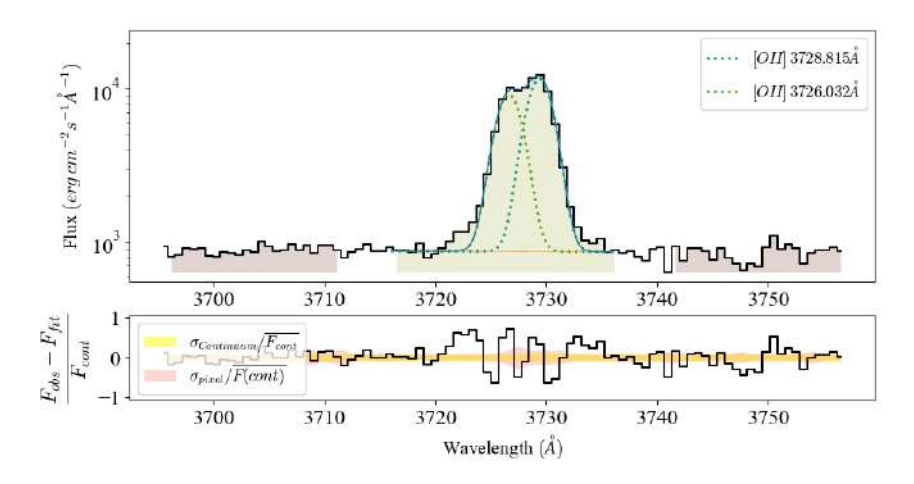


Figure 3.6: Double line fitting of the  $[O II]\lambda3726,3729$  doublet for galaxy ID 16. The top panel is the line fit. The pink areas represent the wavelength range of the continuum surrounding the line; the yellow area represents the wavelength range of the emission line. The green-dashed lines are the independent fits for the blended lines, and the blue line is the total Gaussian fit. The bottom panel represents the residuals of the fit.

Figure 3.6 shows the Gaussian fit of the  $[O II]\lambda\lambda 3727,3729$  doublet for galaxy ID 16. The corresponding configuration file used is represented by

```
#02_3726,29

02_3728.815A_b = 02_3728.815A-02_3726.032A

02_3728.815A_sigma = min:1.8,max:2.3

02_3728.815A_amp = value:1000

02_3726.032A_kinem=02_3728.815A

02_3726.032A_amp=value:1000
```

Here, we fit the strongest line ([O II] $\lambda 3729$ ), and then we use the property kinem to copy the kinematic information from this line to the [O II] $\lambda 3726$  line, while only adjusting the amplitude of the Gaussian curve.

#### 3.4.1 Advantages of incorporating LiMe into line measurement analysis

A highly effective feature by LiMe is the capability to simultaneously fit the nebular contribution of the gas along with the underlying stellar population, which is significant due to the absorption profile combined with the emission. Figure 3.7 illustrates this behavior in H $\beta$  for galaxy ID 35, where the stellar contribution is identified by the greendashed inverted Gaussian labeled as 'H1\_4861.333A-w1'.

An example of this type of instance is represented by the following configuration file:

```
#H1_4861.333A

H1_4861.333A_b = H1_4861.333A-H1_4861.333A_w1

H1_4861.333_sigma = min:0.6,max:1.9

H1_4861.333_amp = value:500
```

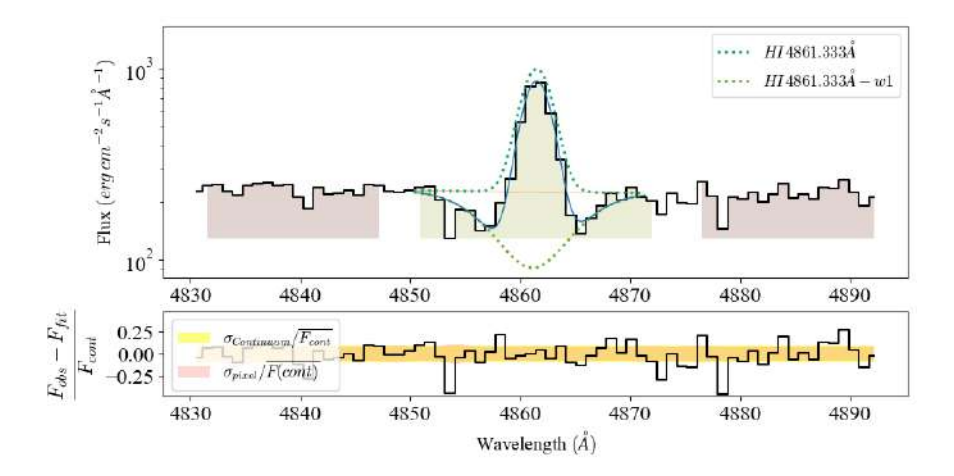


**Figure 3.7:** Gaussian fit around H $\beta$  in galaxy ID 35, showing the underlying stellar contribution fitted by LiMe. The bottom panel shows the residuals of the fit. The colors represent the same as in the previous Figures.

## 3.5 The case of a lensed galaxy identified twice: ID 8 & 20

We now examine the specific case of a galaxy that met the criteria for inclusion in our sample, but was influenced by the gravitational effects of the galaxy cluster, distorting the shape of the galaxy, and due to the position of the lensing, the middle part of the galaxy appeared less bright than the left and right parts, separating the galaxy according to the MUSE datacubes. These galaxies are identified as IDs 8 and 20, corresponding to entries 3342 and 3392 in the DEEPSPACE catalog, respectively. When searching for emission line galaxy candidates, the spatial sampling of MUSE (0.2 "/pix) did not indicate that these two objects are the same. However, when inspecting our sample in the *HST* fields, we realized of the singular appearance of the two galaxies, due to the higher spatial sampling offered by *HST* (0.05 "/pix). Both galaxies display the same redshift, and have been reported in recent works analyzing the lensing effects of A370 (e.g., Richard et al., 2010; Johnson et al., 2014; Lagattuta et al., 2019). We show the two galaxies in an *HST* image in Fig. 3.8, and we include the comparison between the MUSE and the *HST* extractions, as well as the extracted spectra for each MUSE datacube in Fig. 3.9.

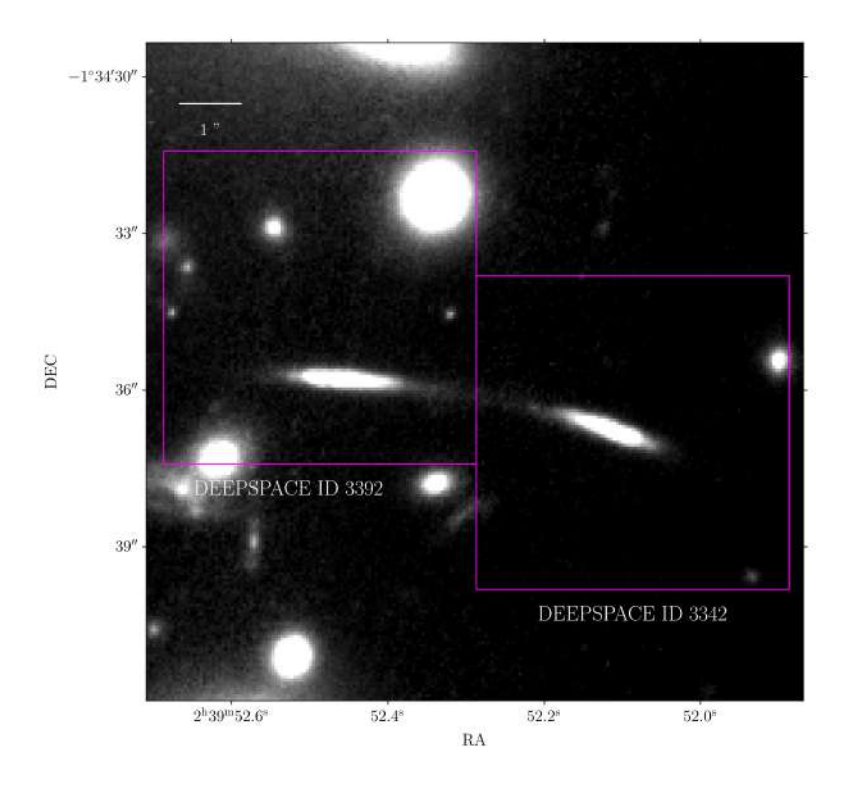


**Figure 3.8:** HST F814W field of A370 showing the lensed galaxy identified as two separated systems (DEEPSPACE ID 3342 and ID 3392). The image is  $10.5'' \times 10.5''$ , and is centered at R.A.=2:39:52.29, Dec.=-1:34:35.69. The magenta boxes represent the area selected for the cutouts of both galaxies.

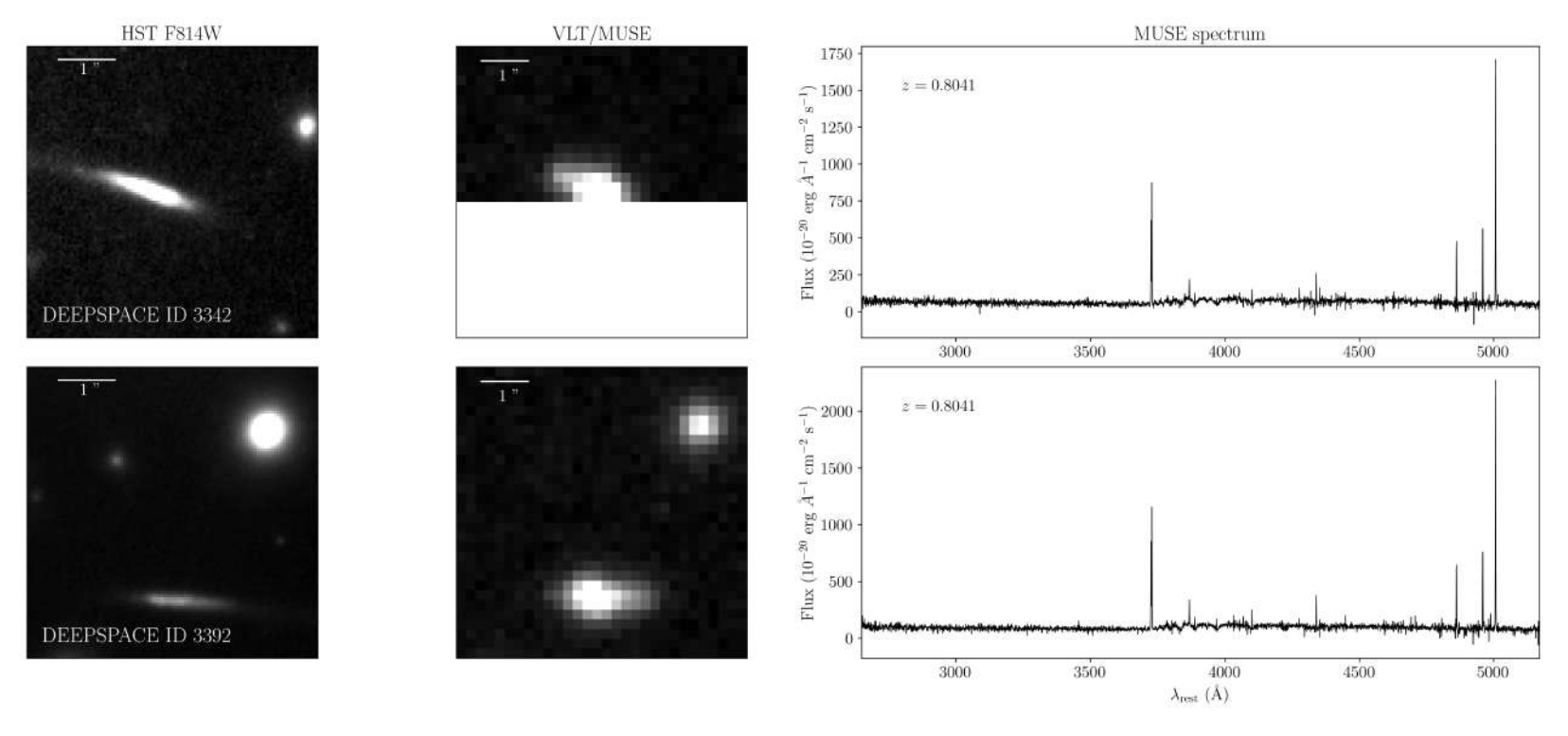


Figure 3.9:  $5'' \times 5''$  separate cutouts made for DEEPSPACE ID 3342 and 3392, based on the magenta boxes from Figure 3.8. The first column shows the galaxies from the HST F814W images with the DEEPSPACE ID from the catalog. The middle column represents the same field but from the VLT/MUSE observations, with the images covering  $6'' \times 6''$  each. DEEPSPACE ID 3342 has a cut in the MUSE observation due to the separation into North and South main datacubes, leaving this galaxy with some pixels out of the new border (see Sect. 2.1.3). The right column shows the extracted spectra of both galaxies, following the method described in Sect. 3.3.

## 4 | Derivation of physical properties

In this chapter we describe the methods applied and the results of the main spectrophotometric properties of the sample selected in Chapter 3. This chapter is structured as follows. We first describe the approach to perform the extinction corrections, considering the Balmer decrement method in Sect. 4.1. In Sect. 4.2, we use classic diagnostic diagrams to examine the type of ionization in our sample. In Sect. 4.3 we perform the SED fitting of the photometric data using the code BAGPIPES, in order to derive stellar masses. We derive the SFR from the extinction-corrected H $\alpha$  luminosity in Sect. 4.5. We describe the magnification corrections in Sect. 4.4, and finally we explain the derivation of the metallicity for our sample, considering the strong-line method, as well as the direct method for the galaxies with the detection of the [O III] $\lambda 4363$  auroral line.

#### 4.1 Nebular dust extinction

An important part of deriving physical properties from spectra is correcting the flux for interstellar extinction. This extinction is generated by dust and gas along the line of sight, which absorb part of the emission and re-emit it in the IR. This effect is heavily dependent on the wavelength of the photons, being more significant at shorter wavelengths due to the size of the grains. We perform the correction for extinction considering the ratio between two recombination lines from the Balmer series, also known as Balmer decrement. This is a commonly used method, as these lines are present in most emission-line spectra and results are highly reliable (e.g., Smith, 1975; Sullivan et al., 2000; Pérez-Montero, 2017; Zamora et al., 2022). Our first step is to derive an expression for the logarithmic extinction at  $H\beta$ , i.e.,  $c(H\beta)$ . This is a key step, as the corrected fluxes are used to obtain expressions for metal abundance, temperature and SFR. Consider the expression for the intrinsic flux for an emission line:

$$I_{\lambda} = F_{\lambda} \cdot e^{\tau_{\lambda}},\tag{4.1}$$

here,  $\tau_{\lambda}$  is the optical depth; it has a dependence on the wavelength and is affected by the physical conditions of the environment of the galaxy. Because of this dependence on wavelength, we can re-write the factor  $\tau_{\lambda}$  as  $c \cdot f(\lambda)$ :

$$I_{\lambda} = F_{\lambda} \cdot e^{c \cdot f(\lambda)},\tag{4.2}$$

we can rewrite equation 4.2, changing the base from base e to base 10 and normalize it with respect to the flux of H $\beta$ , dividing it by itself, setting  $\lambda = 4861$  Å:

$$\frac{I_{\lambda}}{I_{\mathrm{H}\beta}} = \frac{F_{\lambda}}{F_{\mathrm{H}\beta}} \cdot 10^{\log e^{c \cdot [f(\lambda) - f(\mathrm{H}\beta)]}} = \frac{F_{\lambda}}{F_{\mathrm{H}\beta}} \cdot 10^{c \cdot 0.434[f(\lambda) - f(\mathrm{H}\beta)]},\tag{4.3}$$

where  $\log e = 0.434$ . We define the logarithmic extinction coefficient as  $c(H\beta) \equiv c \cdot 0.434$  and replace this in the previous expression:

$$\frac{I_{\lambda}}{I_{H\beta}} = \frac{F_{\lambda}}{F_{H\beta}} \cdot 10^{c(H\beta)[f(\lambda) - f(H\beta)]} \tag{4.4}$$

Using the theoretical values of  $H\alpha/H\beta = 2.86$  and  $H\gamma/H\beta = 0.468$ , when the former is not avalilable (Osterbrock & Ferland, 2006). For a case B recombination, considering  $T_e = 1 \times 10^4$  K,  $n_e = 100$  cm<sup>-3</sup>, as shown in Pérez-Montero (2017), we can derive an expression for the extinction in our sample.

To summarize our work, we can reduce the expression from equation 4.4 introducing the two theoretical ratios, obtaining

$$c(H\beta)_1 = \log\left(\frac{2.86}{H\alpha/H\beta}\right)/f_{H\alpha}$$
 (4.5)

$$c(H\beta)_2 = \log\left(\frac{0.468}{H\gamma/H\beta}\right)/f_{H\gamma},\tag{4.6}$$

where we define the expressions  $f_{H\alpha}$  and  $f_{H\gamma}$  as the extinction laws for  $H\alpha$  and  $H\gamma$ , respectively. They are expressed as

$$F_{\text{H}\alpha} - F_{\text{H}\beta} = -0.346$$
  
 $F_{\text{H}\gamma} - F_{\text{H}\beta} = 0.183,$  (4.7)

according to the extinction law from Cardelli et al. (1989). We present the main emission line fluxes and intensities in Tables 4.1 through 4.4. We detect some negative values for  $c(H\beta)$  (ID 16, 17 and 20 in Table 4.1 and 4.3), which could be explained by very low extinction found in these systems (Fernández et al., 2022). In these cases, we set these extinctions to be zero. The distribution of  $c(H\beta)$  is illustrated in Fig. 4.1. We find an extinction relatively low, showing a mean value of 0.34, with a  $1\sigma$  standard deviation of 0.27. This value is similar to the median of the extinction of the non-EELGs (extreme-emission line galaxies) from Calabrò et al. (2017), with a value of  $c(H\beta) = 0.26$ , for a sample ranging between  $z \sim 0.1$ -0.9.

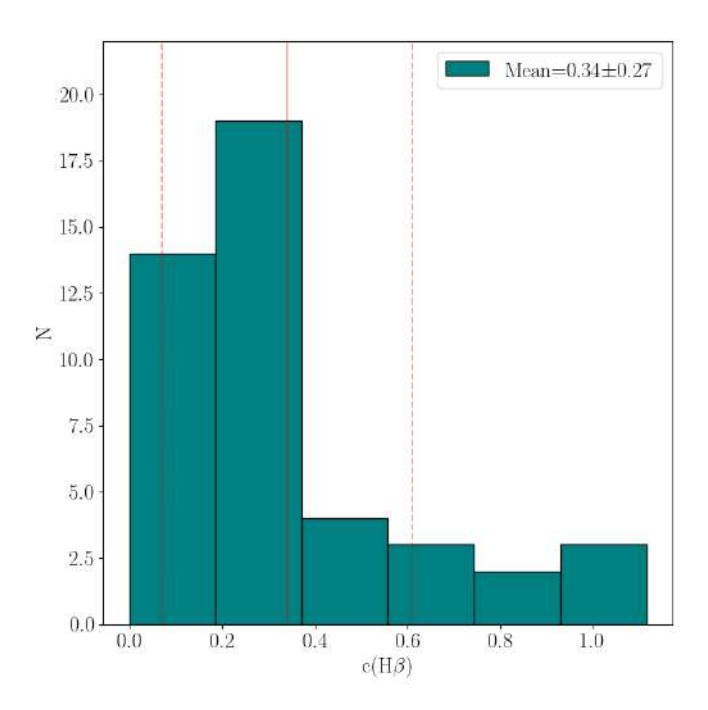


**Figure 4.1:** Histogram distribution of  $c(H\beta)$ . The mean value is represented with a vertical dashed line.

Table 4.1: Main emission line fluxes up until the H $\beta$  line derived for the galaxies of the North (N) zone of the MUSE observations. The row below the emission line names displays the value of the reddening curve. For each galaxy, we present the ID, the extinction coefficient, and the observed flux and extinction-corrected intensity, both relative to  $F(H\beta) = I(H\beta) = 1000$ . For galaxies with negative extinction coefficients, the values of the observed flux are the same as the intensity. In the last two columns, we display the EW[O III] and the observed flux of the H $\beta$  line (the flux units are  $10^{-20}$ erg cm<sup>-2</sup> s<sup>-1</sup>).

	[О п]3727		[О п]3729		[Ne I	11]3869	[O II	ı]4363	Ηβ			
$f(\lambda)$			.38	0.	.38		.34	0.	.17	0.00	$F(H\beta)$	log EW[O III] [Å]
ID	$c(H\beta)$	$F_{\lambda}$	$I_{\lambda}$	$F_{\lambda}$	$I_{\lambda}$	$F_{\lambda}$	$I_{\lambda}$	$F_{\lambda}$	$I_{\lambda}$	$F_{\lambda}$		0 1 111
1	0.73				•••	$571 \pm 192$	$1012\pm341$			$1000\pm136$	310±30	$1.63 \pm 0.02$
2	0.36					$236 \pm 38$	$313 \pm 50$	$82 \pm 27$	$95 \pm 31$	$1000 \pm 46$	$3678 \pm 119$	$1.48 \pm 0.01$
3	0.10	$1031 \pm 83$	$1127 \pm 91$	$1637 \pm 121$	$1790 \pm 132$	$113 \pm 14$	$123 \pm 16$			$1000 \pm 100$	$4687 \pm 333$	$1.47 \pm 0.01$
4	1.12	$979 \pm 87$	$2564 \pm 229$	$1523 \pm 107$	$2564 \pm 229$	$322 \pm 45$	$770 \pm 109$			$1000 \pm 77$	$643 \pm 35$	$1.57 \pm 0.01$
5	0.18									$1000 \pm 90$	$1064 \pm 67$	$1.36 \pm 0.01$
6	0.11	$917 {\pm} 115$	$1004 \pm 126$	$1226 \pm 132$	$1341 \pm 144$	$256 \pm 81$	$278 \pm 88$			$1000 \pm 123$	$749 {\pm} 65$	$1.59 \pm 0.02$
7	1.03	$1360 \pm 175$	$3315 \pm 426$	$2014 \pm 188$	$4910 \pm 458$	$340 \pm 46$	$761 \pm 103$		•••	$1000 \pm 64$	$937 \pm 42$	$1.77 \pm 0.01$
8	0.05	$1366 \pm 70$	$1420 \pm 73$	$2018 \pm 101$	$2099 \pm 105$	$407 \pm 37$	$421 \pm 38$			$1000 \pm 69$	$1246{\pm}61$	2.06
9	0.24					$262 \pm 21$	$315 \pm 25$	$71\pm17$	$78 \pm 19$	$1000 \pm 22$	$1856 \pm 29$	1.84
10	0.20	$1387 \pm 152$	$1652 \pm 181$	$2018 \pm 217$	$2403 \pm 258$	$426 \pm 63$	$498 {\pm} 74$		•••	$1000 \pm 149$	$557 \pm 59$	$1.93 \pm 0.01$
11	0.37	$1271 \pm 26$	$1742 \pm 36$	$1777 \pm 30$	$2436 \pm 41$	$114 \pm 10$	$151 \pm 13$	$34 \pm 11$	$40 \pm 12$	$1000 \pm 20$	$6289 \pm 88$	1.31
12	0.29				•••			$77 \pm 29$	$86 \pm 32$	$1000 \pm 86$	$931 \pm 57$	$1.85 \pm 0.01$
13	0.94	$792 \pm 55$	$1778 \pm 123$	$1171 \pm 63$	$2627 \pm 141$	$326 \pm 35$	$677 \pm 72$	$79 \pm 32$	$115 \pm 46$	$1000 \pm 48$	$535 \pm 18$	$1.55 \pm 0.01$
14	0.32	$1377 \pm 75$	$1814 \pm 99$	$2094 \pm 108$	$2760 \pm 142$	$199 \pm 19$	$256 {\pm} 25$		•••	$1000 \pm 68$	$1369 \pm 65$	$1.64 \pm 0.01$
15	0.23	$1335 \pm 96$	$1635 {\pm} 117$	$1870 \pm 131$	$2291 \pm 161$	$212 \pm 28$	$254 \pm 34$		•••	$1000 \pm 97$	$2745 \pm 188$	$1.73 \pm 0.01$
16	-0.11	834	$\pm 29$	1080	$0\pm 29$	$336 \pm 11$		64	±3	$1000\pm 29$	$29082 \pm 605$	$2.66 \pm 0.01$
17	-0.46	122	8±68	$1846 \pm 97$		$344 \pm 24$				$1000 \pm 62$	$3061 \pm 134$	$2.01 \pm 0.01$
18	0.26								•••	$1000 \pm 70$	$1244 {\pm} 61$	$2.36 \pm 0.01$
19	0.25							$26 \pm 5$	$28 \pm 6$	$1000 \pm 20$	$8045 \pm 113$	1.95
20	-0.14	130	$3\pm 78$	1813	$8 \pm 108$	$341 \pm 31$				$1000 \pm 83$	$1788 {\pm} 105$	1.96
21	0.39				•••					$1000 \pm 133$	$2235 \pm 210$	$1.15 \pm 0.01$
22	0.53	$1699 \pm 829$	$2674 \pm 1305$	$2206 \pm 866$	$3472 \pm 1364$				•••	$1000 \pm 123$	$260 \pm 21$	$1.17 \pm 0.02$
23	0.24	$1089 \pm 51$	$1347 \pm 62$	$1620 \pm 57$	$2002 \pm 70$	$297 \pm 37$	$360 \pm 45$			$1000 \pm 37$	$1384 \pm 36$	1.91
24	0.28	$1283\pm203$	$1635 \pm 259$	$2546 \pm 289$	$3244 \pm 368$					$1000 \pm 104$	$301 \pm 22$	$1.51 \pm 0.02$
25	0.79	$638 \pm 57$	$1262 \pm 112$	$1022 \pm 68$	$2021 \pm 134$	$297 \pm 42$	$551 \pm 78$	$67 \pm 23$	$92 \pm 31$	$1000 \pm 49$	$675 \pm 23$	$3.61 \pm 0.01$
26	0.33								•••	$1000 \pm 60$	$2595 \pm 111$	$1.44 \pm 0.01$
27	0.24	$1137 \pm 62$	$1393 \pm 76$	$1830 \pm 85$	$2241 \pm 104$	$168 \pm 20$	$202 \pm 25$		•••	$1000 \pm 57$	$2730 \pm 111$	$1.94 \pm 0.01$
28	0.11					$154 {\pm} 16$	$169 \pm 17$			$1000 \pm 48$	$6385 {\pm} 217$	1.73
29	0.33	•••	•••							$1000 \pm 60$	$8062 \pm 342$	$1.43 \pm 0.01$
30	0.49	$1283 {\pm} 127$	$1960 \pm 194$	$1857 {\pm} 177$	$2838 \pm 270$	$197 \pm 36$	$289 \pm 53$			$1000 \pm 130$	$2158 {\pm} 198$	$1.89 \pm 0.02$
31	0.43	•••			•••			•••	•••	$1000 \pm 165$	$474 {\pm} 55$	$1.62 \pm 0.01$

		[O 11	3727	[O II	3729	[Ne III]3869 [O III]4363		$_{\mathrm{H}\beta}$				
$f(\lambda)$		0.38		0.38		0.	34	0.	17	0.00	$F(H\beta)$	$EW[O\ III]\ [\AA]$
ID	$c(H\beta)$	$F_{\lambda}$	$I_{\lambda}$	$F_{\lambda}$	$I_{\lambda}$	$F_{\lambda}$	$I_{\lambda}$	$F_{\lambda}$	$I_{\lambda}$	$F_{\lambda}$		
32	0.63	$556 \pm 135$	$956 \pm 232$	$851 \pm 204$	$1462 \pm 351$	$159 \pm 49$	$260 \pm 80$			$1000 \pm 337$	$1121 \pm 267$	2.11
33	0.16					$248 \pm 34$	$281 \pm 39$			$1000 \pm 71$	$6689 \pm 335$	$1.14 \pm 0.01$
34	0.20	$1228 \pm 112$	$1547 \pm 133$	$1577 \pm 108$	$1870 \pm 128$	$370 \pm 43$	$431 \pm 51$			$1000 \pm 58$	$1256 {\pm} 52$	$2.16 \pm 0.01$
35	0.30	$1052 \pm 96$	$1364 {\pm} 125$	$1459 \pm 126$	$1892 \pm 163$	$106 \pm 18$	$135 \pm 23$			$1000 \pm 117$	$2640 \pm 219$	$1.23 \pm 0.01$
36	0.28	$1300 \pm 157$	$1657 \pm 200$	$2190 \pm 244$	$2789 \pm 311$	$285 {\pm} 53$	$355 \pm 66$			$1000 \pm 141$	$1149 \pm 114$	$1.64 \pm 0.01$
37	0.16	$1072 \pm 39$	$1225 \pm 44$	$1512 \pm 41$	$1728 \pm 47$	$243 \pm 22$	$275 \pm 25$	$53 \pm 10$	$57 \pm 11$	$1000 \pm 26$	$3498 {\pm} 63$	2.32
38	0.35	$894 \pm 35$	$1206 \pm 47$	$1342 \pm 35$	$1810 \pm 47$	$308 \pm 14$	$403 \pm 18$			$1000 \pm 25$	$3121 \pm 56$	$2.32 \pm 0.01$
39	0.86	$968 {\pm} 67$	$2032 \pm 140$	$1302 \pm 89$	$2732 {\pm} 187$	$182 \pm 18$	$356 \pm 36$			$1000 \pm 96$	$3109 \pm 212$	2.25
40	0.15	$890 \pm 65$	$1013 \pm 74$	$1229 \pm 87$	$1398 \pm 99$	$251 \pm 22$	$282 \pm 25$	$86 \pm 19$	$91 \pm 20$	$1000 \pm 98$	$1890 \pm 132$	$2.69 \pm 0.01$
41	0.03	$1064 \pm 118$	$1094 \pm 122$	$1444 \pm 137$	$1484 {\pm} 141$	$226 \pm 54$	$231 \pm 55$			$1000 \pm 116$	$668 {\pm} 55$	$1.75 \pm 0.01$
42	$42  0.35 \qquad$								$1000 \pm 254$	$557 \pm 100$	$1.23 \pm 0.01$	
43	0.19	$1125 \pm 99$	$1319 \pm 116$	$1631 \pm 104$	$1911 \pm 122$					$1000 \pm 63$	$490 \pm 22$	$1.51 \pm 0.01$
44	0.56	$457 {\pm} 46$	$741 \pm 75$	$457 \pm 43$	$742 \pm 69$			$190 \pm 29$	$237 \pm 36$	$1000 \pm 43$	$2259 \pm 68$	2.68
45	0.12	$1373 \pm 99$	$1520 \pm 110$	$2249 \pm 126$	$2490 \pm 139$					$1000 \pm 66$	$3078 \pm 145$	$1.28 \pm 0.01$

Table 4.3: Main emission line fluxes ranging from [O III]4959 up until [S II]6730, derived for the galaxies of the North (N) zone of the MUSE observations. The row below the emission line names displays the value of the reddening curve. For each galaxy, we present the ID, the extincion coefficient, and the observed flux and extincion-corrected intensity, both relative to  $F(H\beta) = I(H\beta) = 1000$ . For galaxies with negative extinction coefficients, the values of the observed flux are the same as the intensity. The final column displays the observed flux of the H $\beta$  line (the flux units are  $10^{-20}$ erg cm<sup>-2</sup> s<sup>-1</sup>).

		[O III	[]4959	[O III	]5007	Н	[α	[N II	]6584	[S II]6	716	[S II]	]6730	
$f(\lambda)$		-0.	.03	-0.	.04	-0.	.35	-0.	.35	-0.3	37	-0.	.37	$F(H\beta)$
ID	$c(H\beta)$	$F_{\lambda}$	$I_{\lambda}$	$F_{\lambda}$	$I_{\lambda}$	$F_{\lambda}$	$I_{\lambda}$	$F_{\lambda}$	$I_{\lambda}$	$F_{\lambda}$	$I_{\lambda}$	$F_{\lambda}$	$I_{\lambda}$	
1	0.73	$1159\pm141$	$1102\pm134$	$3577 \pm 367$	$3323\pm341$	$5133 \pm 506$	$2859 \pm 282$			$395 \pm 99$	$211 \pm 53$	$599\pm216$	$319 \pm 115$	310±30
2	0.36	$779 \pm 29$	$759 \pm 28$	$2359 \pm 81$	$2274 \pm 78$	$3812 \pm 128$	$2859 \pm 96$	$97 \pm 18$	$73 \pm 14$	$576 \pm 30$	$347 \pm 33$	$472 \pm 45$	$146 \pm 21$	$3678 \pm 119$
3	0.10	$544 \pm 40$	$541 \pm 40$	$1649 \pm 119$	$1631 \pm 118$	$3106\pm226$	$2858 \pm 208$							$4687 \pm 333$
4	1.12	$1386 \pm 83$	$1285 \pm 77$	$4200 \pm 238$	$3750 \pm 212$									$643 \pm 35$
5	0.18	$722 \pm 56$	$714 \pm 56$	$2186 \pm 153$	$2146 \pm 150$	$3303 \pm 218$	$2857 \pm 189$	$219 \pm 47$	$189 \pm 41$	$550 \pm 52$	$471 \pm 45$	$622 \pm 149$	$533 \pm 128$	$1064 \pm 67$
6	0.11	$561 \pm 59$	$557 \pm 58$	$1670 \pm 161$	$1681 \pm 160$	$3111 \pm 905$	$2862 \pm 833$	$124 \pm 62$	$114 \pm 57$					$749 \pm 65$
7	1.03	$887 \pm 52$	$826 \pm 48$	$2687 \pm 137$	$2424 \pm 123$					$544 \pm 71$	$226 \pm 29$	$523 \pm 72$	$216 \pm 30$	$937 \pm 42$
8	0.05	$1426 \pm 78$	$1423 \pm 78$	$4338 \pm 215$	$4316\pm213$									$1246 \pm 61$
9	0.24	$1290 \pm 25$	$1270 \pm 24$	$3908 \pm 67$	$3818 \pm 66$	$3454 \pm 62$	$2860 \pm 51$	$62 \pm 16$	$51\pm13$					$1856 \pm 29$
10	0.20	$1564 \pm 167$	$1542 \pm 165$	$4739 \pm 501$	$4639 \pm 491$									$557 \pm 59$
11	0.37	$502 \pm 9$	$489 \pm 9$	$1521 \pm 24$	$1466 \pm 23$	$3830 \pm 947$	$2857 \pm 706$	$703 \pm 14$	$524 \pm 10$	$730 \pm 19$	$535 \pm 14$	$543 \pm 17$	$397 \pm 12$	$6289 \pm 88$
12	0.29	$788 \pm 60$	$772 \pm 59$	$2387 \pm 162$	$2318 \pm 158$	$3605 \pm 232$	$2862 \pm 184$	$214 \pm 38$	$169 \pm 30$					$931 \pm 57$
13	0.94	$1209 \pm 55$	$1134 \pm 52$	$3826 \pm 186$	$3481 \pm 169$									$535 \pm 18$
14	0.32	$785 \pm 45$	$767 \pm 44$	$2378 \pm 123$	$2302 \pm 119$									$1369 \pm 65$
15	0.23	$1001 \pm 74$	$985 \pm 73$	$3032 \pm 215$	$2962 \pm 210$									$2745 \pm 188$
16	-0.11	1658	8±50	5327	$\pm 162$									$29082 \pm 605$
17	-0.46	1470	$0\pm72$	4452	$\pm 205$									$3061 \pm 134$
18	0.26	$1690 \pm 89$	$1659 \pm 87$	$5118\pm259$	$4990 \pm 253$	$3509\pm202$	$2860 \pm 165$							$1244 \pm 61$
19	0.25	$1139 \pm 18$	$1121 \pm 17$	$3450 \pm 50$	$3364 \pm 49$	$3487 \pm 53$	$2859 \pm 44$	$269 \pm 8$	$220 \pm 7$	$458 \pm 9$	$371 \pm 8$	$324 \pm 7$	$262 \pm 6$	$8045 \pm 113$
20	-0.14	1337	$7 \pm 80$	4049	$\pm 239$									$1788 \pm 105$
21	0.39	$701 \pm 70$	$682 \pm 69$	$2123\pm205$	$2042 \pm 198$	$3912 \pm 371$	$2860 \pm 271$	$500 \pm 61$	$365 \pm 44$	$1009 \pm 102$	$723 \pm 73$	$642 \pm 73$	$458 {\pm} 52$	$2235\pm210$
22	0.53	$716 \pm 97$	$690 \pm 94$	$1676 \pm 167$	$1589 \pm 158$	$4347 \pm 397$	$2860 \pm 261$	$434{\pm}103$	$285 \pm 68$	$940 \pm 148$	$602 \pm 95$	$401 \pm 109$	$256 \pm 70$	$260 \pm 21$
23	0.24	$1065 \pm 30$	$1047 \pm 30$	$3224 \pm 88$	$3144 \pm 86$	$3474 \pm 96$	$2863 \pm 79$	$170 \pm 24$	$140 \pm 20$	$360 \pm 33$	$293 \pm 27$	$208 \pm 26$	$169 \pm 21$	$1384 \pm 36$
24	0.28	$677 \pm 62$	$665 \pm 61$	$2051 \pm 170$	$1996 \pm 166$	$3573 \pm 275$	$2858 \pm 220$	$444 {\pm} 154$	$355 \pm 123$					$301 \pm 22$
25	0.79	$1490 \pm 60$	$1409 \pm 56$	$4513 \pm 170$	$4165{\pm}157$									$675 \pm 23$
26	0.33	$1106 \pm 52$	$1080 \pm 51$	$3350 \pm 149$	$3242 \pm 144$	$3713\pm170$	$2863 \pm 131$	$340 \pm 48$	$261 \pm 37$	$531 \pm 36$	$402 \pm 27$	$397 \pm 31$	$300 \pm 24$	$2595 \pm 111$
27	0.24	$913 \pm 46$	$898 \pm 45$	$2765 \pm 124$	$2701 \pm 121$									$2730 \pm 111$
28	0.11	$893 \pm 33$	$887 \pm 33$	$2704 \pm 96$	$2674 \pm 94$	$3132 \pm 109$	$2862 \pm 99$	$199 \pm 14$	$182 \pm 13$	$441 \pm 29$	$400 \pm 27$	$316 \pm 56$	$287 \pm 50$	$6385 \pm 217$
29	0.33	$704 \pm 34$	$688 \pm 33$	$2133 \pm 95$	$2061 \pm 92$	$3722 \pm 494$	$2855 \pm 379$	$332 \pm 58$	$254 \pm 44$	$770 \pm 39$	$581 \pm 29$	$571 \pm 31$	$430 \pm 23$	$8062 \pm 342$
30	0.49	$998 \pm 104$	$964 \pm 100$	$3022 \pm 297$	$2874 \pm 282$									$2158 \pm 198$
31	0.43	$1376 \pm 175$	$1336 \pm 170$	$4768 {\pm} 505$	$2989 \pm 483$	$4041 \pm 478$	$2861 \pm 338$	$267 \pm 58$	$188 \pm 41$					$474 \pm 55$

		[O III]4959		[0 111	[О пп]5007		$H\alpha$		6584	[S II]	6716	[S II]6730		
$f(\lambda)$								<u> </u>						D(II a)
		-0.03		-0.04		-0.35		-0.35		-0.37		-0.37		$F(H\beta)$
ID	$c(H\beta)$	$\mathrm{F}_{\lambda}$	$I_{\lambda}$	$\mathrm{F}_{\lambda}$	$I_{\lambda}$	$\mathrm{F}_{\lambda}$	$I_{\lambda}$	$\mathrm{F}_{\lambda}$	$I_{\lambda}$	$\mathrm{F}_{\lambda}$	$I_{\lambda}$	$\mathrm{F}_{\lambda}$	$I_{\lambda}$	
32	0.63	$821 \pm 196$	$786 \pm 188$	$2487 \pm 594$	$2333 \pm 557$	$1490 \pm 375$	$1045 \pm 265$							$1121\pm267$
33	0.16	$670 \pm 36$	$662 \pm 35$	$2028 \pm 105$	$1996 \pm 103$	$3244 \pm 168$	$2858 \pm 148$	$251 \pm 26$	$221 \pm 23$	$595 \pm 38$	$520 \pm 33$	$401 \pm 34$	$350 \pm 30$	$6689 \pm 335$
34	0.20	$1428 \pm 68$	$1408 \pm 67$	$4325 \pm 191$	$4234 \pm 187$	$3342 \pm 192$	$2858 {\pm} 164$							$1256 {\pm} 52$
35	0.30	$362 \pm 34$	$355 \pm 33$	$1158 \pm 98$	$1124 \pm 95$	$3638 \pm 312$	$2863 \pm 246$	$669 \pm 182$	$525 \pm 142$	$813 \pm 72$	$629 \pm 55$	$536 \pm 52$	$414 \pm 41$	$2640 \pm 219$
36	0.28	$1285 \pm 133$	$1262 \pm 131$	$3891 \pm 394$	$3786 \pm 383$	$3575 \pm 370$	$2860 \pm 296$	$247 \pm 61$	$197 \pm 49$	$648 \pm 107$	$510\pm84$	$465 \pm 89$	$366 \pm 70$	$1149 \pm 114$
37	0.16	$1203\pm23$	$1190\pm23$	$3645 \pm 68$	$3587 \pm 67$	$3239 \pm 65$	$2860 \pm 57$	$96 \pm 42$	$84 \pm 37$	$347 \pm 22$	$303\pm19$	$229 \pm 23$	$200 \pm 20$	$3498 \pm 63$
38	0.35	$1348 \pm 33$	$1317 \pm 32$	$4083\pm86$	$3945 \pm 83$									$3121 \pm 56$
39	0.86	$904 \pm 62$	$851 \pm 58$	$2737 \pm 187$	$2507 \pm 171$									$3109 \pm 212$
40	0.15	$1297 \pm 93$	$1282 \pm 92$	$3927 \pm 277$	$3864 \pm 273$									$1890 \pm 132$
41	0.03	$760 \pm 67$	$758 \pm 67$	$2301 \pm 195$	$2297 \pm 195$	$2932 \pm 247$	$2858 \pm 241$			$447 \pm 120$	$436 {\pm} 117$	$115 \pm 65$	$112 \pm 63$	$668 \pm 55$
42	0.35	$1057 \pm 194$	$1031 \pm 189$	$3203 \pm 581$	$3088 \pm 560$	$3787 \pm 684$	$2859 \pm 516$	$270 \pm 70$	$203 \pm 52$					$557 \pm 100$
43	0.19	$884 \pm 44$	$871 \pm 44$	$2677 \pm 126$	$2628 \pm 124$	$3313 \pm 160$	$2859 \pm 138$				•			$490 \pm 22$
44	0.56	$2256 \pm 72$	$2170 \pm 69$	$6834 \pm 210$	$6451 \pm 199$		••				•			$2259 \pm 68$
45	0.12	$562 \pm 30$	$557 \pm 30$	$1701 \pm 85$	$1683 \pm 84$	$3140 \pm 157$	$2864 \pm 143$	$409 \pm 37$	$372 \pm 34$	$767 \pm 55$	$694 \pm 50$	$466 {\pm} 46$	$421 \pm 41$	$3078 \pm 145$

### 4.2 Ionization source from classic emission-line diagnostics

We examine the type of ionization occurring in the galaxies of our sample by comparing classic emission line ratios. These diagnostic diagrams differentiate between Star-Forming (SF) and AGN ionization mechanisms. We employ four diagnostics, considering that, for our redshift range (0.2 < z < 0.85), certain emission lines fall outside the detection range of MUSE.

We utilize the classic Baldwin-Phillips-Terlevich (N2-BPT, Baldwin et al. 1981) diagram, shown in Fig. 4.2a, as well as the [S II]6716,6731/H $\alpha$  line ratio (VO87, Veilleux & Osterbrock, 1987, Fig. 4.2b). In the case of high-z galaxies, we rely on the comparison of the line ratios between [O III]4959,5007/H $\beta$  and [O II]3727,3729/H $\beta$  (O2-BPT, Lamareille et al., 2004, Fig. 4.2c). Overall, our sample is consistent with star formation as the main source of ionization, i.e., consistent with dominant stellar photoionization processes. Two galaxies, ID 21 and 36, show slightly higher [S II]/H $\alpha$  ratios, which can be explained by additional ionization constributions, such as shocks.

Additionally, in Fig. 4.2d we compare the  $O_{32}$  (([O III] $\lambda\lambda4959,5007$ )/[O II] $\lambda3727$ ) line ratio with  $R_{23}$  ( ([O II] $\lambda\lambda3727,3729+$ [O III] $\lambda\lambda4959,5007$ )/H $\beta$ ) (Kobulnicky & Kewley, 2004). These plots have been all color coded by the equuivalent width (EW) of [O III] $\lambda5007$ , up until a value of 200 Å. Galaxies with EWs higher than this are represented with the color black.

Generally, the  $R_{23}$  ratio, suggested by Pagel et al. (1979) is used as a proxy for the oxygen abundance, particularly useful when other lines are redshifted out of the detection range of the instrument, such as  $H\alpha$  or  $[N\ II]\lambda6584$ , and in combination with the  $O_{32}$  ratio, it can compare indicators of metallicity and ionization, respectively. However, the relation between  $R_{23}$  and metallicity is bivalued with a peak around 20% solar, as well as presenting two branches at low and high metallicity. Therefore we only apply it to plot this relationship. A very commonly used way to fix this is to include additional independent line ratios, such as N2, to break the degeneracy, and limit the abundance range covered by the galaxy (Paalvast et al., 2018). In order to have a better appretiation of the place our sample in the  $O_{32}$  vs.  $R_{23}$  diagram, we plot data from the Sloan Digital Sky Survey DR7 (SDSS DR7, York et al., 2000). For this last Figure, we see that our sample reaches in general high values of  $\log O_{32} > -0.5$  (Paalvast et al., 2018), placing our sample above the bulk of SDSS local galaxies, in a region populated by more extreme ionization galaxies, such as the extreme emission-line galaxies (EELGs,Nakajima & Ouchi, 2014; Llerena et al., 2024).

We also include the comparison between  $[O III]\lambda 5007$  EW and the  $O_{32}$  ratio, in the left panel of Fig. 4.3. The  $O_{32}$  ratio can be used as a tracer of the ionization parameter, U (Osterbrock & Ferland, 2006), and when comparing this ratio with the equivalent width of  $[O III]\lambda 5007$ , the trend is for galaxies with a higher ratio to exhibit a stronger EW. This is not surprising, as an increase in equivalent width of  $[O III]\lambda 5007$  would mean a greater production of ionizing photons (Tang et al., 2019), and considering the anticorrelation

between  $O_{32}$  and metallicity (Bian et al., 2018), higher EW values are expected to correspond to low metallicity galaxies (approximately  $0.2Z_{\odot}$ , Amorín et al., 2010). We compare our sample with a sample of EELGs from Pérez-Montero et al. (2021), which show much higher EW values, and are characterized by being much more intense systems. Our sample presents in general higher values of EW and  $O_{32}$  for background galaxies (z > 0.4), and we see a coherent trend between our galaxies and the EELG sample. We include a galaxy with an EW value that was overestimated, and is represented with an arrow. We present the histogram distribution in the right panel of Fig. 4.3. The equivalent width has a mean of  $log(EW[O\ III]5007) = 1.971$ , which is a consequence of the extreme conditions of the medium in which the gas resides, and the high ionization provided by it.

# 4.3 Physical properties from Spectral Energy Distribution (SED) fitting

To derive stellar masses, we utilize the Bagpipes code (Bayesian Analysis of Galaxies for Physical Inference and Parameter EStimation, Carnall et al., 2018). Its purpose is to model the emission of galaxies across the ultraviolet to microwave spectrum, fitting these models to photometric data using the Multinest<sup>1</sup> nested sampling algorithm (Feroz & Hobson, 2008; Feroz et al., 2009, 2019). Bagpipes can generate model spectra from predefined components such as dust, gas, or specific events like starbursts. The main aspect of Bagpipes in the context of our work, is its capability of fitting the previously described models to observational data, being spectroscopic or photometric points. While we provide a brief description of its main elements here, more detailed information regarding the specifics of the code can be found in the cited works.

The luminosity of a spectrum modelled in BAGPIPES is composed of the sum of the following elements:

- 1. Simple Stellar-Population (SSP) models. This is a function of the wavelength,  $\lambda$ , the age of the stellar population, a, and the IMF.
- 2. The Star Formartion History, SFR(t). It is composed over the sum of one or more SFH components.
- 3. The Transmission Function of the ISM, which includes absorption, line emission, ionized continuum emission, and warm dust emission from HII regions.
- 4. The Transmission Function of neutral ISM, due to dust attenuation and emission.

<sup>1</sup>https://github.com/farhanferoz/MultiNest

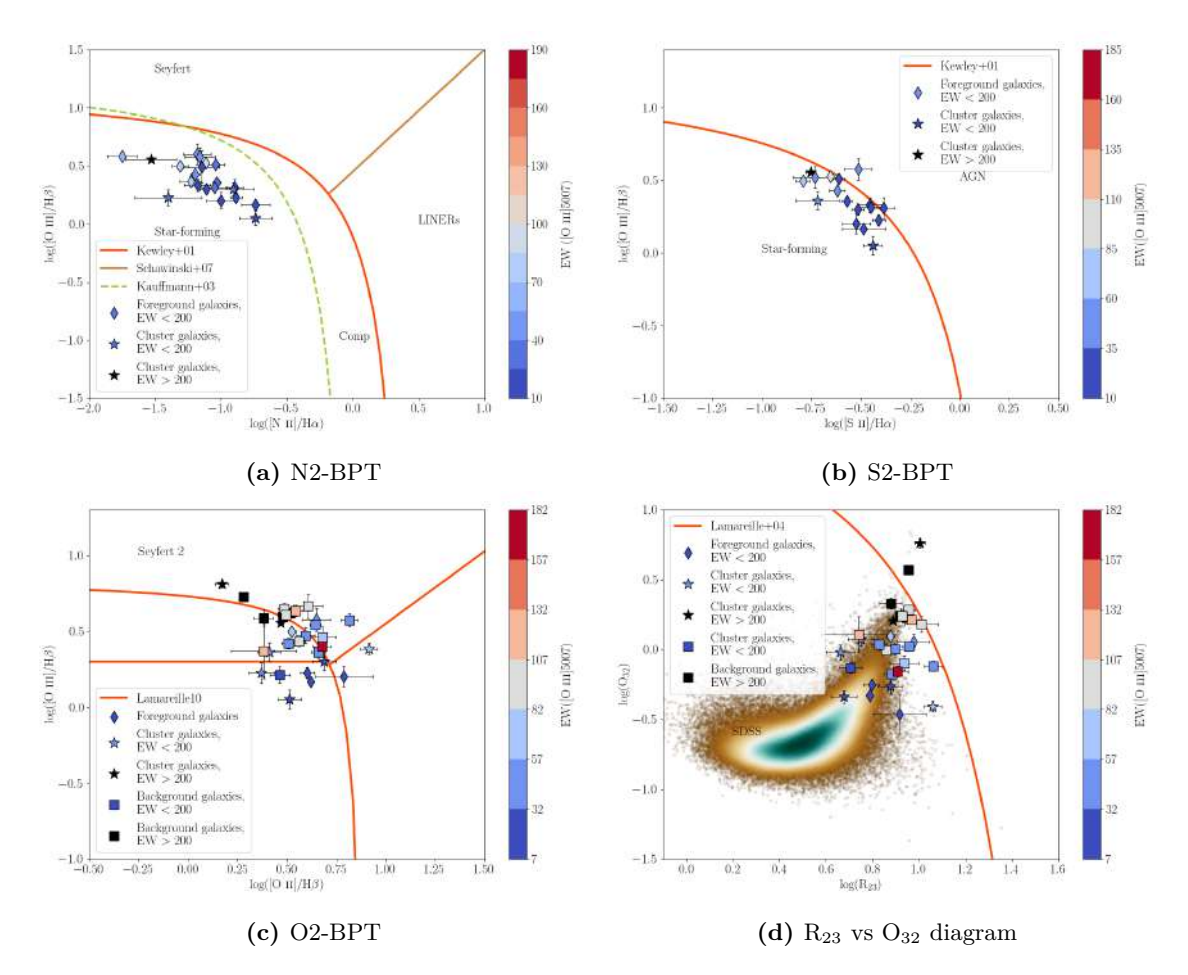


Figure 4.2: Diagnostic diagrams to identify the ionization mechanism for our sample. Top left:  $[N \text{ II}]\lambda6584/H\alpha$  vs.  $[O \text{ III}]\lambda5007/H\beta$ . The red and brown curves represent the parametrizations of Kewley et al. (2001) and Schawinski et al. (2007), and the dashed green curve is the parametrization from Kauffmann et al. (2003). Top right:  $[S \text{ II}]\lambda6716,6731/H\alpha$  vs.  $[O \text{ III}]\lambda5007/H\beta$ , with the parametrization from Kewley et al. (2001). Bottom left: Variation of the traditional BPT diagram, for galaxies at  $z \gtrsim 0.4$ , where the Hα line is redshifted out of the wavelength range of main spectroscopic surveys. The red curves represent the parametrizations of Lamareille (2010) to classify between Star-forming galaxies, Seyfert 2-type galaxies, LINER galaxies, and a composite region. Lower right:  $O_{32}$  vs.  $R_{23}$  diagram, the red curve is the parametrization of Lamareille et al. (2004). The density plot represents SDSS DR7 galaxies. The diamonds and squares associated with the color bar represent foreground and background galaxies, respectively, with equivalent widths (EW) which are less than 200 Å. The stars are representative of galaxies that are cluster members, according to the redshift classification of Lagattuta et al. (2022), and the color bar represents the same parameter as in the other symbols. Black symbols represent galaxies with EWs over 200 Å, in the three redshift groups.

#### 4.3.1 About the Stellar Population Synthesis (SPS)

The BAGPIPES code is written to accept preconfigured SPS models, presented as grids of SSP models, spanning various ages and metallicities. We implement the 2016 version of the SPS models from Bruzual & Charlot (2003), and the models used in the code are based on a Kroupa & Boily (2002) IMF.

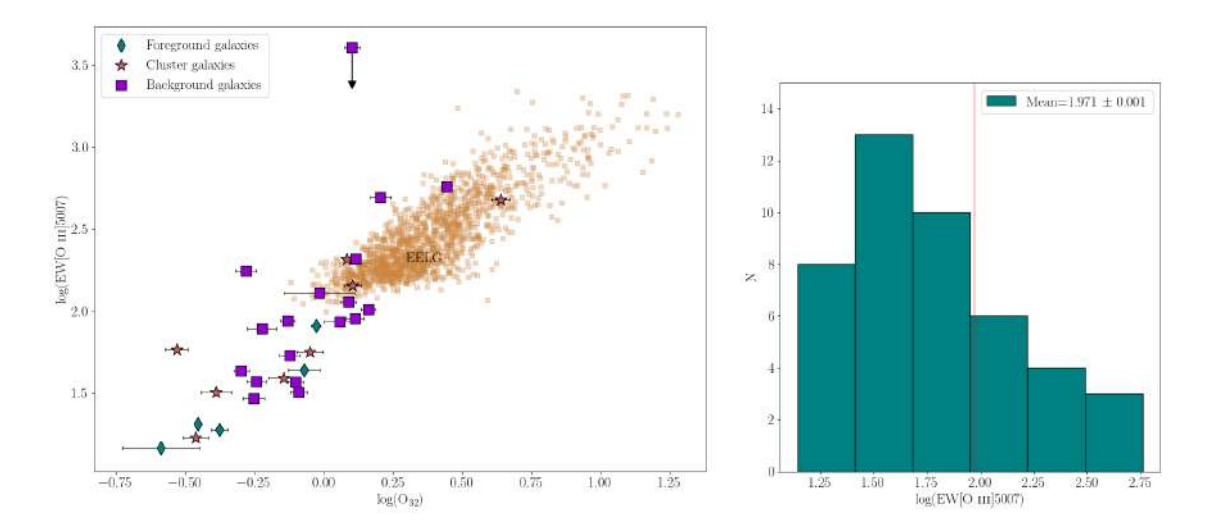


Figure 4.3: Left:  $[O III]\lambda 5007$  equivalent width plotted against  $log(O_{32})$ . Diamonds and squares represent foreground and background galaxies, respectively. Stars represent cluster galaxies. We include a sample of extreme-emission line galaxies (EELGs), from Pérez-Montero et al. (2021), to compare the range covered Right: Histogram distribution of EW[O III] $\lambda 5007$ . The mean value is represented with a vertical dashed line.

#### 4.3.2 About the Star Formation History

We construct the SFH based on one or more components, defined as j, where each specifies some functional form for the SFR as a function of time, represented as  $SFR_j(t)$ . The total SFR is given by the sum of these components,  $SFR(t) = \sum SFR_j(t)$ . The options for the SFHs offered by the code are:

- Delta function (SFR(t)  $\propto$  SFR  $\cdot \delta(t)$ );
- Constant;
- Exponentially declining (SFR(t)  $\propto e^{-t/\tau}$ );
- Delayed exponentially declining (SFR(t)  $\propto t \cdot e^{-t/\tau}$ );
- Log-normal  $\left( \text{SFR}(t) \propto \frac{1}{t \cdot \sqrt{2\pi\tau^2}} \cdot e^{-\frac{(\ln t T_0)^2}{2\tau^2}} \right);$
- Double-power law  $\left( SFR(t) \propto \left[ \left( \frac{t}{\tau} \right)^{\alpha} + \left( \frac{t}{\tau} \right)^{\beta} \right]^{-1} \right);$
- Custom (input of SFR values),

where the parameters  $\delta(t)$  is the Delta function,  $\tau$  is the characteristic time,  $T_0$  is the time when star formation starts, and  $\alpha$  and  $\beta$  are the falling and rising slopes, respectively.

#### 4.3.3 Parameters fitted and details on the sample

In our case, we work assuming an exponentially declining SFH. We constrain the metallicity between 0 and  $2.5Z_{\odot}$ . Because we are dealing with galaxies with intense optical

emission lines, accounting for their nebular contribution is a key input, so we include this parameter for the SED fitting. Following the same line, we define the ionization parameter,  $\log U$ , between -4 and -2. For the dust component, we select the Calzetti law (Calzetti et al., 2000), with the attenuation varying between 0 and 2.

To perform the fittings, we utilize the photometric data from the DEEPSPACE catalogs (Shipley et al., 2018) for 42 of the 45 galaxies of the sample, this is due to inconsistencies in the quality of the measurements of DEEPSPACE IDs 5455, 5741 and 5407, which were marked with 'use\_phot' value of 0 (see their Section 3.10 for more details). In these cases, we rely on the photometric data provided by the ASTRODEEP catalogs (Bradač et al., 2019), which count with three optical (ACS; F435W, F606W, and F814W), and four near-infrared (WFC3; F105W, F125W, F140W, and F160W) bands (also from the HFF initiative).

We present in the upper part of Fig. 4.4 an example of a fit utilizing galaxy ID 27. The blue dots represents the photometric data, and the orange dots represent the posterior photometric points. This example illustrates the nebular contribution by means of the emission lines. The lower part shows the corner plots for the posterior of the analyzed parameters, such as dust attenuation, age, stellar mass, and ionization parameter.

The resulting stellar mass values for our sample ranges between  $10^7 - 10^{9.7} \rm M_{\odot}$  (mean of  $10^{8.81} \rm M_{\odot}$ ). Fig. 4.5 shows the distribution of the stellar mass.

### 4.4 Magnification correction

We take into consideration the effect of the cluster on the background galaxies due to its mass. Performing the cluster lens modeling allows us to study deeper objects considering their intrinsic properties. In Shipley et al. (2018), they considered different lensing models previously derived, and in their catalogs offer ten different lensing models, from different groups. They utilized different approaches to derive the models: assuming that the cluster galaxies trace the cluster mass; assuming that they do not, limited only to lensing observables; and assuming the mass distortions are a superposition of Gaussian functions tracing the light coming from cluster members (see Section 5.5 of Shipley et al., 2018 for details on the specific groups and the models chosen).

To solve this, we perform the median of the ten models, and to obtain a value for the uncertainties, we calculate the Mean Absolute Deviation, which can be written as

$$MAD = \mathbf{median}(|x_i - X_m|), \tag{4.8}$$

where  $x_i$  is the *i*-th value in the dataset, and  $X_m$  is the median value in the dataset. The values present in the rest of the Figures are corrected by the magnification effects.

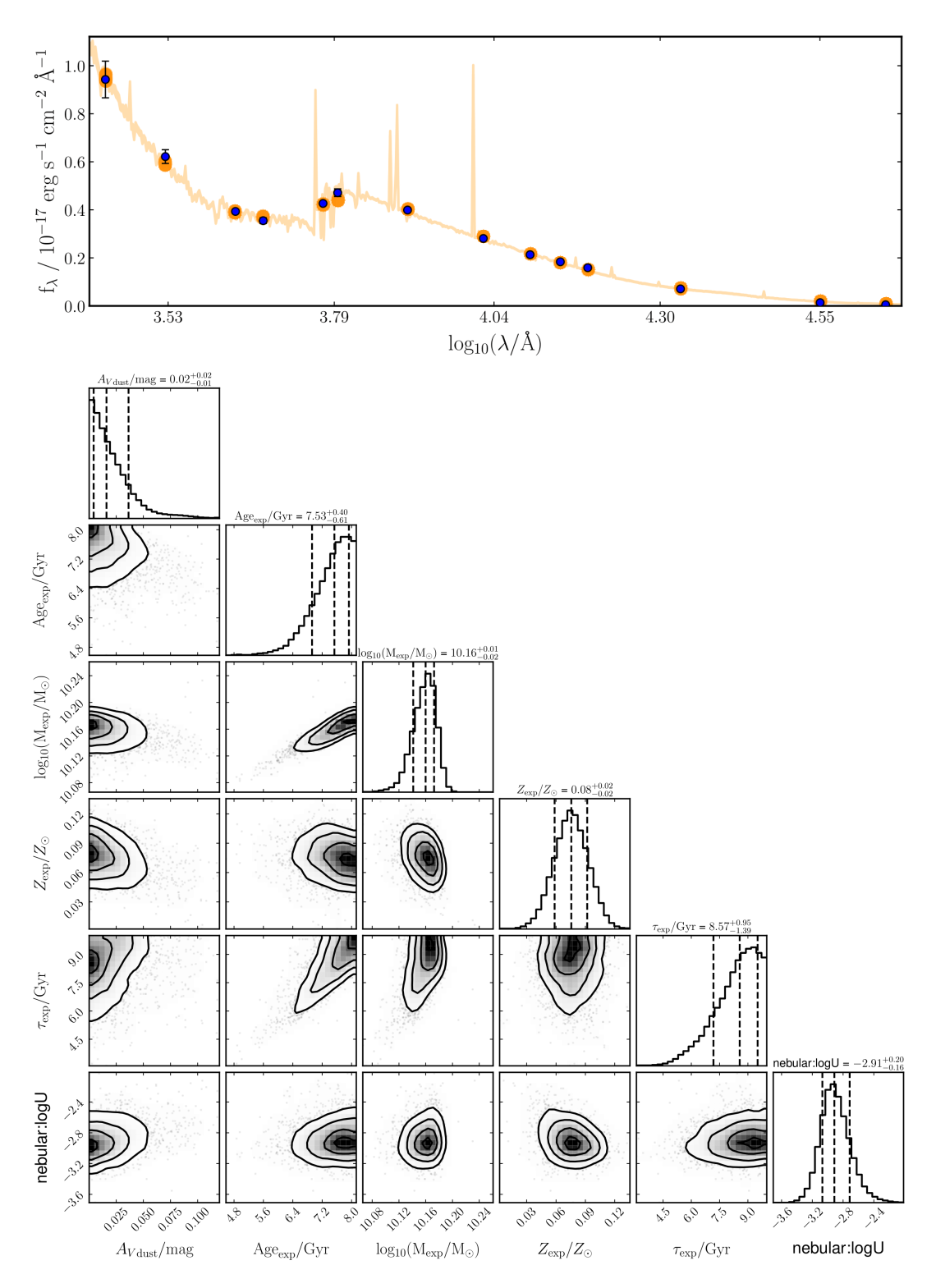


**Figure 4.4:** Example of a BAGPIPES fit for galaxy ID 27 (DEEPSPACE ID 4321), at z=0.5478. The top panel shows the reconstruction of the photometric points (blue). The data are from the HST, HAWK-I and Spitzer observations (see Table 2.1). The uncertainty range is also visible for the posterior photometry (orange). The lower panel shows the corner plots for the different posteriors of the physical parameters obtained from the SED fittings.

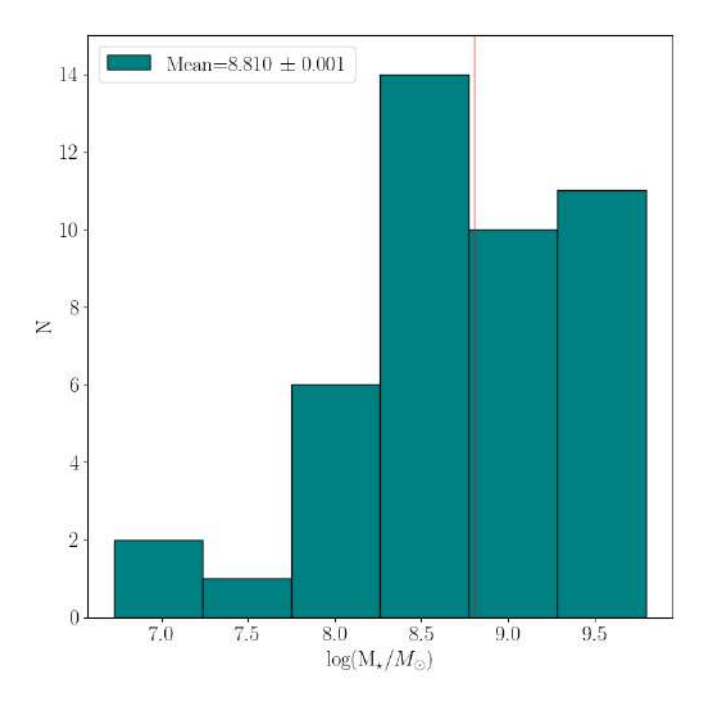


**Figure 4.5:** Histogram distribution of  $log(M_{\star})$ . The mean value is represented with the red vertical line.

#### 4.5 Star formation rates from Balmer lines

We base on the H $\alpha$  luminosities following the method presented in Kennicutt (1998) to derive expressions for the Star Formation Rate (SFR). For the galaxies that do not show the presence of this line (i.e. with  $z \gtrsim 0.42$ ), we apply the theoretical ratio between H $\alpha$  and H $\beta$ , H $\alpha$ /H $\beta$  = 2.86, following a case B recombination, with T<sub>e</sub> = 1×10<sup>4</sup> K. The expression provided is represented by

SFR 
$$(M_{\odot} \text{ yr}^{-1}) = 7.9 \times 10^{-42} L(H\alpha) (\text{erg s}^{-1})$$
 (4.9)

In order to use the data in an appropriate way, we first need to convert the H $\alpha$  fluxes from erg cm<sup>-2</sup> s<sup>-1</sup>, to luminosities, in units of erg s<sup>-1</sup>. Consider the definition of the flux of a source:

$$F = \frac{L}{4\pi D_L^2},\tag{4.10}$$

where L is the luminosity of the source, and  $D_L$  is the luminosity distance. This value is calculated considering the cosmology available in the python library astropy.cosmology, considering a Hubble constant of  $H_0 = 70 \mathrm{km \ s^{-1} Mpc^{-1}}$  and a mass density of  $\Omega_{m,0} = 0.3$ . This provides a robust base for the cosmological calculations. For the uncertainties in the values of SFR, wew employed traditional error propagation methods. This method was applied to the majority of the properties that we study in order to account for individual uncertainties.

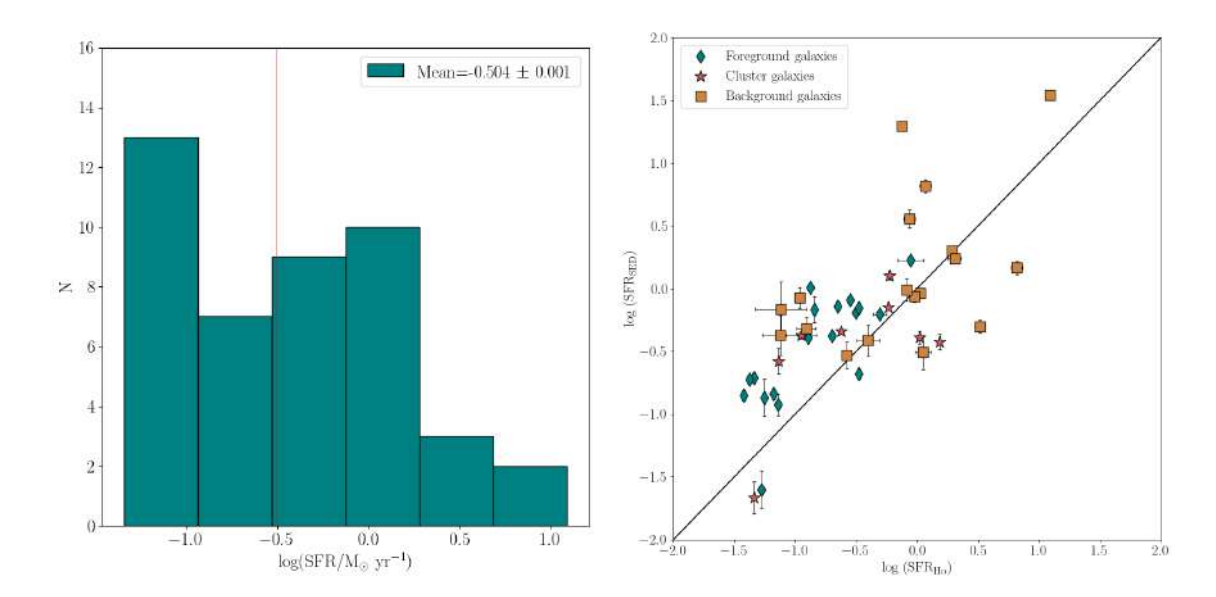


**Figure 4.6:** Left: Histogram distribution of  $\log(SFR)$ . The mean value is represented with the red vertical line. Right: SFR comparison between SED-based SFR and SFR from extinction-corrected H $\alpha$  luminosity. The diamonds, stars and squares represent foreground, cluster and background galaxies, respectively. The black line shows the one-to-one relation.

Although the SED fitting offers a value for the SFR, the timescales can trace longer timescales compared to SFRs based on L(H $\alpha$ ), which traces  $\lesssim 20$  Myr (Janowiecki et al., 2017). In order to avoid biases in the derivation of stellar masses and SFR, we will consider the values from the H $\alpha$  SFR in the posterior analysis. We compare both results on the right panel of Fig. 4.6. We see that foreground, background and cluster galaxies provide higher SFR values when considering the H $\alpha$  luminosity, with a mean difference in SFR of -0.2, -0.2 and -0.06 dex, respectively, compared with the SED fitting, indicating that the SFR derived using this method is slightly higher than that of H $\alpha$  luminosity. The histogram distribution of the H $\alpha$ -based SFR is presented on the left panel Fig. 4.6. Additionally, we present the histogram distribution of the sSFR in Fig. 4.7. The SFR has a mean value of log SFR = -0.504, and the sSFR shows a relatively high mean value of log sSFR = -9.314.

# 4.6 Metallicity diagnostics

We now focus on one of the key aspects in the study of SFGs, namely the determination of the oxygen abundance, or metallicity. It is well established that the observed metal content of a galaxy serves as a proxy for the amount of gas reprocessed by its stars, as well as how this gas and metal-rich content is exchanged between the galaxy and its environment via supernovae (SNe) shocks, or galactic winds (Tremonti et al., 2004; Maiolino & Mannucci, 2019). Due to the shallow gravitational potential wells of low-mass systems, not all heavy elements are reaccreted onto the galaxy; some enrich the intergalactic medium (IGM), contributing metal-rich gas that interacts with other systems

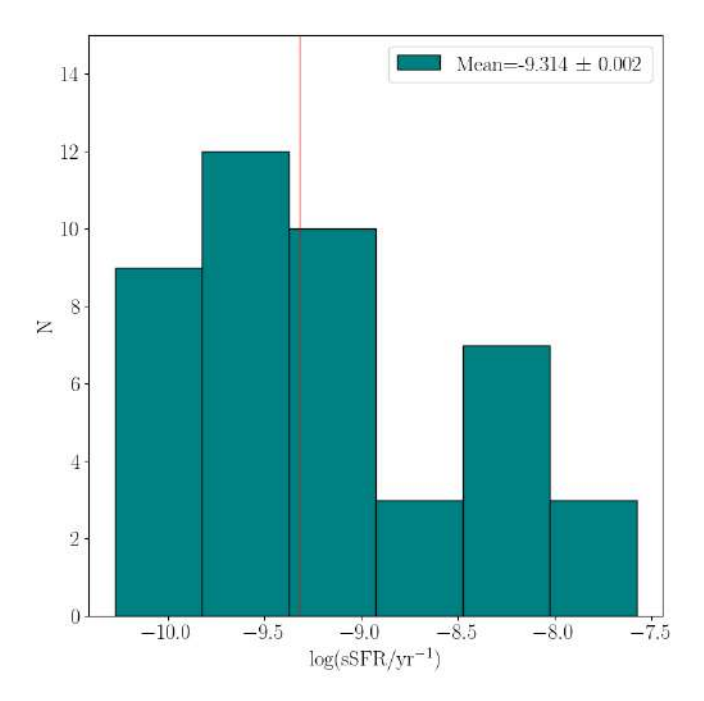


**Figure 4.7:** Histogram distribution of log(sSFR). The mean value is represented with a red vertical line.

and receives external metal-poor gas inflows (Gao et al., 2018). Internally, this sequence is also relevant: inflowing pristine gas provides material to form new stars, which can again enrich the galaxy environment, perpetuating this cycle (Andrews & Martini, 2013). All these interactions modulate very important properties such as stellar mass, metallicity, and SFR, and therefore, provide key information about the evolutive status of galaxies, when analyzed.

#### Approaches to derive abundances

Over time, various methods have been developed to obtain the metallicity of a galaxy, the most resourceful being the so-called direct method (see next Subsection). However, this technique relies on the auroral line  $[O\ III]\lambda4363$ , which is extremely faint, and may not always be detected in galaxy spectra. To overcome this, alternative metallicity diagnostics have been calibrated using strong nebular emission lines against the direct method (Curti et al., 2017; Nakajima et al., 2022), or using photoionization models (McGaugh, 1991; Maiolino et al., 2008). This is useful because these lines are more easily detectable, even when dealing with low S/N spectra (Maiolino & Mannucci, 2019). The following Subsections will delve into these two methods.

#### 4.6.1 Oxygen abundance from the direct method

To obtain a value of the oxygen abundance using the direct method, we follow the relations described in Pérez-Montero (2017). The direct method relies on the determination of

electronic temperature,  $T_e$ , based on the intensity ratio of the auroral line [O III] $\lambda 4363$ , to the [O III] $\lambda \lambda 4959,5007$  doublet:

$$R_{O3} = \frac{I([O \text{ III}]4959) + I([O \text{ III}]5007)}{I([O \text{ III}]4363)}.$$
(4.11)

This result can be combined with a recombination line to calculate a value of oxygen abundance. Following Pérez-Montero (2017), the electronic temperature is derived through

$$T_e = 0.784 - 0.0001357 \cdot R_{O3} + \frac{48.44}{R_{O3}}, \tag{4.12}$$

where  $T_e$  is in units of  $10^4$  K, and is valid in the range  $0.7 \le T_e \le 2.5$ . This fitting was calculated by Pérez-Montero (2017) using the code PyNeb<sup>2</sup> (Luridiana et al., 2015), considering an electronic density  $(n_e)$  of  $100 \text{ cm}^{-3}$ . PyNeb focuses on obtaining nebular information based on atomic data, combined with observational data from emission line measurements, using the direct method as a primary tool. We calculate abundances with the direct method using the following expressions for the abundance of  $O^+$  and  $O^{2+}$ :

$$12 + \log\left(\frac{\mathrm{O}^{+}}{H^{+}}\right) = \log\left(\frac{I([\mathrm{O} \text{ II}]3727) + I([\mathrm{O} \text{ II}]3729)}{I(\mathrm{H}\beta)}\right) + 5.887 + \frac{1.641}{t_{l}}$$

$$-0.543 \cdot \log(t_{l}) + 0.000114 \cdot n_{e}$$
(4.13)

$$12 + \log\left(\frac{\mathrm{O}^{2+}}{H^{+}}\right) = \log\left(\frac{I([\mathrm{O~III}]4959) + I([\mathrm{O~III}]5007)}{I(\mathrm{H}\beta)}\right) + 6.1868 + \frac{1.2491}{t_{h}}$$

$$-0.5816 \cdot \log(t_{h}),$$
(4.14)

where the terms  $t_h$  and  $t_l$ , described in Garnett (1992), as the electronic temperature for the high ionization zone, where elements like [O III] and [Ne III] predominate, and the low ionization zone, characterized by elements such as [O II], [N II] and [S II]. We assume an electron density of  $n_e = 100 \text{ cm}^{-3}$  when applying these equations.

To get the total oxygen abundance we follow the expression of Pérez-Montero (2017):

$$\frac{O}{H} = \frac{O^+ + O^{2+}}{H^+}. (4.15)$$

We get the following relations:

- $T_e = t([OIII]) \approx t_h$
- $t([OII]) \approx t_l$

for the ions that we are currently working with.

<sup>&</sup>lt;sup>2</sup>https://github.com/Morisset/PyNeb\_devel

#### Specific cases

In those cases where we count with the [O III]4363 line, we use Eq. 4.11 to obtain a value for  $t_h$ . An expression for t([O II]) is found in Pérez-Montero (2017):

$$t([OII]) = \frac{2}{t([OIII])^{-1} + 0.8}.$$
(4.16)

For 4 galaxies of our sample (IDs 2, 9, 12, 19), the [O II]3727,3729 doublet was not available due to the redshift of the galaxy, so we could not make use of Eq. 4.13 to derive the ionized oxygen abundance. To solve this, we use the expression proposed in Pérez-Montero et al. (2021), using an empirical relation between the [O III] electron temperature and the total abundance, based on a previous result from Amorín et al. (2015). The relation is a second-degree polynomial, and it is crucial to point out that it must be used carefully, because it is specific for cases where  $t_h >> t_l$ , otherwise the results could include unwanted uncertainties. It is represented by

$$12 + \log(O/H) = 9.72 - 1.70 \cdot t([O III]) + 0.32 \cdot t([O III])^{2}. \tag{4.17}$$

We present the results of the oxygen abundance calculations for the galaxies with an  $[O\ III]\lambda 4363$  detection in Table 4.5.

Table 4.5: Main intensities and derived parameters for galaxies with detection of [O III]4363.

ID	z	R <sub>O3</sub>	$t([O II])^a$	$t([O III])^a$	$I_{[OII]3727}^{\ \ b}$	I <sub>[OII]3729</sub> <sup>b</sup>	I <sub>[OIII]4363</sub> <sup>b</sup>	$I_{H\beta}^{b}$	I <sub>[OIII]4959</sub> <sup>b</sup>	I <sub>[OIII]5007</sub> <sup>b</sup>	$12 + \log(\mathrm{O/H})_{T_e}$
2	0.2558	$26.971 \pm 8.239$	$1.68 {\pm} 0.12$	$2.58{\pm}0.55$			$112 \pm 35$	$1000 \pm 46$	$759 \pm 28$	$2274 \pm 78$	$7.46 {\pm} 0.03$
9	0.2557	$64.78 \pm 15.53$	$1.37 {\pm} 0.07$	$1.52 {\pm} 0.18$			$78 \pm 19$	$1000 \pm 22$	$1270 \pm 24$	$3818 \pm 66$	$7.87 \pm 0.13$
11	0.3263	$49.44 \pm 15.54$	$1.46 {\pm} 0.11$	$1.76 \pm 0.31$	$1742 \pm 36$	$1777 \pm 30$	$40 \pm 12$	$1000\pm 20$	$489 \pm 9$	$1466 \pm 23$	$7.67 {\pm} 0.08$
12	0.2559	$35.93 \pm 13.42$	$1.58 {\pm} 0.14$	$2.13 {\pm} 0.51$		•••	$86 \pm 32$	$1000 \pm 86$	$772 \pm 59$	$2318 \pm 158$	$7.55{\pm}0.18$
13	0.6246	$40.06 \pm 15.96$	$1.54 {\pm} 0.14$	$2.00 {\pm} 0.50$	$1778 \pm 123$	$1171 \pm 63$	$115 \pm 46$	$1000 \pm 48$	$1134 \pm 52$	$3481 {\pm} 169$	$7.72 \pm 0.08$
16	0.8413	$108.29 \pm 5.65$	$1.23 \pm 0.01$	$1.22 \pm 0.02$	$834 \pm 29$	$1080\pm29$	$64 \pm 3$	$1000 \pm 49$	$1658 {\pm} 50$	$5327 {\pm} 162$	$8.12 \pm 0.01$
19	0.2068	$157.71 \pm 31.32$	$1.15 \pm 0.04$	$1.07 \pm 0.07$			$28 \pm 6$	$1000\pm 20$	$1121 {\pm} 17$	$3364 \pm 49$	$8.27 {\pm} 0.07$
25	0.6802	$60.50 \pm 20.30$	$1.39 \pm 0.11$	$1.58 {\pm} 0.27$	$1262 \pm 112$	$2021 \pm 134$	$92 \pm 31$	$1000 \pm 49$	$1409 \pm 56$	$4165{\pm}157$	$7.87 {\pm} 0.05$
37	0.3746	$84.29 {\pm} 16.41$	$1.30 \pm 0.05$	$1.35 \pm 0.11$	$1225 \pm 44$	$1728 \pm 47$	$57 \pm 11$	$1000 \pm 26$	$1190 \pm 23$	$3587 \pm 67$	$7.95 {\pm} 0.03$
40	0.8049	$56.25{\pm}11.52$	$1.42 {\pm} 0.07$	$1.64 {\pm} 0.18$	$1013 \pm 79$	$1398 \pm 99$	$91 \pm 20$	$1000 \pm 98$	$1282 \pm 92$	$2864 \pm 273$	$7.76 \pm 0.04$
44	0.3663	$36.33 \pm 5.39$	$1.57{\pm}0.06$	$2.11 {\pm} 0.20$	$741 \pm 75$	$742 {\pm} 69$	$237\pm36$	$1000 \pm 43$	$2170 \pm 69$	$6451 {\pm} 199$	$7.64 {\pm} 0.02$

 $<sup>^</sup>a$  electron temperatures are given in units of  $10^4 {\rm K.}$   $^b$  Intensities are normalized following the expression  $\frac{{\rm I}_{\lambda}}{{\rm I}_{{\rm H}\beta}} \cdot 1000$ 

#### 4.6.2 Gas-phase metallicity from strong-line methods

We now turn to the derivation of the oxygen abundance relying on the observation of strong emission lines, comparing ratios of selected lines, following the work of Sanders et al. (2021), where they analyzed a sample of high-redshift galaxies (1.4 < z < 3.8), from the MOSDEF survey, from observations with the Multi-Object Spectrometer for Infrared Exploration (MOSFIRE), on the 10m Keck I Telescope. Aditionally, a local sample was employed from SDSS data, at redshift  $z \sim 0.08$ . The choice of utilizing the method described by Sanders et al. (2021), is for increasing the number of line ratios that can be used, along with the number of galaxies of our sample that show these lines (the sample covers a wide redshift range, so we find that some emission lines fall out of the observational range offered by MUSE), and avoid biases for the oxygen-abundance values. The indicators are calibrated to metallicities obtained with the direct method.

The fitted line ratios are:

• 
$$R3 = \frac{[O \text{ III}]\lambda\lambda4959,5007}{H\beta};$$

• 
$$R2 = \frac{[O \text{ II}]\lambda\lambda3727,3729}{H\beta};$$

• 
$$O_{32} = \frac{[O \text{ III}]\lambda\lambda4959,5007}{[O \text{ III}]\lambda\lambda3727,3729};$$

• Ne3O2 = 
$$\frac{[\text{Ne III}]\lambda 3869}{[\text{O II}]\lambda \lambda 3727,3729};$$

• 
$$N2 = \frac{[N \text{ II}]\lambda 6584}{H\alpha}$$
;

• O3N2 = 
$$\frac{[O \text{ III}]\lambda 5007/H\beta}{[N \text{ II}]\lambda 6584/H\alpha}$$
.

They are fitted with cubic functions of the form

$$\log(\mathbf{R}) = c_0 + c_1 x + c_2 x^2 + c_3 x^3, \tag{4.18}$$

where  $x = 12 + \log(O/H) - 8.69$ .

We estimate the metallicity following a  $\chi^2$  reduction for the previously described line ratios, considering the expression

$$\chi^{2} = \sum_{i} \frac{(R_{\text{obs},i} - R_{\text{cal},i}(x))^{2}}{(\sigma_{\text{obs},i}^{2} + \sigma_{\text{cal},i}^{2})},$$
(4.19)

where we have:

- the sum over i, which represents the number of line ratios applied (in our case we have i going from 1 to 6);
- $R_{obs,i}$ , the logarithm of the *i*th line ratio;
- $R_{cal,i}(x)$ , the logarithm of the *i*th line ratio of the calibration, at  $x = 12 + \log(O/H)$ ;
- $\sigma_{{
  m obs},i}$  is the uncertainty of the corresponding ith line ratio;

Line Ratio (R)	$c_0$	$c_1$	$c_2$	$c_3$
$\overline{\text{[O III]}\lambda 5007/\text{H}\beta}$	0.111	-2.390	-3.300	-1.240
$[{ m O~II}]\lambda~3727/{ m H}\beta$	0.498	-0.479	-1.550	-0.654
$O_{32}$	-0.388	-1.910	-1.740	-0.570
[Ne III] $\lambda 3869/[{\rm O~II}]\lambda 3727$	-1.190	-1.290	-1.440	-0.601
$[\mathrm{N}~{ ext{II}}]\lambda 6584/\mathrm{H}lpha$	-0.663	1.470	0.215	-0.102
O3N2	0.772	-3.860	-3.330	-0.939
Ratio	[Ο III] Ηβ	[О II] Н <i>В</i>	$O_{32}$	[Ne III] [O II]
$\sigma_{ m cal}$	0.100	0.130	0.190	0.200
Ratio	[N II] Ηα	O3N2		
$\sigma_{ m cal}$	0.150	0.160		

Table 4.6: Calibrations for the Strong-line method shown in Sanders et al. (2021).

•  $\sigma_{\text{cal},i}$  is the uncertainty of the *i*th line ratio at fixed O/H of the calibration. The value for each line ratio was derived taking the average value reported in previous works.

The details of the calibrations for each line ratio are given in table 4.6. We did not consider Diffuse ionized gas (DIG)-corrected calibrations, due to its smaller effect on our sample. It is highly possible, however, that this contributes with extra uncertainties in galaxies with smaller equivalent widths, which are more prone to have higher DIGs. A more detailed description of the methods can be found in the original article (Sanders et al., 2021).

We perturb the calculations to obtain uncertainties varying the line ratios according to their standard deviation, and applying a Monte Carlo simulation. We perform this procedure 250 times, and calculate oxygen abundances from these results. Fig. 4.8 shows a typical result for the simulation, where we make a cut in the 16th and 84th percentiles, in order to obtain a value for the  $1\sigma$  standard deviation.

We encounter that some galaxies showed a bimodality in the resulting Gaussian profile, as seen in Fig. 4.9, where the metallicity derived for this galaxy was 7.870, and the Monte Carlo simulation presents two likely values, one centered around 8.5, and the most likely value, which was centered around 7.8. This ended in a higher value for the uncertainties. In this case, we perform a cut in the values, leaving only those less than an upper limit according to the shape of the distribution. We then repeat the process of selecting the 16th and 84th percentiles, in the new distribution.

Fig. 4.10 shows the line ratios defined in Sec. 4.6.2, plotted against the oxygen abundance from the  $\chi^2$  minimization. The different curves represent calibrations by different authors (see caption for more details). In general, the galaxies of our sample fit well with most calibrations by the different authors, with some exceptions in the galaxies with  $\log R_2 = [OII]\lambda\lambda 3727, 3729/H\beta$ , being 0.4 dex higher than those expected by the calibrations. Part of the objectives of the calibrations from these authors was to extend the MZR, and further understand galaxy evolution up to higher z. For the calibrations that were used for the sample, Sanders et al. (2021) used a uniform set of emission lines at all z, in

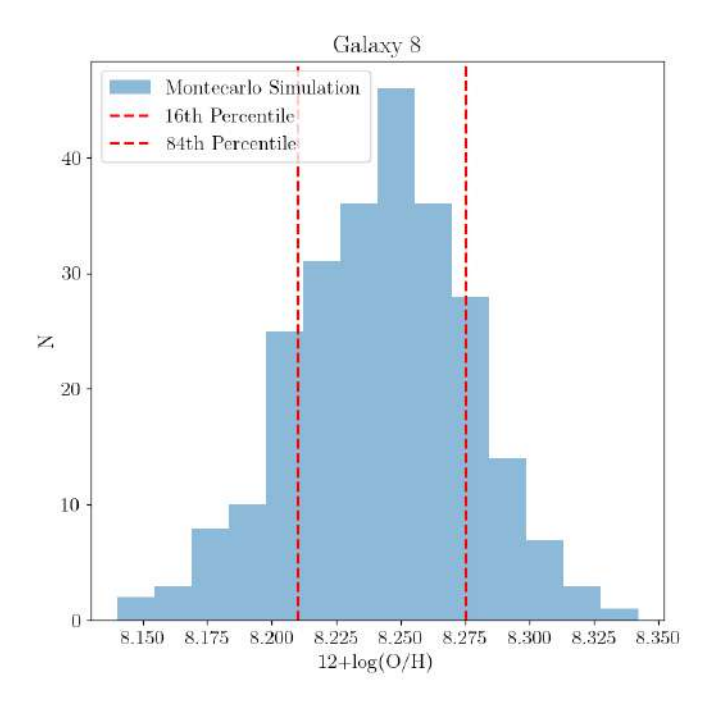


**Figure 4.8:** Monte Carlo simulation example for galaxy ID 8. The abundance derived for this galaxy was 8.244. The red vertical dashed lines represent the cut in the 16th and 84th percentiles.

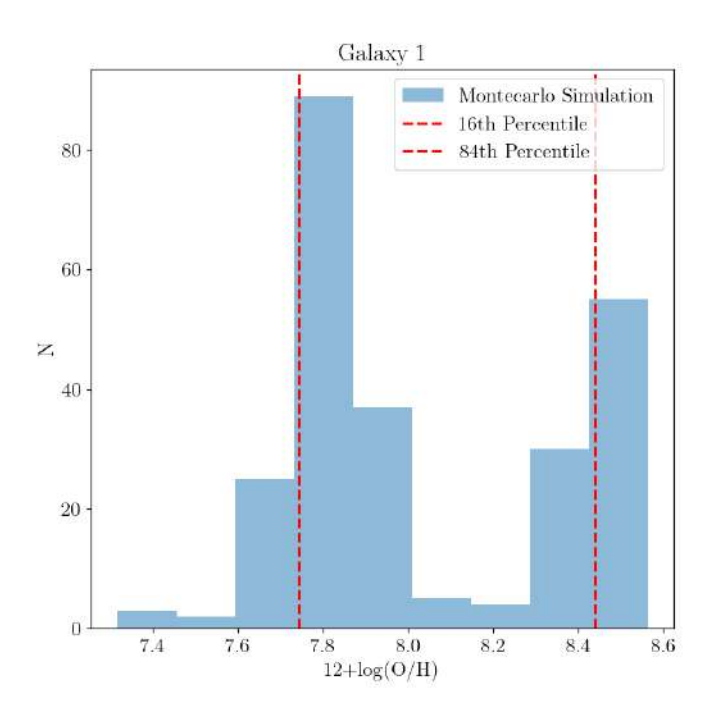


**Figure 4.9:** Monte Carlo simulation example for galaxy ID 1. The abundance derived for this galaxy was 7.870. We made a cut in order to keep the values close to this abundance. The red vertical dashed lines indicate the same as in Fig. 4.8.

addition to different calibrations. These measures were used because in their sample, they were working with a wide range of redshifts (0 < z < 3.3), and they were looking to avoid biases in the calculations of metallicity for the high-redshift galaxies, as differences in the

[N II] $\lambda 6584$  BPT diagram have been reported to be different for  $z \sim 1$  and z > 1 samples, attributed to differences in N/O abundances, as well as differences in the properties of ionized gas (Shapley et al., 2015). It is important to point out the importance of utilizing the calibrations within the validity range of metallicity, as some line ratios lie in different values and uncertainties could increase if not taken into consideration.

We show a comparison between the two approaches used to derive metallicity (direct-method and strong-line method), in Fig. 4.11. We find that four galaxies (IDs 2, 11, 12, 13) present lower values of metallicity following the direct-method, but this could be due to an ambiguous fit of the [O III] $\lambda$ 4363 line, due to low S/N, and we consider this metallicities as lower limits, represented by the black arrows in the Figure. The mean difference in the metallicity derived from the strong-line method is 0.44 dex higher than the mean metallicity from the direct method.

We also include a comparison with other calibrations from the literature (Maiolino et al., 2008; Curti et al., 2020; Sanders et al., 2021; Nakajima et al., 2022), in order to check for significant differences. We present in Table 4.7 the weighted mean of metallicity according to the different calibrations, which are mostly T<sub>e</sub>-based (the calibrations from Maiolino et al. (2008) considers  $T_e$ -based calibrations for the metallicity range  $12 + \log(O/H) < 8.3$ , while for higher values the calibration is based on photoionization models), and also the mean of the difference between the strong-line and direct-method. Table 4.8 presents the individual values of metallicity for our sample from all calibrations, and we show in Fig. 4.12 the deviation from these values and the direct-method to complement our analysis. We see that all calibrations follow a similar pattern, with lower metallicities exhibiting a larger deviation from the direct-method. The galaxies with the most deviation are the galaxies with values of metallicity according to the direct-method considered as lowerlimits, so the discrepancies should be lower than presented. For all galaxies considered, the calibration from Maiolino et al. (2008) is somewhat lower. Being a calibration focused on a sample of high-redshift galaxies, this result might be explained by the difference in abundance of elements at higher redshifts compared to our sample, located at lower redshifts.

Table 4.7: Comparison of the averages of metallicity calibrations. We show: (1) The sources of the calibrations employed, i.e., Maiolino et al. (2008); Curti et al. (2020); Sanders et al. (2021) and Nakajima et al. (2022), (2) The weighted mean and standard deviation of each calibration, (3) The mean differences between the metallicity according to the strong-line method and the direct-method.

Calibration	12+log(O/H) (mean)	$\Delta (\log(O/H)_{\text{strong-line}} - \log(O/H)_{\text{direct}}) \text{ (mean)}$
(1)	(2)	(3)
Maiolino+08	$8.327 \pm 0.005$	0.214
Curti+20	$8.439 \pm 0.002$	0.503
Sanders+21	$8.434 \pm 0.006$	0.444
Nakajima+22	$8.322 \pm 0.01$	0.402

In Fig. 4.13 we present two histograms displaying the differences between the methods

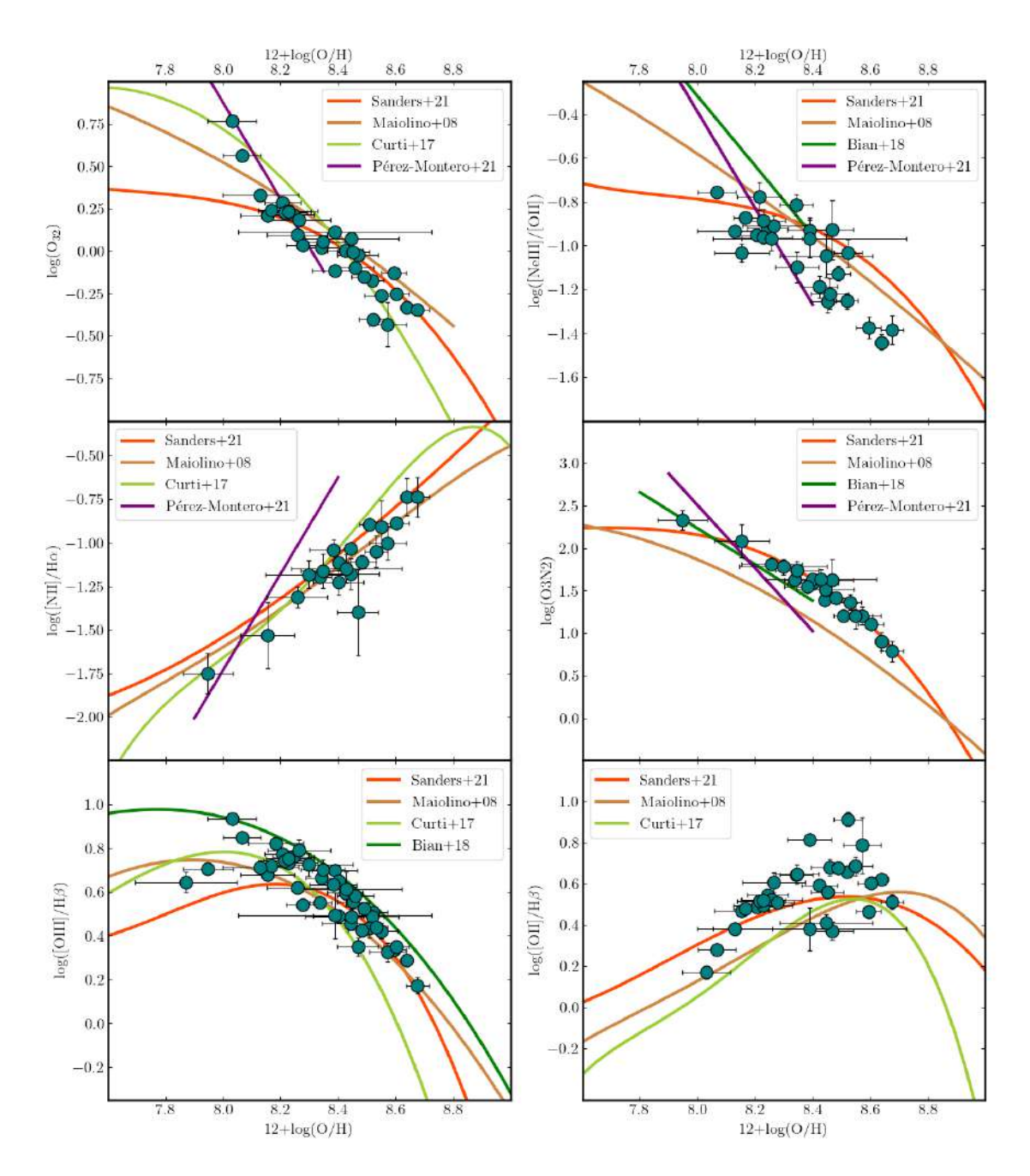


Figure 4.10: Emission line ratios versus derived metallicities using the strong-line method for our sample (teal circles), described in Sec. 4.6.2. We display different calibrations from different authors to compare the position of the sample in the plane. The orange lines represent the calibration suggested by Sanders et al. (2021). The brown and light-green lines are the calibrations for  $z \sim 0$  galaxies from Maiolino et al. (2008) and Curti et al. (2017), respectively. The dark-green and purple curves represent the calibrations proposed in the works of Bian et al. (2018), and Pérez-Montero et al. (2021), respectively.

employed to derive metallicities. The vertical dashed lines represent the weighted mean values found in each group. For the strong-line method group, this value was 8.36, with a  $1\sigma$  standard deviation of 0.18. In the case of galaxies with [O III]4363 detection, this value was 7.81, with a  $1\sigma$  standard deviation.

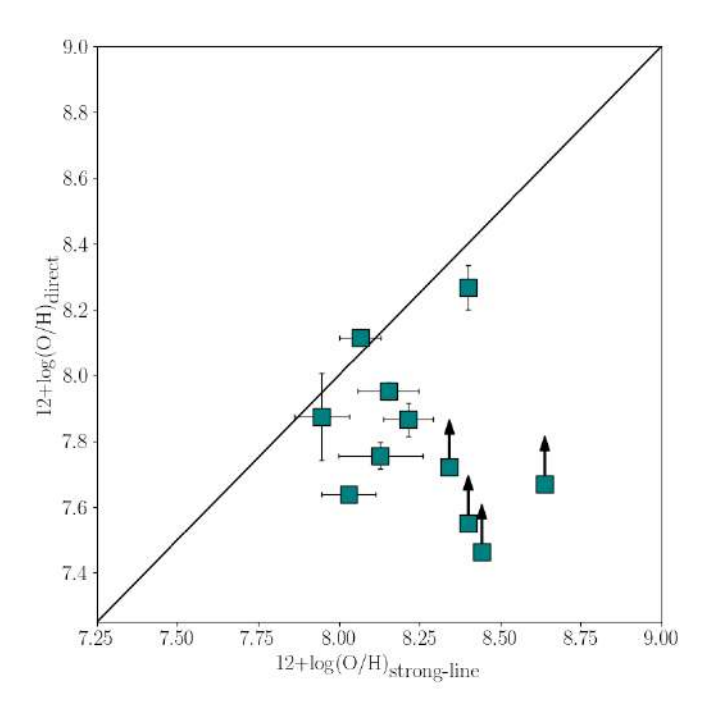


Figure 4.11: Comparison between the direct method and strong-line method for the metallicity derivation. The arrows represent lower limits. The diagonal line represents a one-to-one relation.

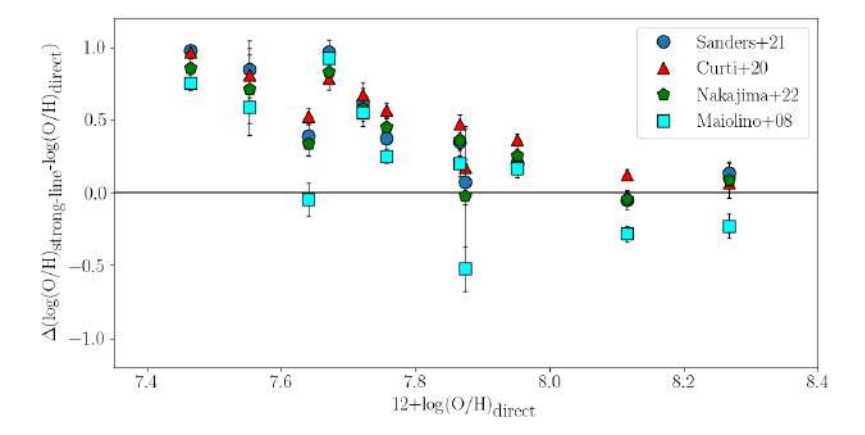


Figure 4.12: Comparison between the difference between metallicity following the strong-line method and the direct-method, for the calibrations from Maiolino et al. (2008); Curti et al. (2020); Sanders et al. (2021) and Nakajima et al. (2022). The blue circles, red triangles, green pentagons and light-blue squares are the calibrations from Sanders et al. (2021); Curti et al. (2020); Nakajima et al. (2022) and Maiolino et al. (2008), respectively. The black line represents a  $\Delta(\log(O/H)=0.$ 

This results are not surprising, as the direct method is expected to provide more reliable and lower metallicities in comparison to the strong-line method (see Fig. 4.11), representing more accurately the behavior of star-forming galaxies. However, some caveats exist regarding this method. Metallicities based on electron temperatures do tend to be biased towards lower values, and vary considerably when compared to other methods, such as photoionization models, tending to overestimate metallicity between 0.2 and 0.6 dex. Reasons for these discrepancies have been weighed, for instance that direct method

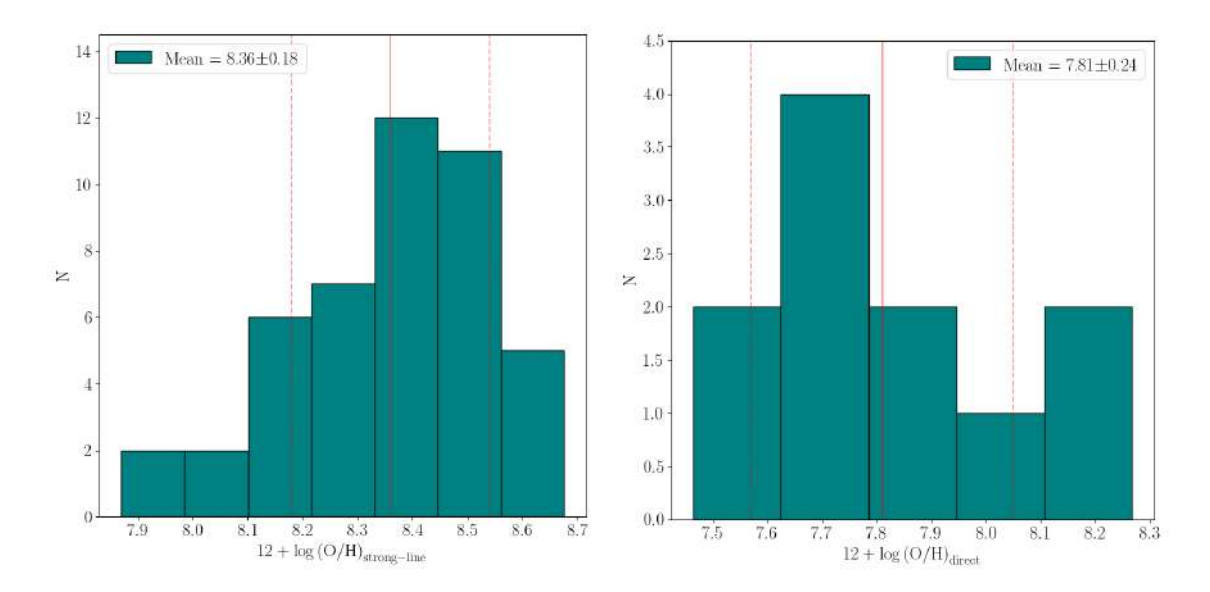


Figure 4.13: Histogram of metallicities for the different methods. Left: metallicities derived using the strong-line method. Right: metallicities derived using the direct method. The red continuous line represent the mean metallicity, and vertical dashed lines represent  $1\sigma$  uncertainty.

describes the gas phase abundance, while photoionization models describe gas abundance and also takes into consideration the contribution of the dust depletion (see Maiolino & Mannucci, 2019 for a discussion). On the other hand, it is well known that metallicities derived through the strong-line method present intrinsec dispersion, of  $\sim 0.15$ , that must also be taken into consideration (see, e.g., Kewley & Ellison, 2008; Curti et al., 2017, 2020).

#### 4.7 Review of results

Now we review the main results of the different methods employed in previous sections. We present the main physical parameters derived in Table 4.9, for the galaxies in the North and South sections of A370. It is important to point out that some of the values presented in the aforementioned Table are benefited by the cluster's magnification effects. For this reason, we also include the magnification values obtained from the median values of the lensing models from different groups, as described in Sect. 4.4. Parameters such as stellar mass and SFR are presented without correcting for magnification, although the reported values of magnification were applied for the quantities displayed in the Figures and Discussion presented below.

**Table 4.8:** Comparison of the metallicity calibrations from Maiolino et al. (2008); Curti et al. (2020); Sanders et al. (2021) and Nakajima et al. (2022) for the galaxies in our sample. We derive the uncertainties in the same way described in Sect. 4.6.2

	$12 + \log(O/H)_{\text{strong-line}}$								
ID	Maiolino+08	Curti+20	Sanders+21	Nakajima+22					
1	$7.31 \pm 0.99$	$7.56 \pm 0.61$	$7.87 \pm 0.18$	$7.40 \pm 0.97$					
2	$8.22 {\pm} 0.05$	$8.43 {\pm} 0.04$	$8.44 {\pm} 0.02$	$8.32 \pm 0.13$					
3	$8.47 {\pm} 0.03$	$8.46 {\pm} 0.01$	$8.59 \pm 0.04$	$8.45 {\pm} 0.05$					
4	$8.37 {\pm} 0.07$	$8.42 {\pm} 0.05$	$8.39 \pm 0.08$	$8.32 {\pm} 0.06$					
5	$8.22 {\pm} 0.09$	$8.39 \pm 0.06$	$8.44 {\pm} 0.10$	$8.29 \pm 0.14$					
6	$8.35 {\pm} 0.07$	$8.43 {\pm} 0.03$	$8.47 {\pm} 0.07$	$8.37 {\pm} 0.07$					
7	$8.46 {\pm} 0.09$	$8.46 {\pm} 0.02$	$8.52 {\pm} 0.05$	$8.42 {\pm} 0.05$					
8	$8.12 \pm 0.03$	$8.35 {\pm} 0.04$	$8.24 {\pm} 0.07$	$8.23 {\pm} 0.05$					
9	$7.35 {\pm} 0.07$	$8.05 \pm 0.23$	$7.95 {\pm} 0.09$	$7.86 {\pm} 0.46$					
10	$8.16 \pm 0.03$	$8.36 {\pm} 0.05$	$8.26 {\pm} 0.11$	$8.23 {\pm} 0.07$					
11	$8.60 {\pm} 0.02$	$8.46 {\pm} 0.01$	$8.64 {\pm} 0.02$	$8.50 \pm 0.04$					
12	$8.14 \pm 0.09$	$8.36 {\pm} 0.05$	$8.40 \pm 0.09$	$8.26 {\pm} 0.15$					
13	$8.27 {\pm} 0.05$	$8.40 \pm 0.03$	$8.34 {\pm} 0.06$	$8.31 {\pm} 0.05$					
14	$8.49 \pm 0.03$	$8.46 {\pm} 0.01$	$8.52 {\pm} 0.04$	$8.40 {\pm} 0.05$					
15	$8.34 {\pm} 0.03$	$8.41 \pm 0.03$	$8.42 {\pm} 0.06$	$8.33 {\pm} 0.06$					
16	$7.83 {\pm} 0.05$	$8.24 \pm 0.03$	$8.07 \pm 0.07$	$8.08 \pm 0.05$					
17	$8.06 \pm 0.05$	$8.33 \pm 0.03$	$8.21 {\pm} 0.06$	$8.21 \pm 0.06$					
18	$7.62 {\pm} 0.20$	$7.85 {\pm} 0.37$	$8.18 \pm 0.10$	$7.61 {\pm} 0.64$					
19	$8.04 \pm 0.05$	$8.34 \pm 0.01$	$8.40 \pm 0.01$	$8.36 \pm 0.10$					
20	$8.10 \pm 0.02$	$8.34 \pm 0.04$	$8.23 \pm 0.10$	$8.23 \pm 0.06$					
21	$8.34 \pm 0.06$	$8.46 \pm 0.02$	$8.51 \pm 0.03$	$8.48 \pm 0.12$					
22	$8.40 \pm 0.09$	$8.46 \pm 0.02$	$8.57 \pm 0.06$	$8.46 {\pm} 0.07$					
23	$8.21 \pm 0.03$	$8.34 \pm 0.02$	$8.26 \pm 0.11$	$8.28 \pm 0.04$					
24	$8.48 \pm 0.07$	$8.46 \pm 0.01$	$8.55 \pm 0.06$	$8.44 \pm 0.05$					
25	$8.07 \pm 0.08$	$8.34 \pm 0.04$	$8.22 \pm 0.08$	$8.23 \pm 0.05$					
26	$8.08 \pm 0.07$	$8.36 \pm 0.03$	$8.38 \pm 0.08$	$8.29 \pm 0.09$					
27	$8.34 \pm 0.03$	$8.42 \pm 0.03$	$8.45 \pm 0.06$	$8.35 \pm 0.05$					
28	$8.08 \pm 0.06$	$8.36 \pm 0.04$	$8.34 \pm 0.04$	$8.25 \pm 0.15$					
29	$8.31 \pm 0.06$	$8.40 \pm 0.06$	$8.53 \pm 0.04$	$8.45 \pm 0.14$					
30	$8.42 \pm 0.05$	$8.44 \pm 0.03$	$8.46 \pm 0.06$	$8.35 \pm 0.07$					
31	$7.96 \pm 0.14$	$8.29 \pm 0.08$	$8.30 \pm 0.15$	$8.22 \pm 0.13$					
32	$8.24 \pm 0.04$	$8.41 \pm 0.08$	$8.39 \pm 0.34$	$8.35 \pm 0.09$					
33	$8.23 \pm 0.07$	$8.41 \pm 0.03$	$8.48 \pm 0.05$	$8.44 \pm 0.13$					
34	$8.08 \pm 0.07$	$8.34 \pm 0.04$	$8.23 \pm 0.08$	$8.23 \pm 0.05$					
35	$8.66\pm0.03$	$8.46 \pm 0.01$	$8.68 \pm 0.04$	$8.54 \pm 0.05$					
36	$8.25 \pm 0.06$	$8.36 \pm 0.05$	$8.35 \pm 0.08$	$8.30\pm0.06$					
37	$8.12\pm0.02$	$8.32 \pm 0.03$	$8.15 \pm 0.09$	$8.21 \pm 0.06$					
38	$8.09\pm0.05$	$8.34\pm0.03$	$8.17 \pm 0.04$	$8.23 \pm 0.04$					
39	$8.49\pm0.01$	$8.45\pm0.02$	$8.49\pm0.04$	$8.38\pm0.05$					
40	$8.01\pm0.03$	$8.32\pm0.03$	$8.13\pm0.13$	$8.21 \pm 0.06$					
41	$8.27 \pm 0.06$	$8.42 \pm 0.04$	$8.45 \pm 0.16$	$8.36\pm0.07$					
42	$8.07\pm0.14$	$8.37\pm0.11$	$8.43 \pm 0.19$	$8.38\pm0.17$					
43	$8.28\pm0.04$	$8.41\pm0.03$	$8.28\pm0.06$	$8.26\pm0.17$					
44	$7.59\pm0.12$	$8.16\pm0.06$	$8.03\pm0.08$	$7.98\pm0.08$					
45	$8.49 \pm 0.03$	$8.46 \pm 0.01$	$8.60 \pm 0.05$	$8.50 \pm 0.08$					

Table 4.9: Main physical parameters derived for the North zone of A370. The value of the magnification effect due to the galaxy cluster is presented in the third column. The values of SFR are based on the measurements of the H $\alpha$  line, following the expression from Kennicutt (1998). The oxygen abundance values are obtained following the strong-line method.

$\begin{array}{cccccccccccccccccccccccccccccccccccc$	
$\begin{array}{cccccccccccccccccccccccccccccccccccc$	$O/H)_{strong-line}$
$\begin{array}{cccccccccccccccccccccccccccccccccccc$	$37 \pm 0.18$
$\begin{array}{cccccccccccccccccccccccccccccccccccc$	$14 \pm 0.02$
$\begin{array}{cccccccccccccccccccccccccccccccccccc$	$59 \pm 0.04$
$\begin{array}{cccccccccccccccccccccccccccccccccccc$	$39 \pm 0.08$
$\begin{array}{cccccccccccccccccccccccccccccccccccc$	$14 \pm 0.10$
$\begin{array}{cccccccccccccccccccccccccccccccccccc$	$17 \pm 0.07$
$\begin{array}{cccccccccccccccccccccccccccccccccccc$	$52 \pm 0.05$
$\begin{array}{cccccccccccccccccccccccccccccccccccc$	$24 \pm 0.07$
$\begin{array}{cccccccccccccccccccccccccccccccccccc$	$95 \pm 0.09$
$\begin{array}{cccccccccccccccccccccccccccccccccccc$	$26 \pm 0.11$
$\begin{array}{cccccccccccccccccccccccccccccccccccc$	$64 \pm 0.02$
$\begin{array}{cccccccccccccccccccccccccccccccccccc$	$40 \pm 0.09$
$\begin{array}{cccccccccccccccccccccccccccccccccccc$	$34 \pm 0.06$
$\begin{array}{cccccccccccccccccccccccccccccccccccc$	$52 \pm 0.04$
$\begin{array}{cccccccccccccccccccccccccccccccccccc$	$12 \pm 0.06$
$\begin{array}{cccccccccccccccccccccccccccccccccccc$	$07 \pm 0.07$
$\begin{array}{cccccccccccccccccccccccccccccccccccc$	$21 \pm 0.06$
$\begin{array}{cccccccccccccccccccccccccccccccccccc$	$18 \pm 0.10$
21 $0.2515$ $1.00$ $7.596 \pm 0.001$ $-0.554 \pm 0.006$ $-8.150 \pm 0.006$ $8.5$	$40 \pm 0.01$
	$23 \pm 0.10$
	$51 \pm 0.03$
22 $0.3272$ $1.00$ $8.795 \pm 0.057$ $-1.076 \pm 0.010$ $-9.871 \pm 0.058$ $8.5$	$57 \pm 0.06$
23 $0.3296$ $1.00$ $8.649 \pm 0.033$ $-0.666 \pm 0.004$ $-9.315 \pm 0.033$ $8.2$	$26 \pm 0.11$
$24  0.3829 \qquad 1.00 \qquad 8.498 \pm 0.044 \qquad -1.137 \pm 0.012 \qquad -9.635 \pm 0.046 \qquad 8.5$	$55 \pm 0.06$
25 $0.6802$ $2.29 \pm 0.34$ $8.753 \pm 0.04$ $0.049 \pm 0.066$ $-8.344 \pm 0.100$ $8.2$	$22 \pm 0.08$
	$38 \pm 0.08$
	$45 \pm 0.06$
28 $0.2557$ $1.00$ $8.983 \pm 0.002$ $-0.408 \pm 0.003$ $-9.391 \pm 0.004$ $8.3$	$34 \pm 0.04$
$29   0.2251   1.00   8.908 \pm 0.001   -0.178 \pm 0.054   -9.086 \pm 0.054   8.5$	$53 \pm 0.04$
30 $0.6030$ $1.35 \pm 0.11$ $9.747 \pm 0.009$ $0.308 \pm 0.054$ $-9.308 \pm 0.065$ $8.4$	$16 \pm 0.06$
31 $0.2257$ $1.00$ $8.598 \pm 0.035$ $-1.284 \pm 0.008$ $-9.882 \pm 0.036$ $8.3$	$30 \pm 0.15$
32 $0.4226$ $1.21 \pm 0.04$ $8.509 \pm 0.028$ $-0.578 \pm 0.039$ $-9.004 \pm 0.050$ $8.3$	$39 \pm 0.34$
33 $0.2560$ $1.00$ $9.039 \pm 0.004$ $-0.334 \pm 0.006$ $-9.373 \pm 0.008$ $8.4$	$18 \pm 0.05$
$34  0.3864  1.05 \pm 0.01  8.612 \pm 0.010  -0.625 \pm 0.018  -9.215 \pm 0.021  8.2$	$23 \pm 0.08$
35 $0.3605$ $1.00$ $9.633 \pm 0.001$ $-0.228 \pm 0.010$ $-9.861 \pm 0.010$ $8.6$	$68 \pm 0.04$
$36  0.3238  1.00  9.201 \pm 0.023  -0.724 \pm 0.011  -9.925 \pm 0.025  8.3$	$35 \pm 0.08$
37 $0.3746$ $1.00$ $8.733 \pm 0.006$ $-0.236 \pm 0.004$ $-8.969 \pm 0.007$ $8.1$	$15 \pm 0.09$
38 $0.5802$ $2.56 \pm 0.07$ $9.185 \pm 0.016$ $-0.019 \pm 0.015$ $-8.796 \pm 0.025$ $8.1$	$17 \pm 0.04$
	$19 \pm 0.04$
40 $0.8049$ $2.37 \pm 0.09$ $8.619 \pm 0.032$ $-0.085 \pm 0.034$ $-8.329 \pm 0.050$ $8.1$	$13 \pm 0.13$
41 $0.3737$ $1.70 \pm 0.06$ $6.960 \pm 0.113$ $-1.337 \pm 0.019$ $-8.066 \pm 0.115$ $8.4$	$45 \pm 0.16$
	$43 \pm 0.19$
43 $0.4100$ $1.00$ $8.945 \pm 0.041$ $-0.963 \pm 0.008$ $-9.908 \pm 0.042$ $8.2$	$28 \pm 0.06$
44 $0.3663$ $1.00$ $8.206 \pm 0.024$ $0.022 \pm 0.013$ $-8.184 \pm 0.027$ $8.0$	$0.08 \pm 0.08$
45 $0.3264$ $1.00$ $9.796 \pm 0.019$ $-0.476 \pm 0.008$ $-10.272 \pm 0.022$ $8.6$	$60 \pm 0.05$

<sup>&</sup>lt;sup>a</sup> Magnification provided by the DEEPSPACE catalog. The value represented is the median of ten different approaches used by different groups to define lensing models for the cluster. The specifics are described in Shipley et al. (2018).

# 5 | Discussion

After describing the steps taken to derive the nebular properties of the galaxies in our sample, as well as the derivation of the stellar mass by means of the spectral energy distribution, we place these results in the fundamental scaling relations that are relevant for galaxy evolution. In particular, we study the position of our sample in these relations, and discuss them in the context of previous works and models. This chapter is structured as follows. We first investigate the mass-star formation rate and mass-specific star formation rate relationships existing for star-forming galaxies in Sect. 5.1. In Sect. 5.2 we compare the metallicity (derived following the strong-line method) with stellar mass. In Sect. 5.3 we discuss the relation between the specific star formation rate, metallicity and SFR. In Sect. 5.4, we join all the previous relationships in the so-called fundamental metallicity relation, combining the analysis of stellar mass, star formation rate, and metallicity. In Sect. 5.5 we review the specific cases of galaxies with detections of [O III] $\lambda$ 4363, and the difference of the previous relations considering a metallicity derived following the direct method. Finally, in Sect. 5.6 we discuss the discovery of a high-z association of dwarf galaxies with intense [O III] $\lambda$ 5007 equivalent widths.

# 5.1 The relation between Star Formation Rate and Stellar Mass

There is a direct correlation between the SFR, and the Stellar Mass  $(M_{\star})$  of star-forming galaxies, pointing towards a commonly called 'Star-Formation Main Sequence' (Guo et al., 2015), where galaxies display an increase in SFR with redshift. Various articles suggest a power-law-type of relation for SFR and  $M_{\star}$  (SFR  $\propto M_{\star}^{\alpha}$ ), although the value of  $\alpha$  is subject to changes, due to the methodologies applied. This has been seen up to  $z \sim 5$ , with a particular interest in extending this relation towards the local Universe (e.g., Whitaker et al., 2014), but there are still many unknowns regarding the shape or slope of this 'Local Main Sequence' for low mass  $(M_{\star} < 10^9 M_{\odot})$  galaxies. We measure  $M_{\star}$  following standard procedures, performing SED fitting to the photometric data (see Sect. 4.3), and while the code BAGPIPES provides a value for SFR, this value is derived considering the whole SFH of the galaxy, and is highly dependent on the input models, like IMF and SFH. We decided to rely on a different approach to derive this quantity (see Sect. 4.5), based on the emission from Balmer lines, sensitive to a shorter timescale ( $\sim 10^6$  yr, Conroy, 2013).

Fig. 5.1 shows the Star-Formation Main Sequence for the galaxies of our sample, displaying the Main Sequence derived in Whitaker et al. (2014) in red, with an extrapolation towards lower values of stellar mass ( $\log M_{\star}/M_{\odot} < 8.4$ ), denoted in the dashed red line. The black dashed lines represent values of constant sSFR, starting from  $10^{-10}$  up to  $10^{-7}$  yr<sup>-1</sup>. We separate our sample into three redshift bins: squares and diamonds represent foreground and background galaxies, respectively, with the redshift range set at  $0.35 \le z \le 0.40$  for a cluster member (Lagattuta et al., 2022). Additionally, the logarithm of the [O III] $\lambda$ 5007 equivalent width is associated with our galaxies in the colormap. The green dots are the VUDS star-forming dwarf galaxies (SFDGs, 0.1 < z < 0.9) from Calabrò et al. (2017), and the pink pentagons are the [O III] $\lambda$ 4363-non-detected sample from the Metal Abundances across Cosmic Time ( $\mathcal{MACT}$ ) Survey (Ly et al., 2016a,b), for comparison purposes, as their sample is composed of star-forming galaxies and were selected to study the evolution of the MZR, in particular covering the low-mass end of the main scaling relations. The redshift range and the methodologies applied in our sample and these works are compatible with this analysis.

We see that the galaxies from our sample follow the same trend as the VUDS SFDGs and the  $\mathcal{MACT}$  survey, with our sample more centered towards a sSFR of  $10^{-10}$  yr<sup>-1</sup>. This could be explained by the selection criteria for the comparison samples, focused on detecting galaxies with more extreme properties, hence the lack of low-SFR galaxies. Some of our galaxies are centered in the range  $10^{-9}$ - $10^{-8}$  yr<sup>-1</sup>, and there is no discernible trend among the different bins, as the three types of galaxies share similar values, although we detect that overall the higher SFRs correspond to high-z galaxies. In general, there is a trend of lower values of [O III] equivalent widths for galaxies with lower sSFR, which is expected, considering that equivalent width can be used as a proxy for the sSFR (Khostovan et al., 2021).

The masses of our sample follow the trend fairly well, with the exception of one fore-ground galaxy and a cluster galaxy (ID 18 and 41, star and diamond respectively in Fig. 5.1), showing values considerably lower than in the rest of the sample. This is probably due to uncertainties in the photometric data, which in both cases may have caused problems when performing the SED fitting. This results in derivations that can be underestimated, so these specific cases must be treated carefully.

A complementary plot is shown in Fig. 5.2, comparing stellar mass with sSFR. We use the VUDS sample again for comparison purposes, and the markings are the same as in the previous plot. Here, we can see the same behavior but from another vantage point, noticing the trend of our SFGs to be more centered towards sSFR values of  $10^{-10}$  yr<sup>-1</sup>, while the VUDS SFDGs are more distributed to values greater than  $10^{-9.5}$  yr<sup>-1</sup>. For the  $\mathcal{MACT}$  galaxies, they are spread between the VUDS and our galaxies, with an average of  $10^{-8.8}$  yr<sup>-1</sup>, slightly higher than our sample, with an average of  $10^{-9.2}$  yr<sup>-1</sup>. Although our galaxies appear to be less extreme than the VUDS sample, the trend is indeed being followed by the three groups, showing a deviation from the normal star-forming galaxies from the Main Sequence (red line). Similar to the stellar mass vs. SFR plot, the [O III]5007

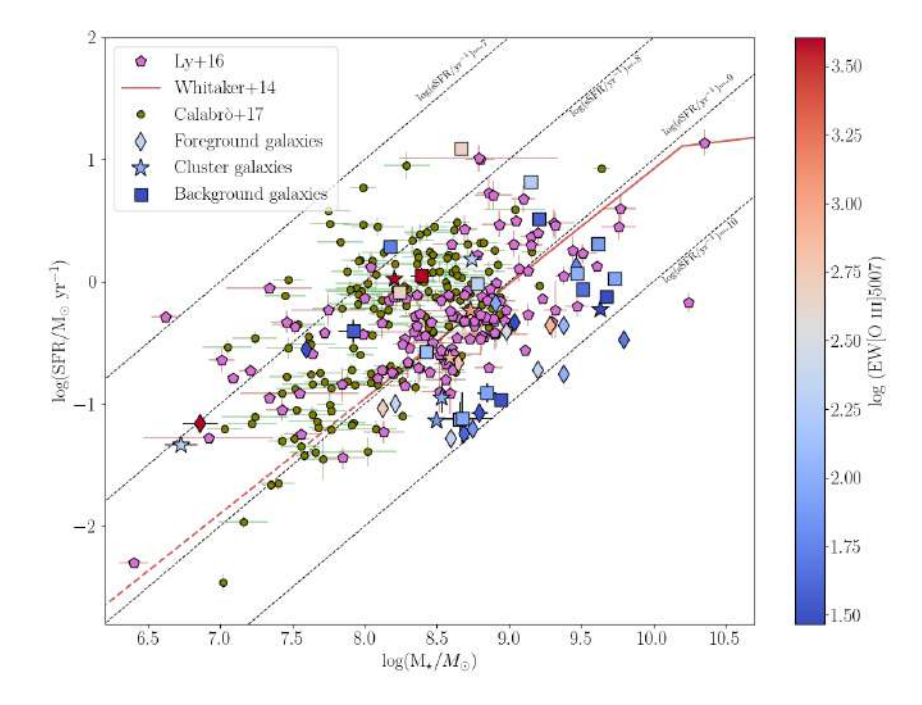


Figure 5.1: Galaxy stellar mass vs. SFR diagram for our sample. The green dots represent the VUDS SFDGs from Calabrò et al. (2017), and the pink pentagons are the sample of [O III] $\lambda$ 4363-non-detected galaxies. Cluster galaxies are defined to be those within the redshift range 0.35 < z < 0.40, following Lagattuta et al. (2022). Foreground galaxies are those below this range (z < 0.35), and background galaxies those above it (z > 0.40). The color map represents the logarithm of the [O III]5007 EW. The dashed lines are continuous sSFR values, starting at  $10^{-7}$  yr<sup>-1</sup>, and down to  $10^{-10}$  yr<sup>-1</sup>. The red line is the fit of the Main Sequence from Whitaker et al. (2014), with its extrapolation towards stellar masses lower than  $10^8$  M<sub>\*</sub> yr<sup>-1</sup> as the red-dashed line.

EW exhibits the same pattern, with more massive galaxies showing lower equivalent widths and, consequently, lower sSFRs.

# 5.2 The stellar mass and metallicity relationship

To better understand the tight relationship between the stellar mass of a star-forming galaxy and its metallicity, we present Figure 5.3 showing our sample, described with the same markings as in previous plots, in addition to the already known SFG sample from Calabrò et al. (2017) and the  $\mathcal{MACT}$  survey from Ly et al. (2016a). The functional form of the MZR that we apply is described in Moustakas et al. (2011), suggesting the following functional form:

$$12 + \log(O/H) = 12 + \log(O/H)_{asm} - \log\left[1 + \left(\frac{M_{TO}}{M_{\star}}\right)^{\gamma}\right],$$
 (5.1)

with the parameters of the function being  $12 + \log(O/H)_{asm}$  the asymptotic metallicity,  $M_{TO}$  the turnover mass, and the parameter  $\gamma$  the one controlling the slope of the MZR. We use in our analysis the values described in Andrews & Martini (2013), namely an asymptotic metallicity of 8.798, turnover mass of  $10^{8.901}$   $M_{\odot}$ , and a  $\gamma$  value of 0.640. We

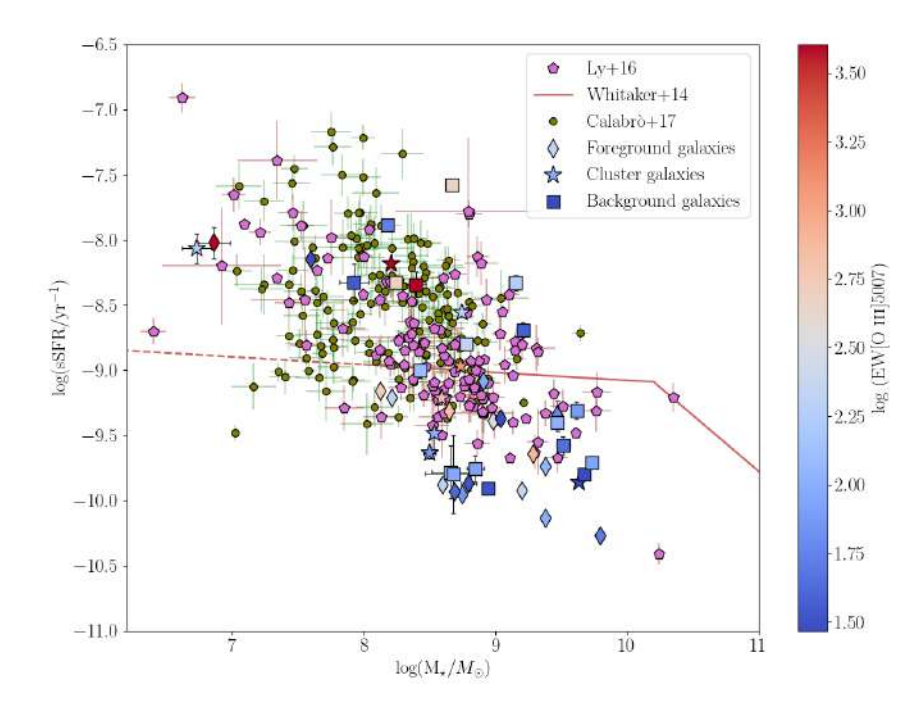


**Figure 5.2:** Galaxy stellar mass vs. sSFR diagram for the sample. The symbols and colorbar are the same as in the previous Figure.

see that our galaxies stay relatively close to the MZR proposed by Andrews & Martini (2013), with no distinctions between the redshift bins defined, although we see again that, in general, background galaxies present lower oxygen abundances compared to foreground and cluster galaxies, with a difference in the weighted means of foreground and background galaxies of 0.077 dex, with an uncertainty of 0.016. There is some scatter at lower stellar masses, probably explained by the conditions in which the stellar masses of these galaxies were derived, but for galaxies at  $M_* > 10^{8.0} M_{\odot}$ , the fit represents well enough the MZR.

# 5.3 The dependence of metallicity on stellar mass and SFR

We now review the connection between metallicity and sSFR in our sample. These properties are defined as intensive, due to their quality of being inherent to a system, contrary to extensive properties, which are dependent of the system (Lara-Lopez et al., 2013). One way of understanding the behavior of SFGs is through the Z-sSFR relation, shown in Fig. 5.4. The [O III]5007 EW is also used as a color bar, to denote the galaxies with the highest values. We see that for our sample, galaxies with lower [O III]5007 EW tend to have higher oxygen abundances, with no preference in the redshift bins. In terms of sSFR values, the trend shares similarities with the sample of VUDS galaxies from Calabrò et al. (2017), with the most metal-poor galaxies in our sample presenting the highest values of sSFR, and likewise for the highest EWs.

In addition, Lara-Lopez et al. (2013) proposed a model in which the position of a galaxy in the Z-sSFR relation reveals information about its efficiency in star-formation (Fig. 5.5),

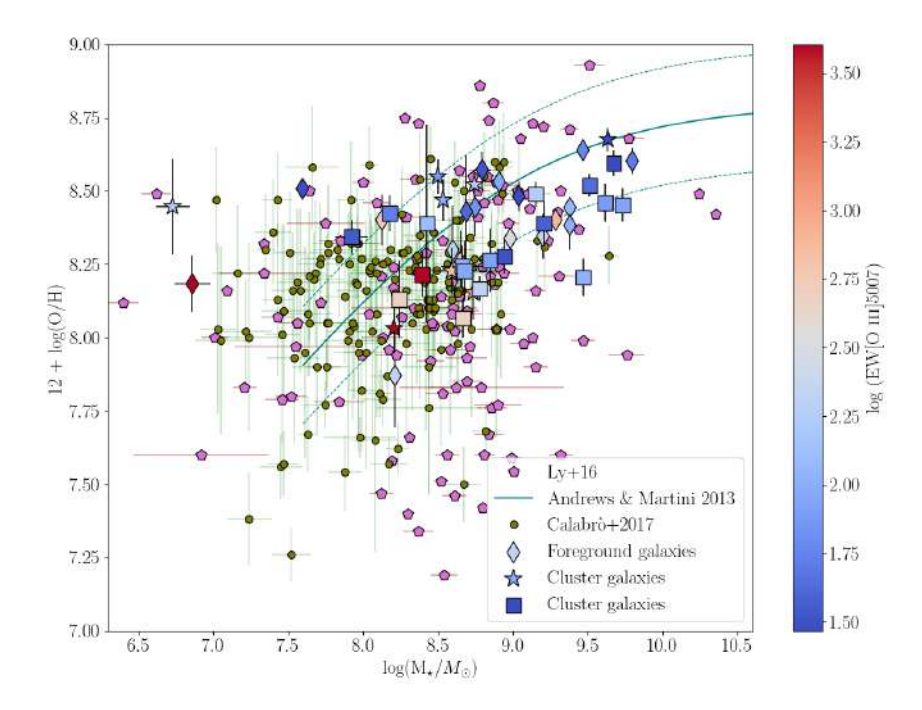


**Figure 5.3:** Mass-metallicity relation (MZR) for the galaxies in our sample. The blue curve and its offset represent the fit suggested by Andrews & Martini (2013), with the dashed lines the  $1\sigma$  uncertainty. The symbols and color bar are the same as in Fig. 5.1.

as well as its gas consumption: according to this model, galaxies with higher-sSFRs are more efficient in SF, whereas galaxies with lower-sSFRs tend to be less SF-efficient. This also correlates with their stellar mass: as we have seen in Fig. 5.2, lower mass galaxies have shown to have higher values of sSFR.

Following this approach, we plot the same parameters (sSFR and metallicity), but switching the axes, and we replace the EW color bar with a stellar mass one. The results are presented in Fig. 5.6. In their work, they consider the contribution of H I gas in a system, suggesting that the amount of neutral hydrogen content varies for a given stellar mass.

### 5.4 The Fundamental Metallicity Relation

In this section, we review the effect of the SFR and the stellar mass in the called Fundamental Metallicity Relation (FMR, Mannucci et al., 2010), defined as

$$\mu_{\alpha} = \log\left(\frac{M_*}{M_{\odot}}\right) - \alpha \cdot \log\left(\frac{SFR}{M_{\odot} \text{ yr}^{-1}}\right),$$
 (5.2)

where  $\alpha$  is a free parameter. Mannucci et al. (2010) found that the value of  $\alpha$  that minimizes the scatter in their sample (SDSS + high-redshift galaxies, 0 < z < 3.3), was  $\alpha = 0.32$ . Other values have been proposed as well, such as that of Sanders et al. (2021), where for their sample (MOSDEF survey, 0 < z < 3.3), the value that reduced the scatter of the  $z \sim 0$  sample was  $\alpha = 0.60$ . We use the latter parameter because for the estimation

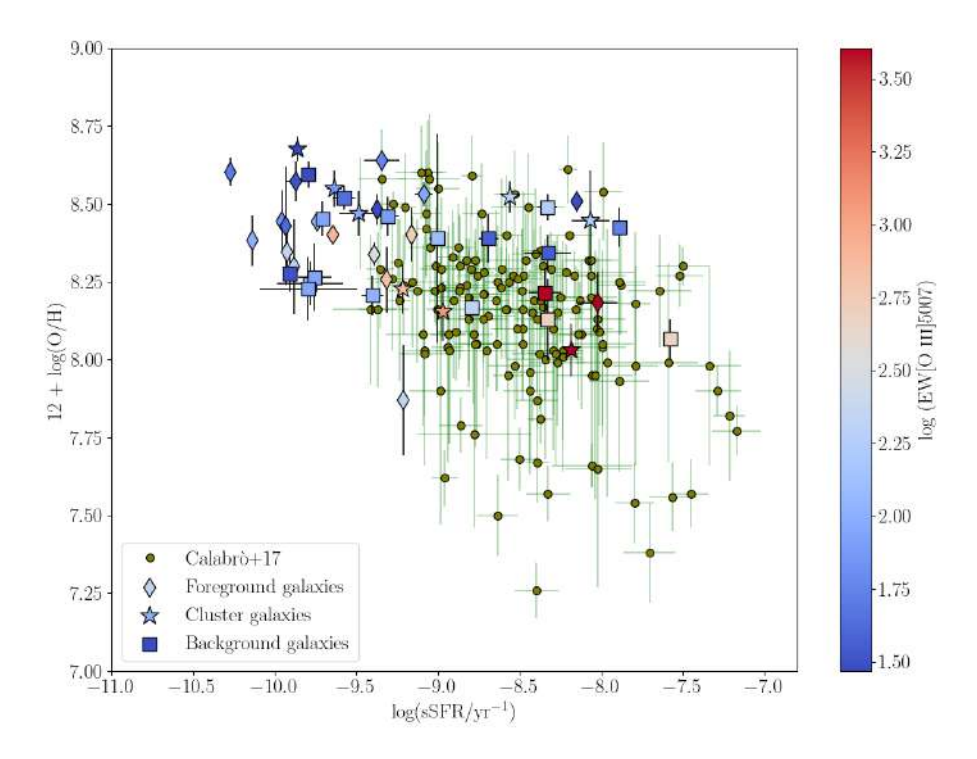


**Figure 5.4:** Diagram of metallicity vs. sSFR for the sample. The symbols are the same as Fig. 5.1. The color bar represents the [O III]5007 EW.

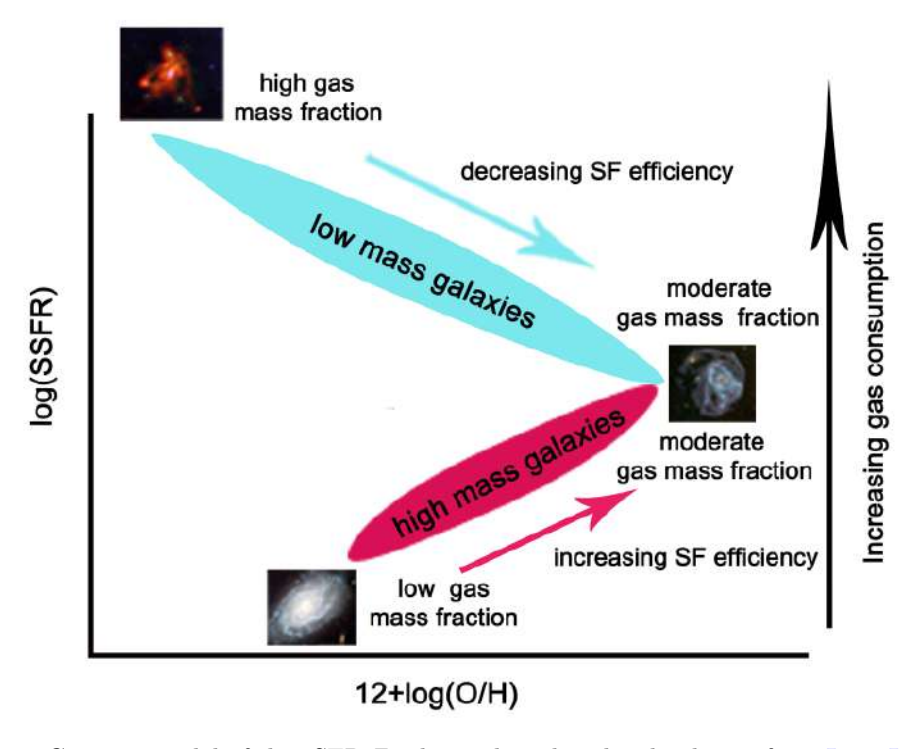


**Figure 5.5:** Cartoon model of the sSFR-Z relation based on local galaxies from Lara-Lopez et al. (2013). The blue ellipse corresponds to low-mass galaxies, and the red ellipse to high-mass galaxies.

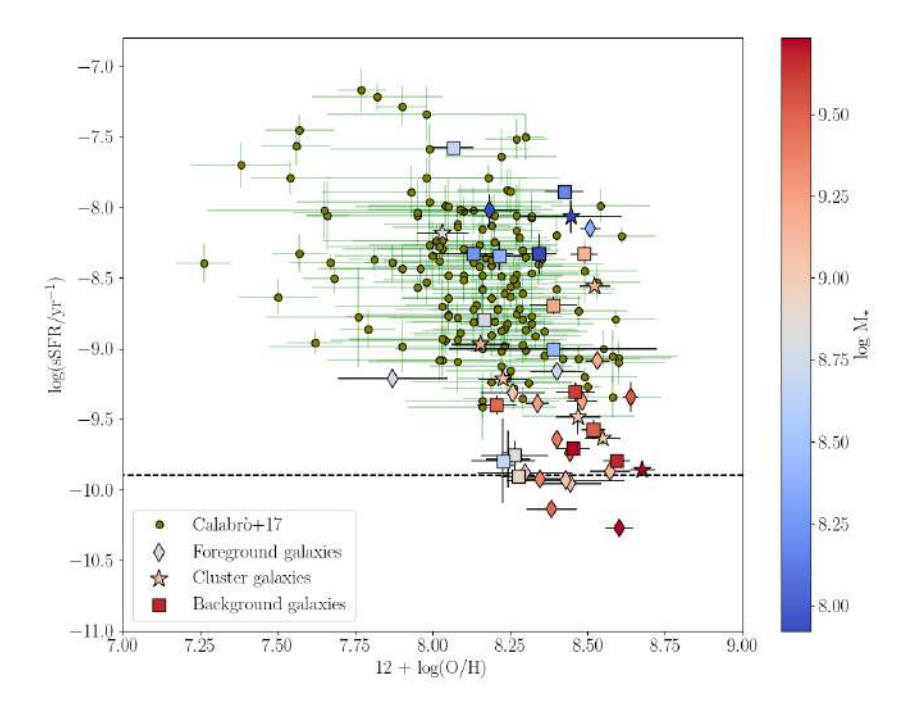


Figure 5.6: Diagram of metallicity vs. sSFR for the sample. Symbols are the same as in Fig. 5.4. Here we present the same axis as in the previous figure, but they are inverted, in order to match the description presented in Lara-Lopez et al. (2013). The color bar represents the stellar mass. The dashed line represents the turnover at  $\log(\text{sSFR}) = -9.9$ .

of metallicities via the strong-line method, the calibrations from Sanders et al. (2021) were followed. Figure 5.7 shows the results for our sample, color-coded with the [O III] $\lambda$ 5007 equivalent width, where we also display the third-degree polynomial fit proposed, defined as

$$12 + \log(O/H) = 8.80 + 0.188y - 0.220y^2 - 0.0531y^3,$$
(5.3)

with  $y = \mu_{0.60} - 10$ . There is clearly a scatter between our data and the FMR, which can be caused by some reasons we review here. Firstly, the  $\alpha$  parameter from Sanders et al. (2021) was obtained from the value that minimized the scatter of the sample utilized  $(z \sim 0 \text{ stacks})$ , so it is not probable that it is responsible for the behavior observed. The next possible explanation is that one of the two physical parameters that comprise the FMR definition (Eq. 5.2), namely  $M_{\star}$  or SFR, the former obtained via the SED fitting of the photometric data, and the latter utilizing the  $H\alpha$  emission (Section 4.5, Eq. 4.9). For the SFR, there might have been inconsistencies with the Gaussian fitting of the emission lines, which affected the posterior analysis.

To better understand this result, we compare the values of the  $\mu_{0.60}$  parameter with the difference between the metallicity derived by the calibrations from Sanders et al. (2021), and the metallicity from the polynomial fit proposed, such that we have  $\Delta FMR = \log{(O/H)} - \log{(O/H)}_{FMR}$ . We plot the results in Fig. 5.8. We see that for galaxies with a  $\mu_{0.60}$  value between  $\sim 9.0-9.4$ -, the difference in the metallicities is close to zero,

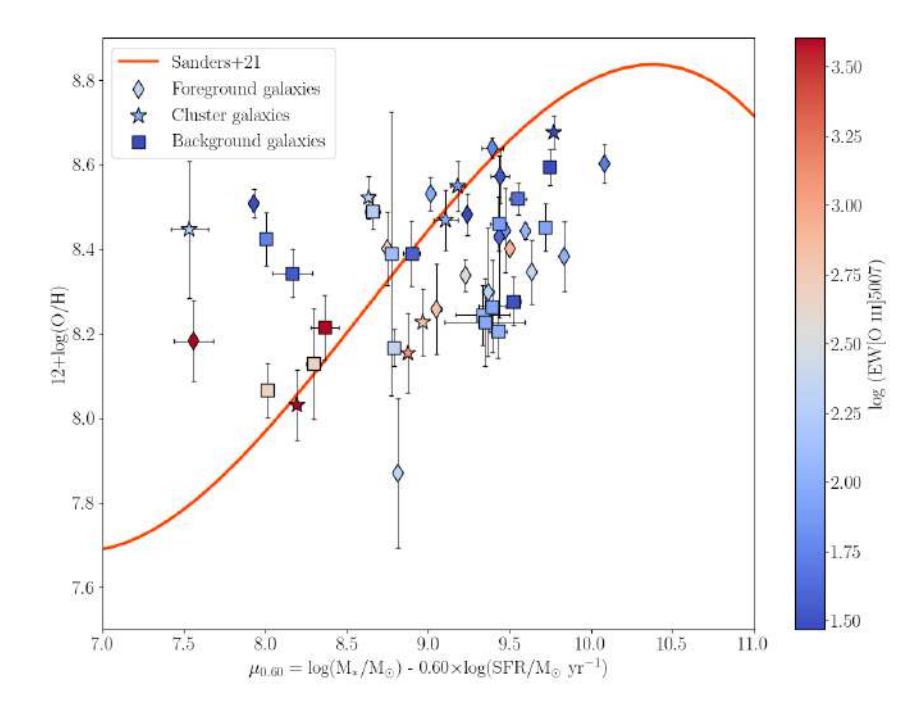


Figure 5.7: Diagram showing the relation between the FMR and the metallicity from the strong-line method. The red curve represents the polynomial fit of the FMR, described in Sanders et al. (2021). Diamonds are foreground galaxies, the stars are cluster galaxies, and squares are background galaxies. The color bar applied to the sample represents the logarithm of the [O III]5007 EW.

while for galaxies with a  $\mu_{0.60}$  value below this, the difference increases, showing that the metallicity according to the strong-line method provides a higher value than that of the polynomial fit, i.e., the metallicity predicted for the SFR and stellar mass given is lower. In the other end, for values above  $\sim 9.4$ , the  $\Delta FMR$  results in higher values for the fit, instead of the calibrations. This correlates with the results viewed in the previous Figure, where galaxies with a low  $\mu_{0.60}$  values were not falling in the theoretical curve. The same behavior occurs for galaxies with higher values.

# 5.5 The Mass-Metallicity Relation for galaxies with detection of [O III]4363

For 11 out of the 45 galaxies of our sample, we could effectively detect the  $[O\ III]\lambda4363$  auroral line (see Table 4.5 for details). We dedicate this section to study their behavior and see the differences between the metallicity derived using the strong-line method and the more reliable direct method. The first plot we review is presented in Fig. 5.9. We see that the slope is flatter than the best fit from Andrews & Martini (2013), similar to the results from Shi et al. (2014), in which their MZR considering abundances following the direct-method deviates from the fit from Tremonti et al. (2004), and also from the values of metallicity derived following the strong-line method. This is a consequence of

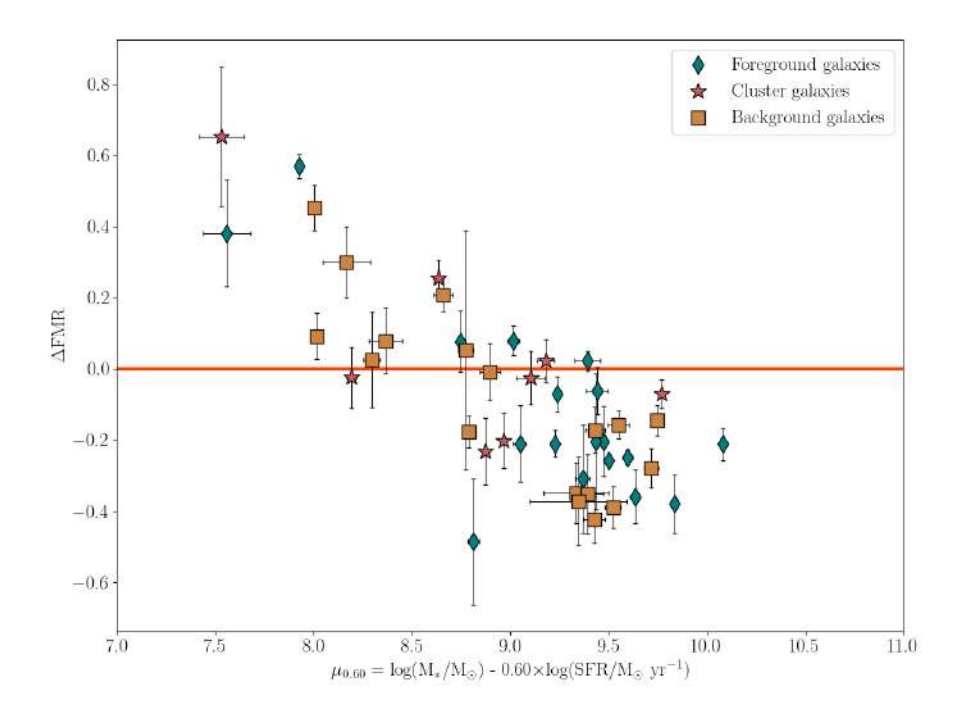
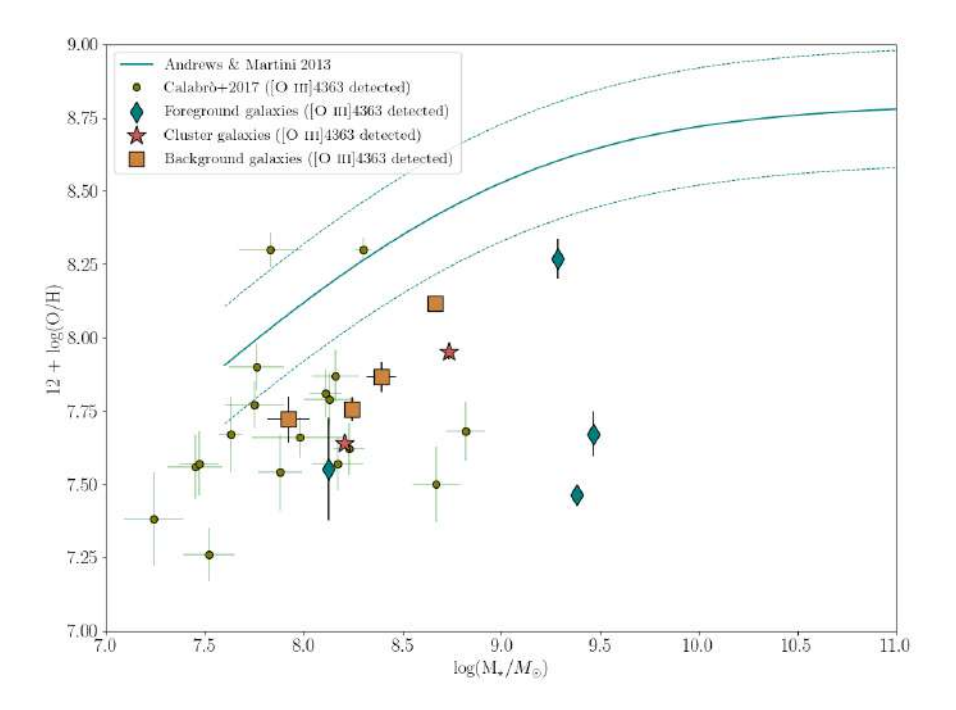


Figure 5.8: Comparison between the  $\mu_{0.60}$  parameter and  $\Delta FMR = \log(O/H) - \log(O/H)_{FMR}$ . The expression for the abundance in terms of the FMR is defined in Eq. 5.3, and is dependent on SFR and  $M_*$ . The markers are the same as in Fig. 5.7. The red line represents a  $\Delta FMR = 0$ .

the method employed to study the MZR, showing clear differences in its overall shape and normalization (Maiolino & Mannucci, 2019). Metallicities follow the same pattern, with an upper limit set by 8.268, and a lower limit set by 7.464. The second relation that we explore is shown in Figure 5.10, where our galaxies remain consistent with the [O III] $\lambda$ 4363-detected VUDS galaxies, with a maximum of log(sSFR/yr<sup>-1</sup>) = -7.578. In the case of the VUDS SFGs, the galaxies are more centered towards higher values of sSFR, reaching a maximum of (sSFR/yr<sup>-1</sup>) = -7.172.

In general, our sample is consistent with the VUDS sample, although our galaxies tend to have higher stellar masses. This is expected, as the VUDS sample possesses a deeper selection function, probing very faint targets ( $I_{AB} \sim 23-25.5$ ), and includes some galaxies that have more extreme properties, which in turn ends in lower values of stellar mass. The galaxies in our sample, on the other hand, present magnitudes ranging between F814W<sub>AB</sub>  $\sim 20.9-27.6$ , with a median at 23.5 mag, and with moderate to low magnifications (average magnification at 2.23), that allowed us to detect low-mass galaxies (e.g., ID 13, with  $log(M_{\star}/M_{\odot}) \sim 7.9$ , with a magnification of 6.2).



**Figure 5.9:** MZR for galaxies with detection of [O III]4363. The diamonds are foreground galaxies, the stars are cluster galaxies, and the squares are background galaxies. Green circles are VUDS SFDGs from Calabrò et al. (2017). The blue curve and its offset represent the fit suggested by Andrews & Martini (2013), with the dashed lines the  $1\sigma$  uncertainty.

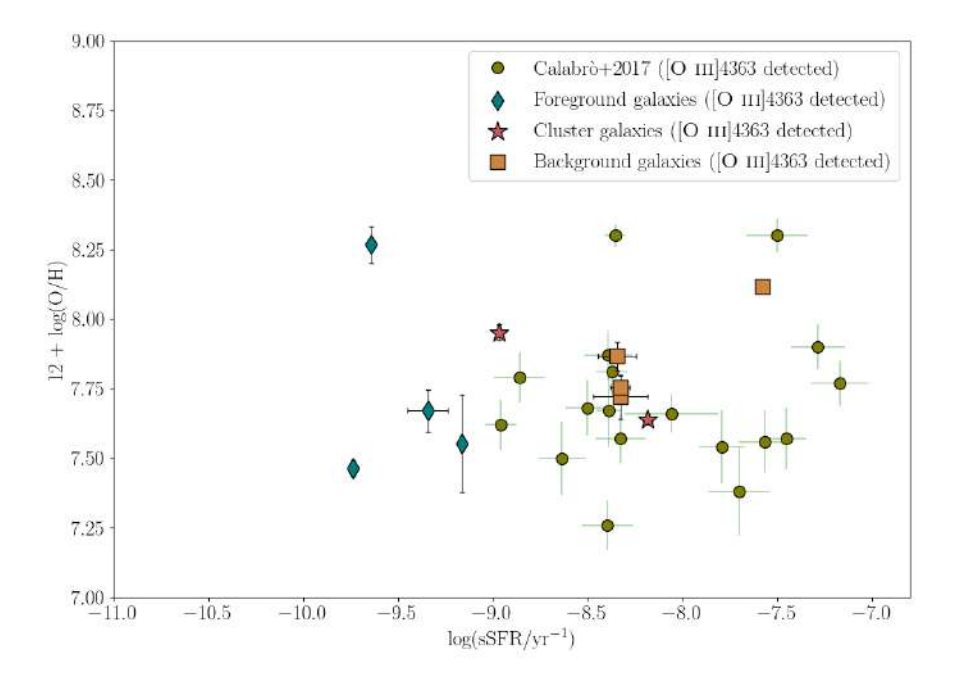


**Figure 5.10:** Diagram showing sSFR vs. Metallicity for the sample with detection of [O III]4363. The symbols are the same as in the previous Figure.

# 5.6 The serendipitous discovery of a dwarf galaxy group at z = 0.84

From our sample, we report the fortuitous detection of a galaxy association consisting of three galaxies (galaxy 14, 16 and 17 hereafter), with a fourth smaller galaxy near galaxies 16 and 17. Fig. 5.11 depicts the group in a MUSE narrowband filter centered on the [O III] $\lambda$ 5007 line, as well as HST false color images. The main galaxies are inside the green circles, and the smaller galaxy is in the orange circle. We check that galaxies 16 and 17 (the two closest systems) are not multiple images of the same target, but two galaxies at z=0.8413, projected at a short distance of d=48.6 kpc of each other, while galaxy 14 has a projected distance of 176.4 kpc and 187.9 kpc towards galaxies 16 and 17, respectively.

Galaxies 14, 16 and 17 present stellar masses of  $10^{9.5} \mathrm{M}_{\odot}$ ,  $10^{8.7} \mathrm{M}_{\odot}$  and  $10^{9.5} \mathrm{M}_{\odot}$ , respectively, and star formation rates of  $10^{-0.1} \mathrm{M}_{\odot} \mathrm{yr}^{-1}$ ,  $10^{1.1} \mathrm{M}_{\odot} \mathrm{yr}^{-1}$  and  $10^{0.1} \mathrm{M}_{\odot} \mathrm{yr}^{-1}$ , respectively. They present high [O III]5007 equivalent widths at 43 Å, 461 Å and 102 Å, respectively, with the latter two corresponding with the EELG type. The metallicities derived using the strong-line method are 8.52, 8.07 and 8.21, respectively. For galaxy 16, the detection of [O III]4363 allowed to use the direct method, yielding a T<sub>e</sub>-based metallicity of 8.12. The smaller galaxy (marked in orange in Fig. 5.11) has an spectroscopic redshift of 0.8411. It is located at 21 kpc from galaxy 16 and at 31 kpc from galaxy 17. We find that this galaxy is reported in the DEEPSPACE catalog with the ID 5525. From this, we perform a SED fitting considering the same SFH as the rest of the sample (exponentially declining), and derive a stellar mass of  $M_{\star} = 7.97 \pm 0.1 M_{\odot}$ . The absolute magnitude of galaxies 14, 16 and 17 are -19.7, -21.9 and -20.7, respectively. The smaller system has an absolute magnitude of -19.2. Galaxy 14 presents a clump that might be associated with it, although it is possible that it is related to another spiral galaxy located south of galaxy 14, at  $z \sim 0.71$ . The spatial resolution of MUSE cannot solve this scale, so alternative approaches, such as photometry, might be helpful for clarification.

This association could explain the intense emission lines, and in the case of galaxies 16 and 17 might be the reason of the strong starburst detected, as interactions between dwarf galaxies can boost and maintain star formation (Pearson et al., 2019). It is particularly of interest to study this type of system, as there are fewer examples of dwarfs in groups in the local universe (see Stierwalt et al., 2015; del Valle-Espinosa et al., 2023 for a more extreme case), with a very limited number of groups in the field predicted by simulations (Besla et al., 2018) compared to the early universe, and these processes might be tied to the hierarchical scenario of high-z galaxies according to  $\Lambda$ CDM cosmology. Detecting a dwarf galaxy association at this redshfit using such deep and high-quality data might be indicative that they might not be that rare with increasing redshift, and could shed some light on the conditions necessary for galaxy formation and evolution. It is also worth mentioning that in general, it is expected to find dwarf galaxy associations bound to a

massive galaxy ( $M_{\star} > 5 \times 10^9 \ M_{\odot}$ ), which was not the case for this group, although this configurations are known to not last long (González & Padilla, 2016). Considering the definition of Besla et al. (2018) of 'dwarf multiples', they are two or more dwarf galaxies with projected separations smaller than 150 kpc, and relative line-of-sight velocities smaller than 150 km s<sup>-1</sup>. For our discovered group, we find that, taking galaxy 17 as the central galaxy of the system (due to its higher stellar mass and proximity to galaxy 16), and considering the peak of [O III] $\lambda$ 5007 emission as reference with v=0, we find that galaxy 16 has a relative velocity of 149.8 km s<sup>-1</sup>, and galaxy 14 has a relative velocity of 74.9 km s<sup>-1</sup>. The smallest galaxy of the group presents a relative velocity consistent with 0 km s<sup>-1</sup> within the uncertainties, exhibiting the same wavelength at the [O III] $\lambda$ 5007 peak. This tells us that this association might be a isolated dwarf multiple, experiencing an interaction, or having interacted recently. This finding goes beyond the scope of this thesis, but will be systematically explored in future works.

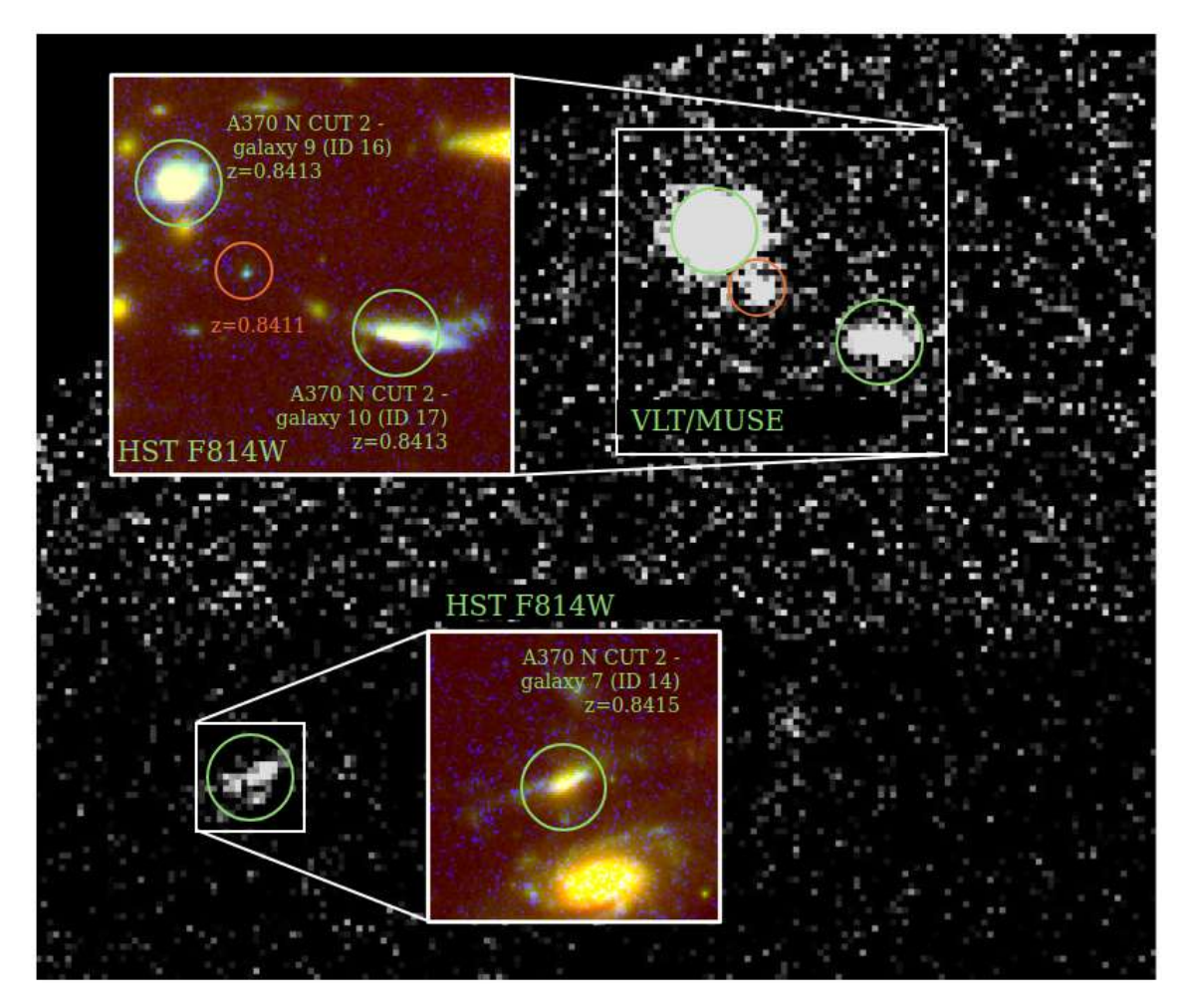


Figure 5.11: Dwarf galaxy association formed by galaxies 14, 16 and 17. The image presents the MUSE image with a narrowband filter for  $[O~III]\lambda5007$  plus a continuum subtraction of a region including the three main members (green circles), and also considering the smaller system around galaxies 16 and 17 (orange circle). The cutouts are false color HST stamps using the F275W, F814W and F160W filters showing the main members of the group, with their spectroscopic redshifts and names included.

## 6 | Conclusions and outlook

We present the spectrophotometric search and characterization of star-forming galaxies, covering the redshift range 0.2-0.9, obtained by means of examining one of the *HST* Frontier Fields, the massive galaxy cluster Abell 370. We use deep photometry from the DEEPSPACE program, ranging from the ultraviolet to the near-infrared, and deep spectroscopy from VLT/MUSE datacubes, in order to search for emission line galaxies in the central part of the Abell 370 cluster. We investigate the presence of low-luminosity star-forming galaxies, including those within the cluster, as well as those in the foreground and background. This work's primary objective is to extract the physical properties of the selected galaxies and use these to investigate the low-mass end of the essential scaling relations in the context of galaxy evolution. We summarize our conclusions below:

- 1. From the study of the MUSE datacube, we identify a sample of 45 faint (F814W<sub>AB</sub> ~ 20.9-27.6) star-forming dwarf galaxies, in the redshift range 0.2 < z < 0.9. In all cases we effectively detect the presence of the emission lines H $\beta$  and [O III] $\lambda\lambda4959,5007$ , and depending on the measured redshift, we detect the [N II] $\lambda\lambda3727,3729,$  H $\alpha$ , and [N II] $\lambda\lambda6548,6584$  lines. We measure the emission lines using the Python package LIME from the spectra extracted from the datacubes. The range of EW([O III] $\lambda5007$ ) is 14-500 Å, with a median of 54 Å. We perform an extinction correction, with an upper value of c(H $\beta$ ) = 1.115, and a mean of c(H $\beta$ ) ~ 0.34 ± 0.27. After the extinction correction, we study the emission line ratios in classic diagnostic diagrams. We find that all the selected galaxies are consistent with pure stellar photoionization.
- 2. From our sample, we find that 11 galaxies present the typical features of EELGs, with EW([O III]λ5007) between 100-450 Å, and a median strong-line method metallicity of 8.2.
- 3. We investigate the metallicity properties adopting different approaches. Employing the well-known strong-line method and  $T_e$ -based calibrations from Sanders et al. (2021), we consider the O32, N2, Ne3O2, O3N2, R2 and R3 line ratios. Our results shows metallicities relatively low ranging  $7.87 < 12 + \log(O/H) < 8.76$ , with a median of 8.36. This result can also be inferred from their relatively large O32 values, which indicate that they have on average higher ionzization conditions. We detect the  $[O\ III]\lambda4363$  auroral line in 11 galaxies from our sample, with 36% corresponding to

- the EELG classification, according to the definition of EW(5007) > 100 Å. From this subset, we obtain  $T_e([O~{\sc iii}])$  values between 11000 K and 23000 K. After applying the direct method, we derive  $T_e$ -based metallicities ranging between 7.4 and 8.3, and 0.44 dex lower when compared to the strong-line method.
- 4. Using our measurements of Balmer emission lines from the MUSE spectra, we derive the ongoing SFR, ranging between  $10^{-1.3}~\rm M_{\odot}~\rm yr^{-1} \leq SFR \leq 10^{1.1}~\rm M_{\odot}~\rm yr^{-1}$ , with a mean SFR  $\sim 10^{-0.44}$ . We perform the method of Kennicutt (1998), using the extinction-corrected luminosity of the H $\alpha$  recombination line. Combined with the stellar masses derived from the SED fitting, we obtain sSFR values, ranging from  $10^{-10.2}~\rm yr^{-1}$  to  $10^{-7.5}~\rm yr^{-1}$ . From this, we can conclude that the sample selected is effectively at an active phase of star formation, with EELGs likely showing bursty star formation, characterized by the intense emission lines, low metal content, and SFR reported.
- 5. We perform a SED fitting of the photometric data from the DEEPSPACE catalog utilizing the python package BAGPIPES, considering UV to IR observations. We derive stellar masses ranging between  $10^7~\rm M_{\odot} < M_{\star} < 10^{9.7}~\rm M_{\odot}$ , corresponding to the low-mass range. From this, we see the behavior of our sample in the mass-metallicity relation (MZR), and in the mass-star formation rate relation, in which the expected trends for mass and metallicity/SFR are followed as described in the evolutionary analysis from literature, in which less massive galaxies are more metalpoor, with lower SFRs, and also showing higher sSFR values.
- 6. We explore the relationship existing between stellar mass, metallicity, and star formation rate, the so-called FMR. We compare the position of our sample with precious results from literature. For a FMR based on the one suggested by Sanders et al. (2021), we find that 30 galaxies do not seem to adjust to the expected metallicity curve, with some scatter present in the M<sub>\*</sub>-SFR-Z relation. This could be explained due to uncertainties on the derivation of the properties such as metallicity or stellar mass, or intrinsic differences in the star formation histories. An in-depth analysis of the detailed star-formation histories for the sample would be helpful, combining photometric and spectroscopic fittings with parametric and non-parametric SFH models, such as those available in BAGPIPES. Recent JWST photometry in the near-infrared and mid-infrared will also be a very useful tool for our future steps for this project.
- 7. We conclude that there is no systematic deviation in our sample in the MZR or M-SFR relation in the low-mass end. Our sample fits well with previous results, and there are no significant deviations when extrapolating the fits from literature towards low-masses. We observe that there is no need to describe the place of our sample in the scaling relations with events beyond the usual.

8. Finally, we detect three galaxies at the same spectroscopic redshift ( $z_{spec} \sim 0.841$ , ID 14, 16 and 17), with a smaller system near galaxies 16 and 17. The projected distance between galaxy 16 and galaxy 17 is 48.6 kpc, while the projected distance between the smaller galaxy and galaxies 16 and 17 is 21 kpc and 31 kpc, respectively. The third member of the group is located at a projected distance of 176.4 kpc and 187.9 kpc from galaxies 16 and 17, respectively. Taking the most massive member of the two closest galaxies (galaxy 17) as the central member, we find relative velocities of 74.9 km s<sup>-1</sup> and 149.8 km s<sup>-1</sup> for galaxies 14 and 16, respectively, while the smaller system presents a relative velocity of 0 km s<sup>-1</sup>. We find that this association might be a dwarf multiple, due to the proximity of its members, although a detailed analysis of this galaxies is crucial to confirm this possibility.

While this thesis represents a first attempt to study the fainter star-forming dwarfs at z < 1 with an exquisite spectrophotometric dataset, a natural future step in our project is to increase the sample, extending the methodology to the other five Hubble Frontier Fields, namely Abell 2744, Abell S1063, MACS 0416, MACS 0717, and MACS 1149 (Lotz et al., 2017). We contemplate adding new photometric and spectroscopic data, in particular covering the rest-NIR with from JWST surveys (Treu et al., 2022; Curti et al., 2024), which will be paramount to refine our spectroscopic analysis and study, in larger detail, additional properties such as morphology. Such a project will be key to delve into the least massive and most extreme star-forming systems at  $z \lesssim 1$ , probing their key physical properties (metallicity, stellar mass, star-formation rate), with larger statistical significance.

# Appendices

# A | Extracted spectra and LiMe Gaussian fits

In the following section we present the best Gaussian fits obtained with LIME for the main emission lines of the sample. We highlight the measurements of the lines involved in the processes of Balmer decrement and line ratios for metallicity derivation. The format is as follows. In each figure, we present the extracted spectrum following the segmentation map method, along with its uncertainty, denoted in red, in the upper left figure; we present in the upper right figure the extracted galaxy in the MUSE datacube, centered on the spaxel range containing the [O III] $\lambda$ 5007 line, along with its spectroscopic redshift. Finally, we present the Gaussian fitting of the lines in the lower figures, as displayed by the LIME code. In the LiMe fittings, the top panel presents the line fit and the bottom panel shows the residuals of the fit. The pink areas represent the wavelength range of the continuum surrounding the line; the yellow area represents the wavelength range of the emission line. The solid blue line is the Gaussian fit. The orange-dashed line represents the continuum of the spectrum. The red crosses represent masked pixels.

### A.1 A370 N CUT 1

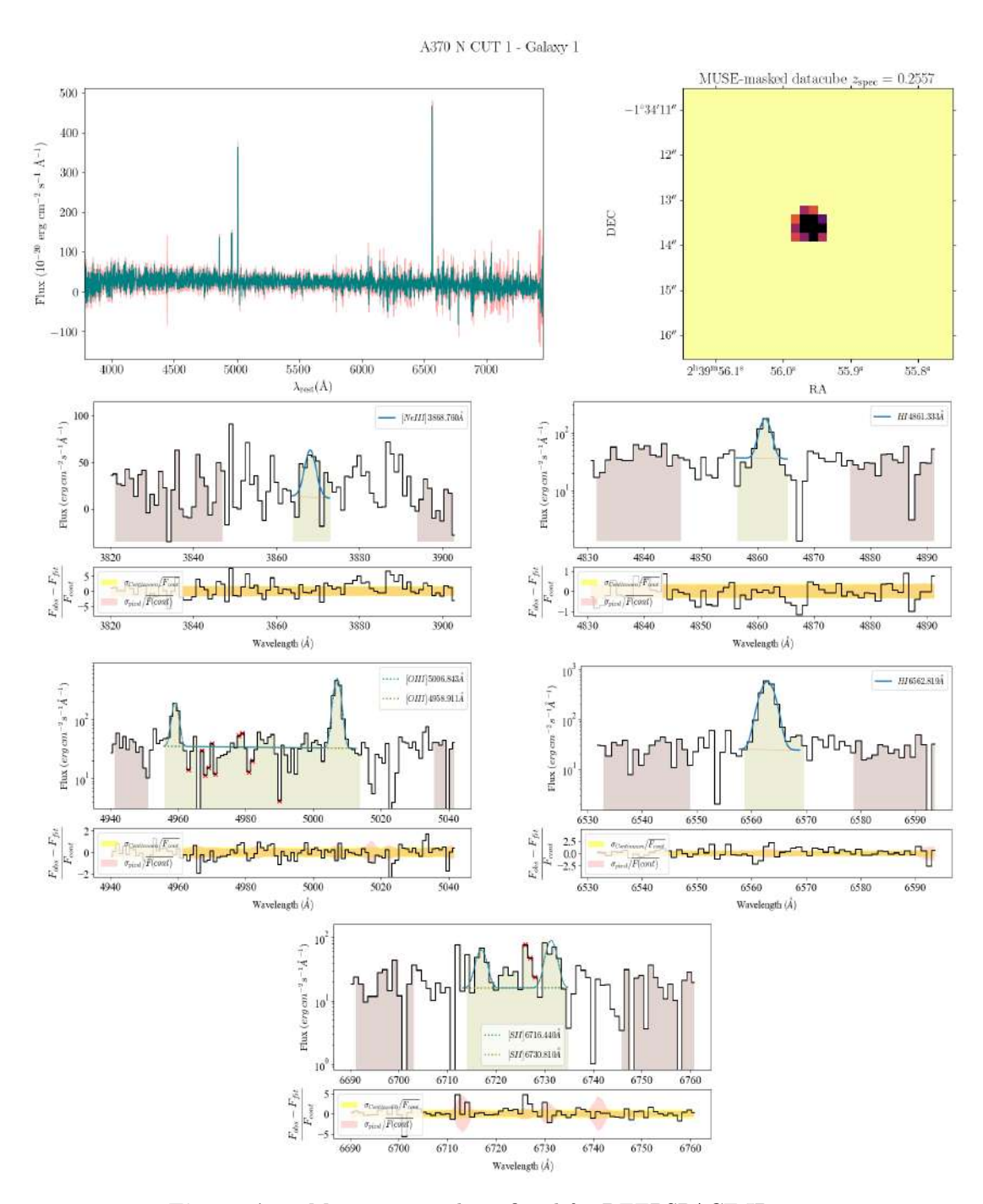


Figure A.1: Main emission lines fitted for DEEPSPACE ID 4112.

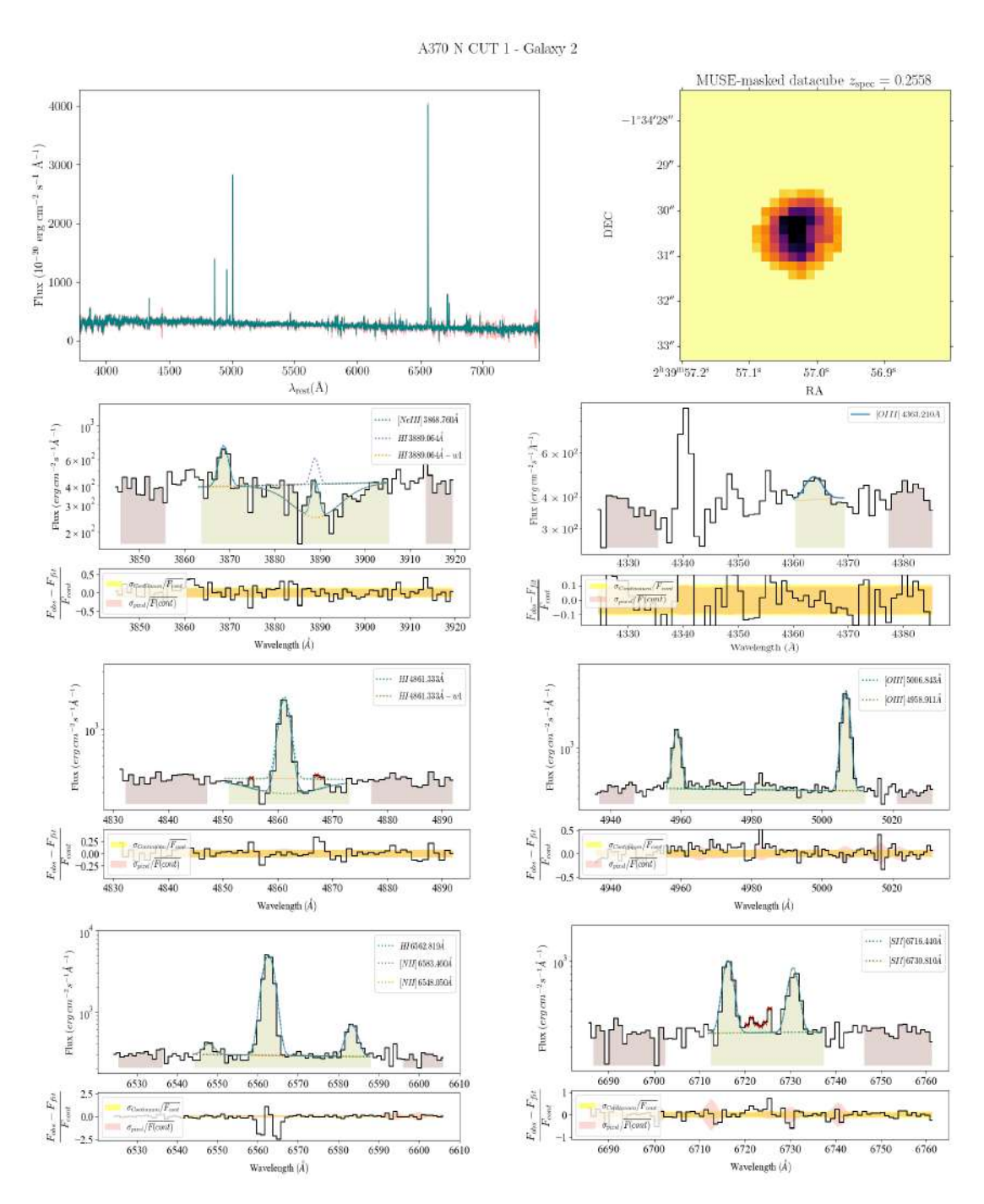


Figure A.2: Main emission lines fitted for DEEPSPACE ID 3628.

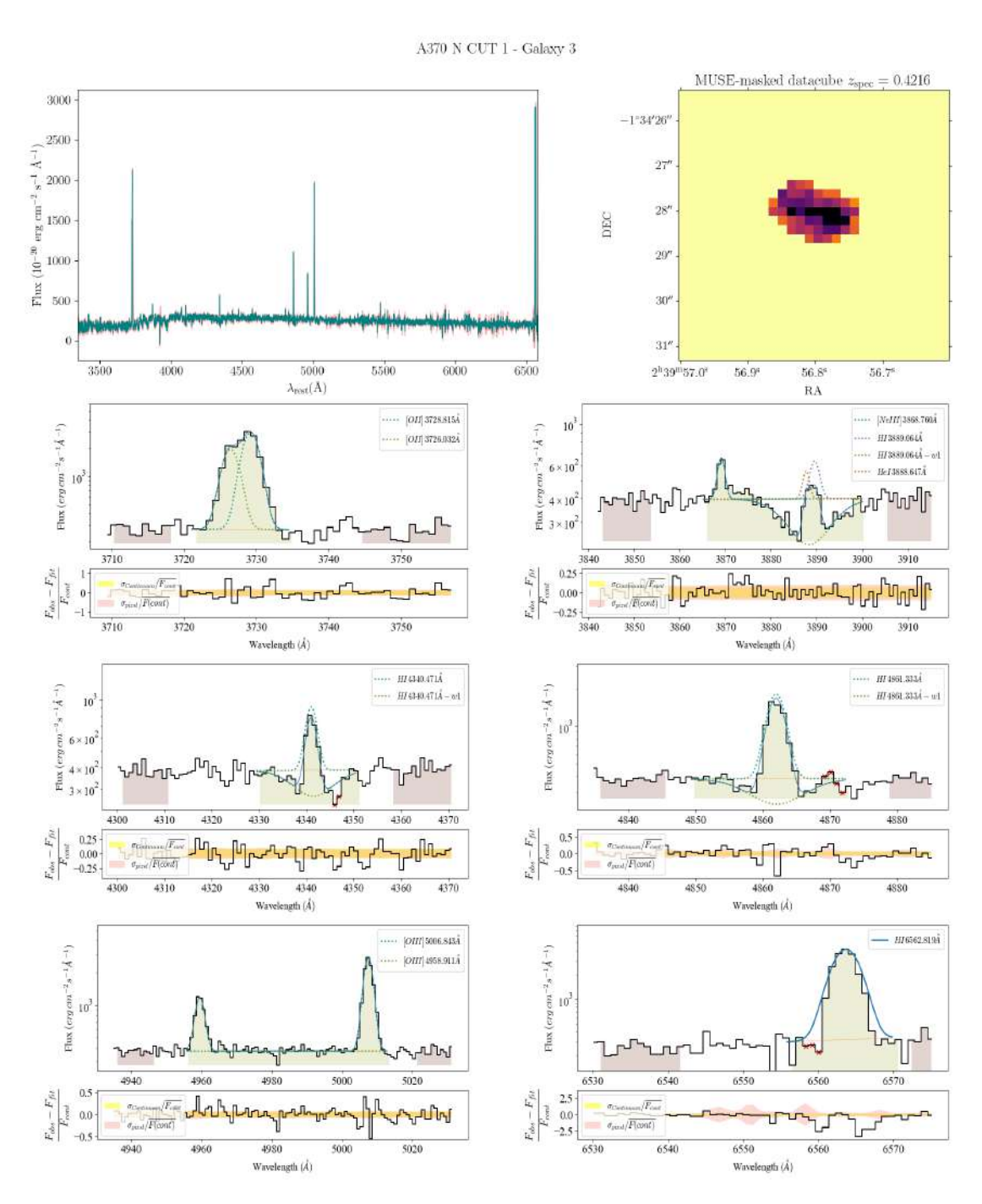


Figure A.3: Main emission lines fitted for DEEPSPACE ID 4225.

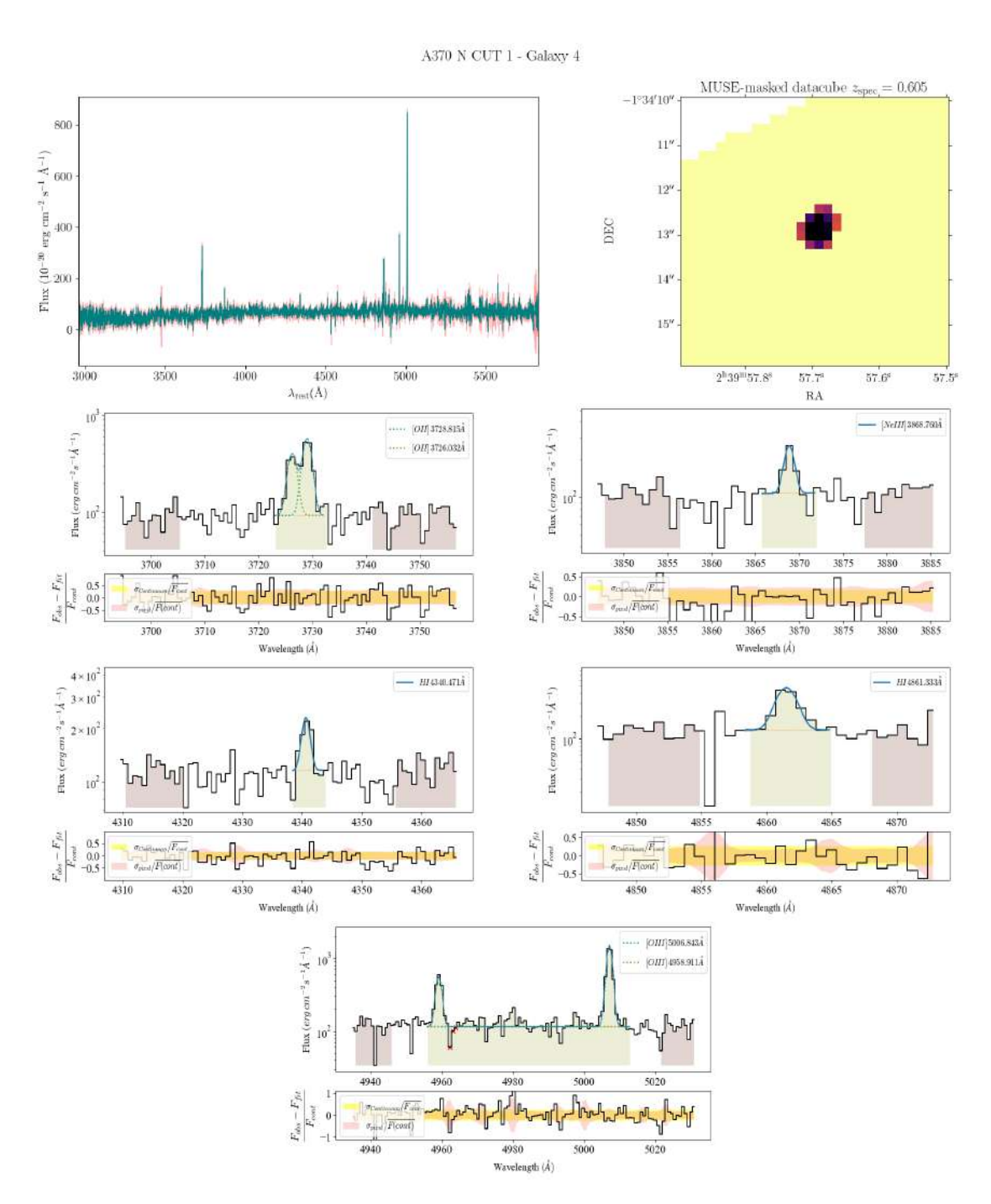


Figure A.4: Main emission lines fitted for DEEPSPACE ID 4178.

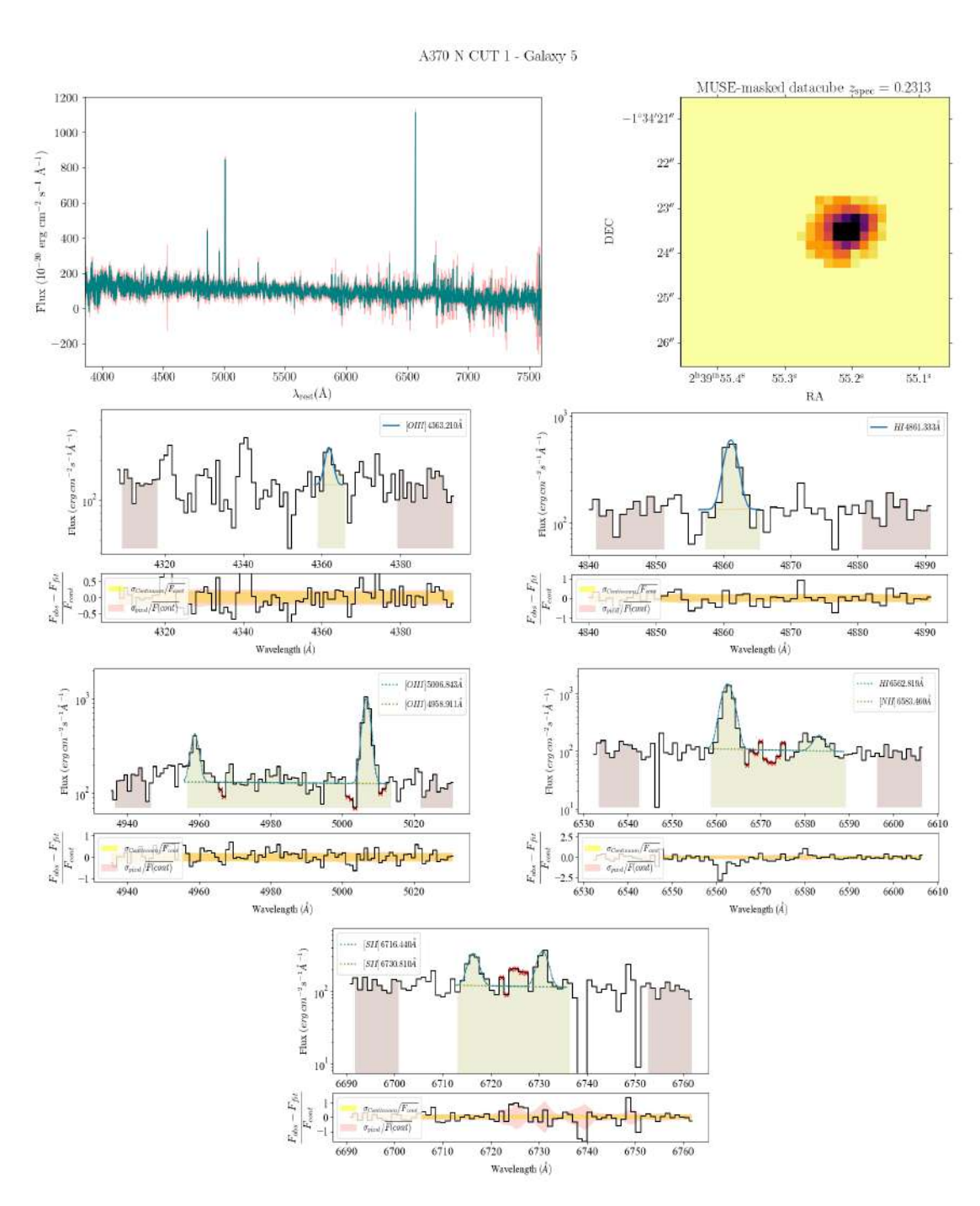


Figure A.5: Main emission lines fitted for DEEPSPACE ID 3806.

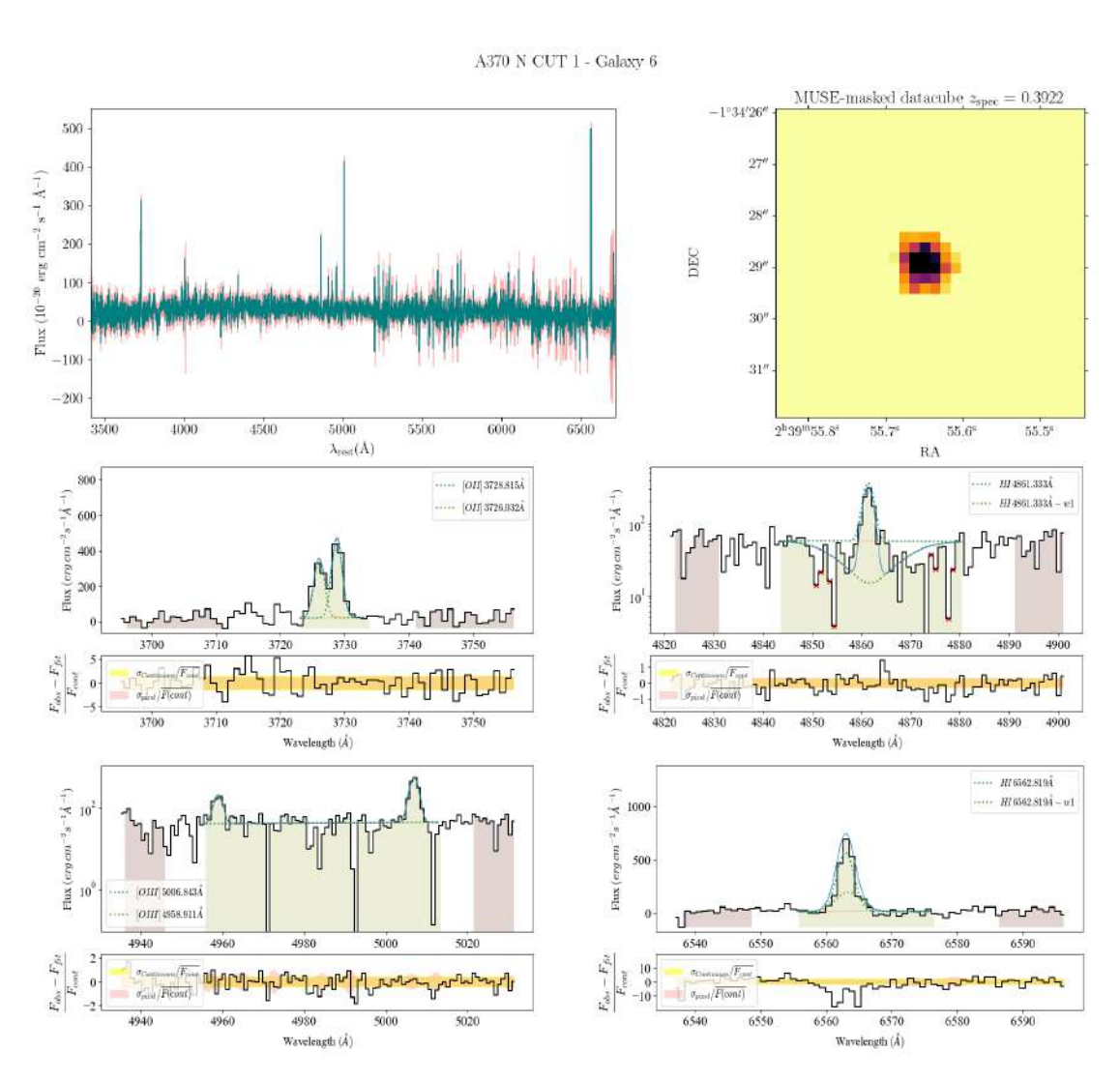


Figure A.6: Main emission lines fitted for DEEPSPACE ID 3595.

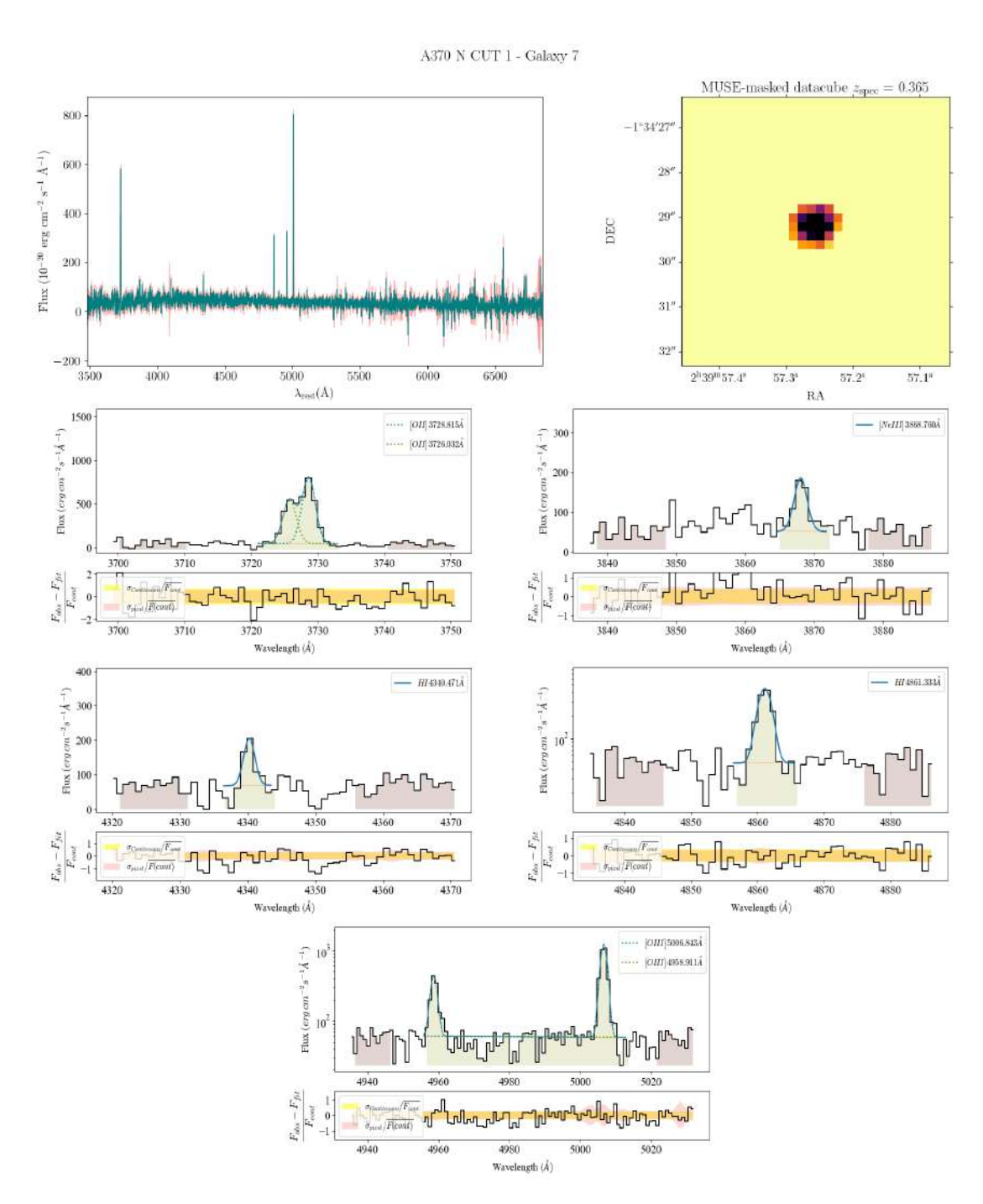


Figure A.7: Main emission lines fitted for DEEPSPACE ID 3529.

#### A.2 A370 N CUT 2

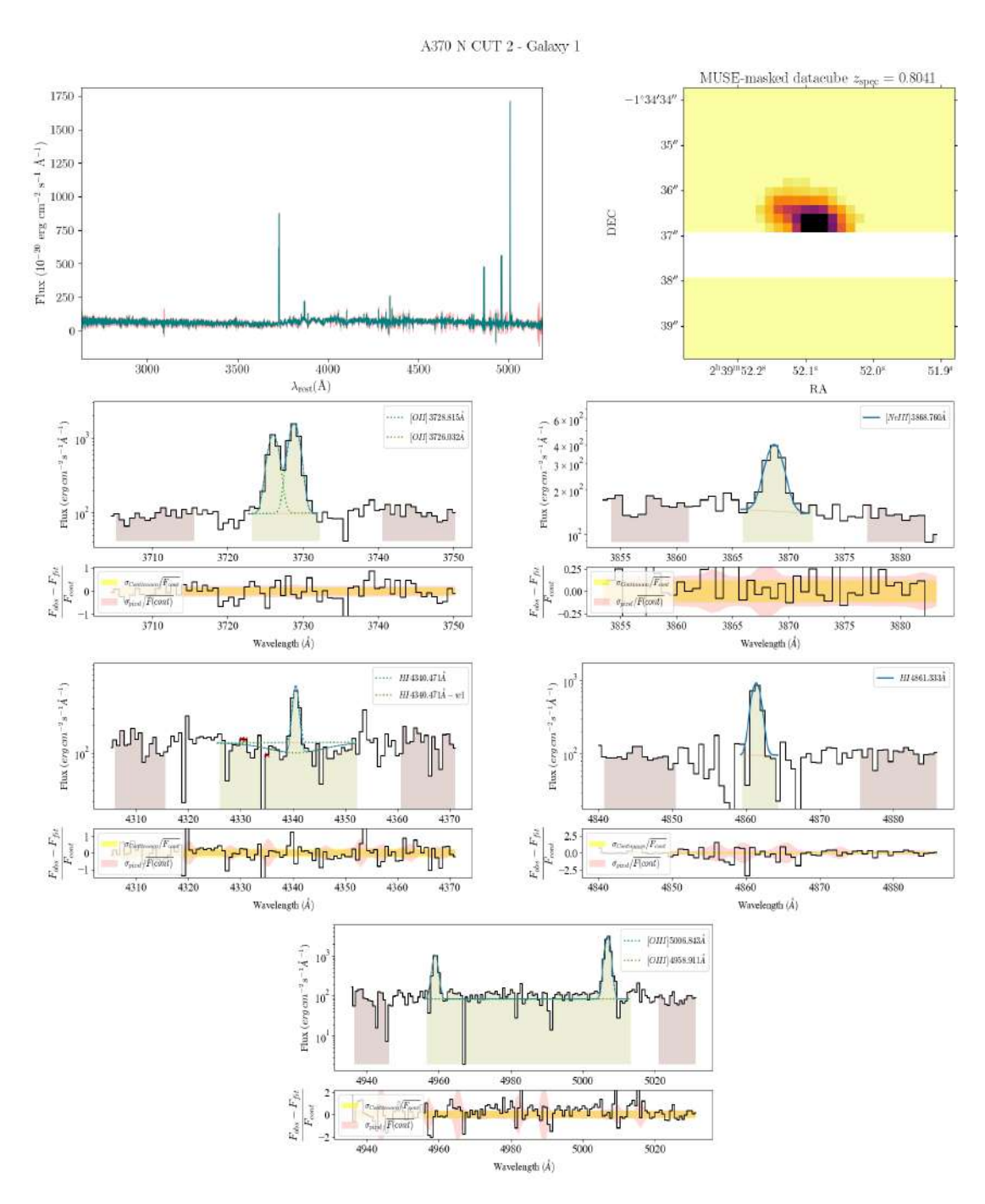


Figure A.8: Main emission lines fitted for DEEPSPACE ID 3342.

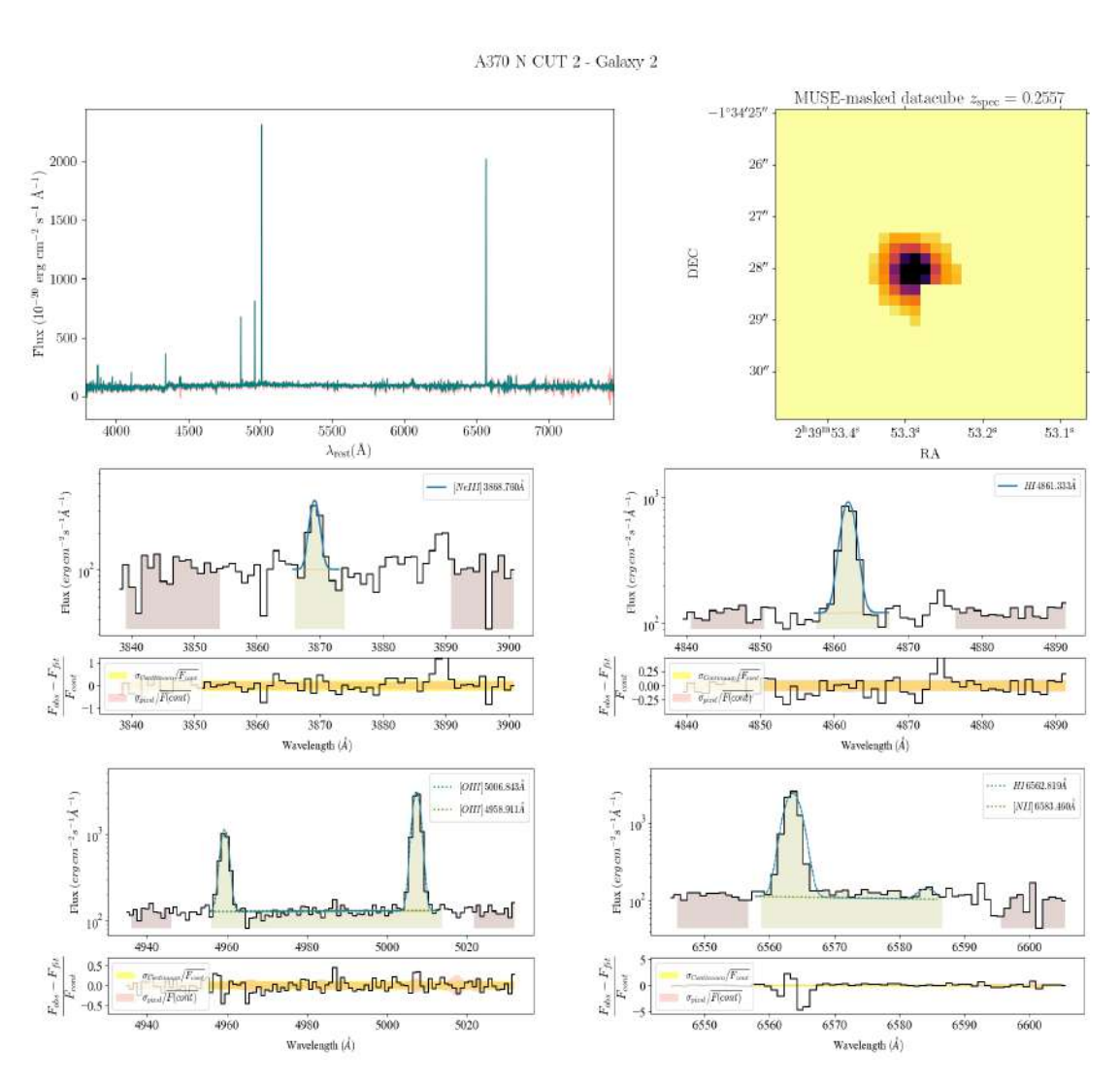


Figure A.9: Main emission lines fitted for DEEPSPACE ID 3826.

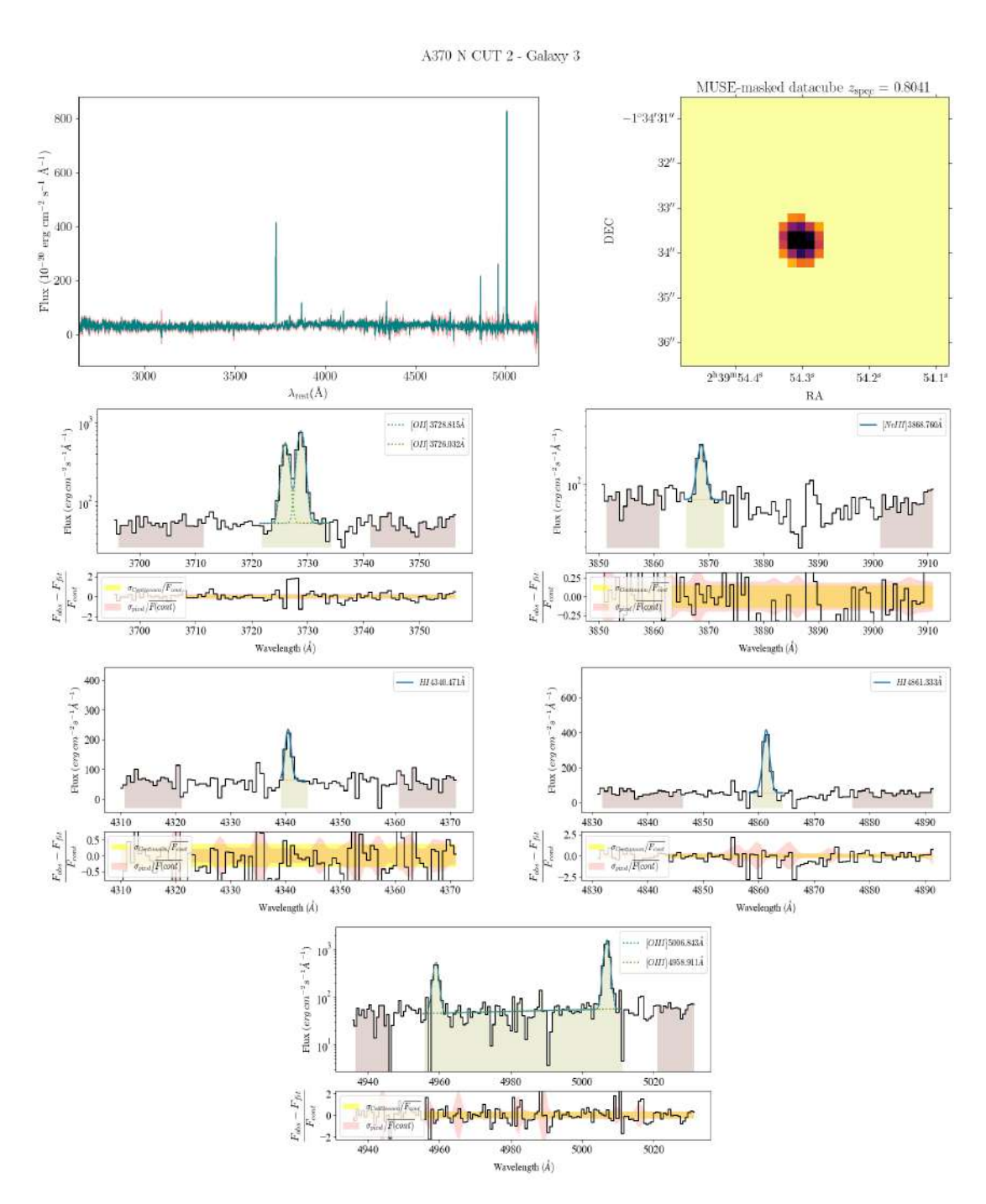


Figure A.10: Main emission lines fitted for DEEPSPACE ID 3440.

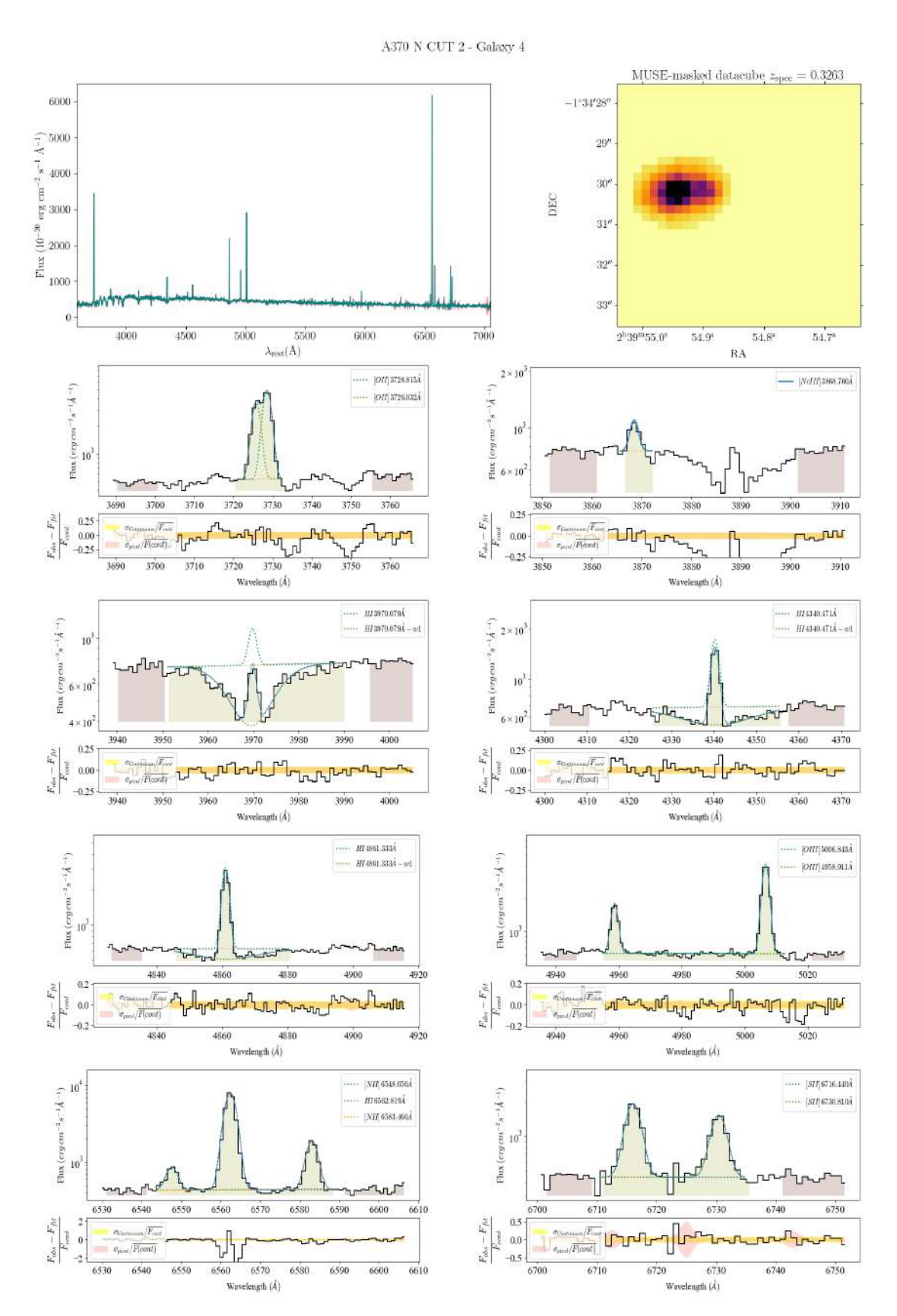


Figure A.11: Main emission lines fitted for DEEPSPACE ID 3633.

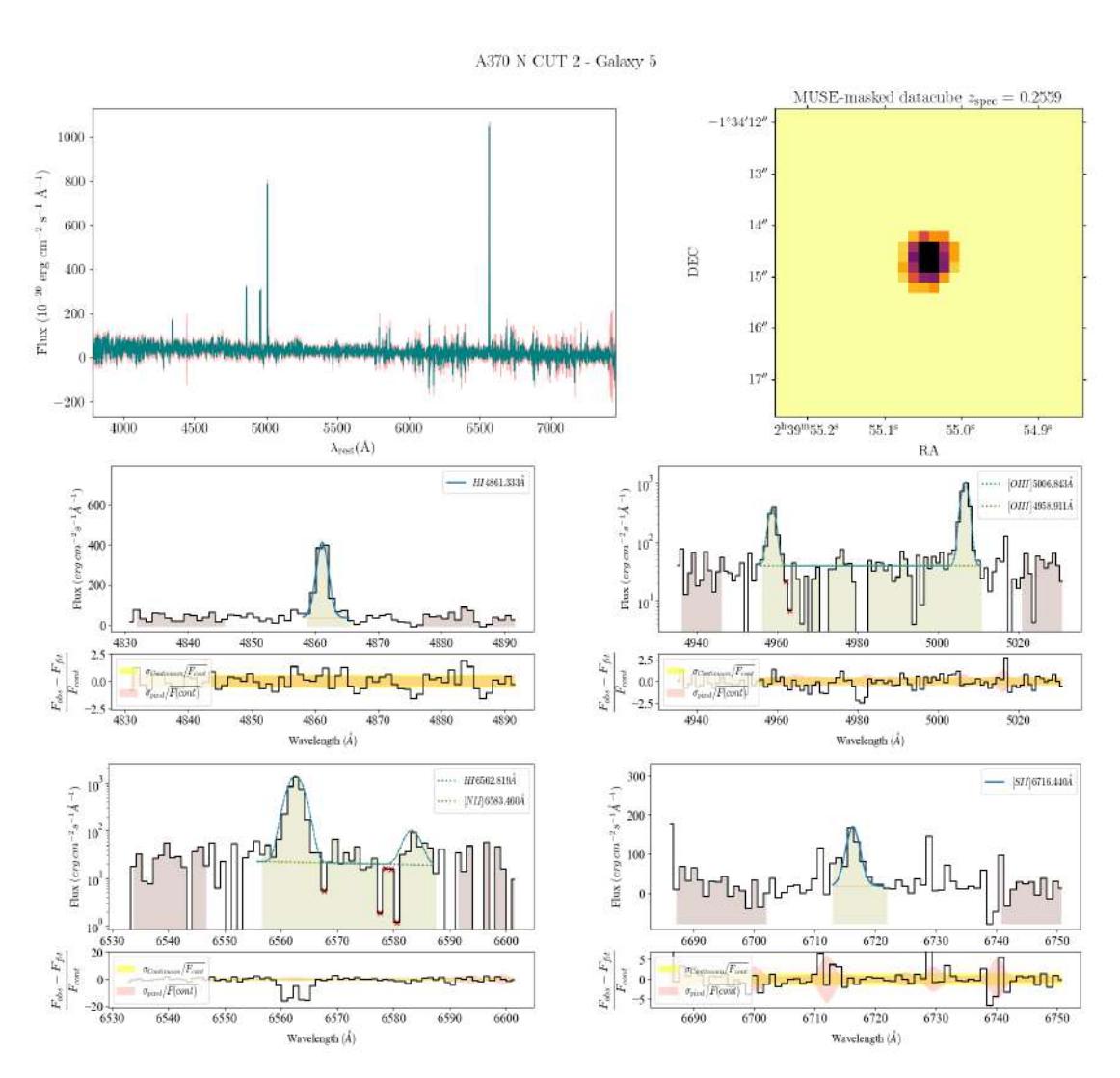


Figure A.12: Main emission lines fitted for DEEPSPACE ID 4070.

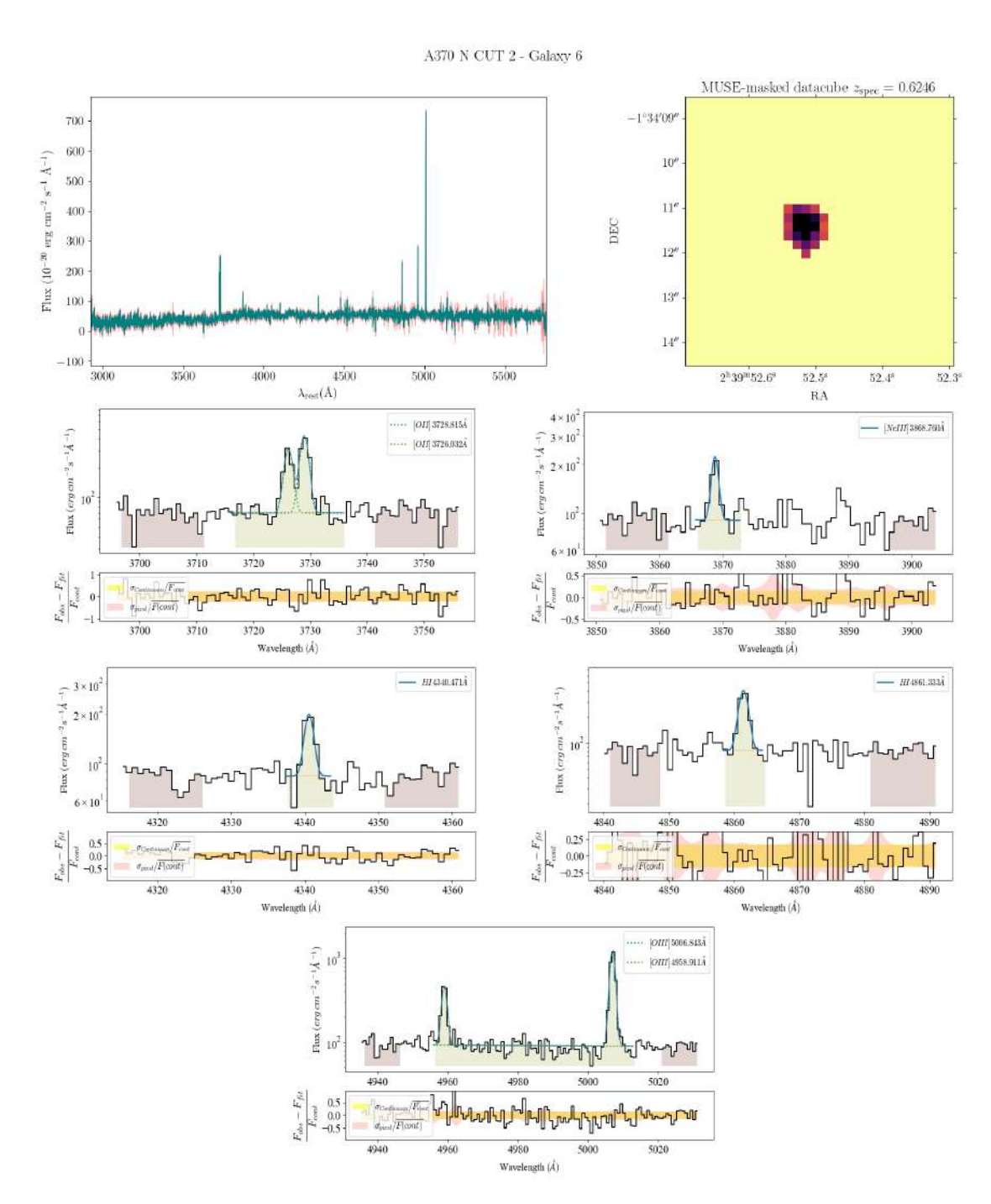


Figure A.13: Main emission lines fitted for DEEPSPACE ID 4266.

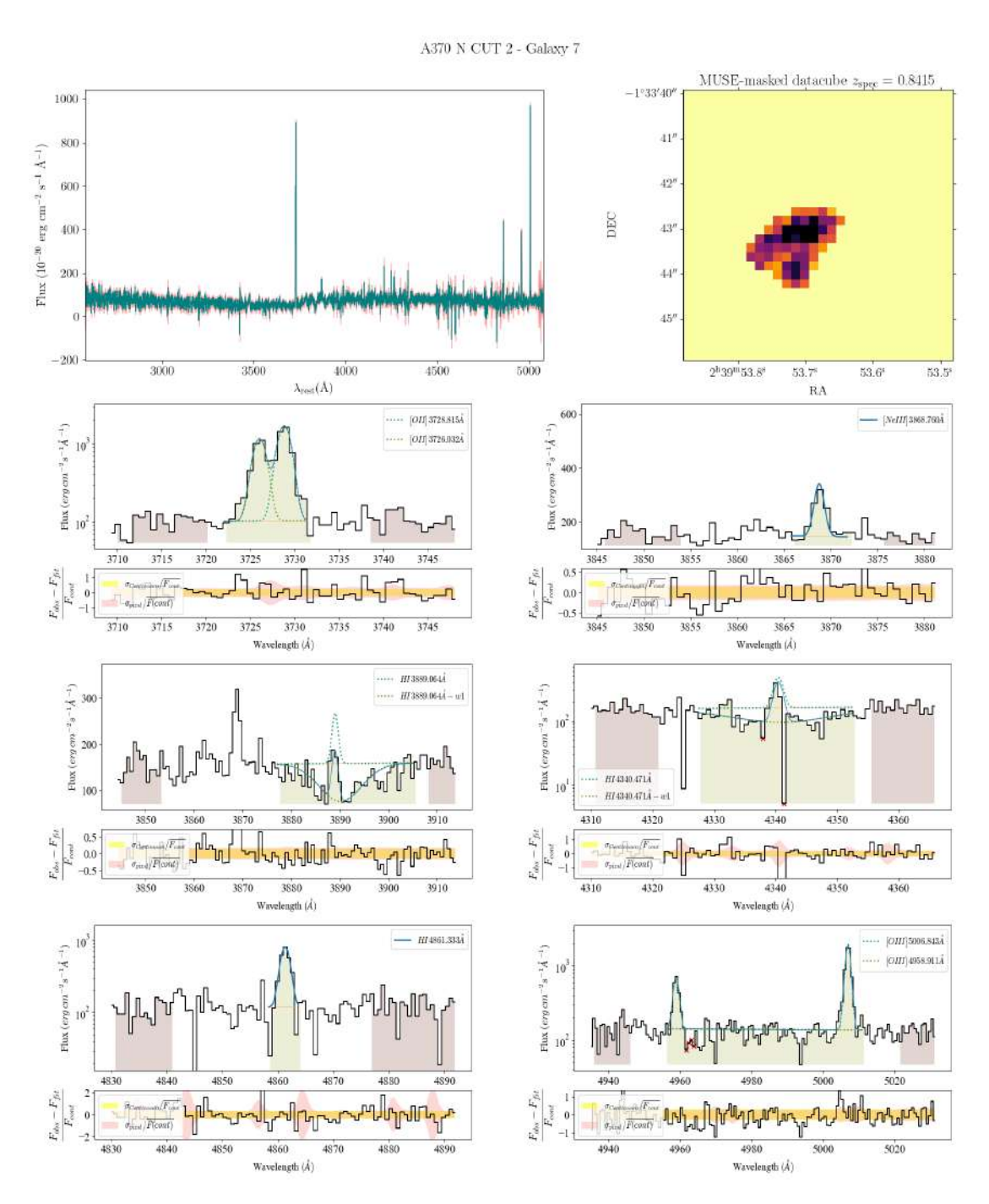


Figure A.14: Main emission lines fitted for DEEPSPACE ID 5165.

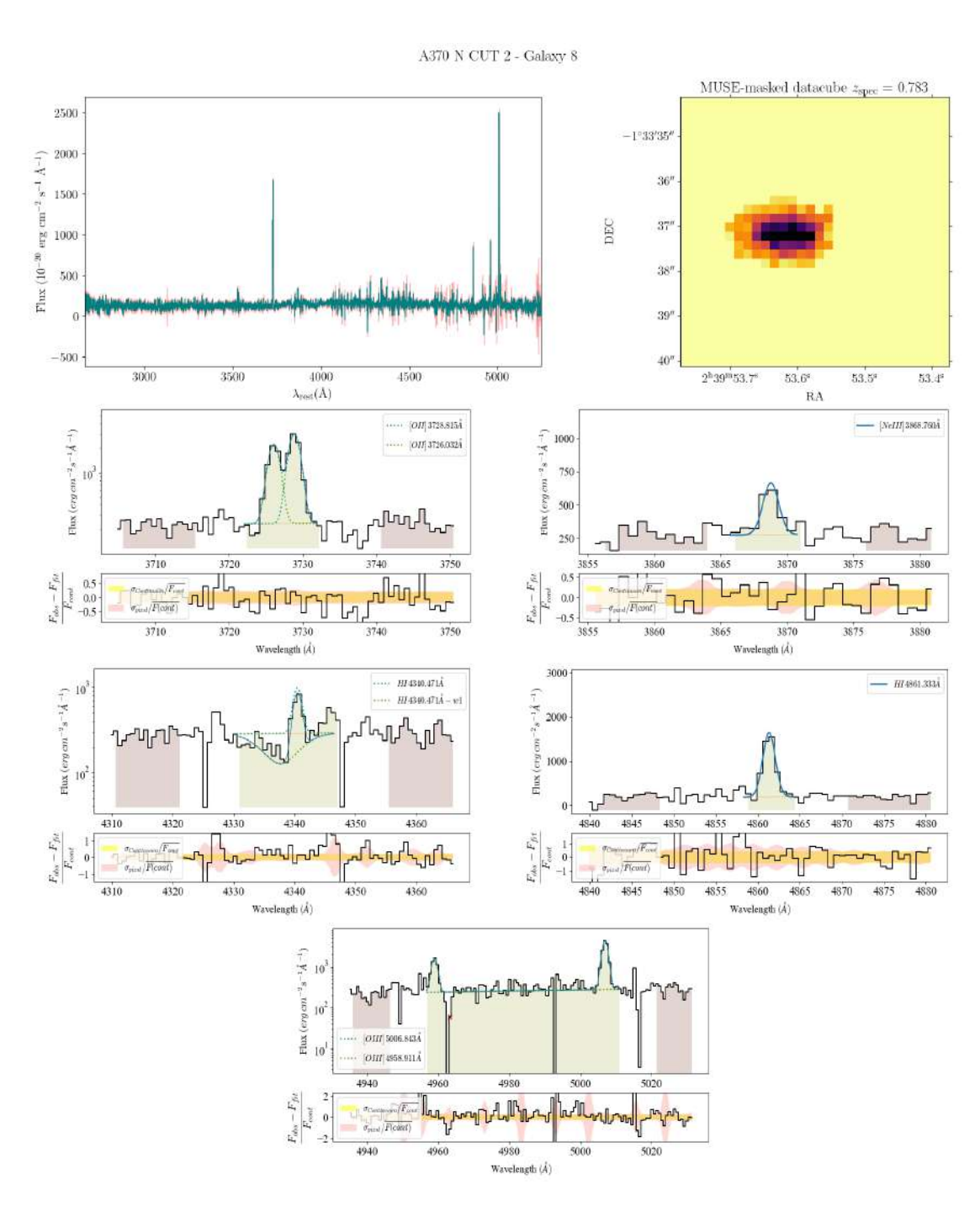


Figure A.15: Main emission lines fitted for DEEPSPACE ID 5455.

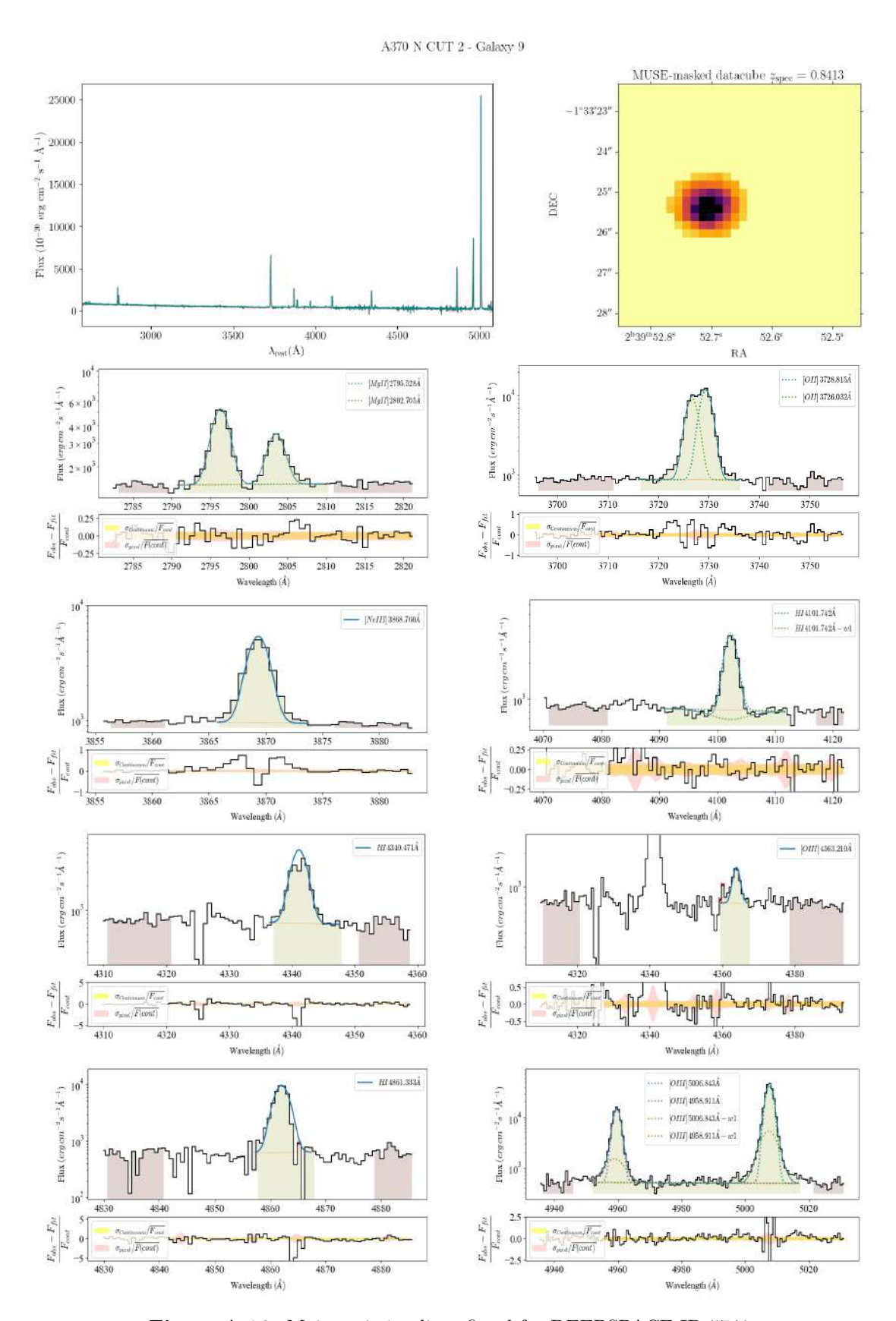


Figure A.16: Main emission lines fitted for DEEPSPACE ID 5741.

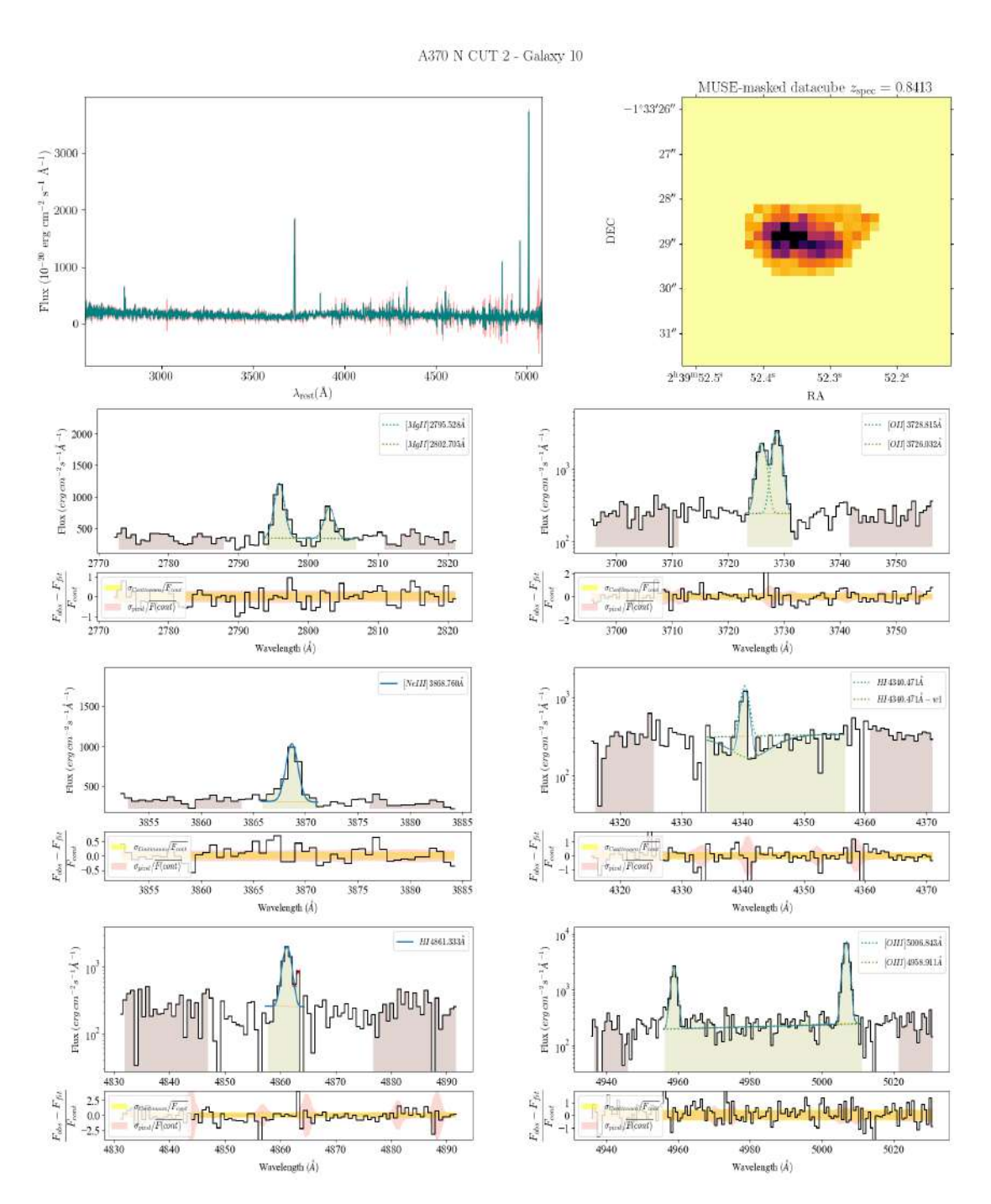


Figure A.17: Main emission lines fitted for DEEPSPACE ID 5522.

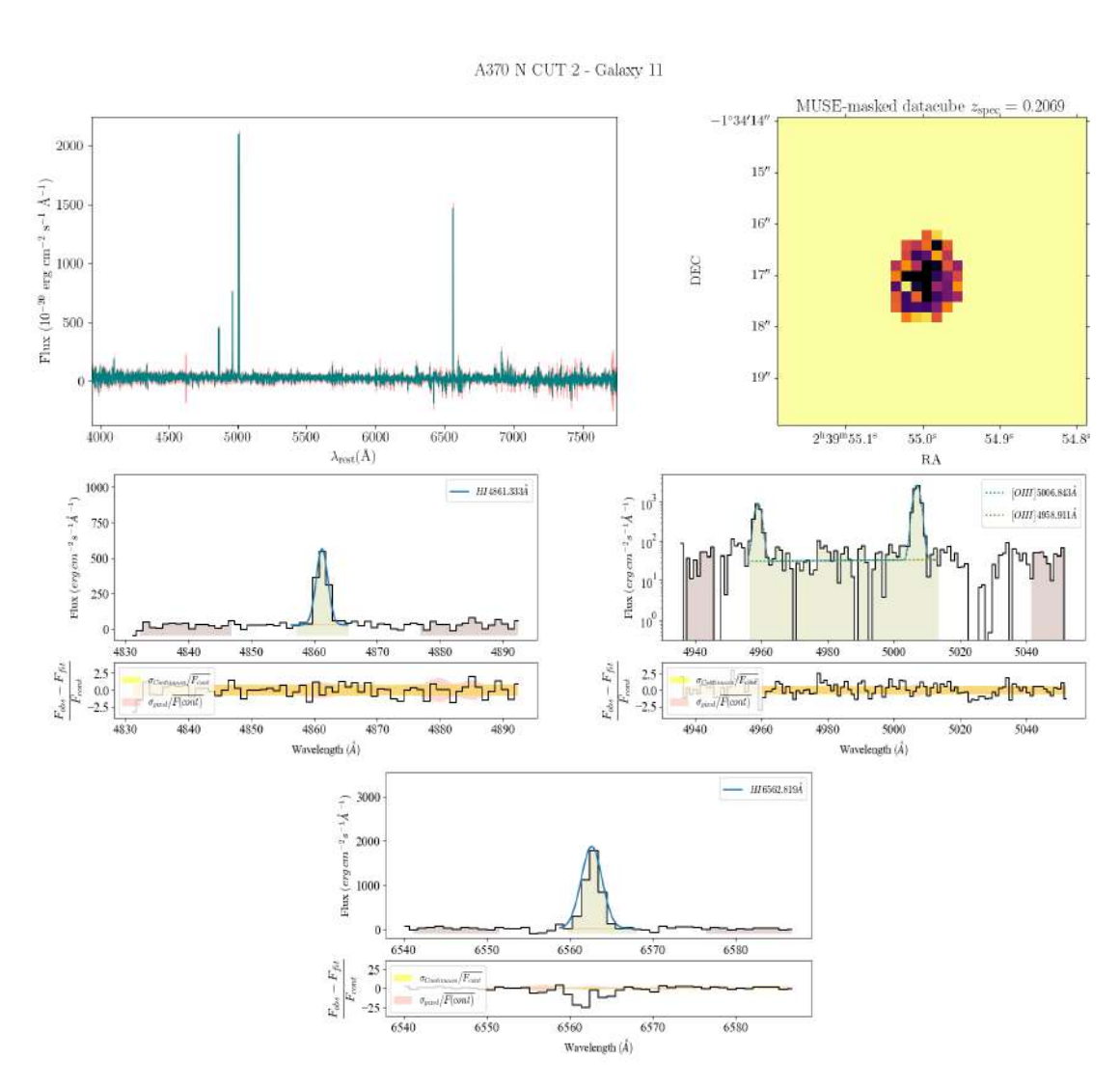


Figure A.18: Main emission lines fitted for DEEPSPACE ID 3910.

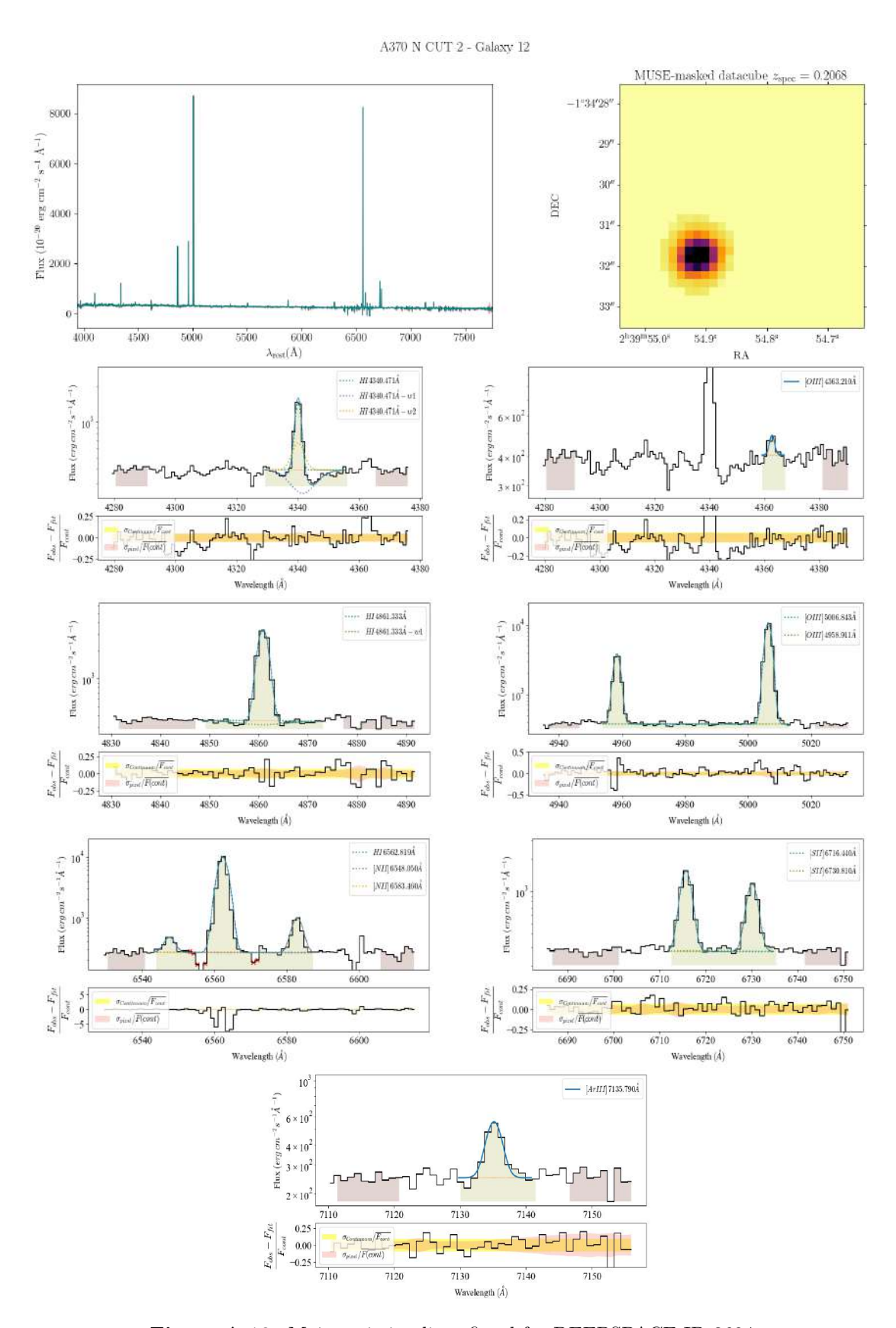


Figure A.19: Main emission lines fitted for DEEPSPACE ID 3684.

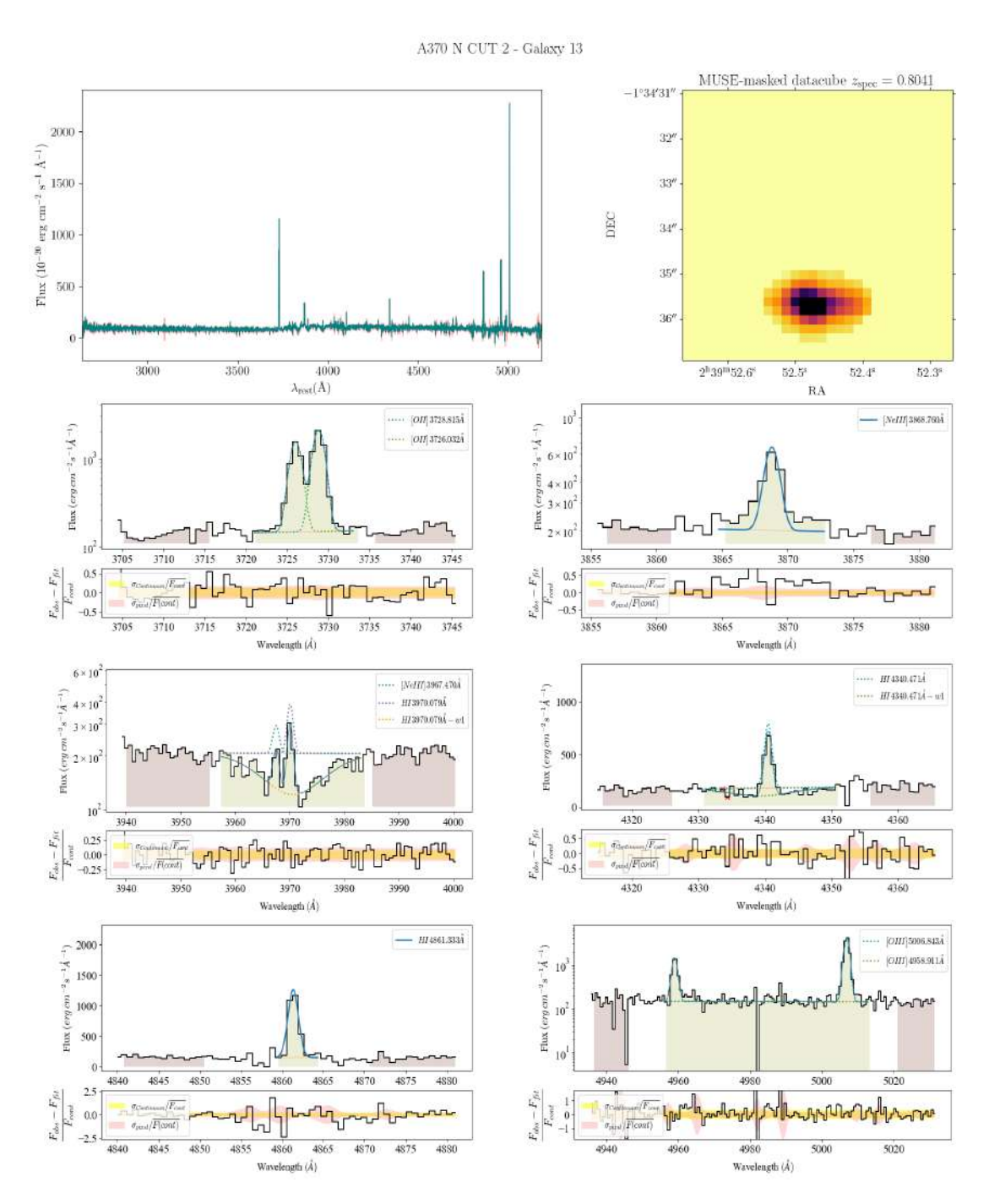


Figure A.20: Main emission lines fitted for DEEPSPACE ID 3392.

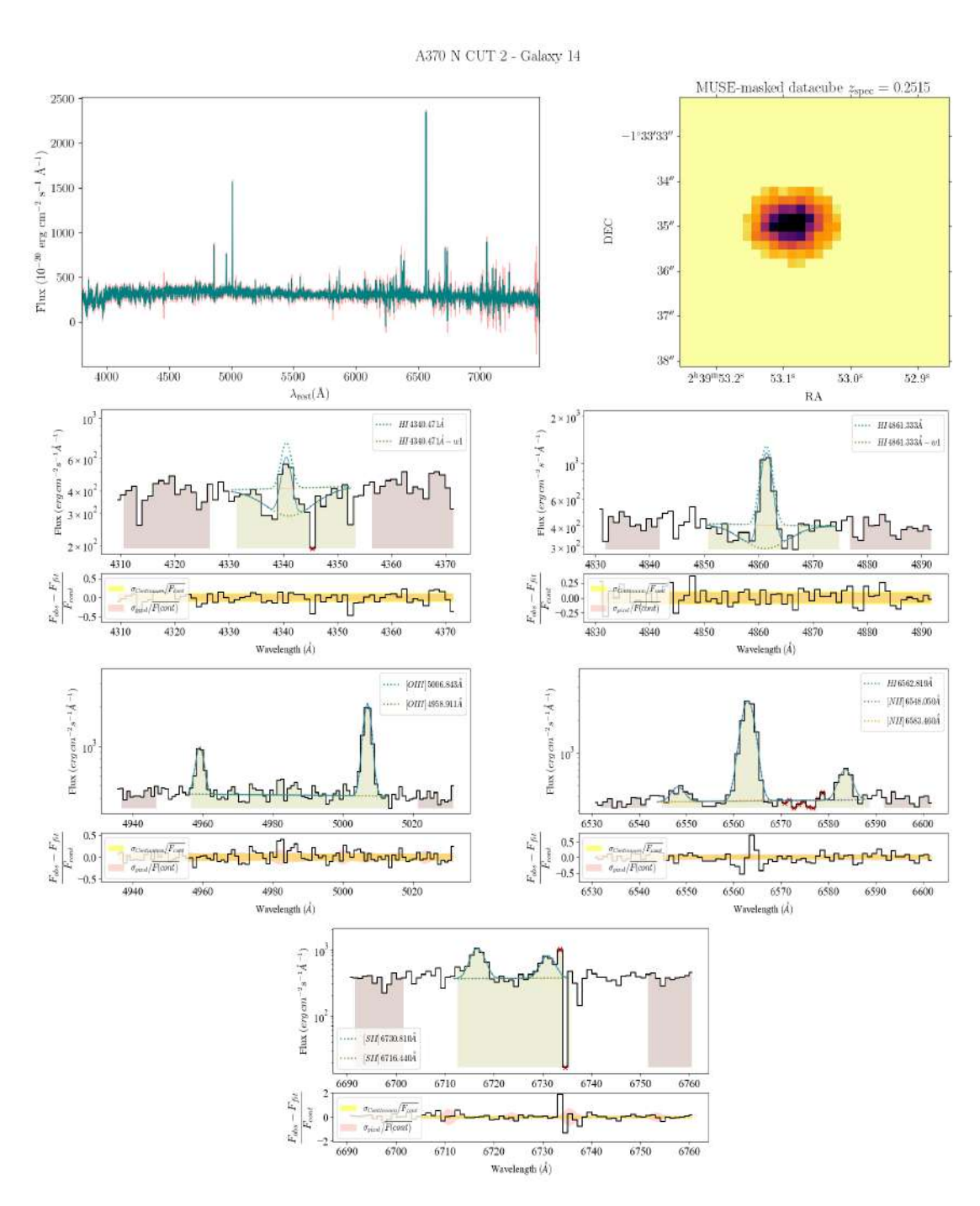


Figure A.21: Main emission lines fitted for DEEPSPACE ID 5407.

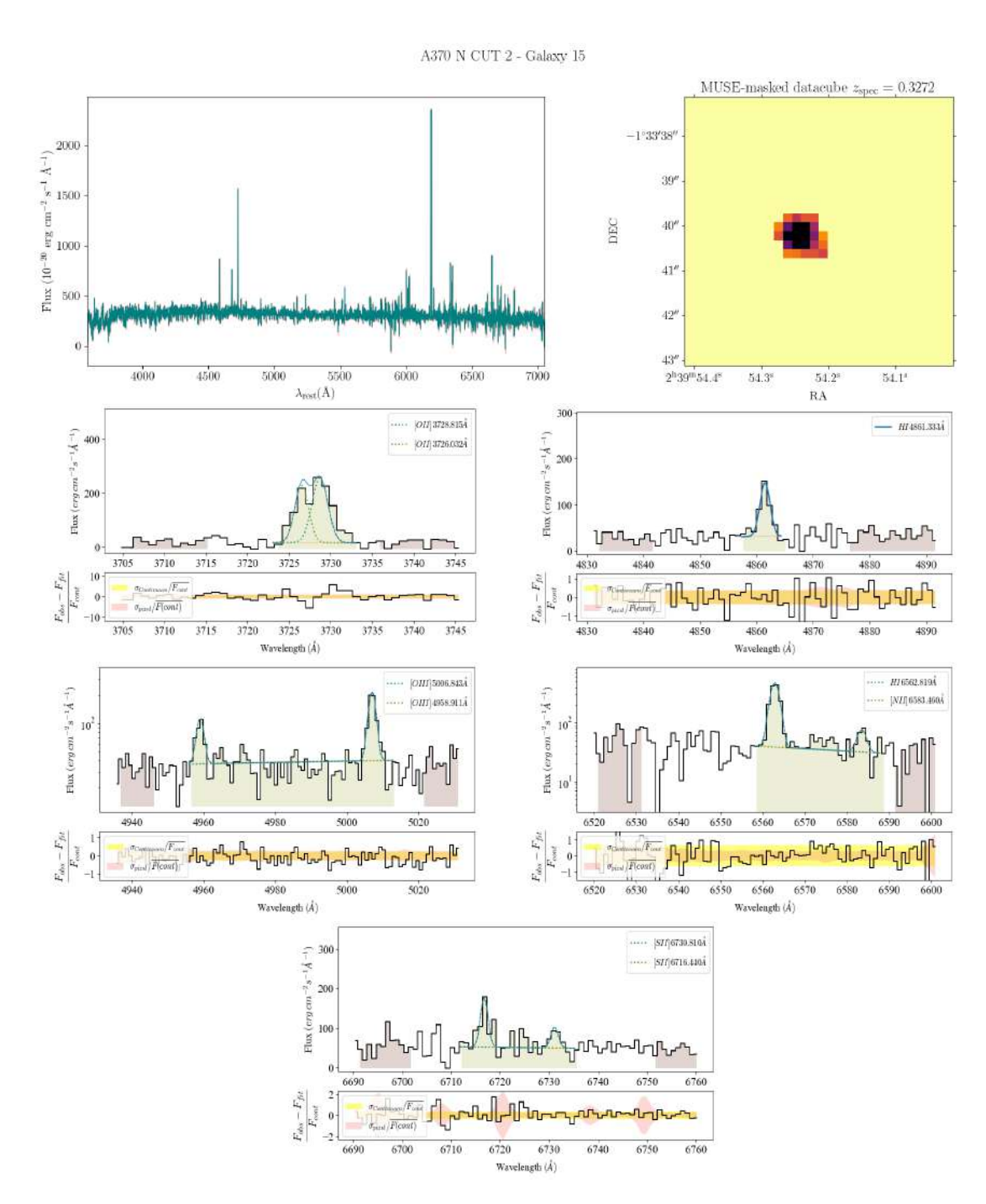


Figure A.22: Main emission lines fitted for DEEPSPACE ID 5271.

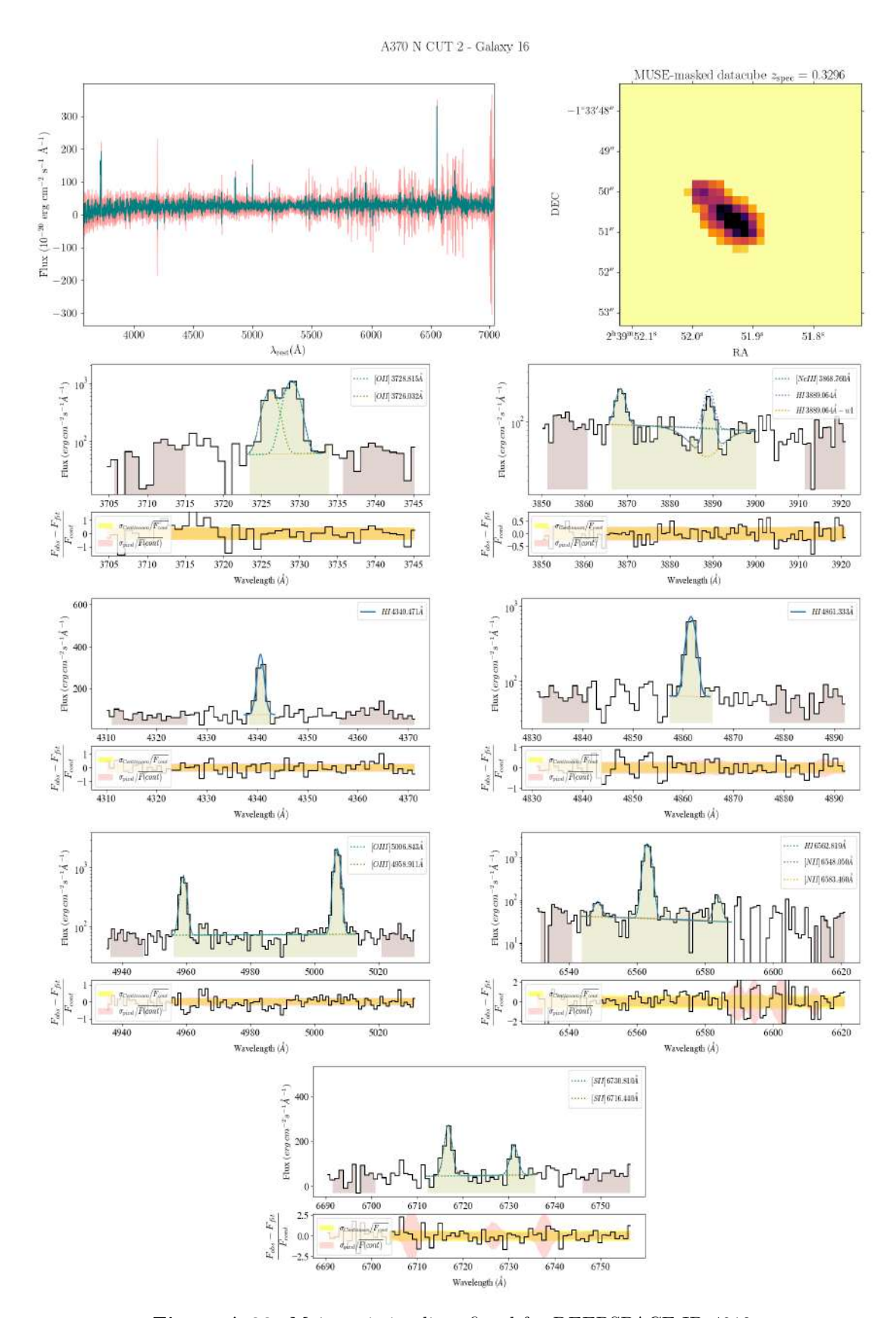


Figure A.23: Main emission lines fitted for DEEPSPACE ID 4912.

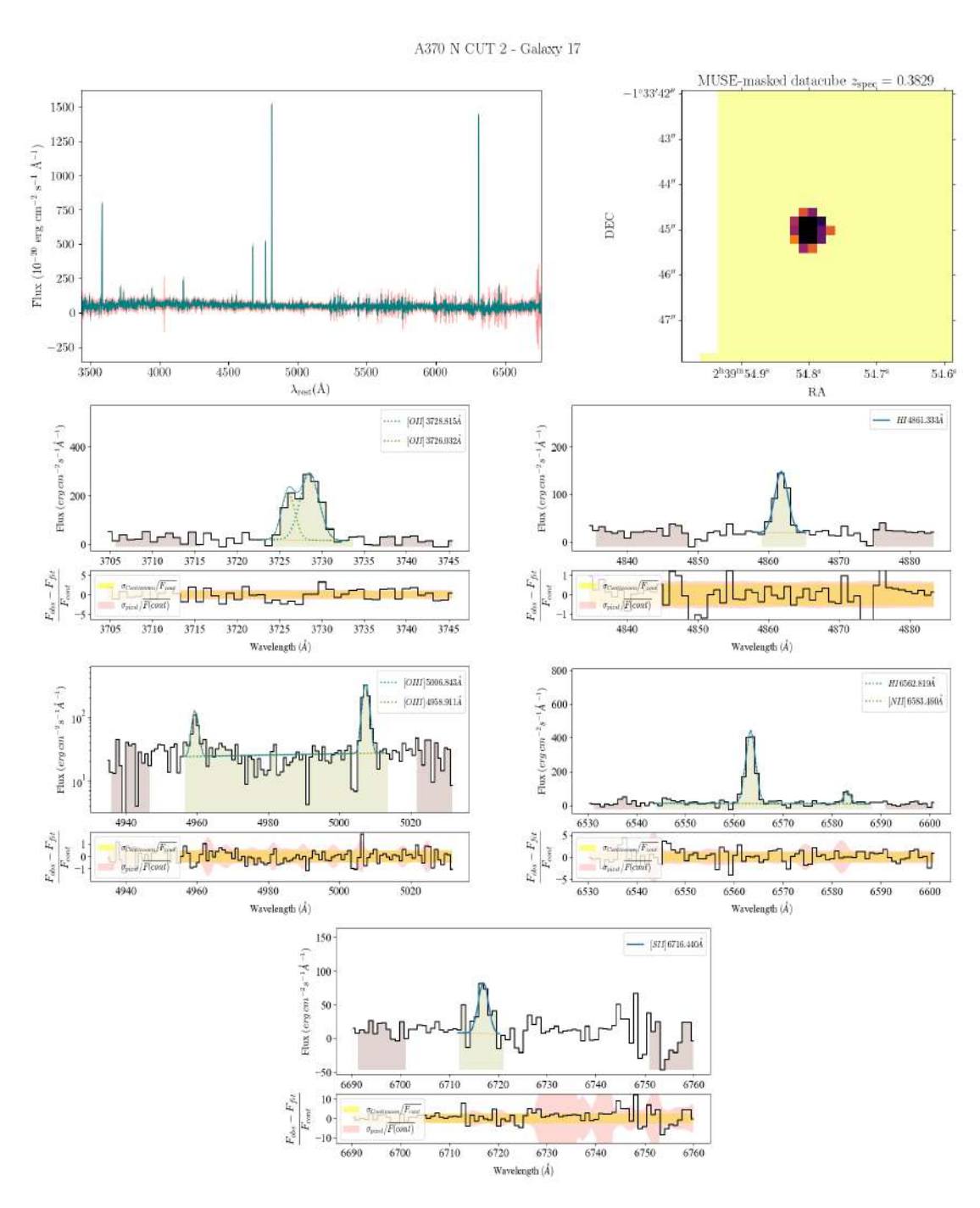


Figure A.24: Main emission lines fitted for DEEPSPACE ID 5041.

### A.3 A370 N CUT 3

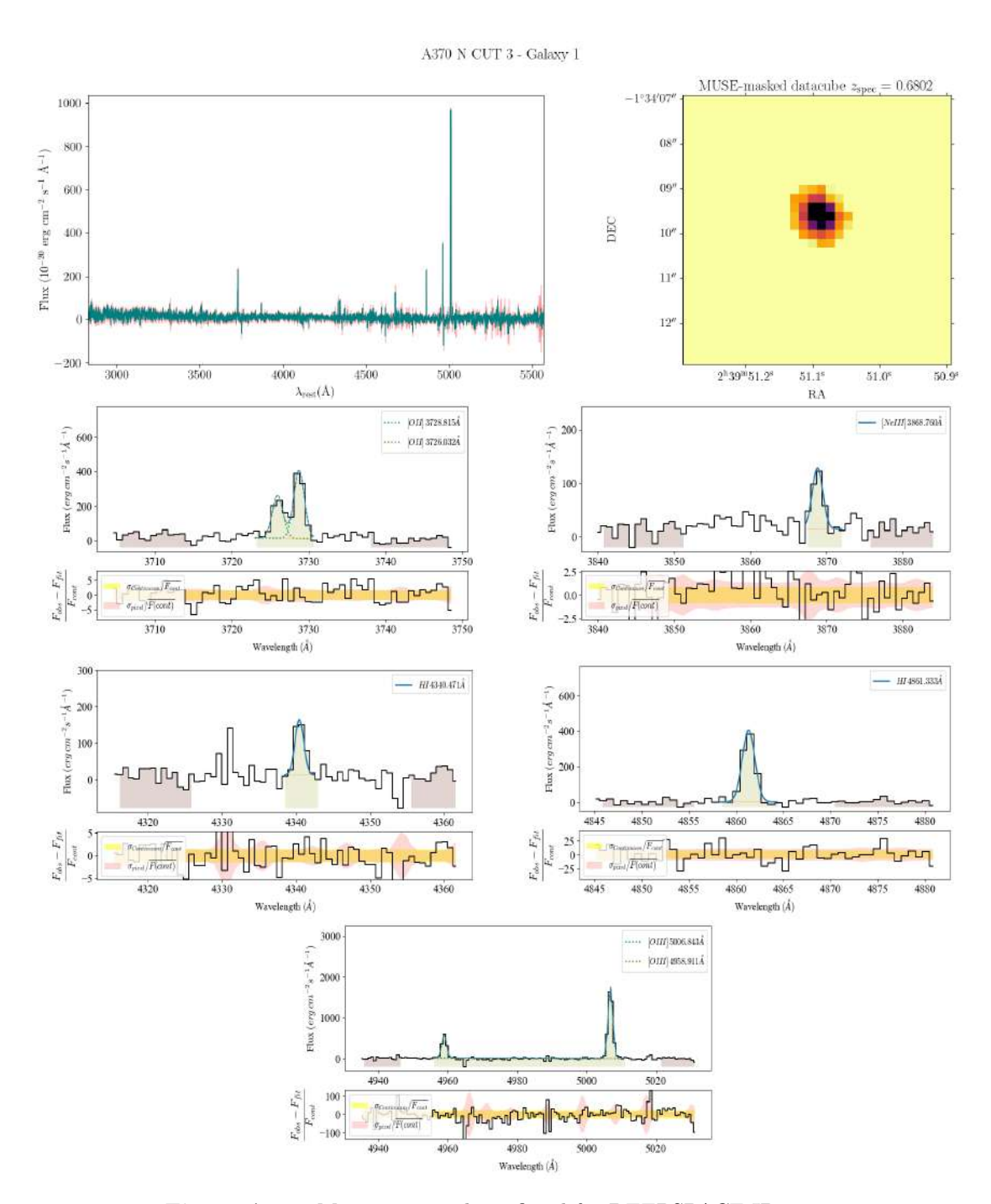


Figure A.25: Main emission lines fitted for DEEPSPACE ID 4284.

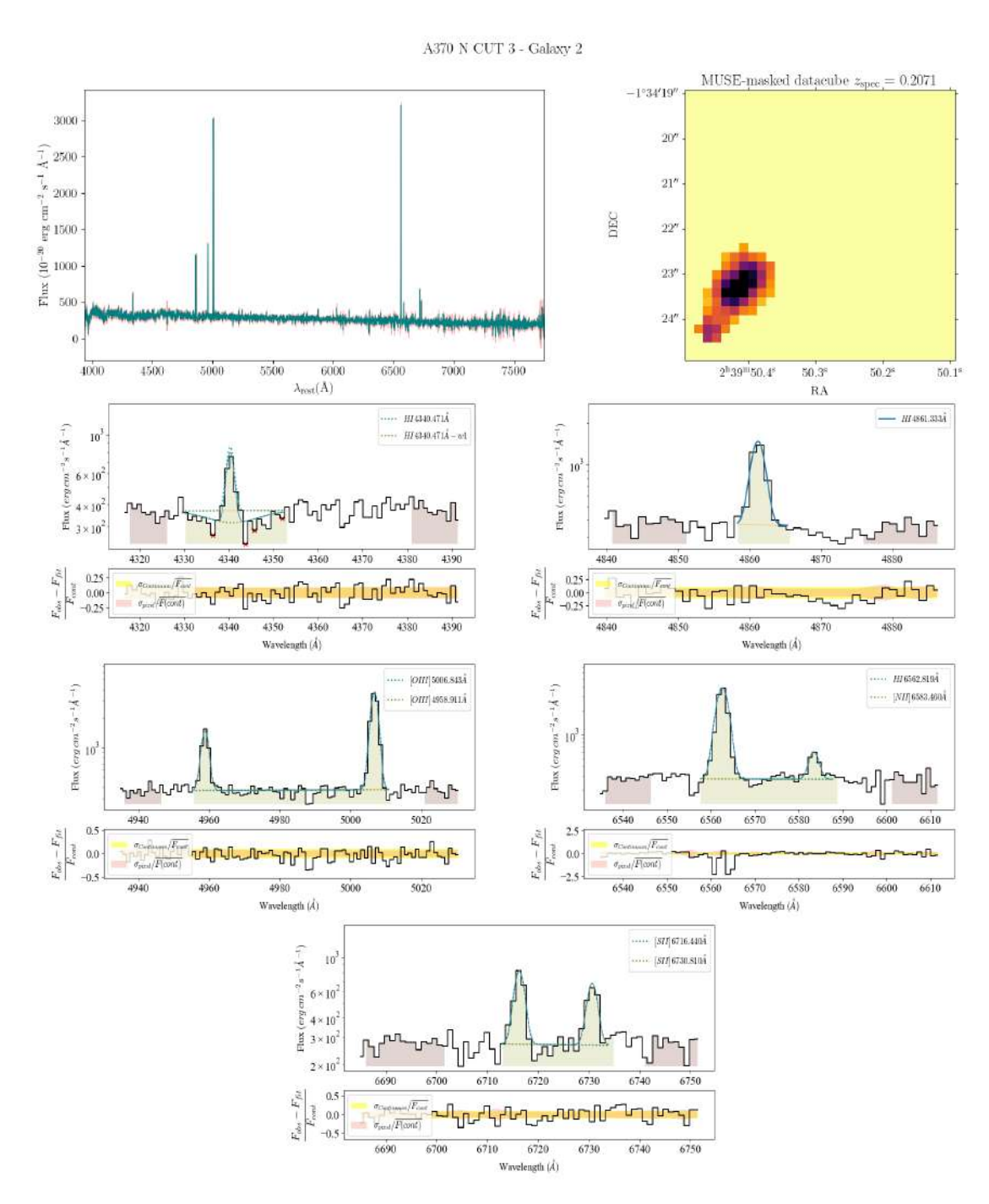


Figure A.26: Main emission lines fitted for DEEPSPACE ID 4031.

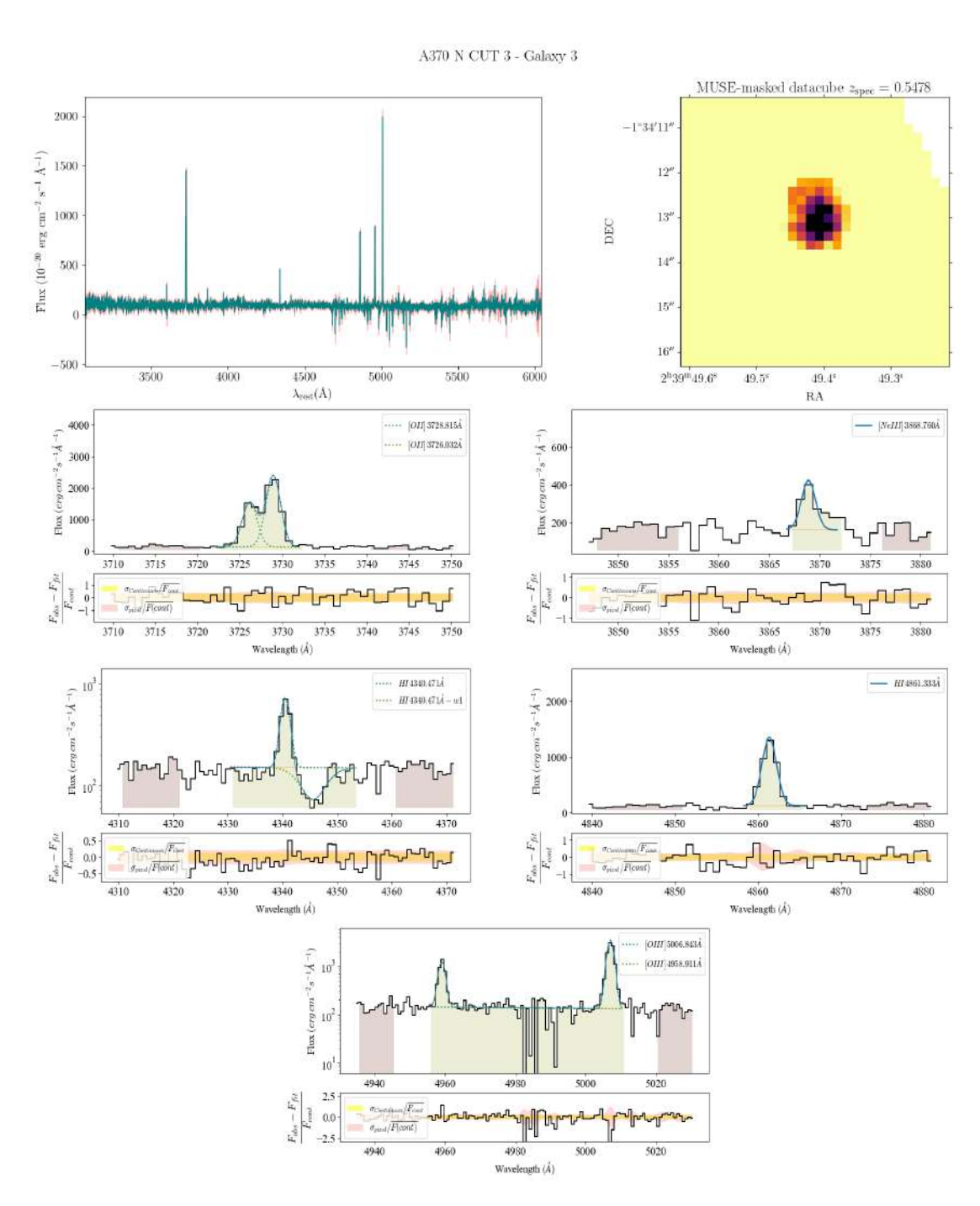


Figure A.27: Main emission lines fitted for DEEPSPACE ID 4321.

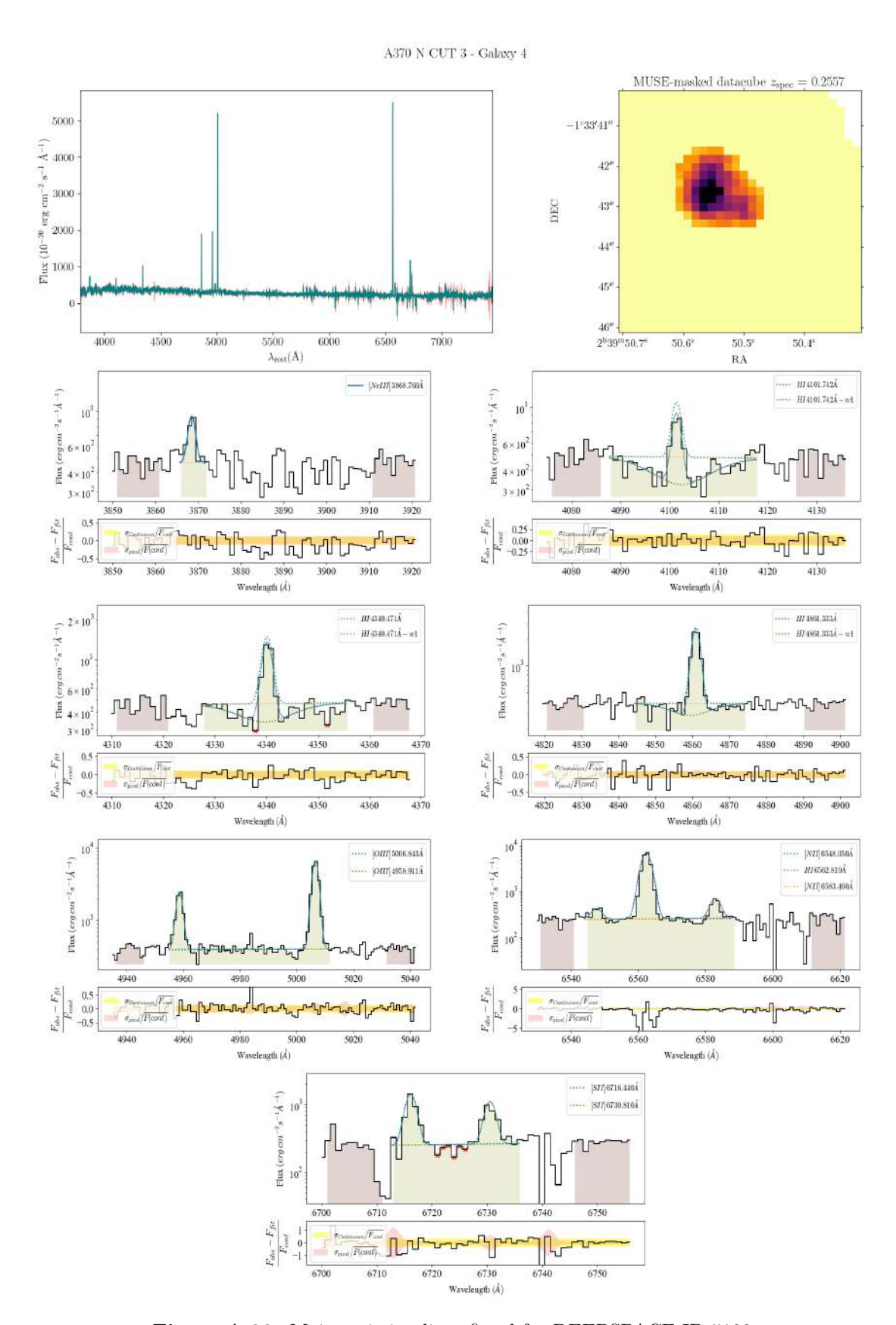


Figure A.28: Main emission lines fitted for DEEPSPACE ID 5199.

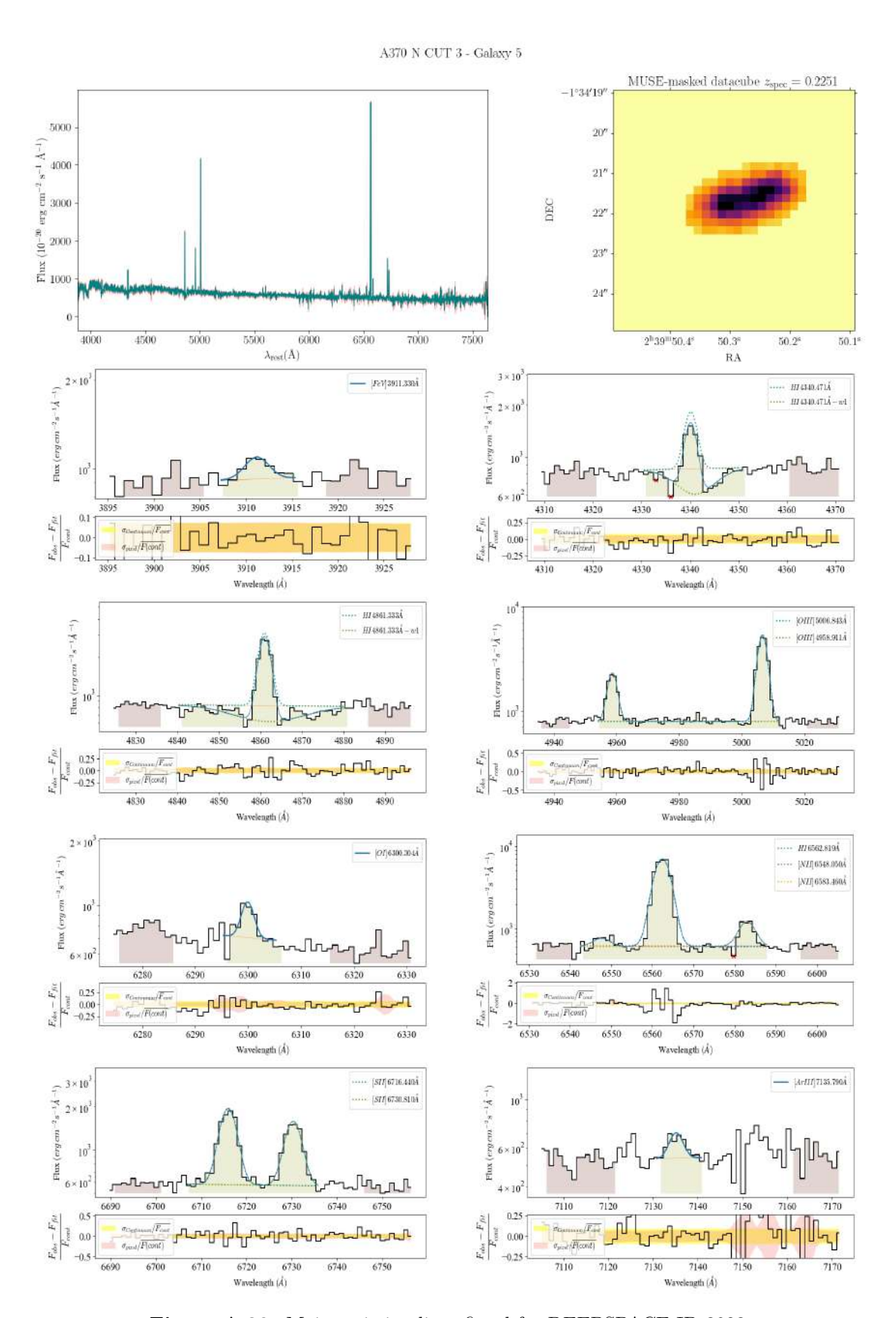


Figure A.29: Main emission lines fitted for DEEPSPACE ID 3923.

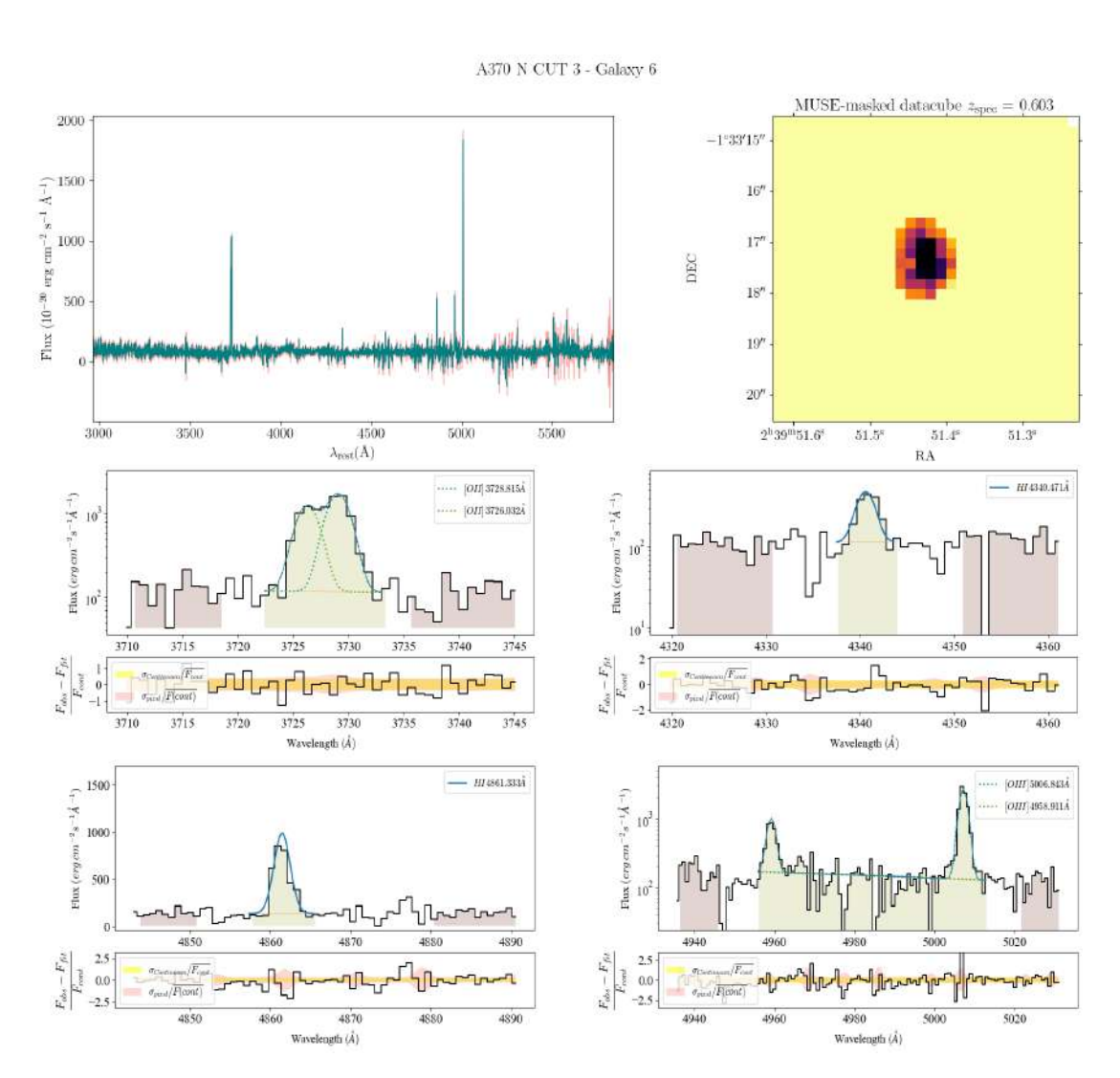


Figure A.30: Main emission lines fitted for DEEPSPACE ID 5915.

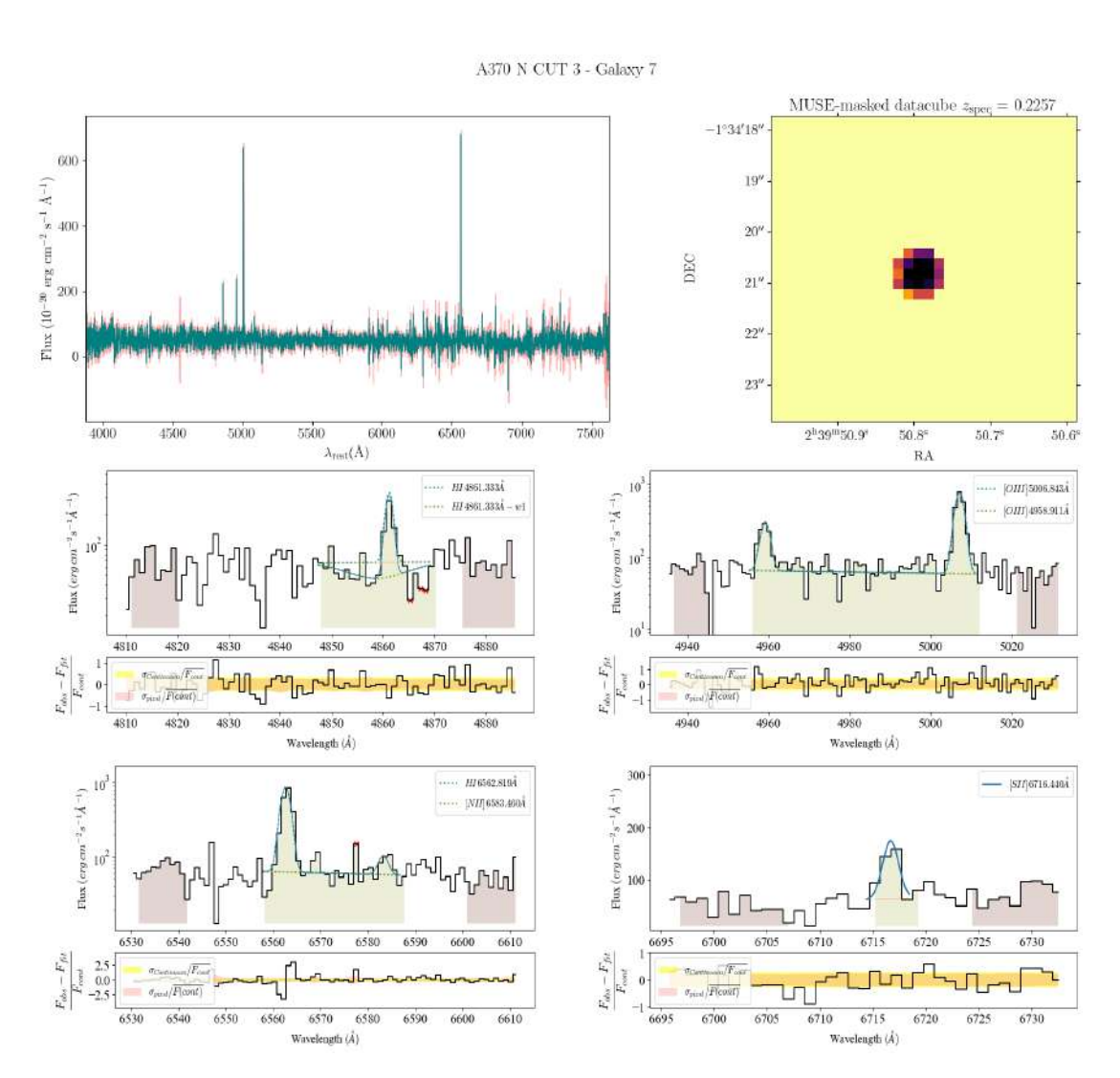


Figure A.31: Main emission lines fitted for DEEPSPACE ID 3906.

## A.4 A370 S CUT 1

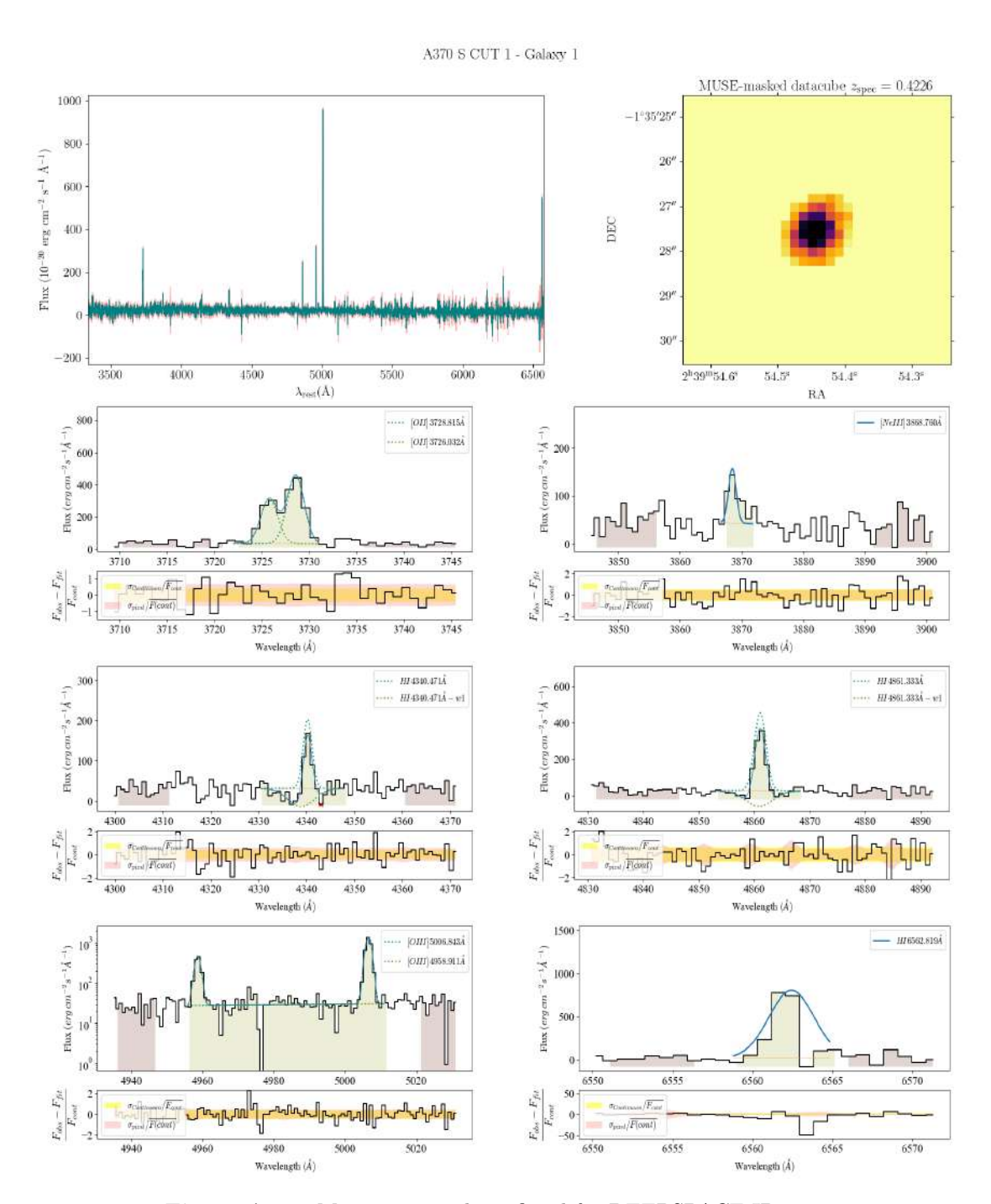


Figure A.32: Main emission lines fitted for DEEPSPACE ID 1602.

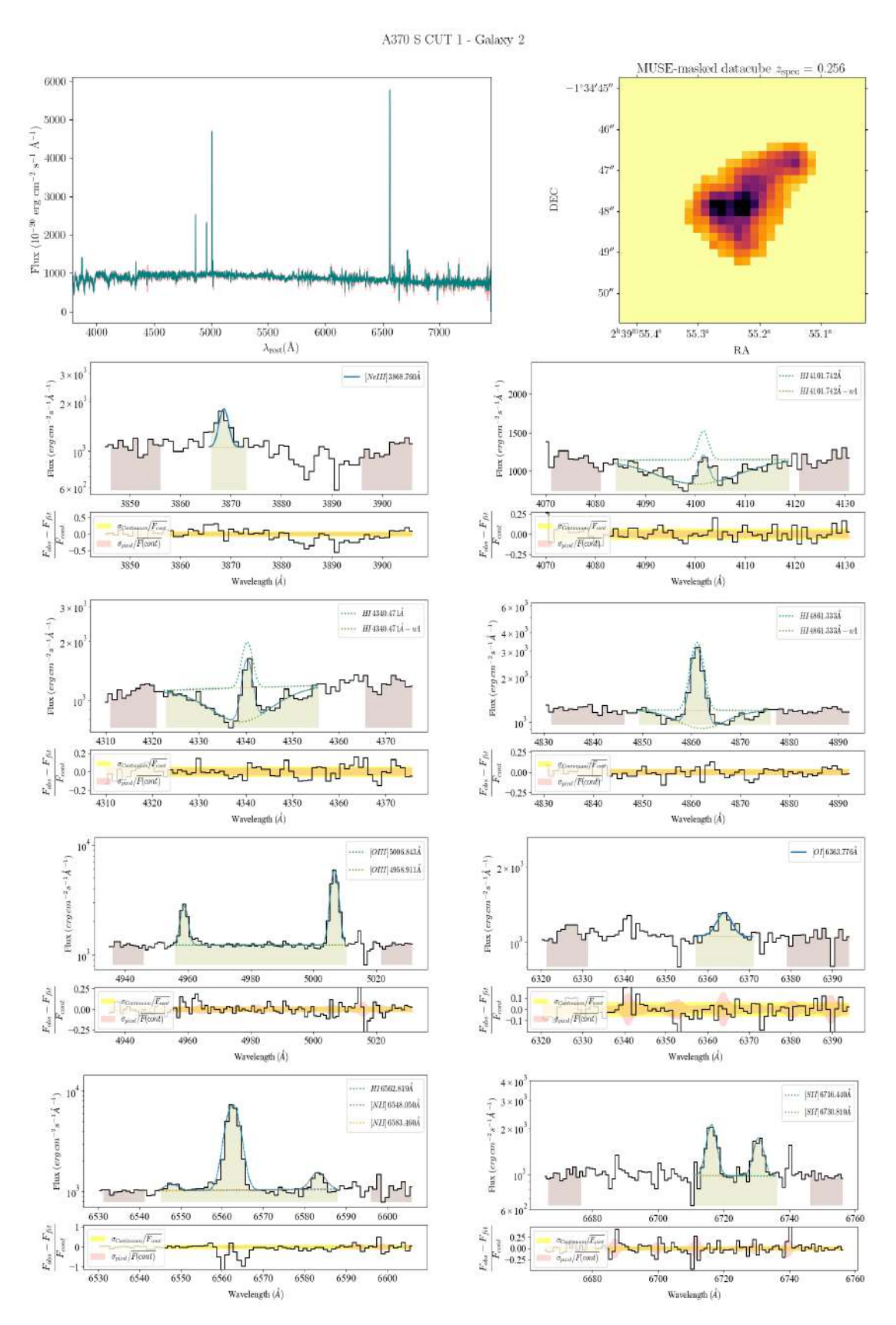


Figure A.33: Main emission lines fitted for DEEPSPACE ID 2807.

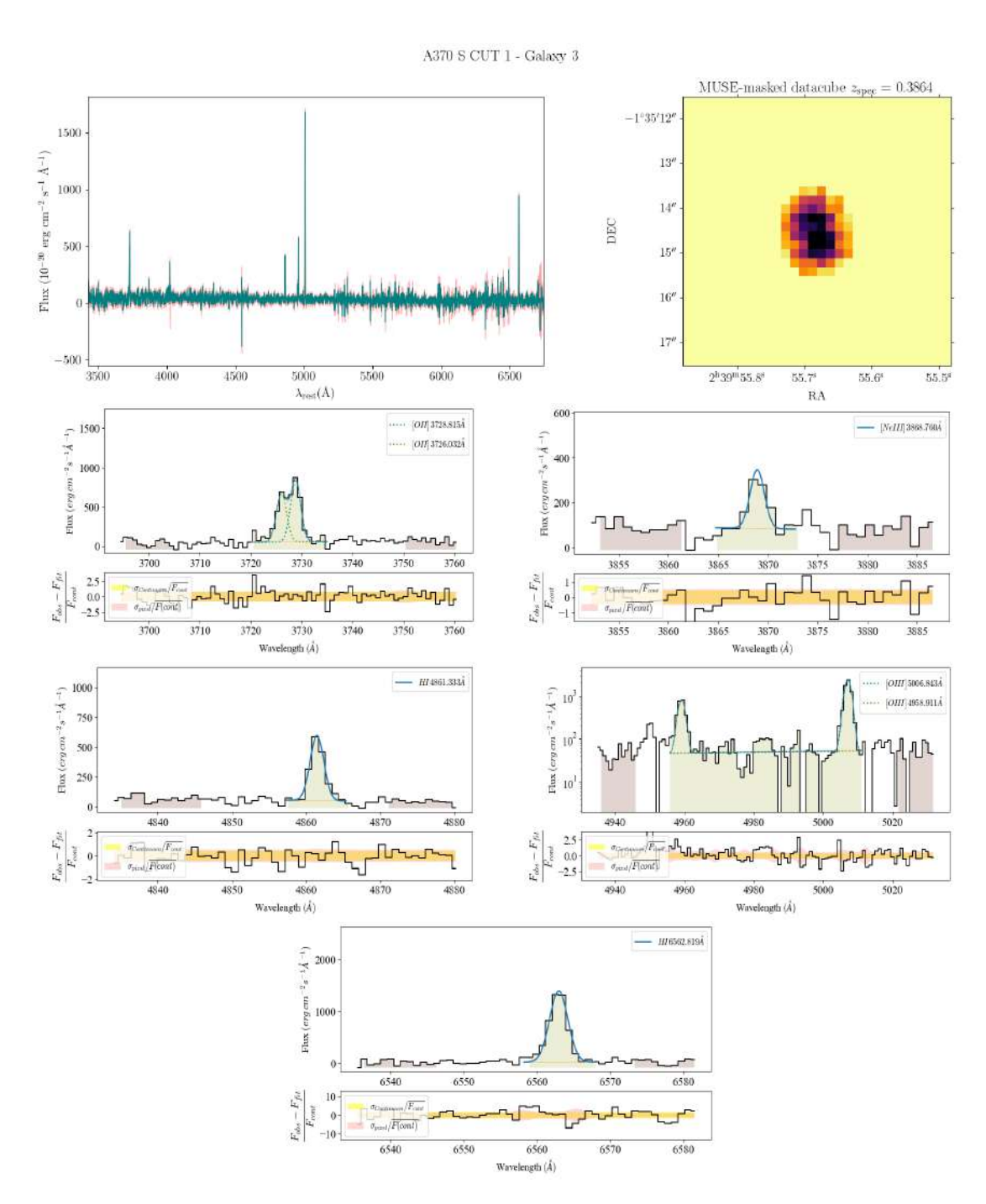


Figure A.34: Main emission lines fitted for DEEPSPACE ID 2002.

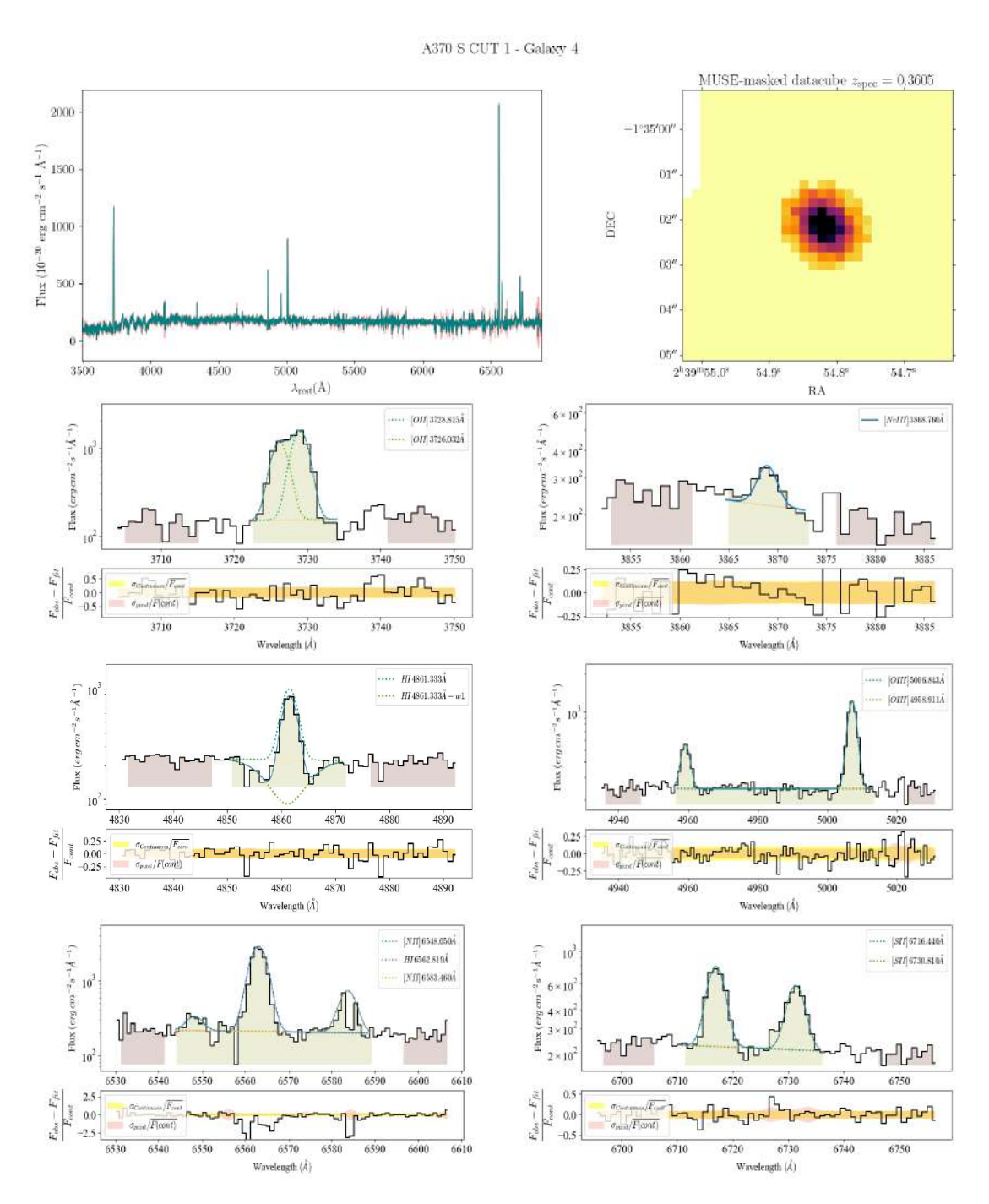


Figure A.35: Main emission lines fitted for DEEPSPACE ID 2441.

## A.5 A370 S CUT 2

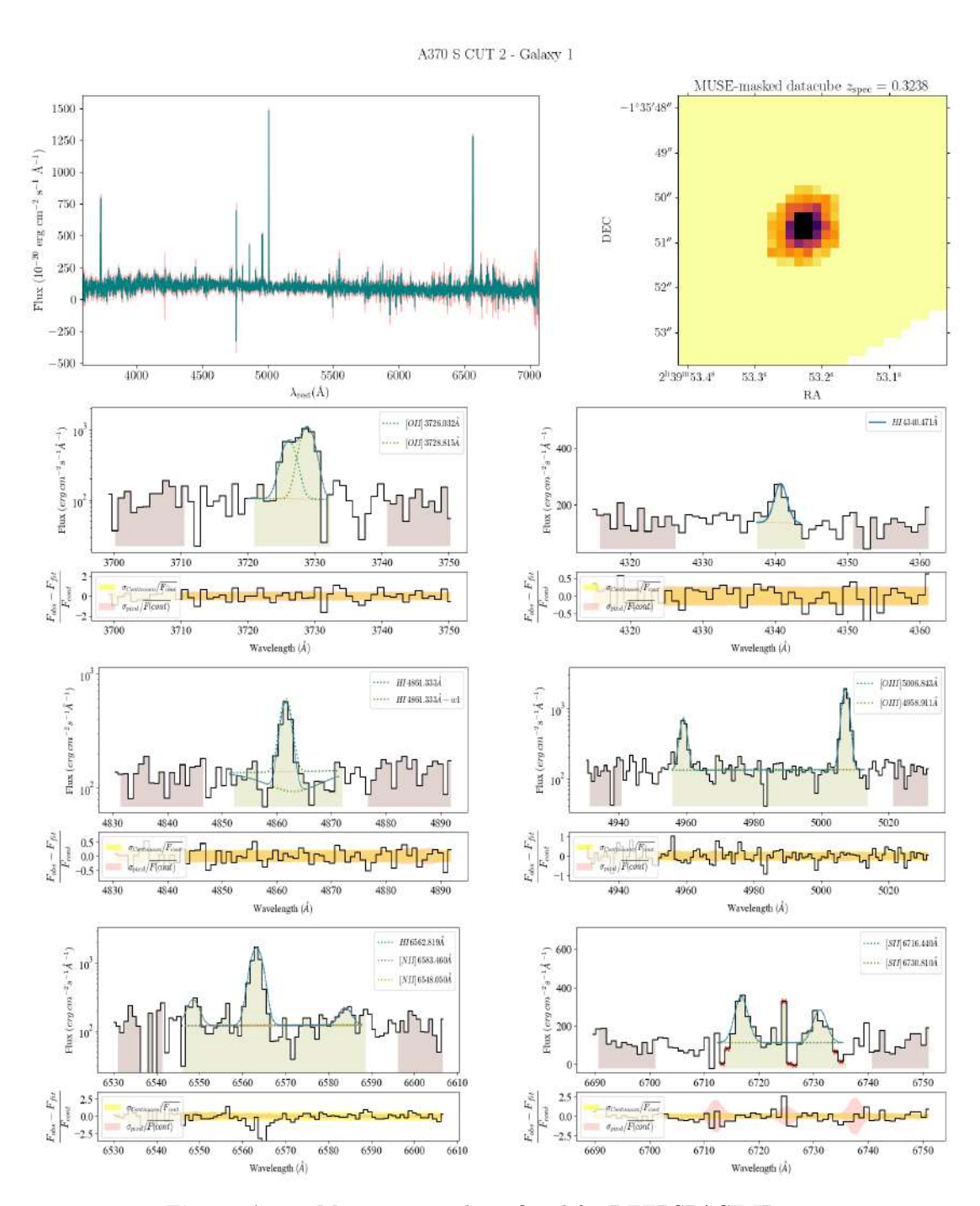


Figure A.36: Main emission lines fitted for DEEPSPACE ID 998.

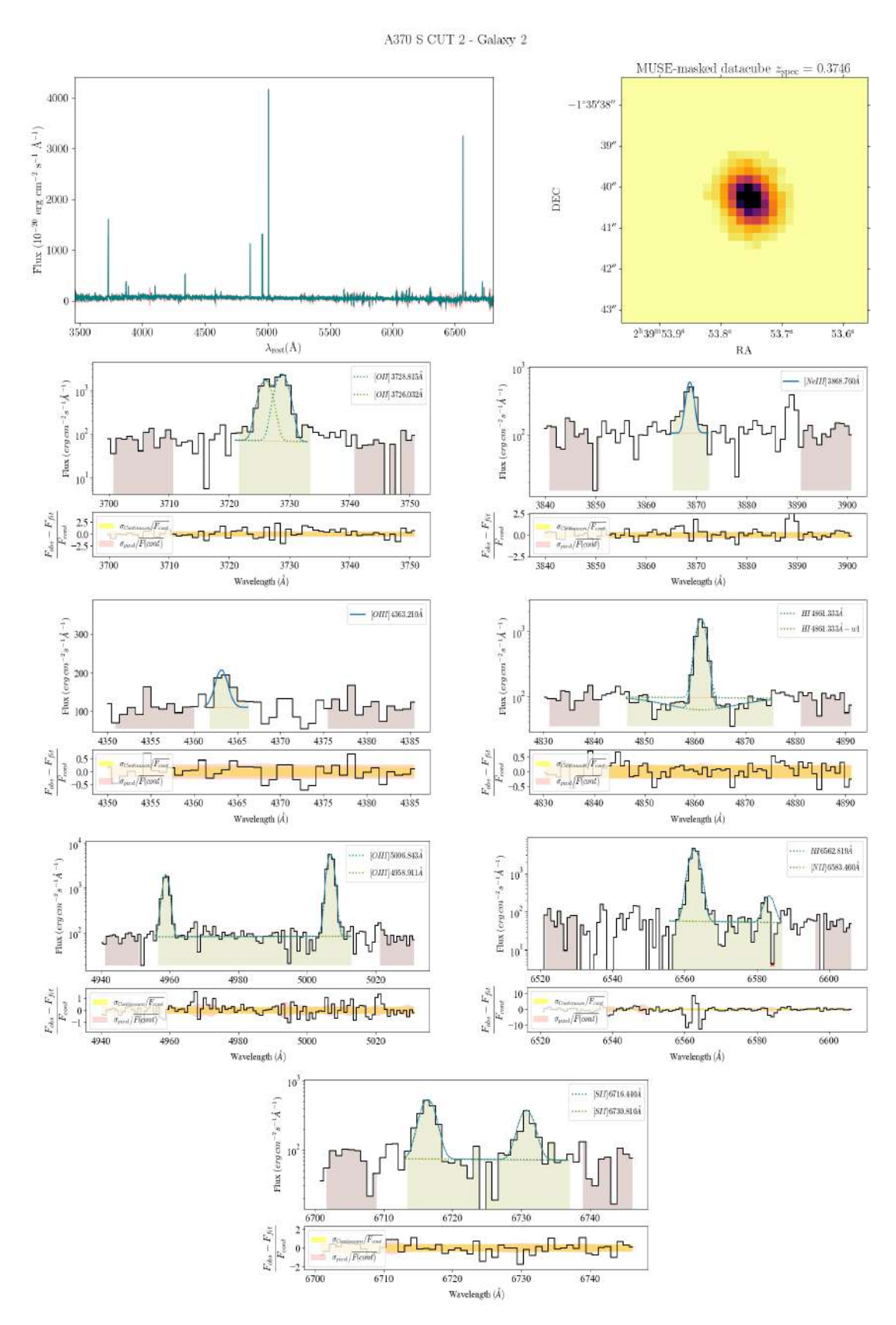


Figure A.37: Main emission lines fitted for DEEPSPACE ID 1247.

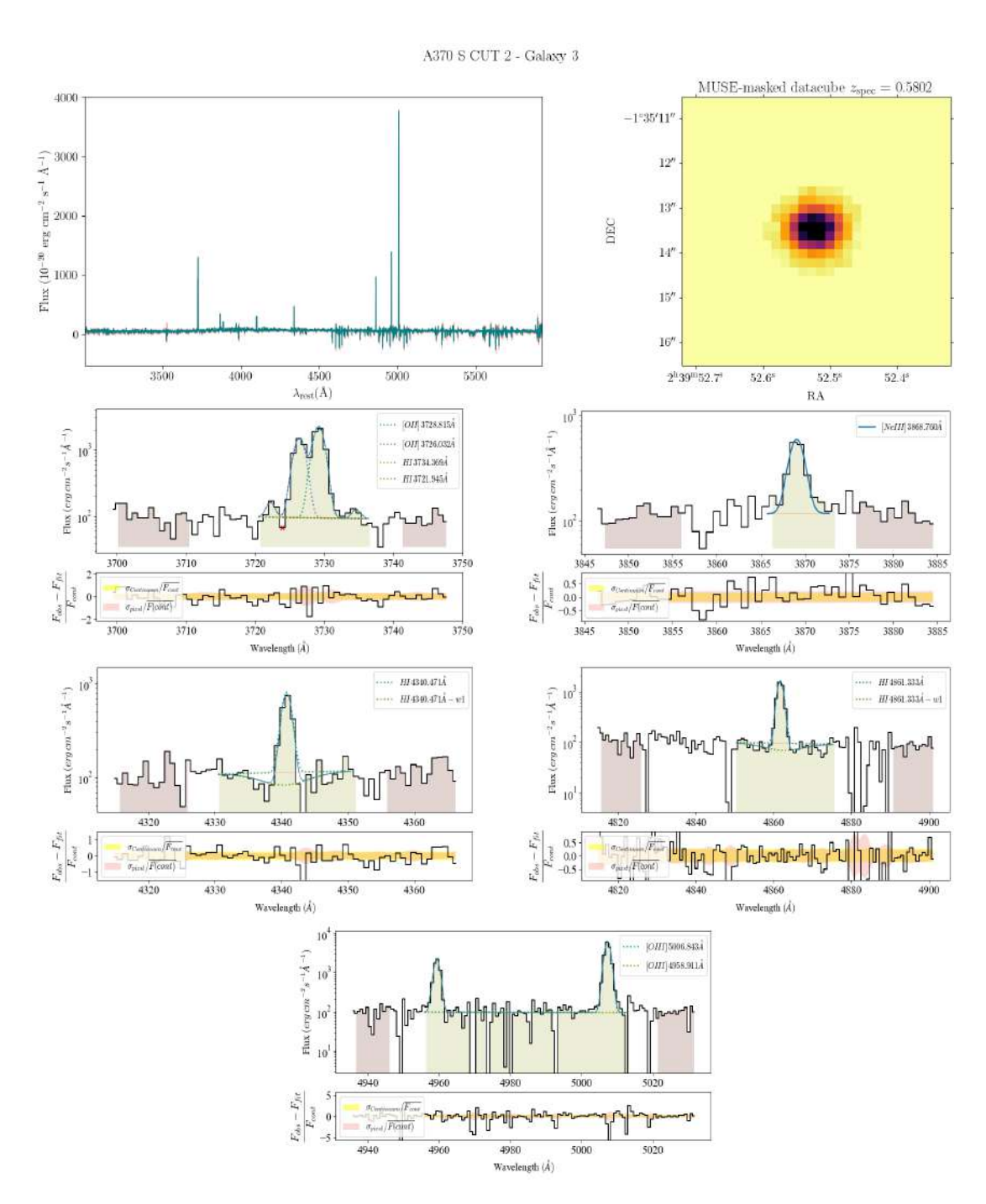


Figure A.38: Main emission lines fitted for DEEPSPACE ID 1989.

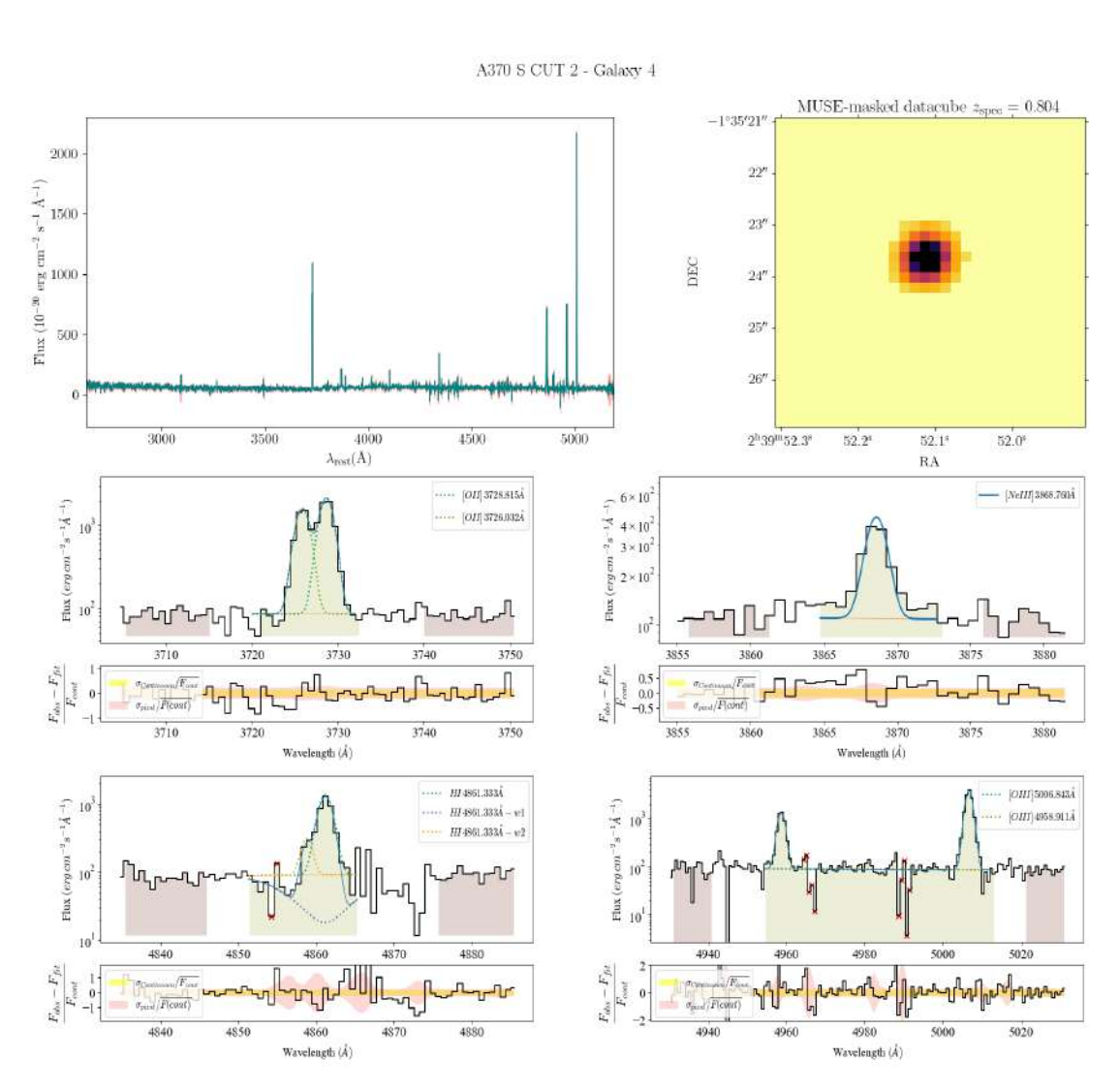


Figure A.39: Main emission lines fitted for DEEPSPACE ID 1666.

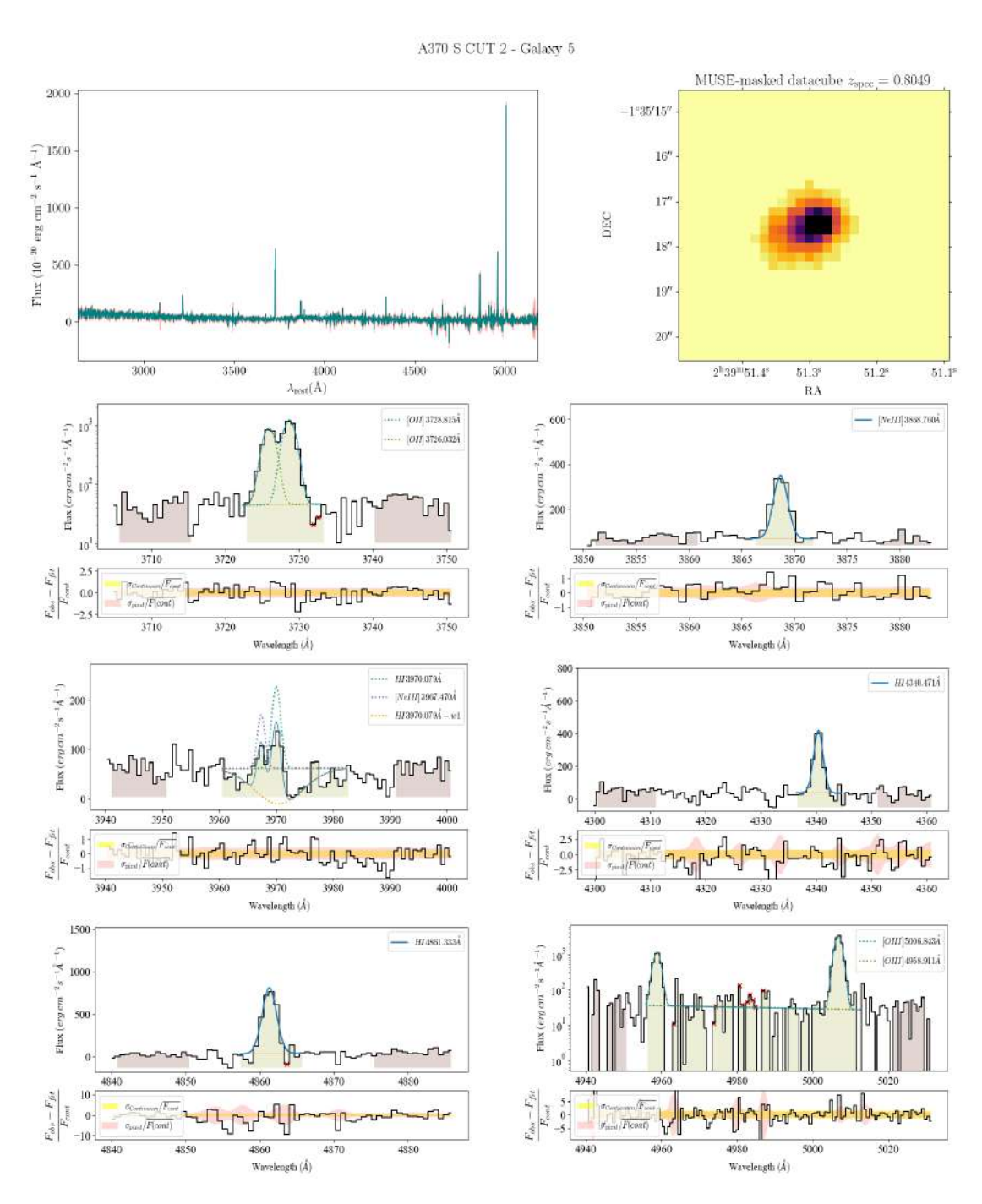


Figure A.40: Main emission lines fitted for DEEPSPACE ID 1857.

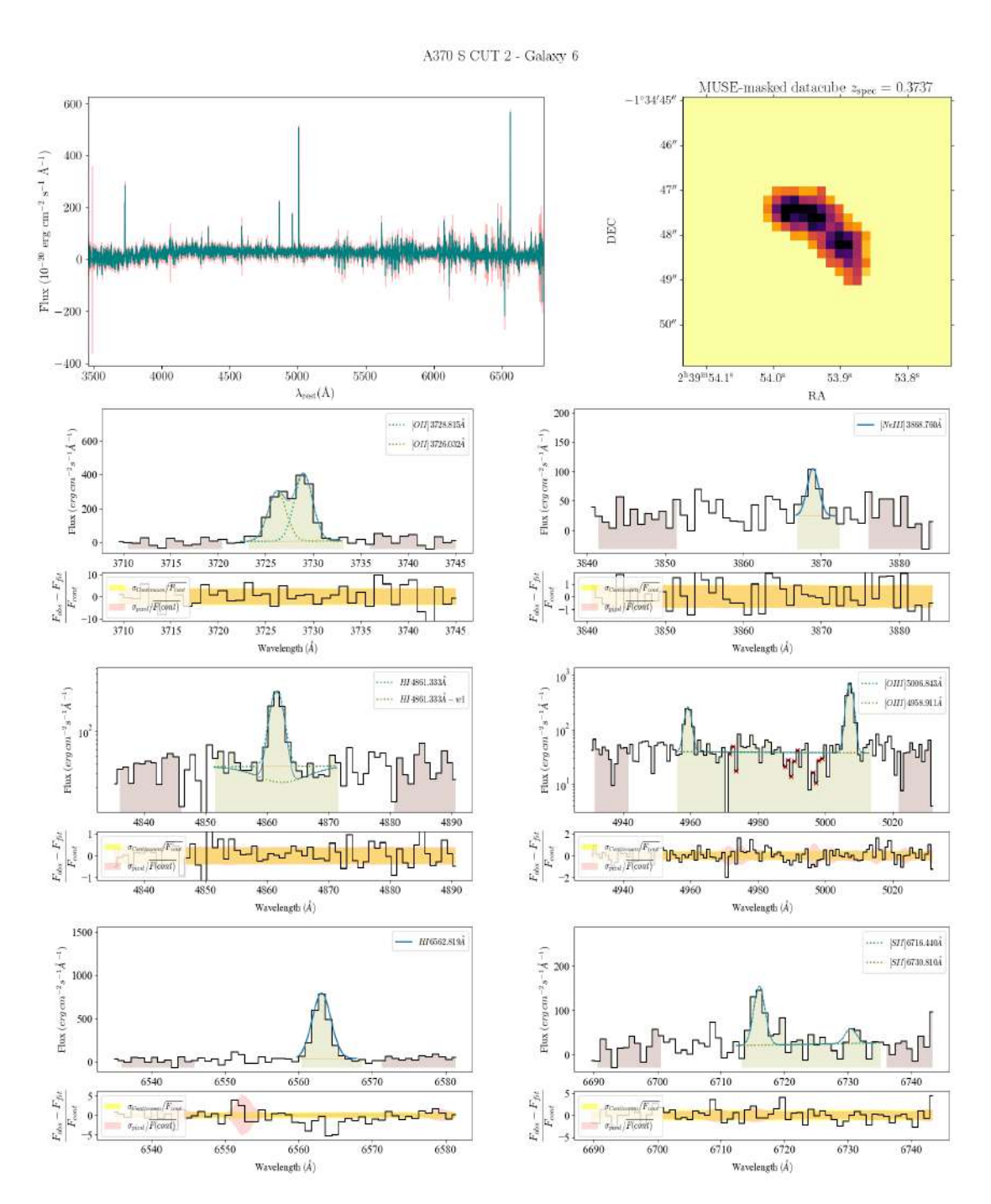


Figure A.41: Main emission lines fitted for DEEPSPACE ID 2753.

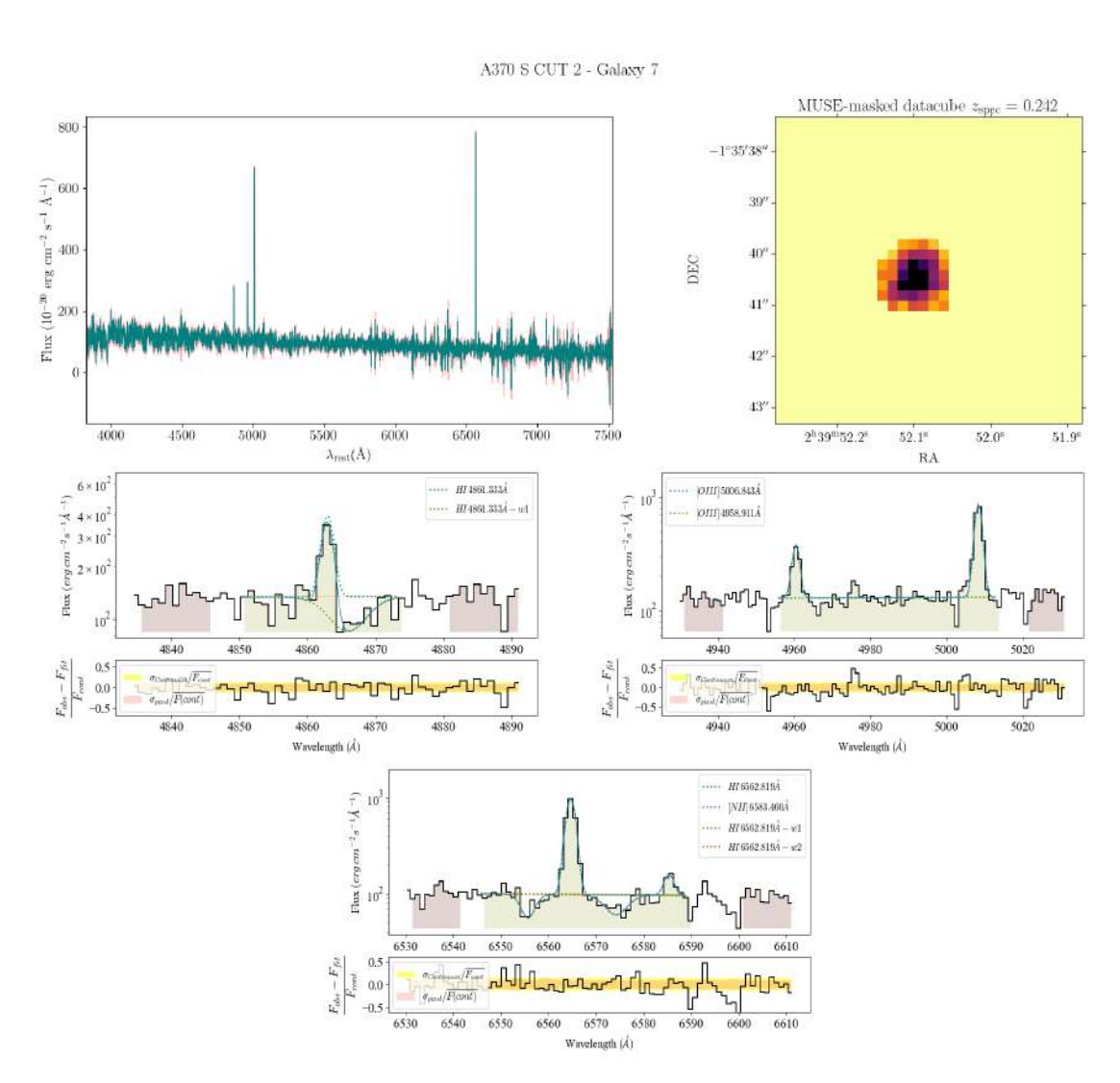


Figure A.42: Main emission lines fitted for DEEPSPACE ID 1227.

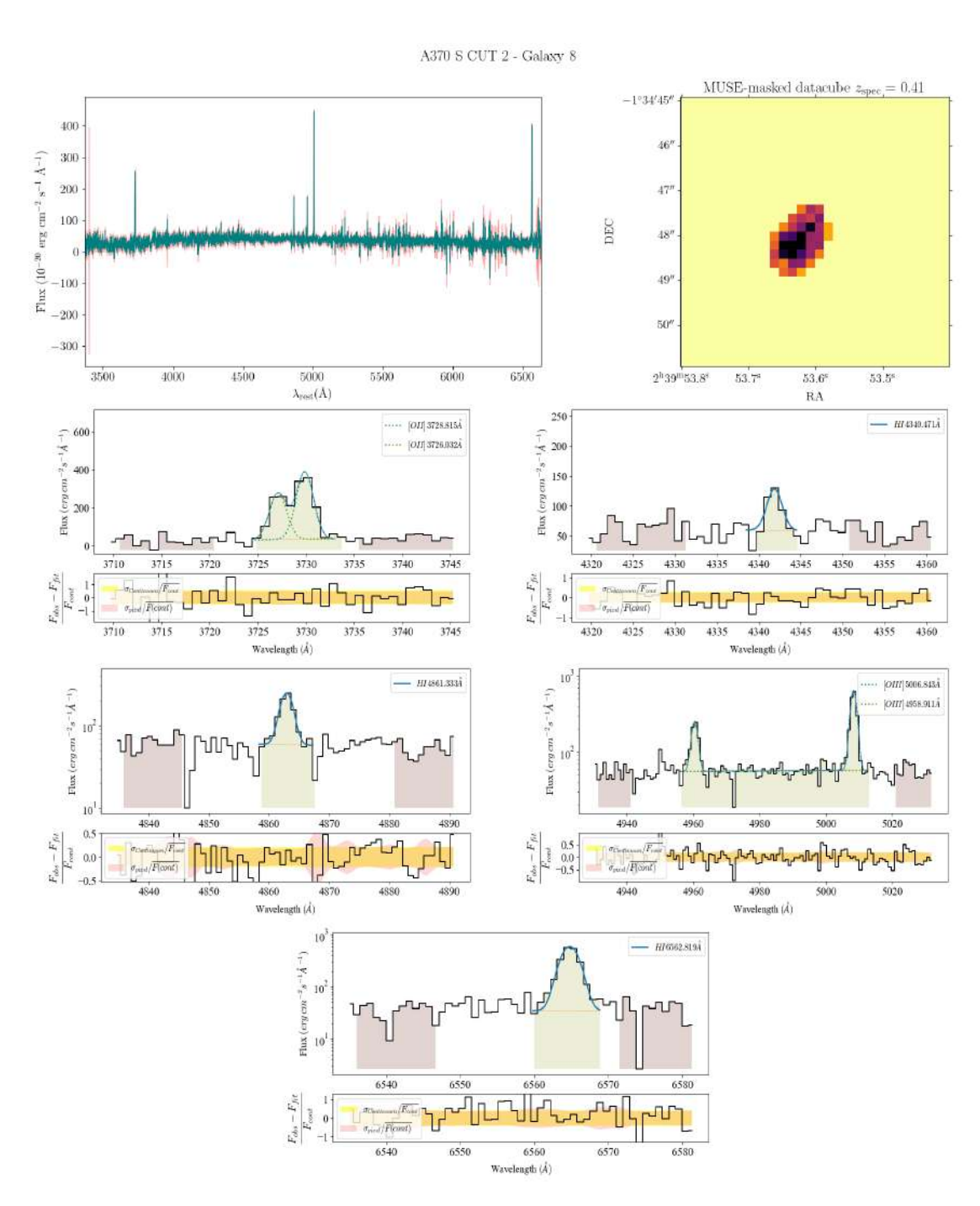


Figure A.43: Main emission lines fitted for DEEPSPACE ID 3060.

## A.6 A370 S CUT 3

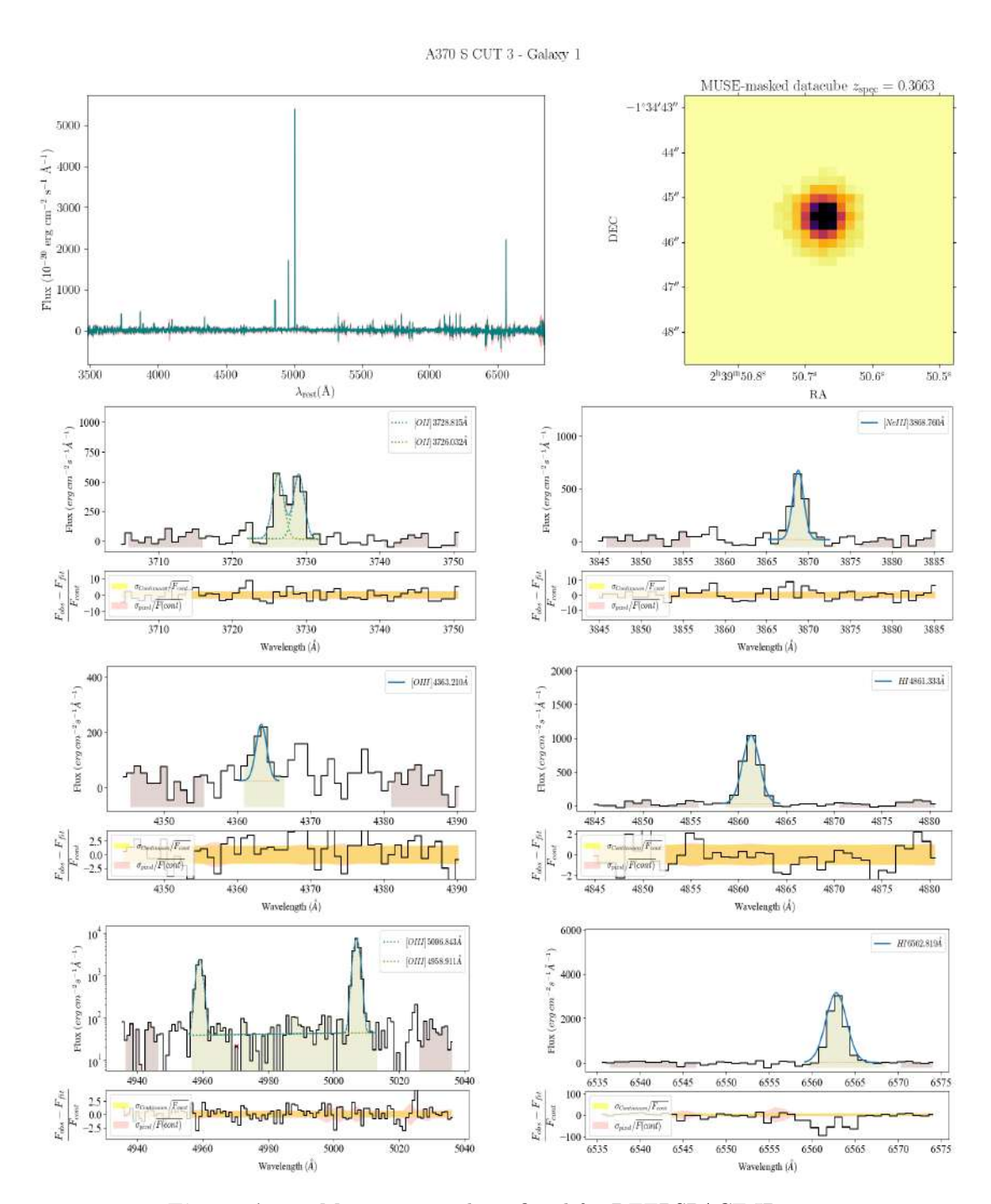


Figure A.44: Main emission lines fitted for DEEPSPACE ID 2935.

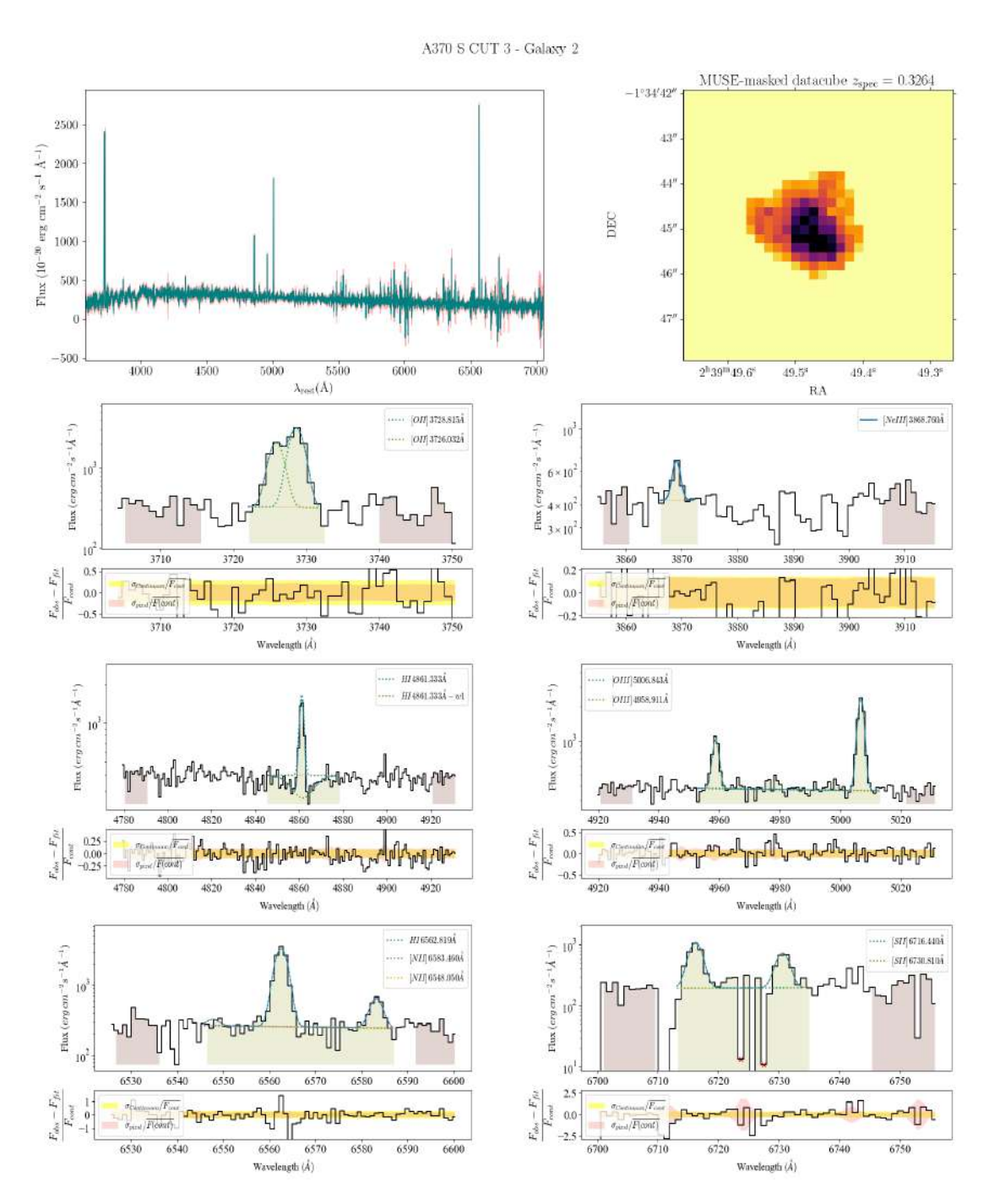


Figure A.45: Main emission lines fitted for DEEPSPACE ID 3187.

# B | HST, HAWK-I and Spitzer photometry

In this section, we present the extracted HST, HAWKI and Spitzer images for our sample. Each stamp is  $6 \times 6$  arcsec wide. Filters with no observations show a plain color, due to the galaxy falling outside of the field covered.

# B.1 A370 N CUT 1



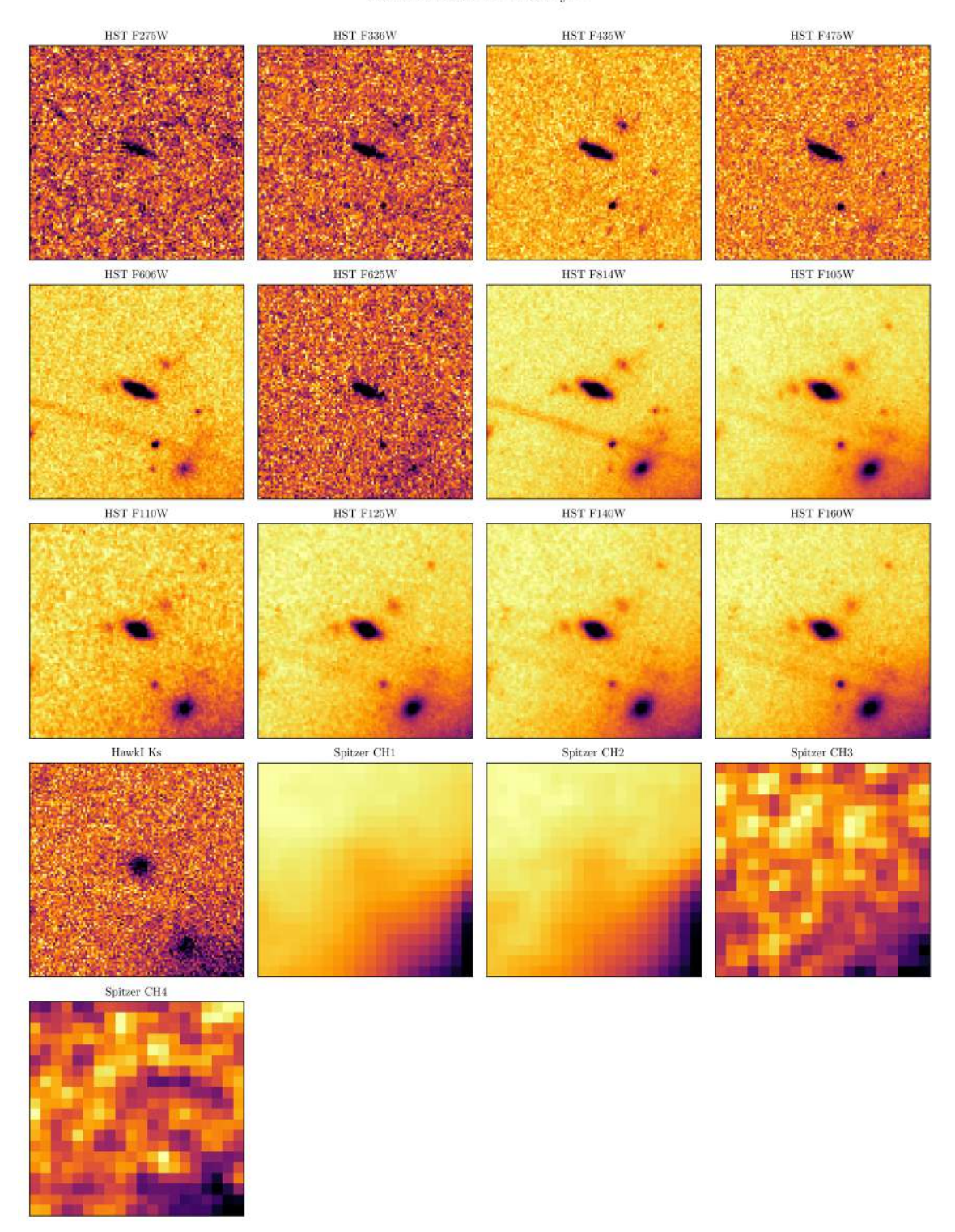


Figure B.1: HST, HAWK-I and Spitzer images of DEEPSPACE ID 4112.

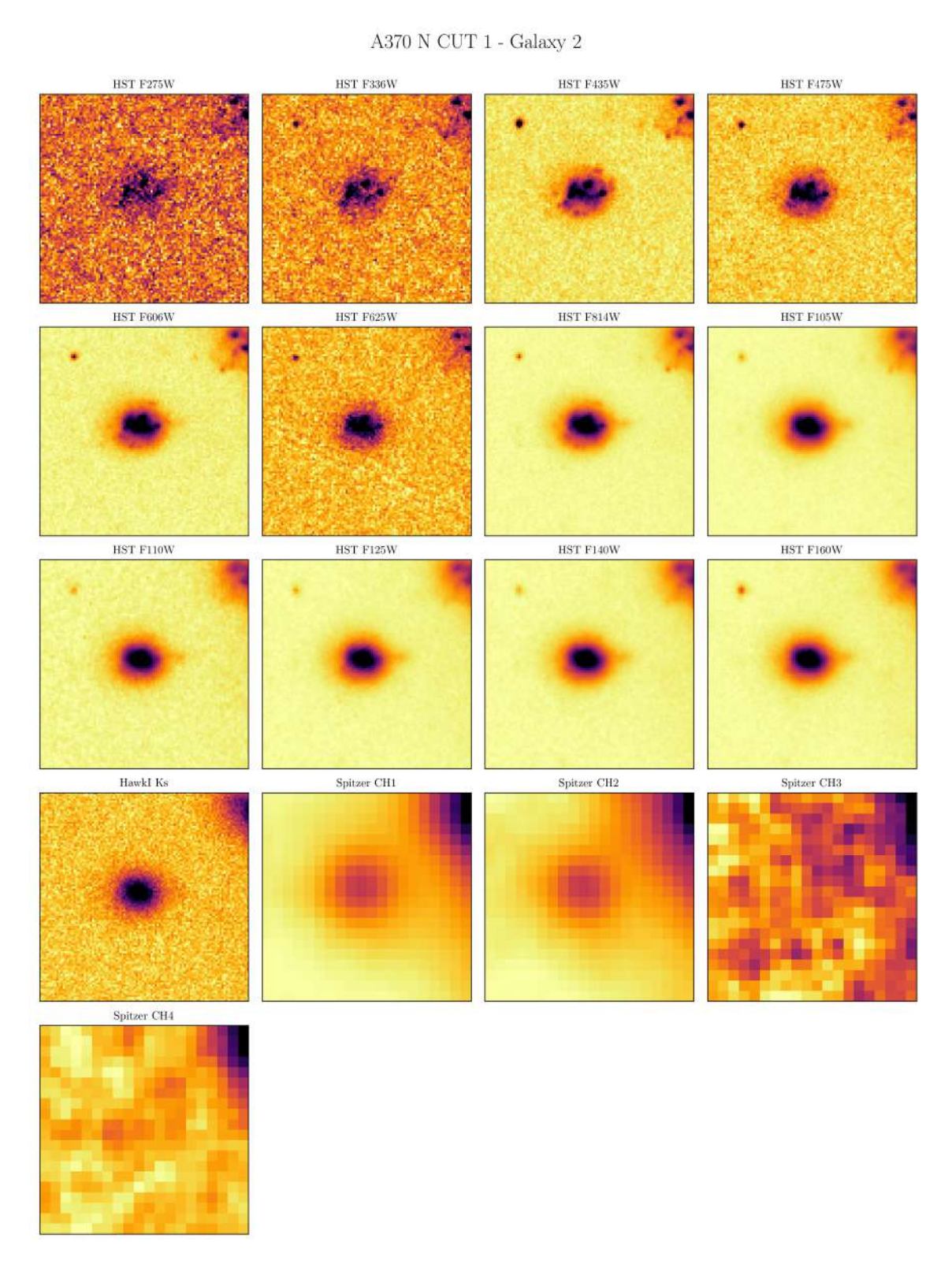


Figure B.2: HST, HAWK-I and Spitzer images of DEEPSPACE ID 3682.

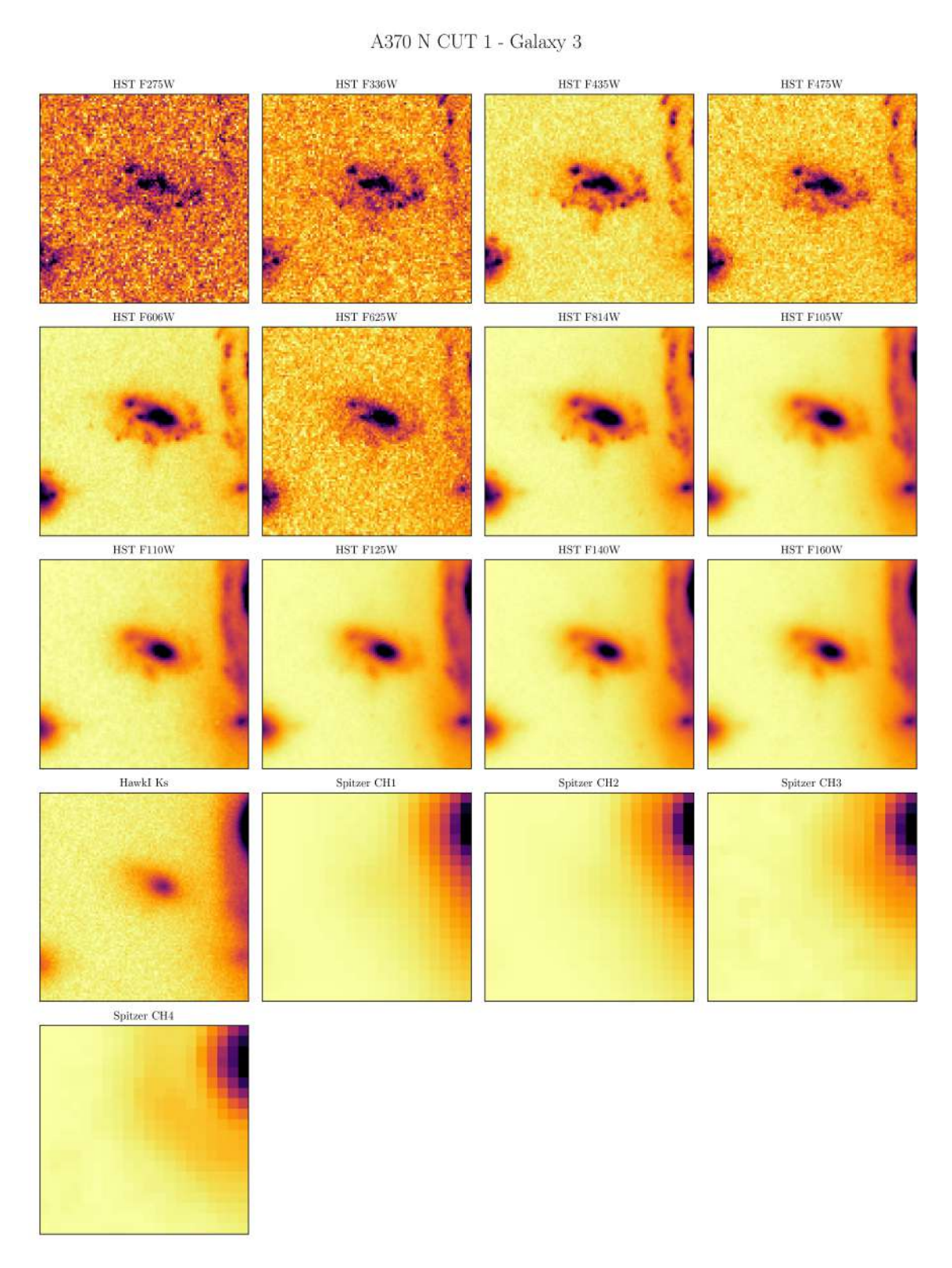


Figure B.3: HST, HAWK-I and Spitzer images of DEEPSPACE ID 4225.

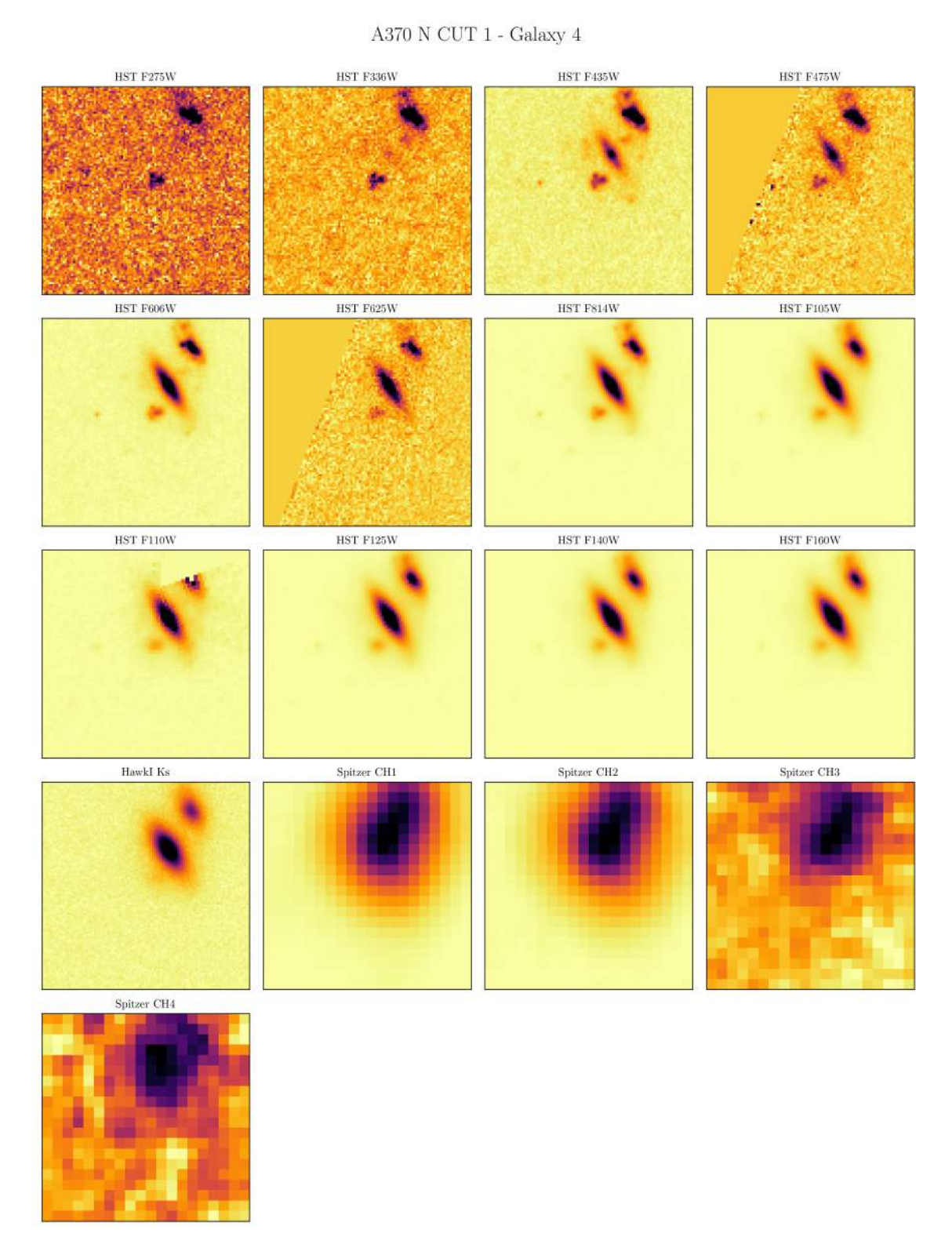


Figure B.4: HST, HAWK-I and Spitzer images of DEEPSPACE ID 4178.

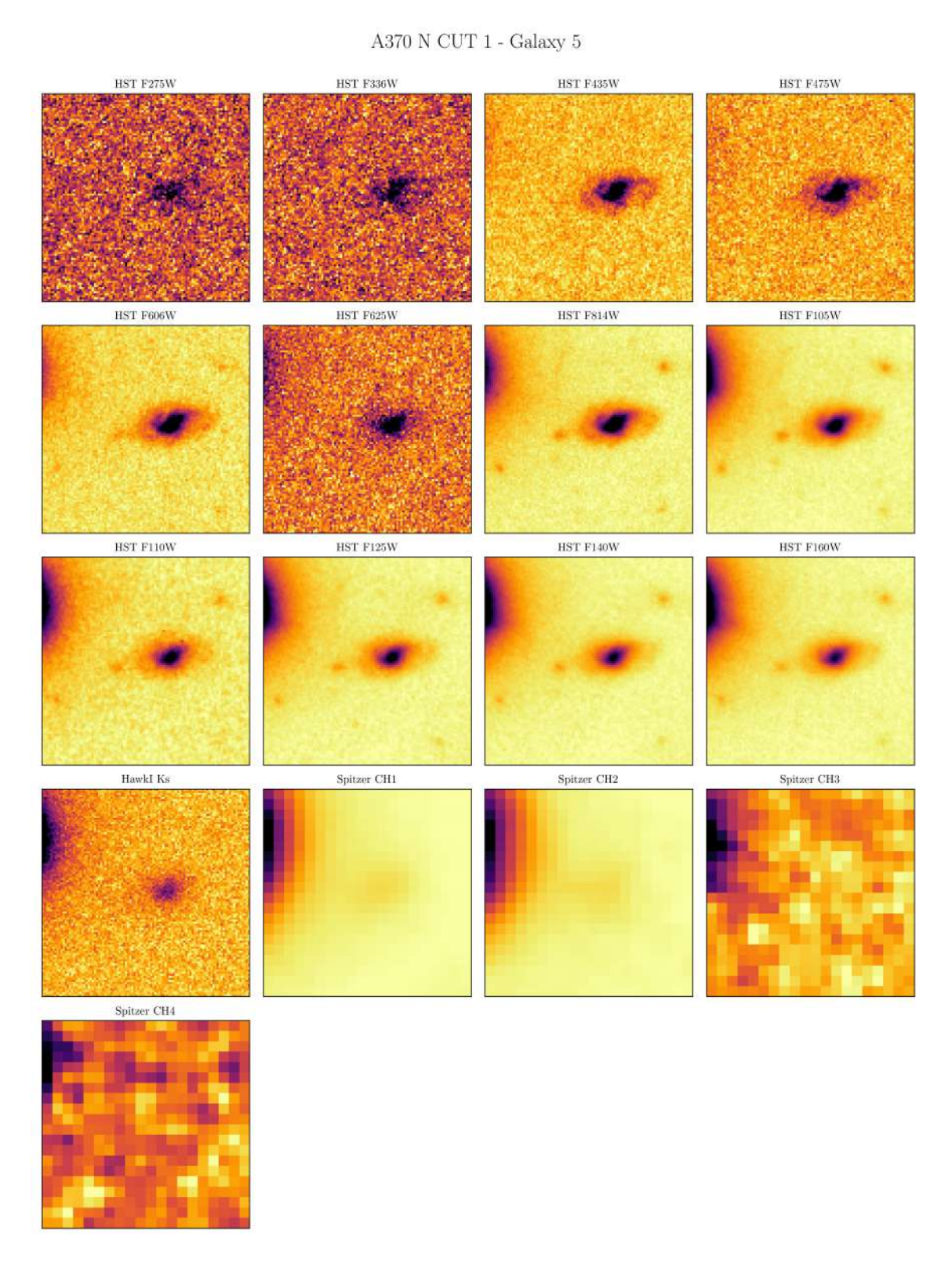


Figure B.5: HST, HAWK-I and Spitzer images of DEEPSPACE ID 3806.

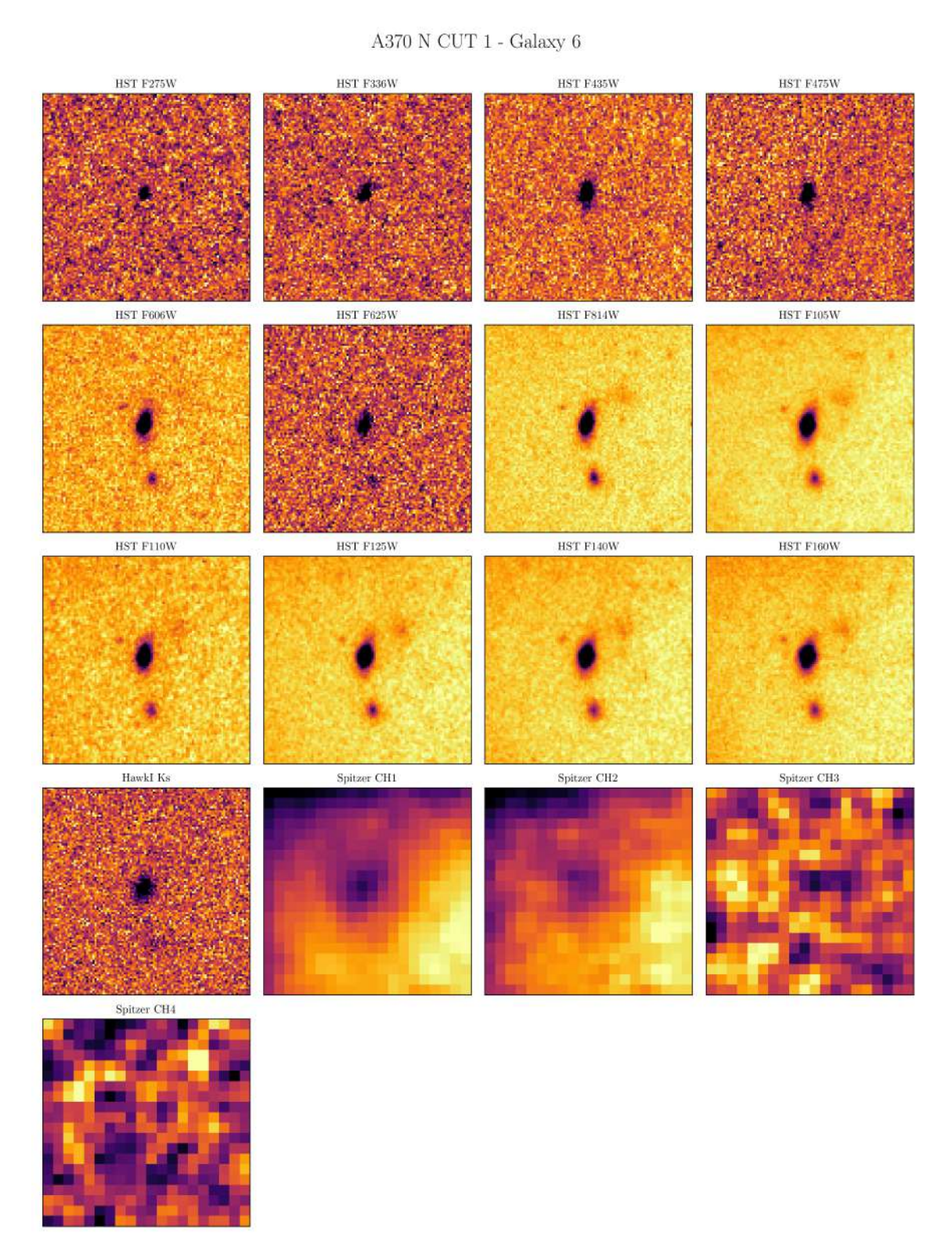


Figure B.6: HST, HAWK-I and Spitzer images of DEEPSPACE ID 3595.

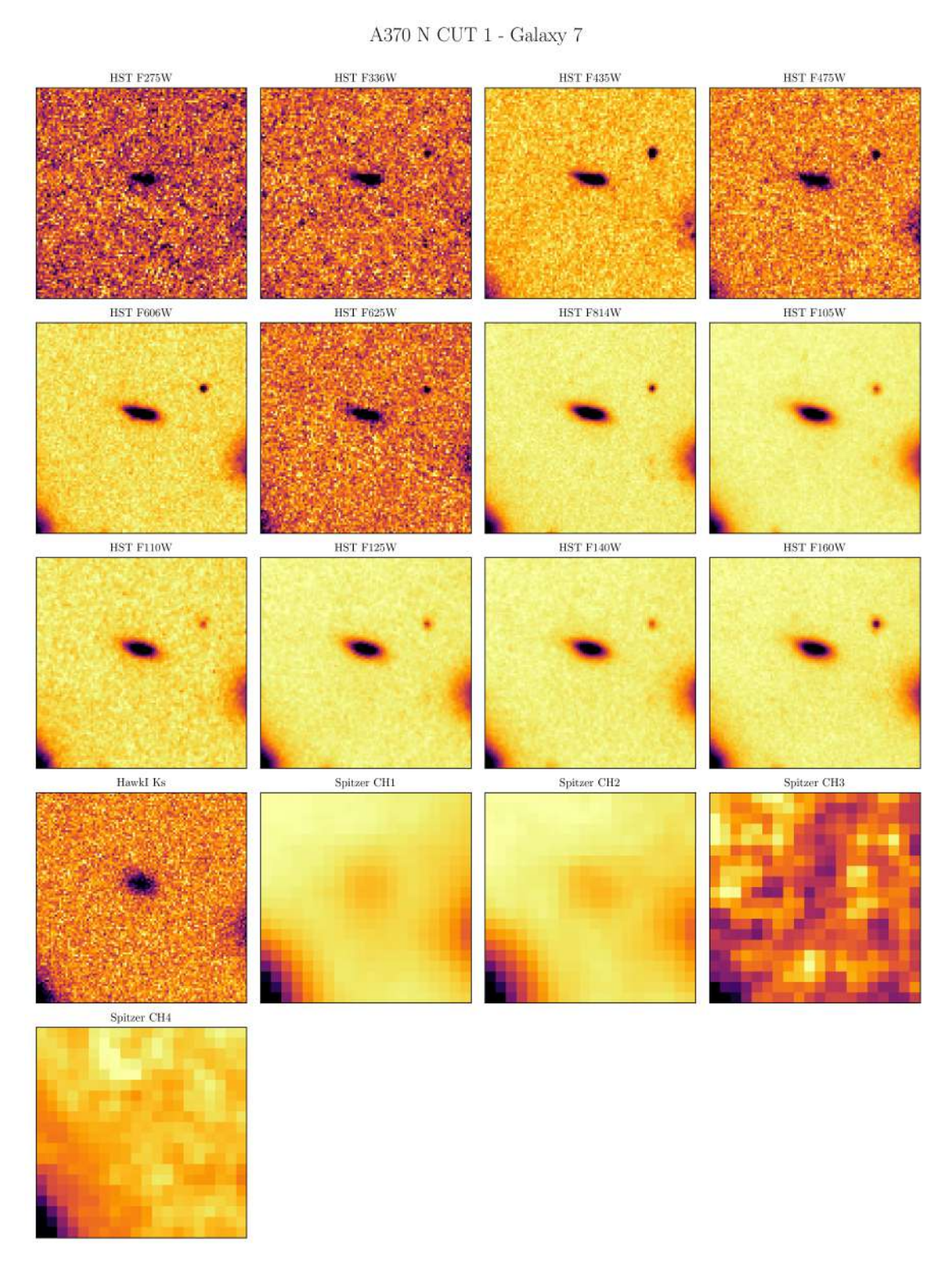
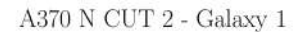


Figure B.7: HST, HAWK-I and Spitzer images of DEEPSPACE ID 3529.

# B.2 A370 N CUT 2



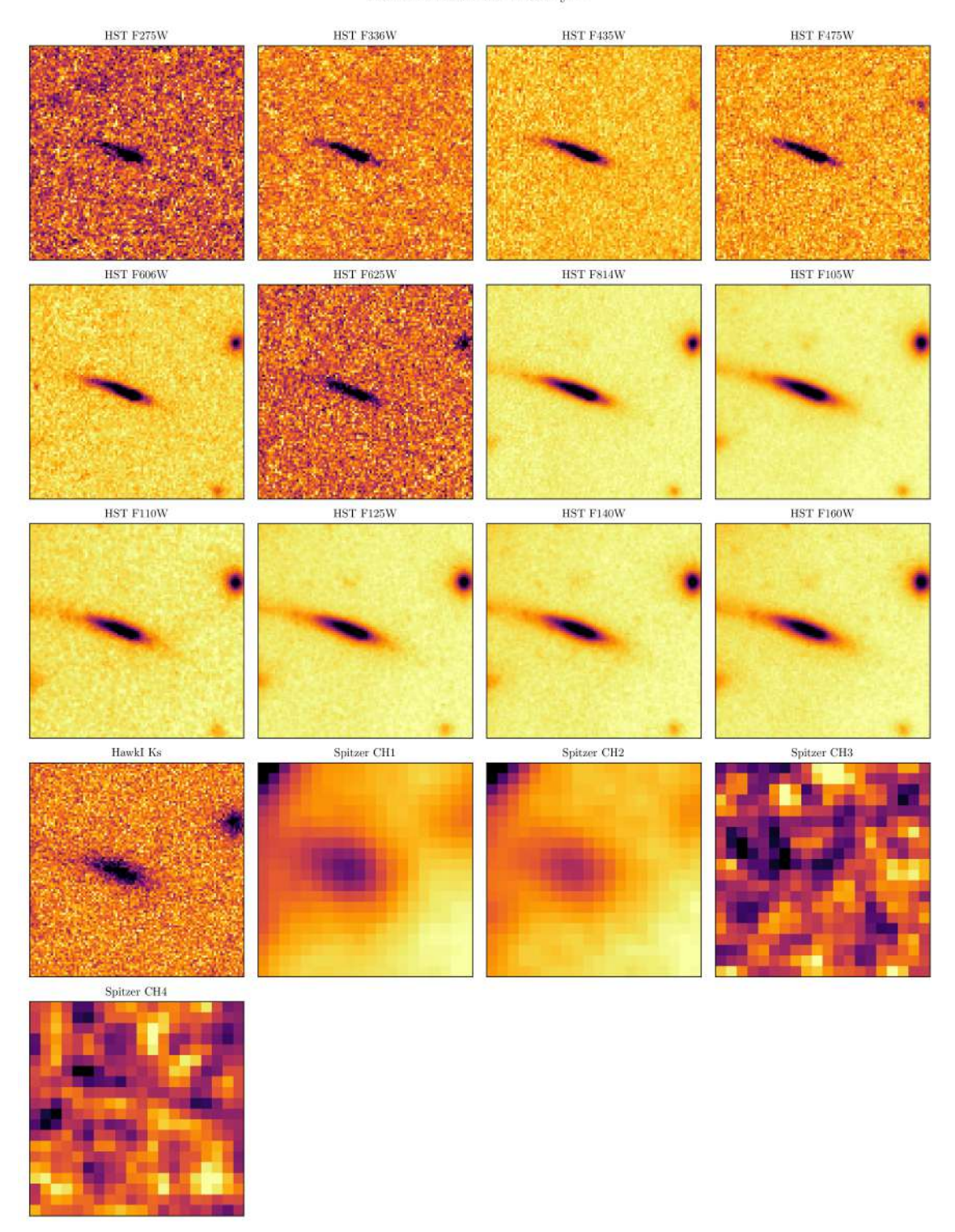


Figure B.8: HST, HAWK-I and Spitzer images of DEEPSPACE ID 3342.

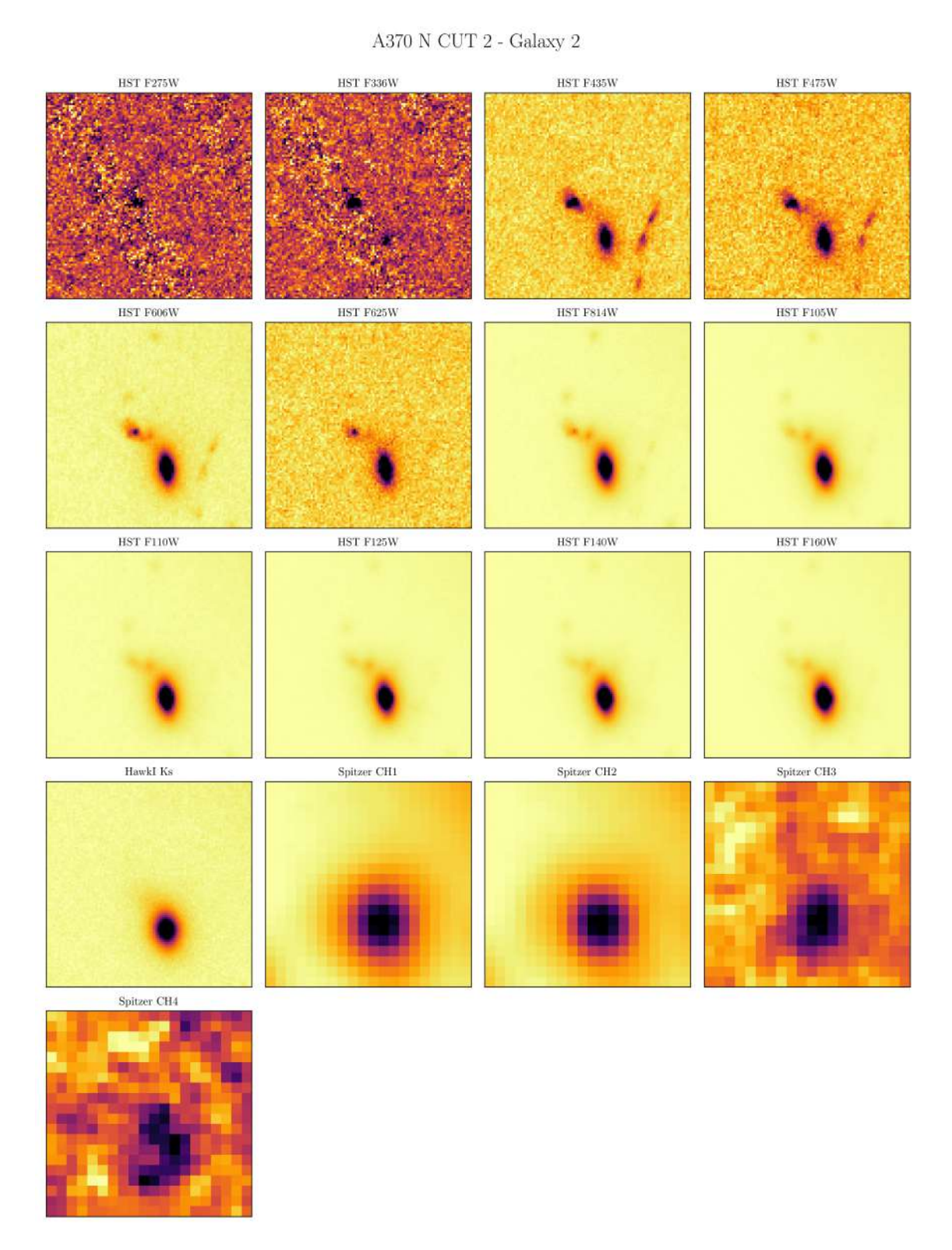


Figure B.9: HST, HAWK-I and Spitzer images of DEEPSPACE ID 3826.

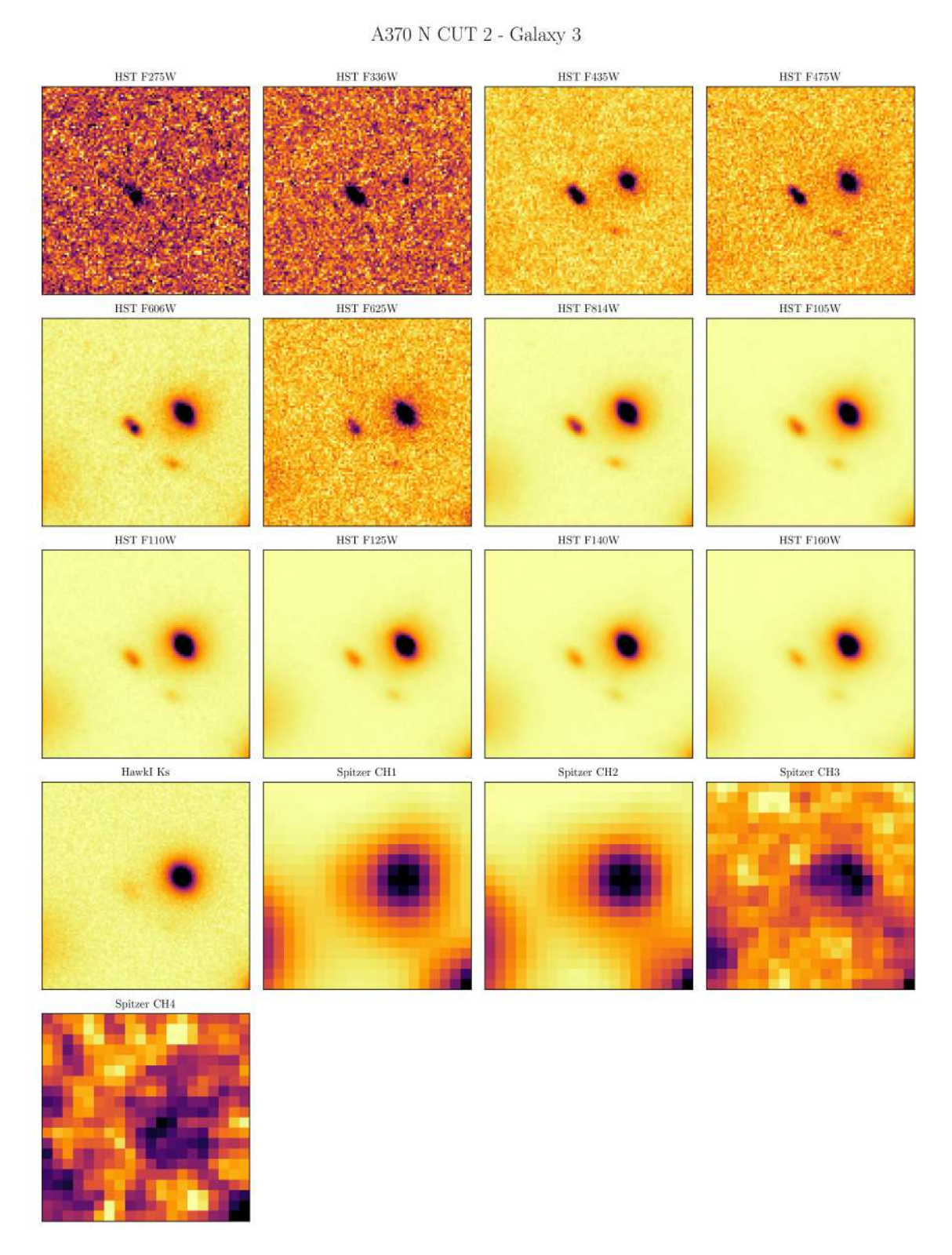


Figure B.10: HST, HAWK-I and Spitzer images of DEEPSPACE ID 3440.

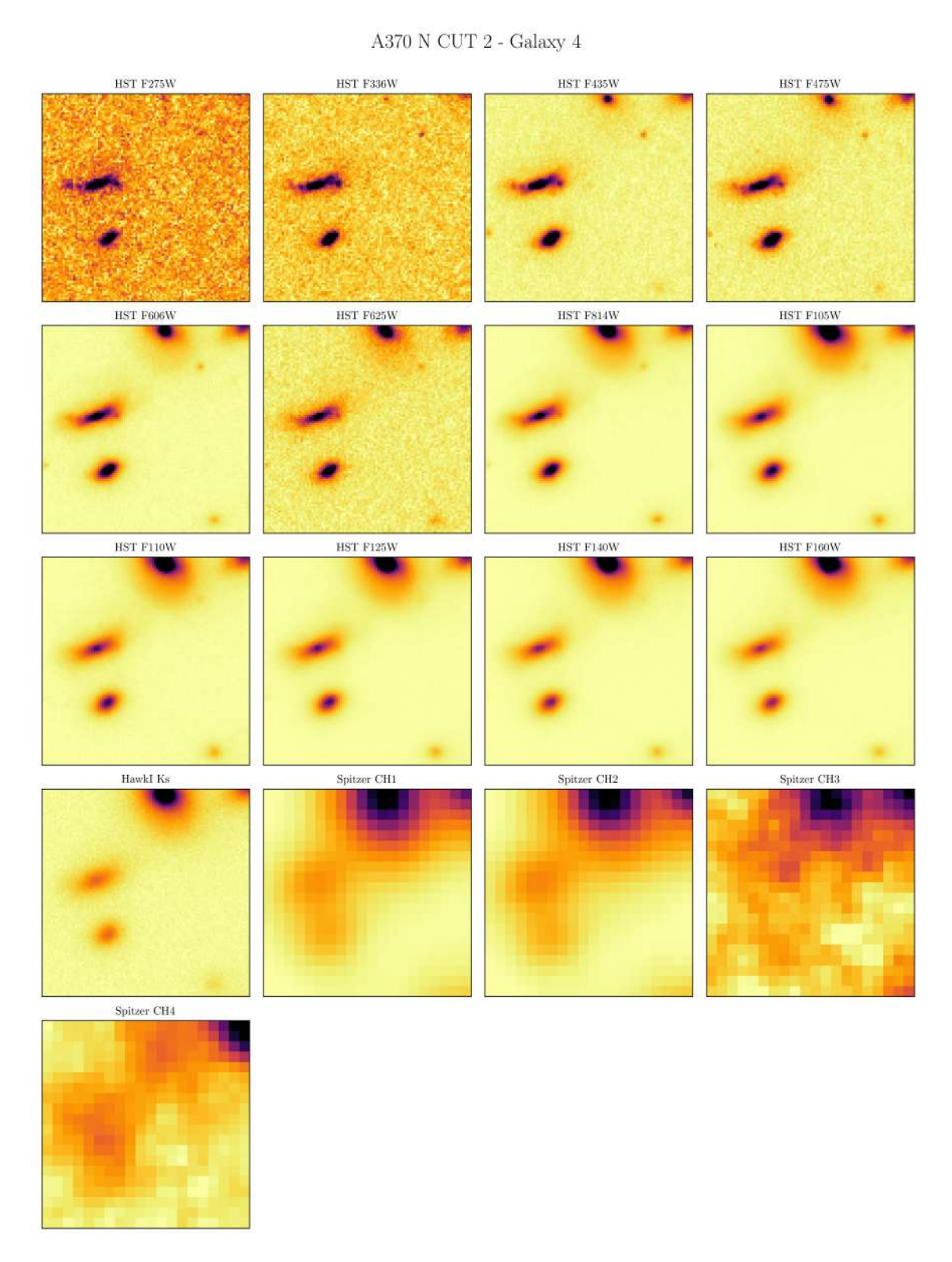


Figure B.11: HST, HAWK-I and Spitzer images of DEEPSPACE ID 3633.

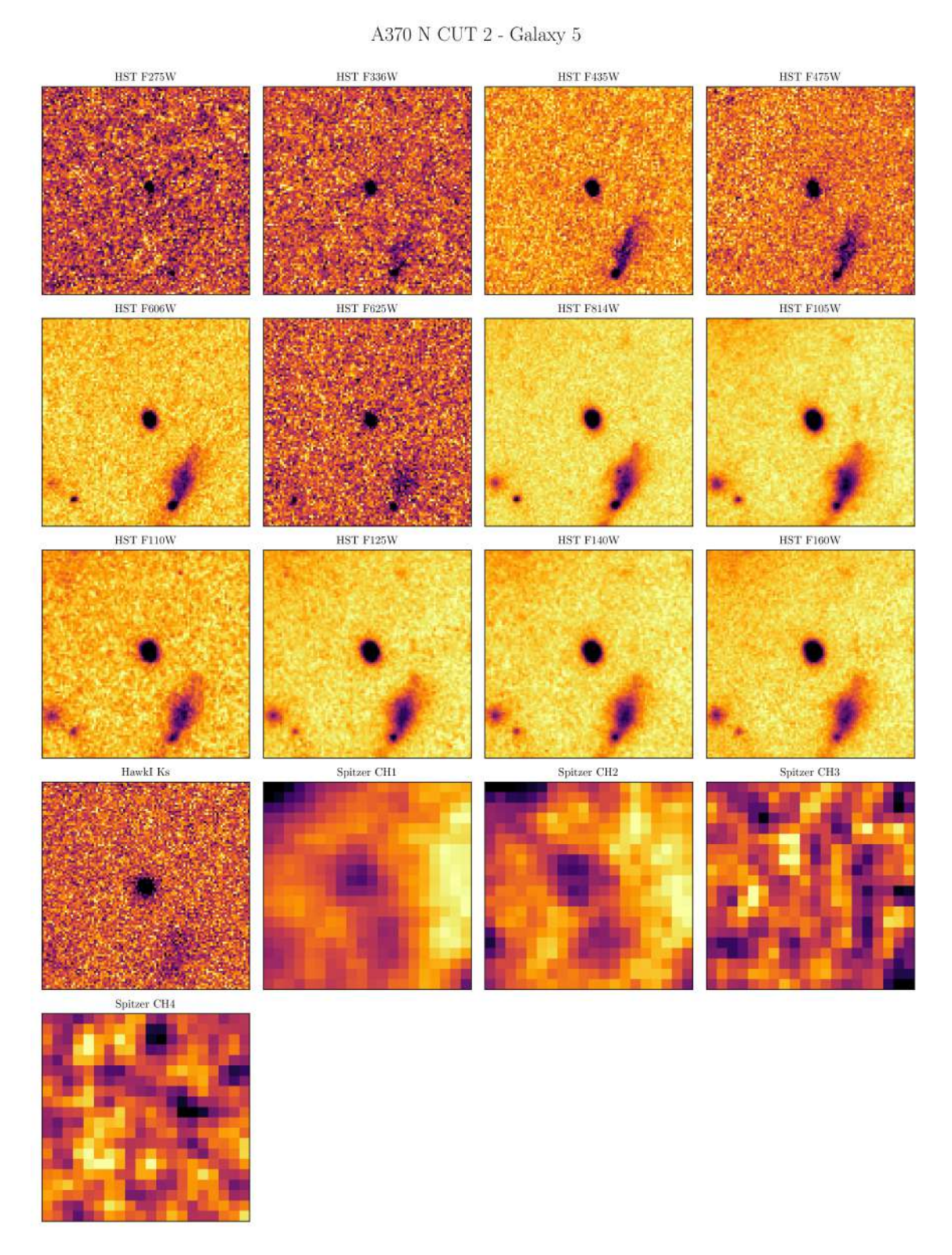


Figure B.12: HST, HAWK-I and Spitzer images of DEEPSPACE ID 4070.

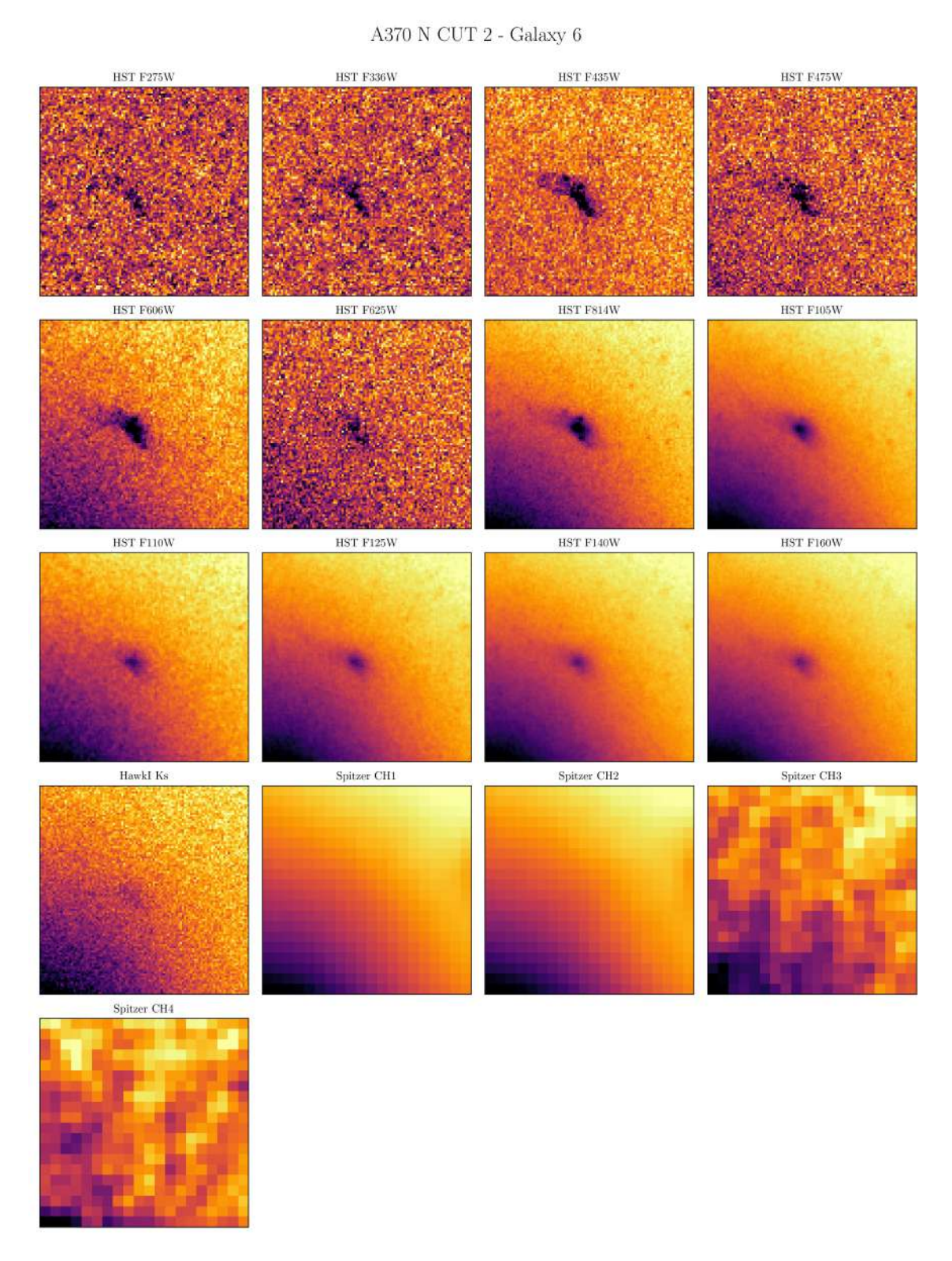


Figure B.13: HST, HAWK-I and Spitzer images of DEEPSPACE ID 4266.

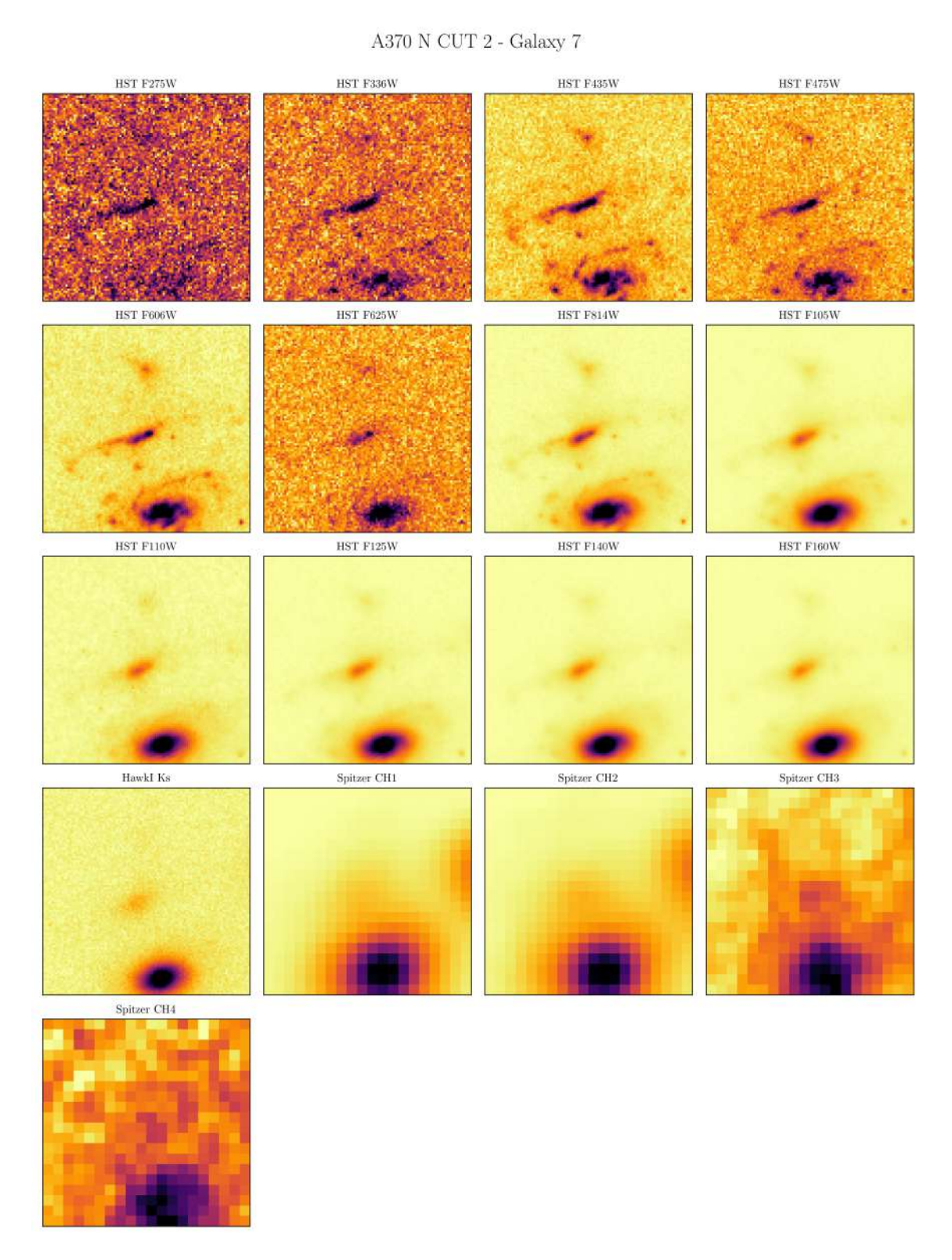


Figure B.14: HST, HAWK-I and Spitzer images of DEEPSPACE ID 5165.

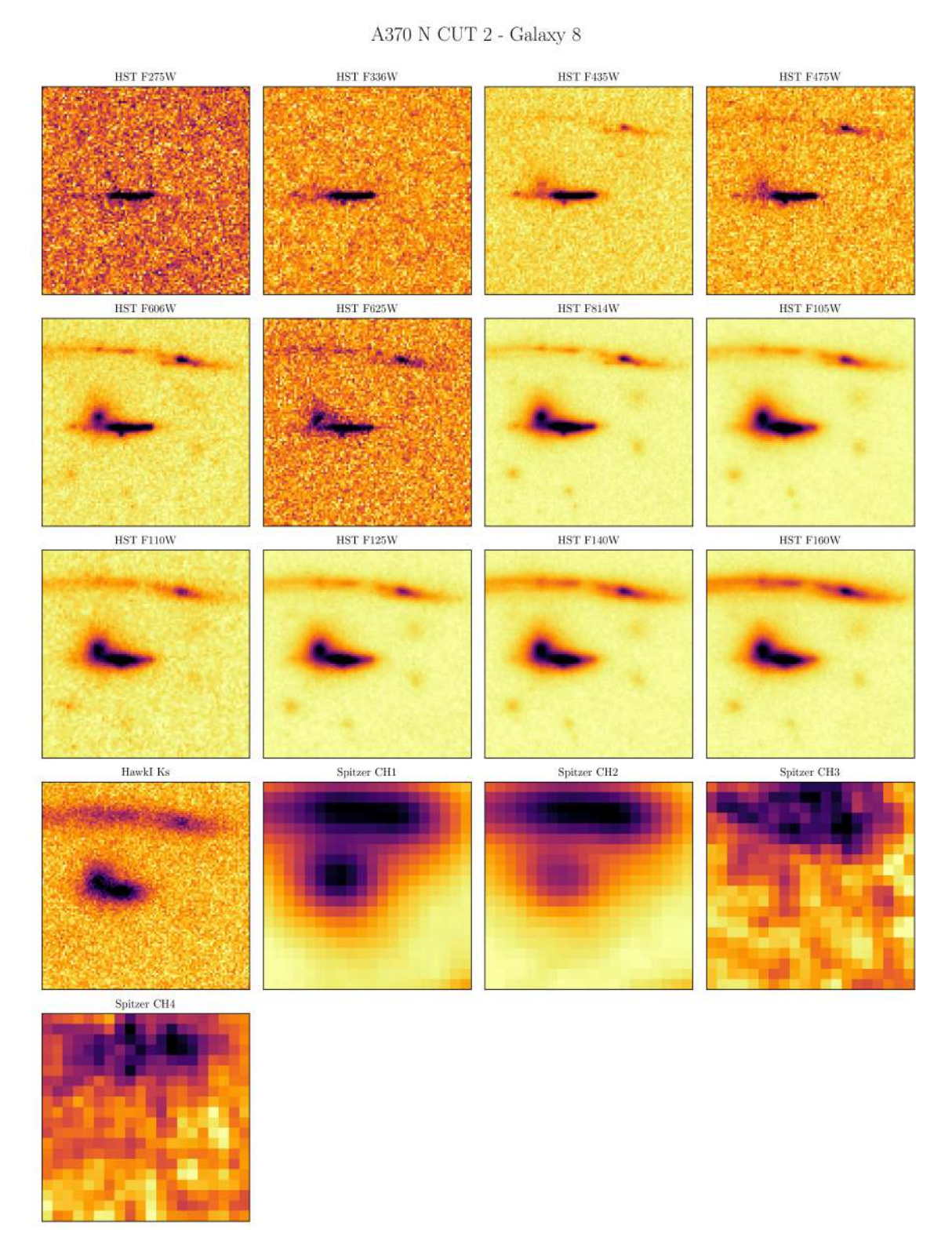


Figure B.15: HST, HAWK-I and Spitzer images of DEEPSPACE ID 5455.

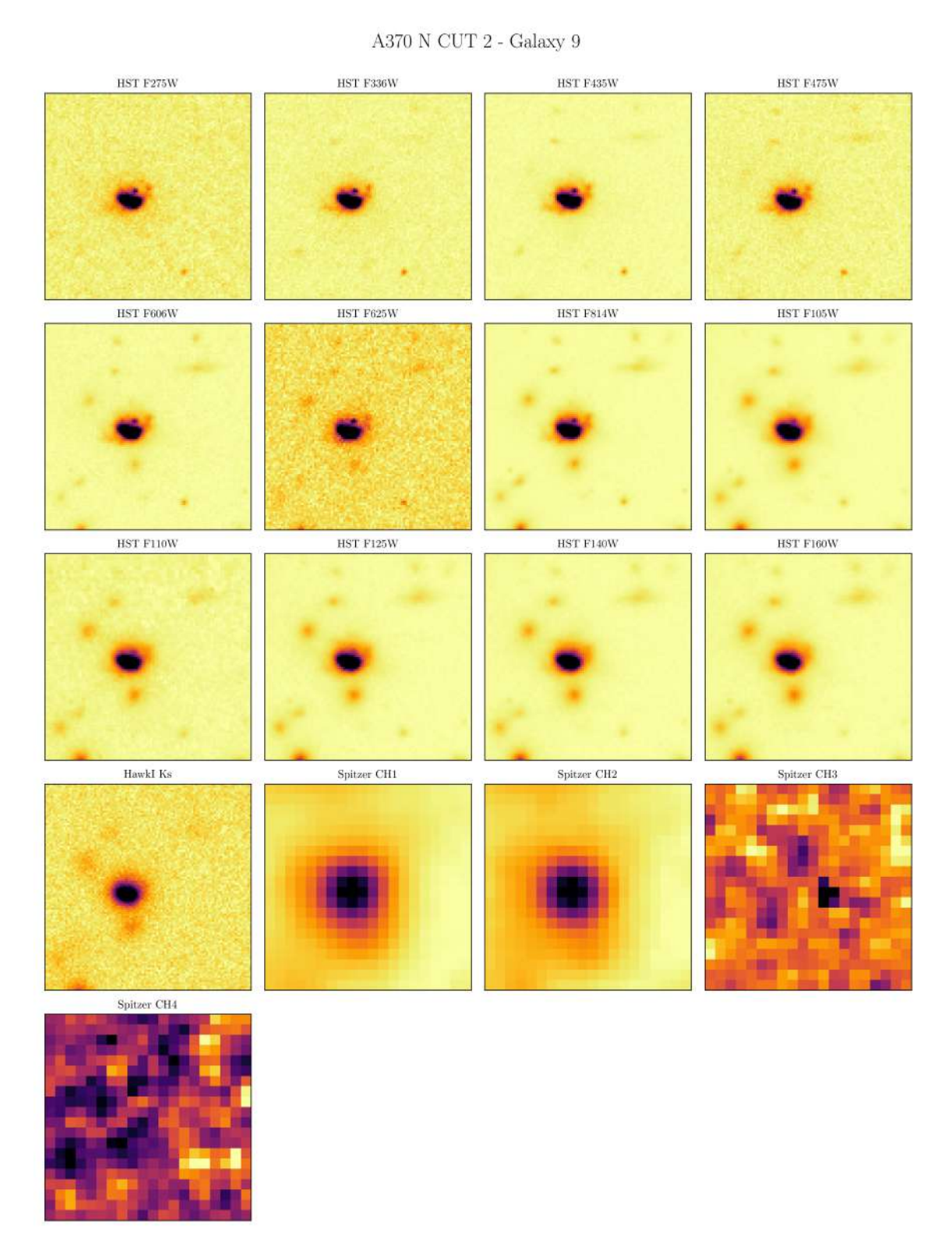


Figure B.16: HST, HAWK-I and Spitzer images of DEEPSPACE ID 5741.

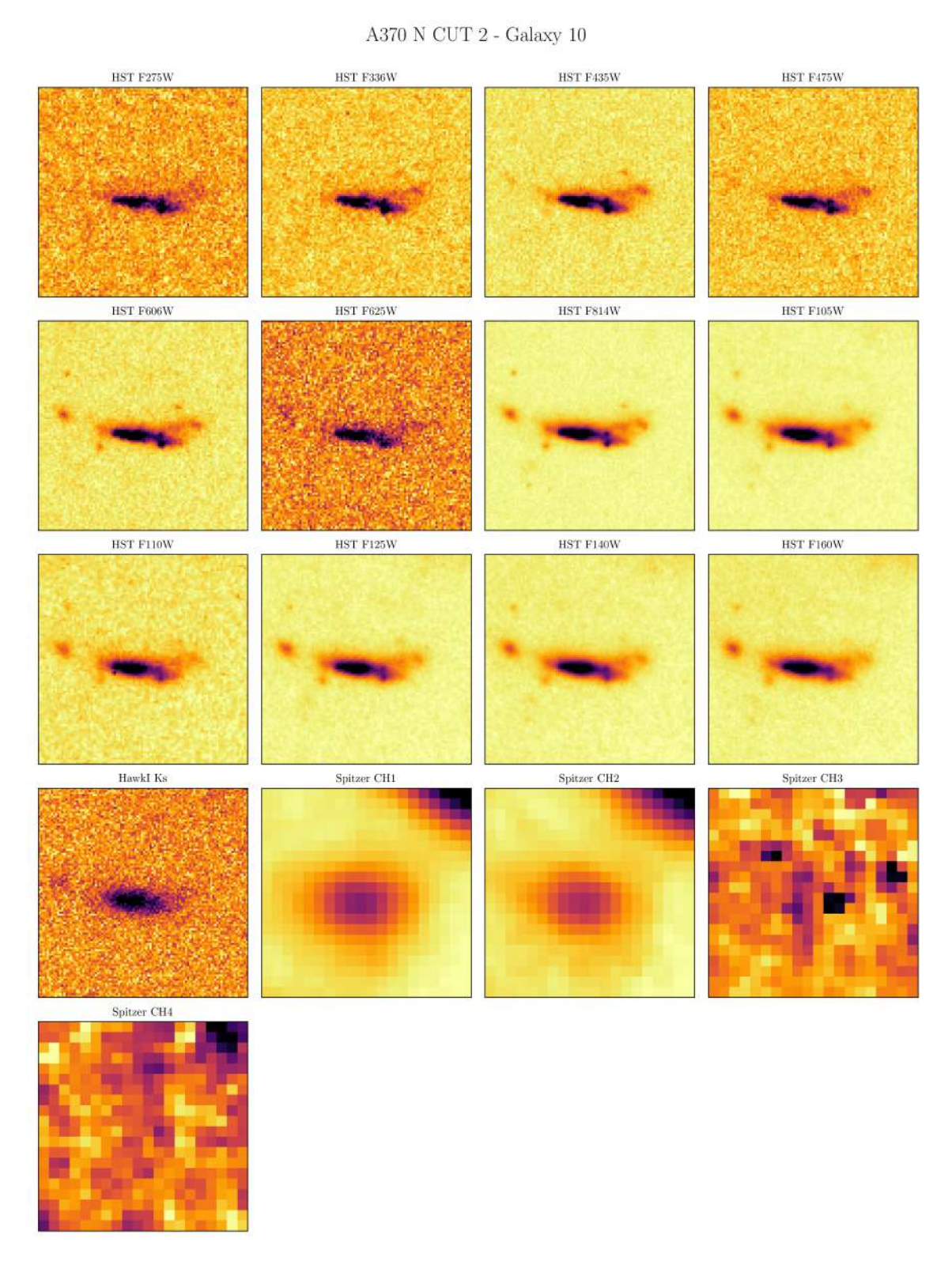


Figure B.17: HST, HAWK-I and Spitzer images of DEEPSPACE ID 5522.

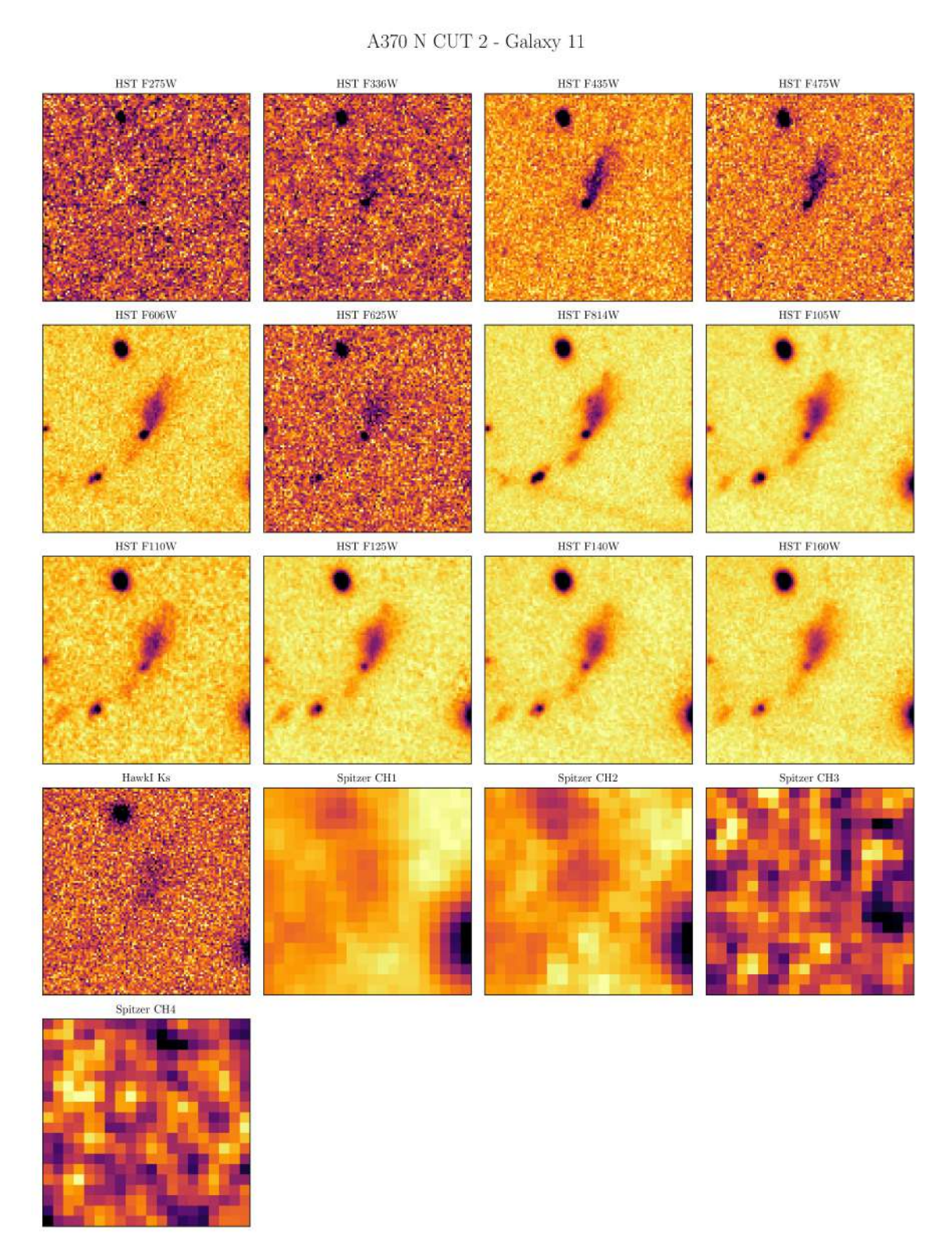


Figure B.18: HST, HAWK-I and Spitzer images of DEEPSPACE ID 3910.

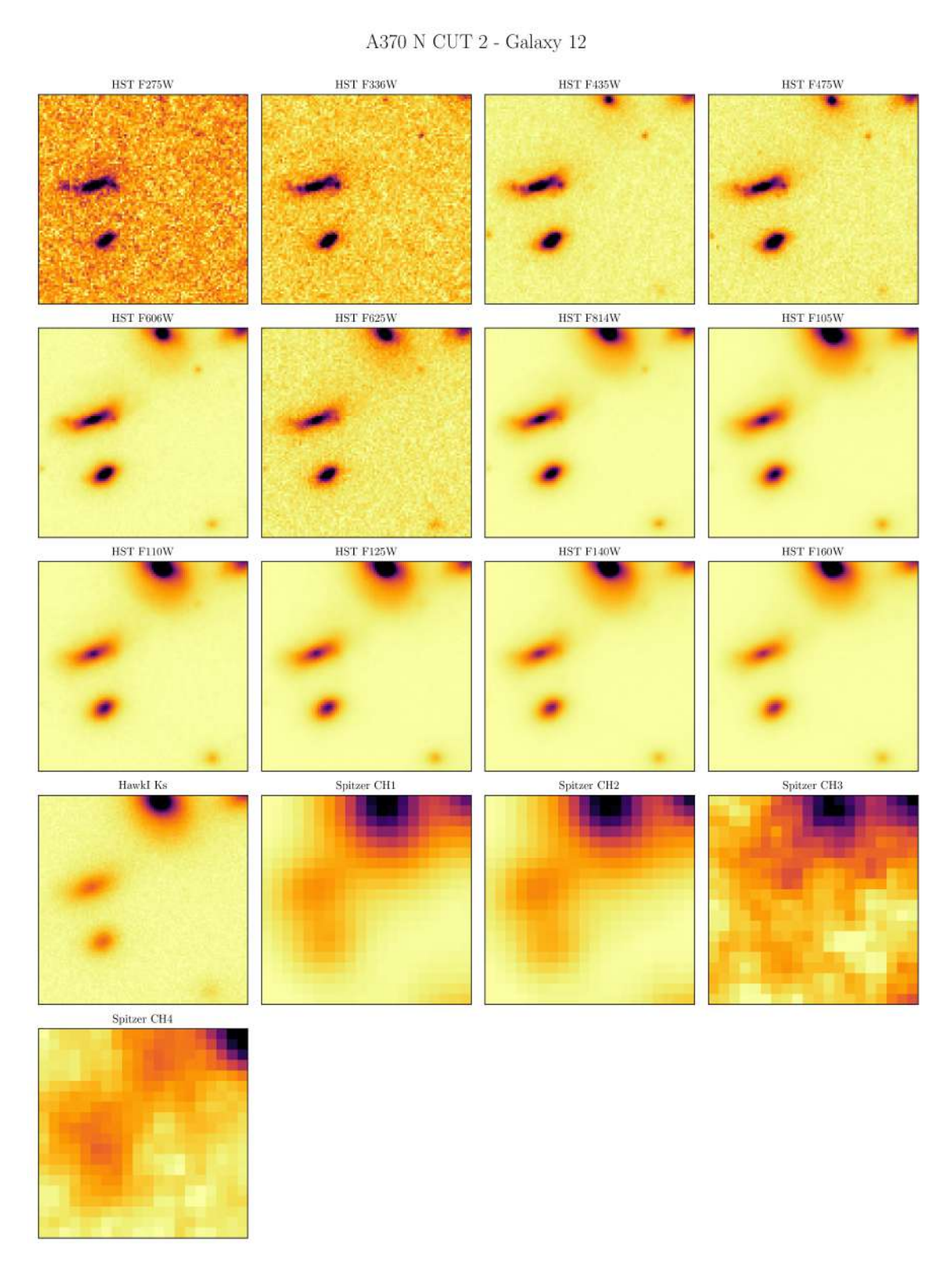


Figure B.19: HST, HAWK-I and Spitzer images of DEEPSPACE ID 3684.

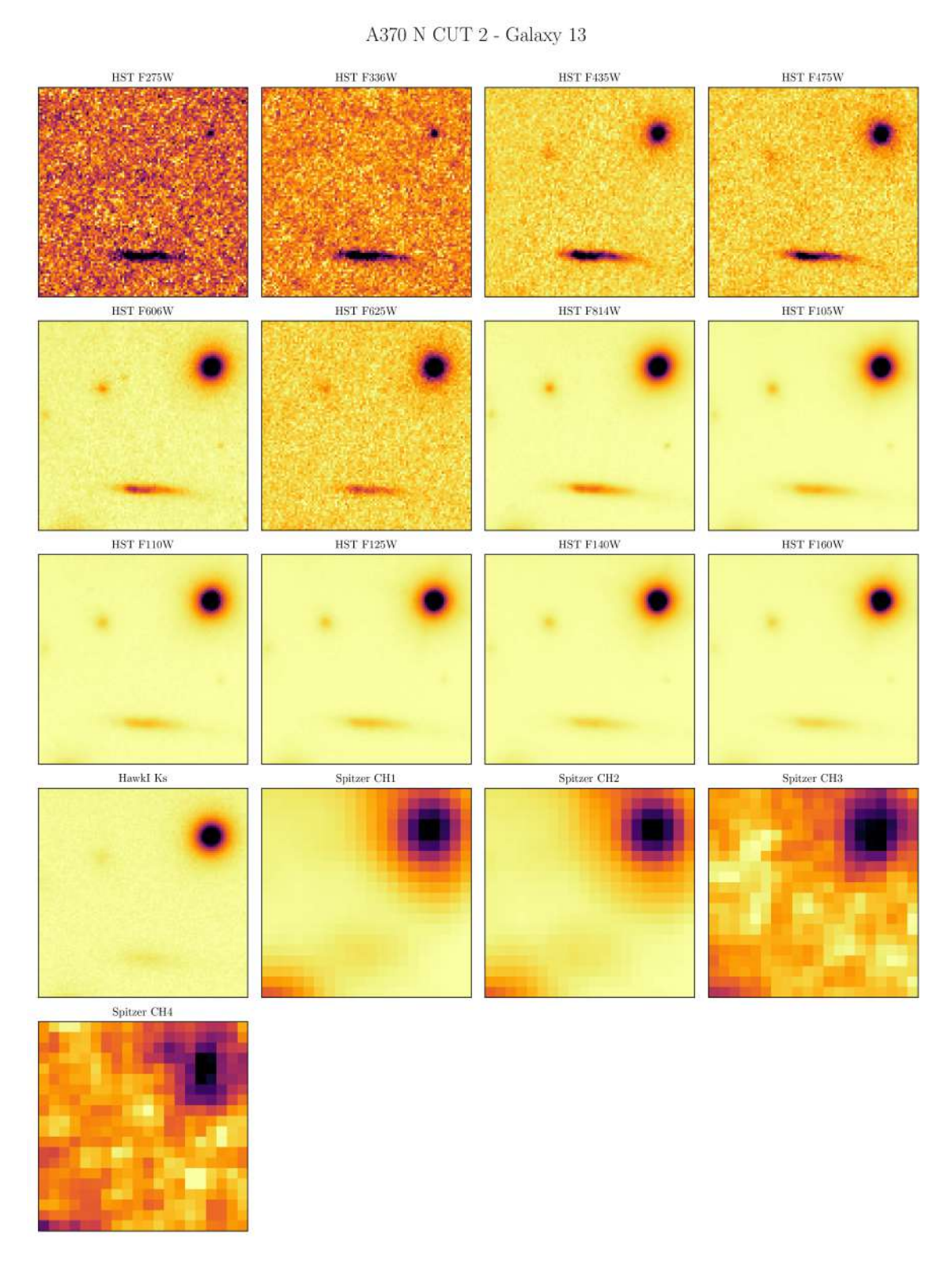


Figure B.20: HST, HAWK-I and Spitzer images of DEEPSPACE ID 3392.

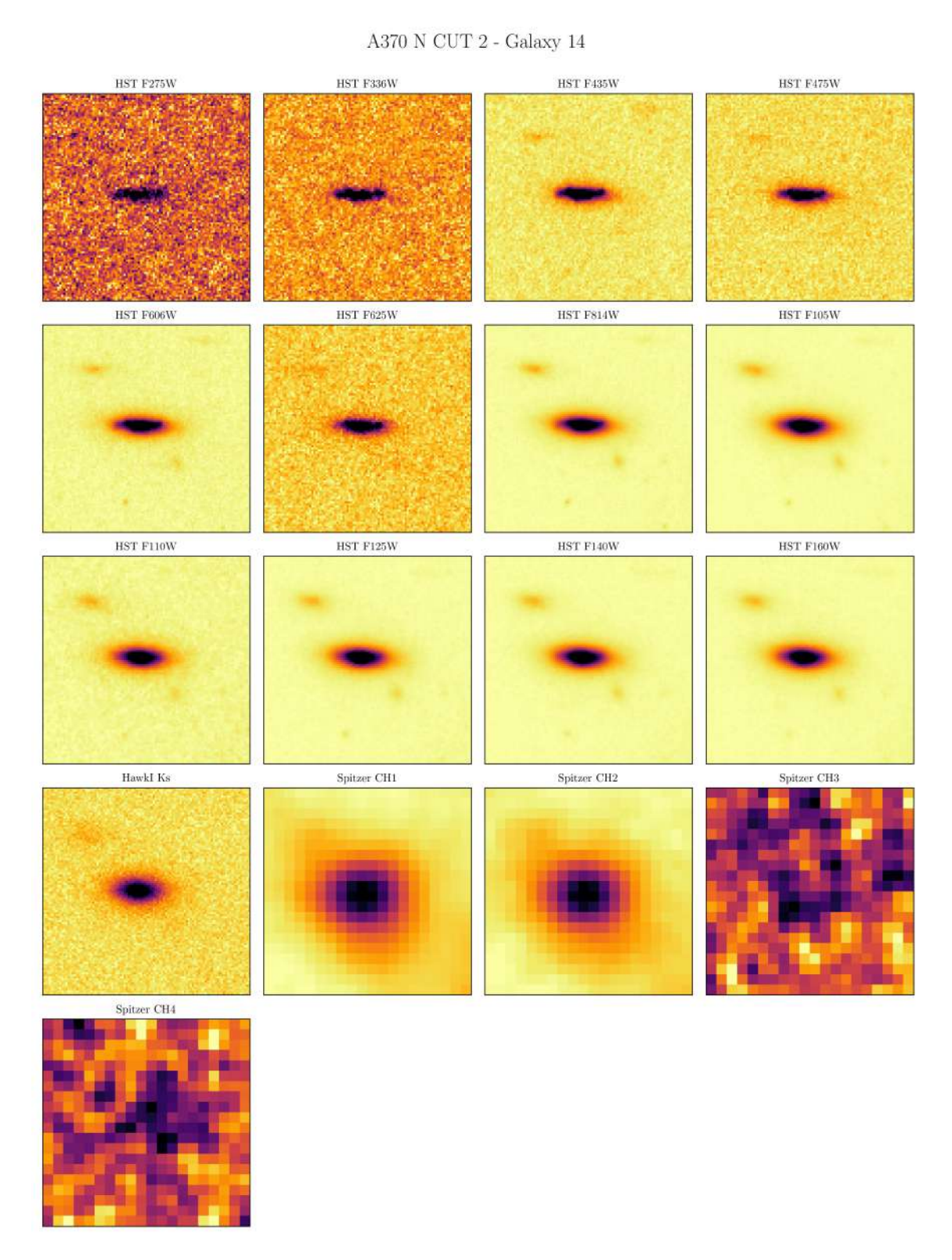


Figure B.21: HST, HAWK-I and Spitzer images of DEEPSPACE ID 5407.

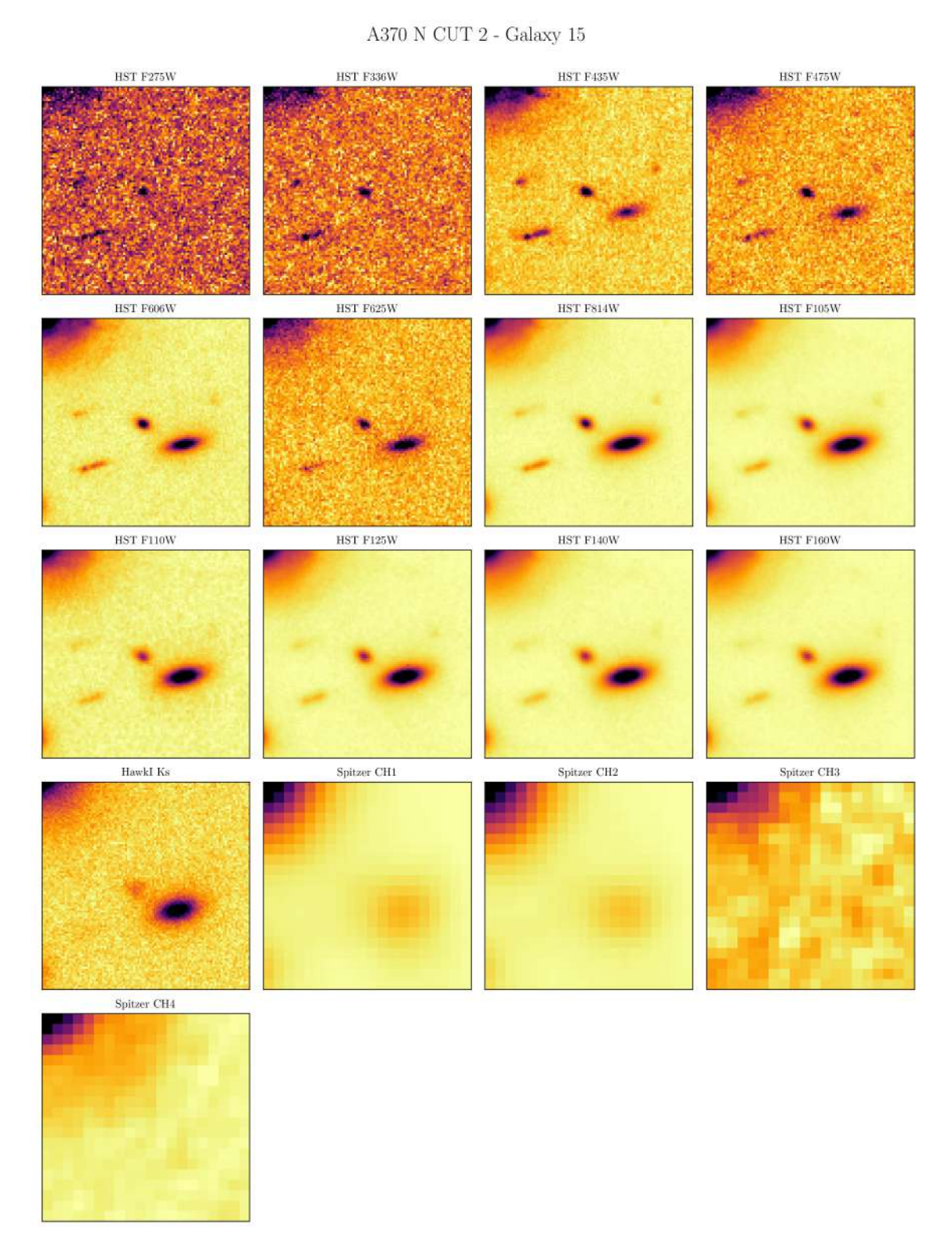


Figure B.22: HST, HAWK-I and Spitzer images of DEEPSPACE ID 5271.

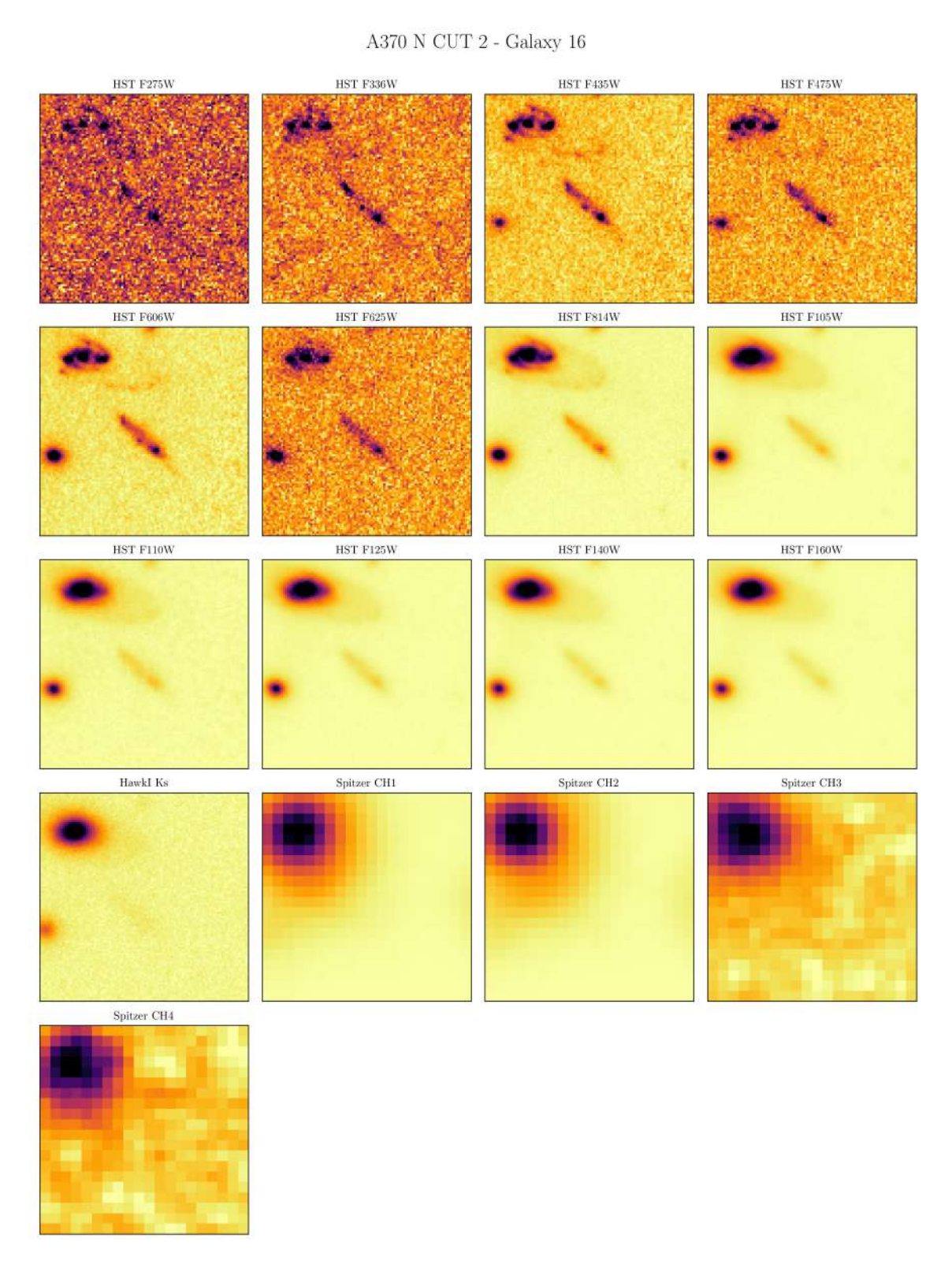


Figure B.23: HST, HAWK-I and Spitzer images of DEEPSPACE ID 4912.

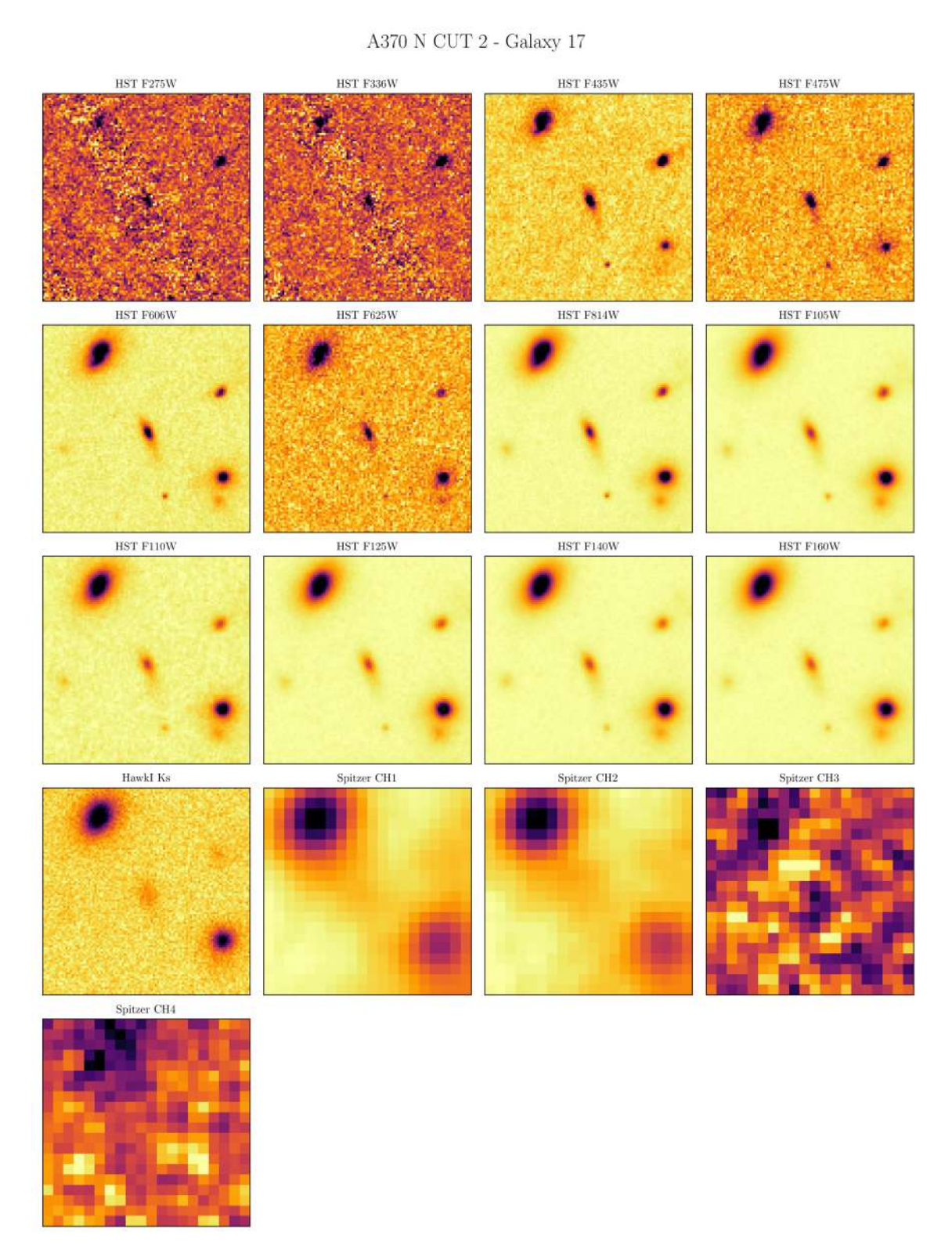


Figure B.24: HST, HAWK-I and Spitzer images of DEEPSPACE ID 5041.

## B.3 A370 N CUT 3

A370 N CUT 3 - Galaxy 1

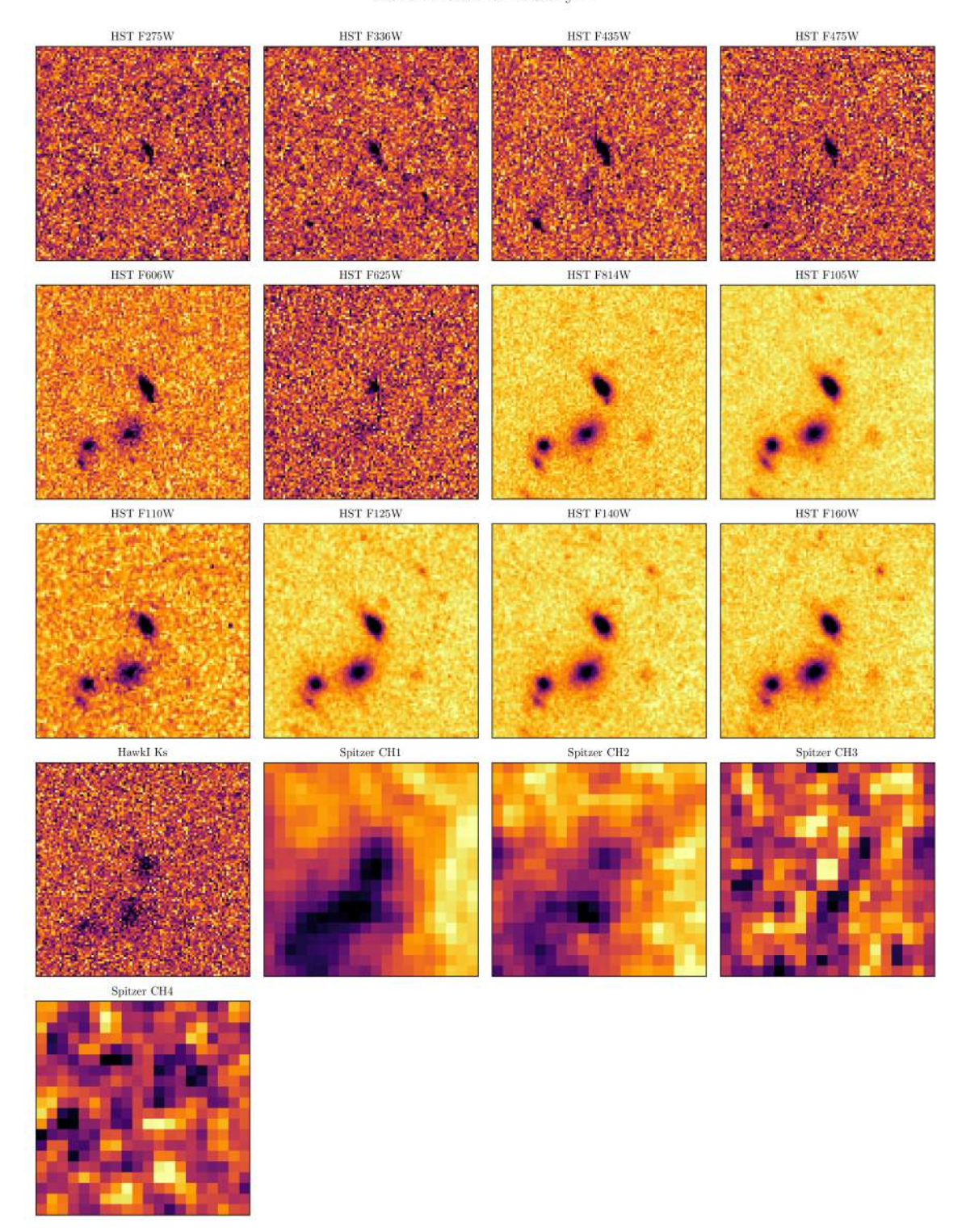


Figure B.25: HST, HAWK-I and Spitzer images of DEEPSPACE ID 4284.

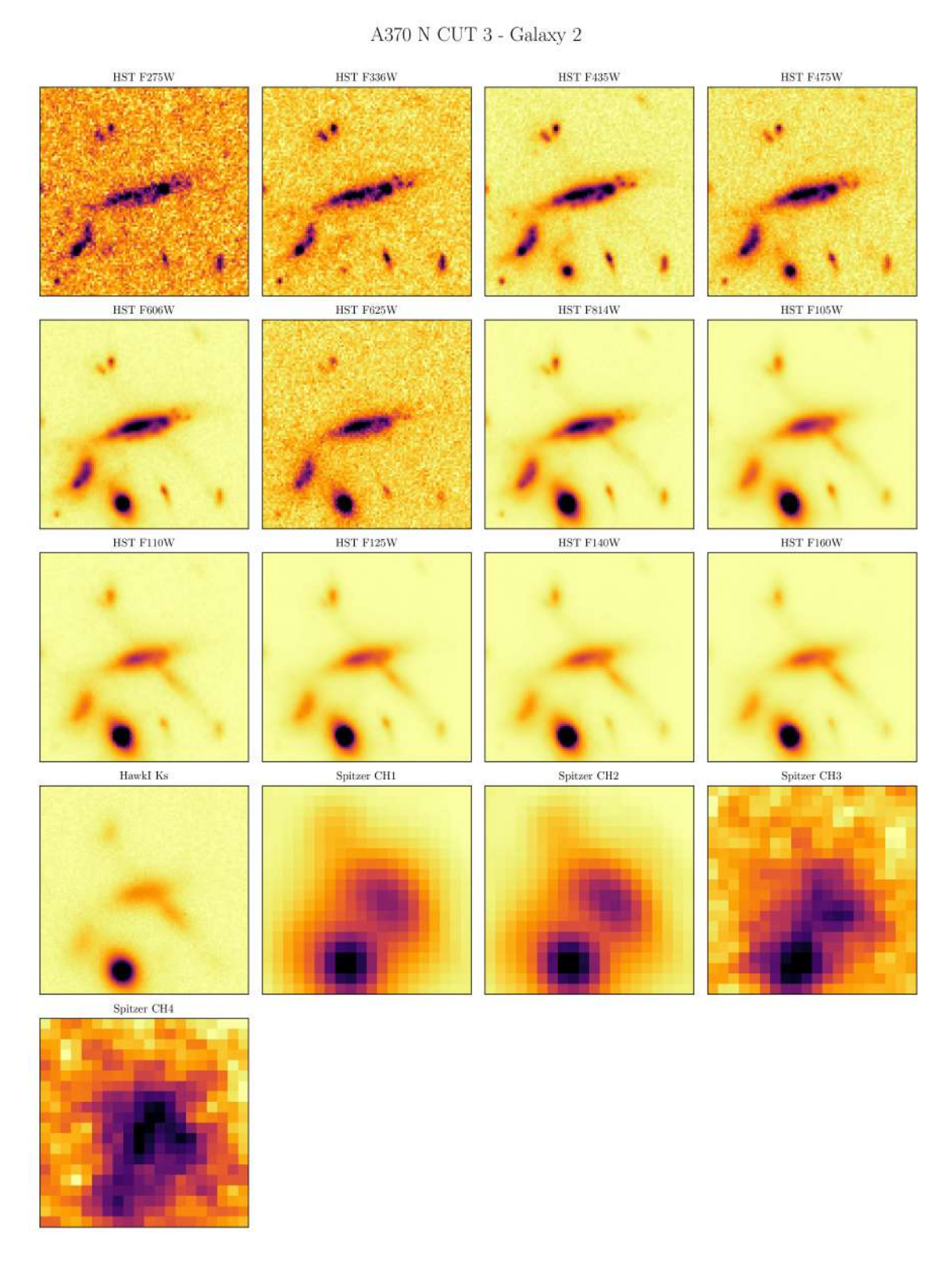


Figure B.26: HST, HAWK-I and Spitzer images of DEEPSPACE ID 4031.

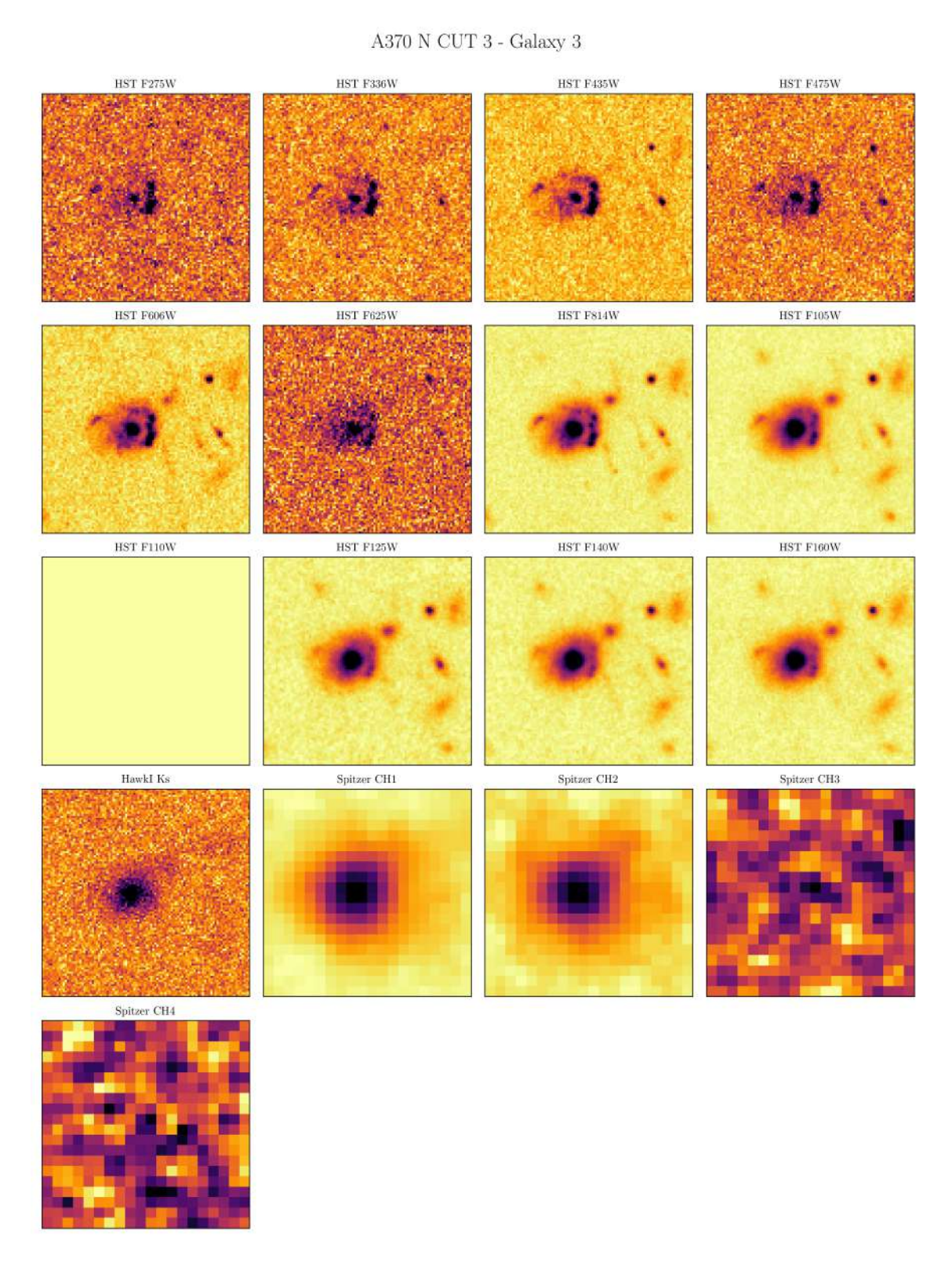


Figure B.27: HST, HAWK-I and Spitzer images of DEEPSPACE ID 4321.

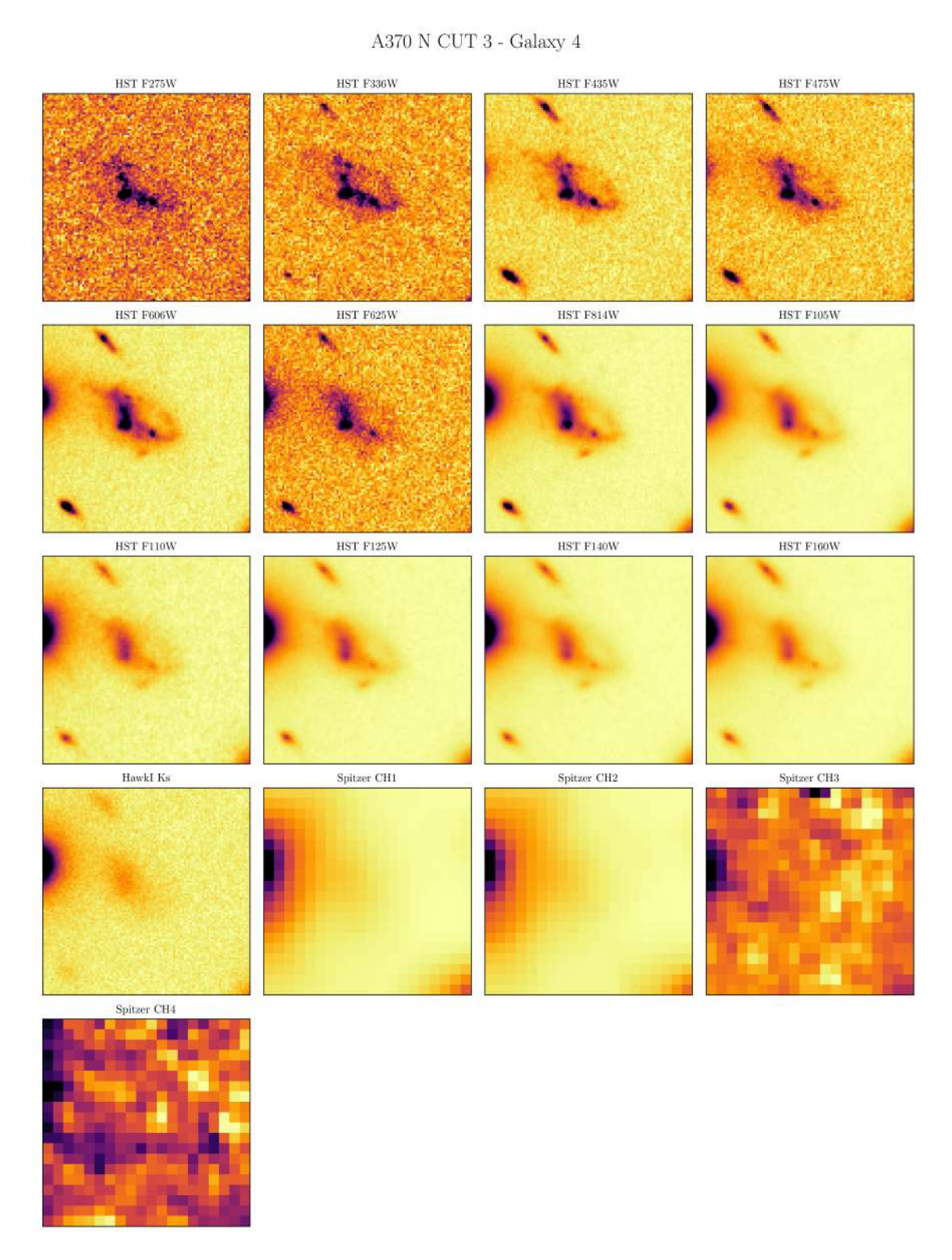


Figure B.28: HST, HAWK-I and Spitzer images of DEEPSPACE ID 5199.

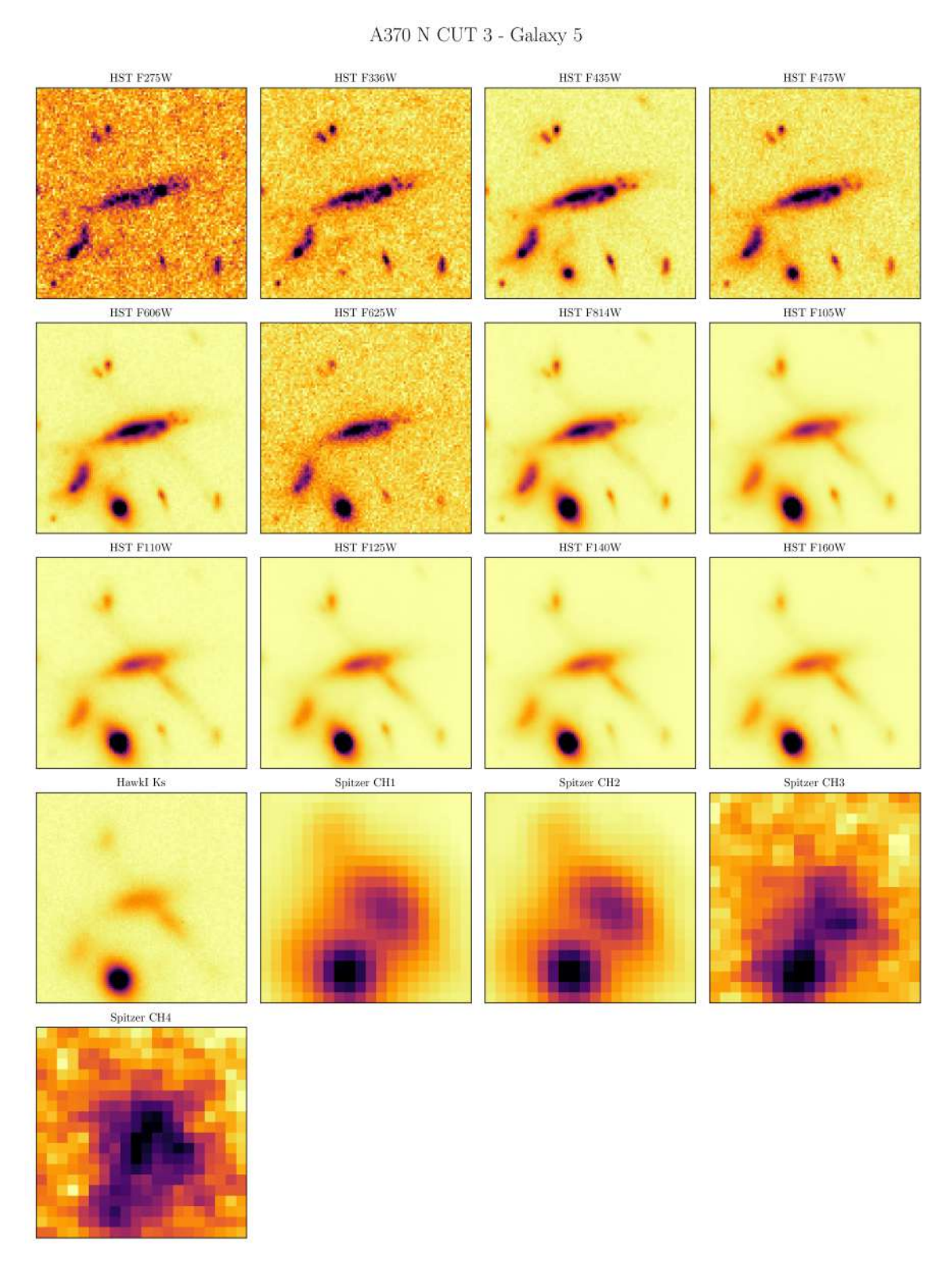


Figure B.29: HST, HAWK-I and Spitzer images of DEEPSPACE ID 3923.

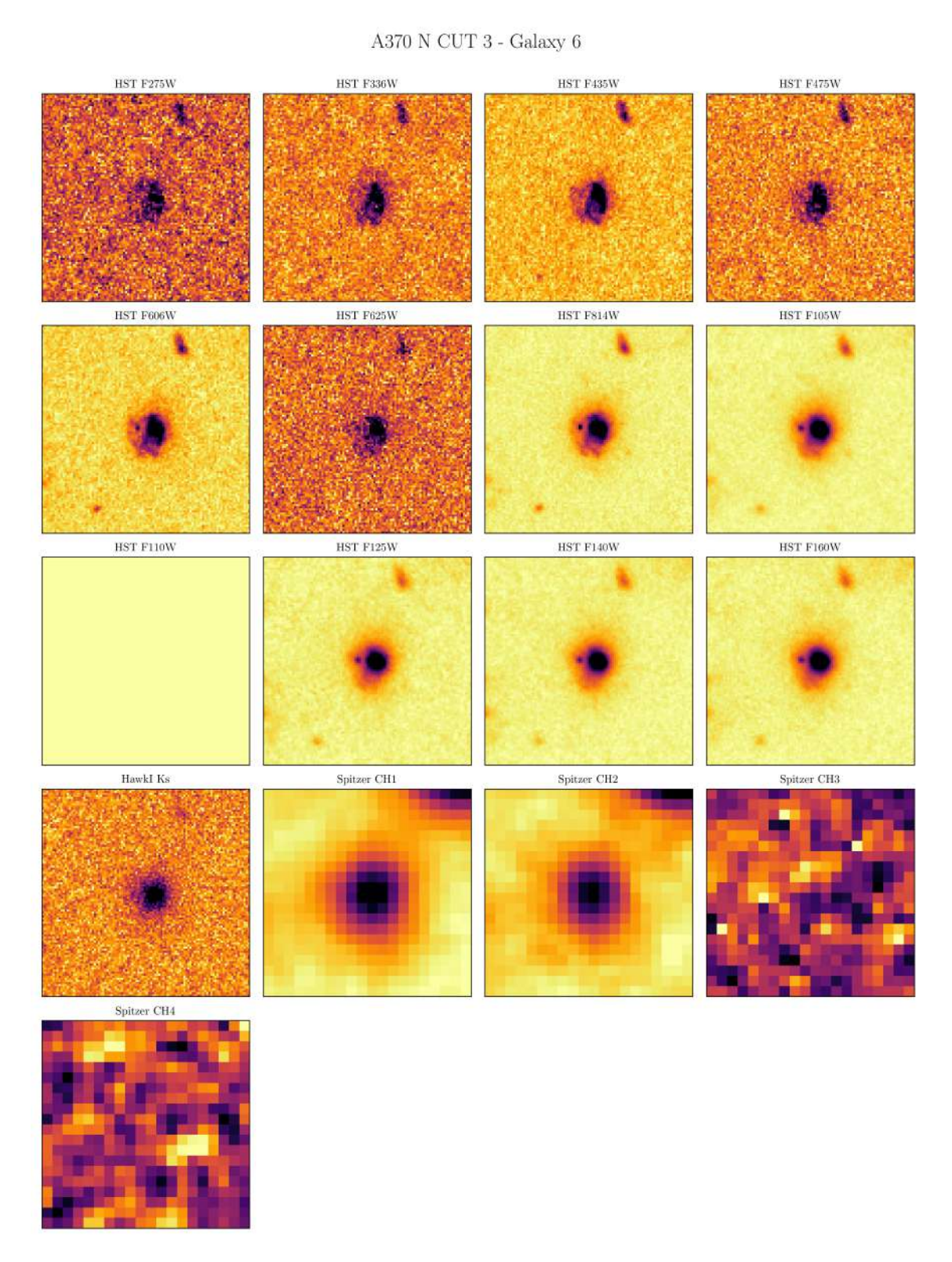


Figure B.30: HST, HAWK-I and Spitzer images of DEEPSPACE ID 5915.

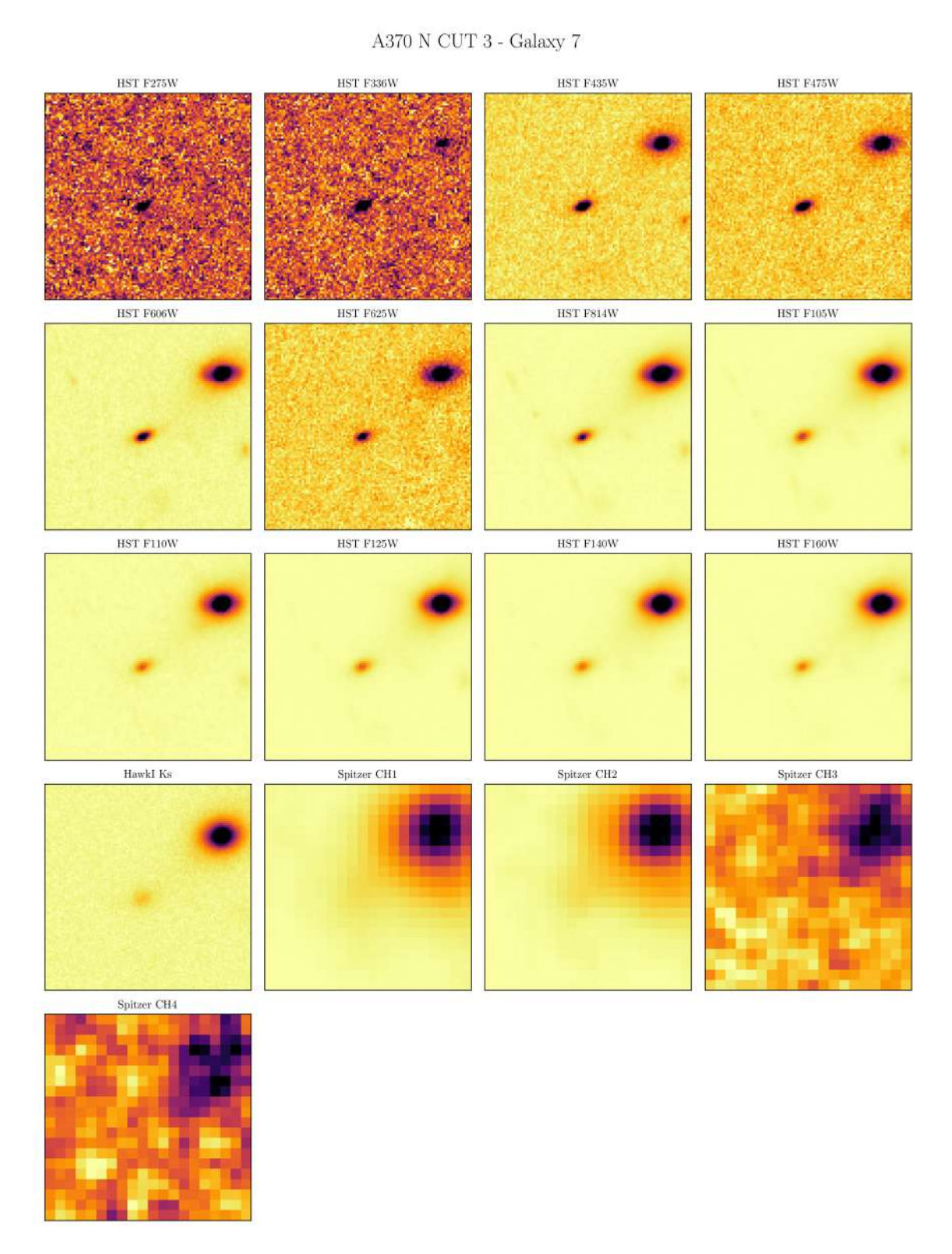


Figure B.31: HST, HAWK-I and Spitzer images of DEEPSPACE ID 3906.

### B.4 A370 S CUT 1



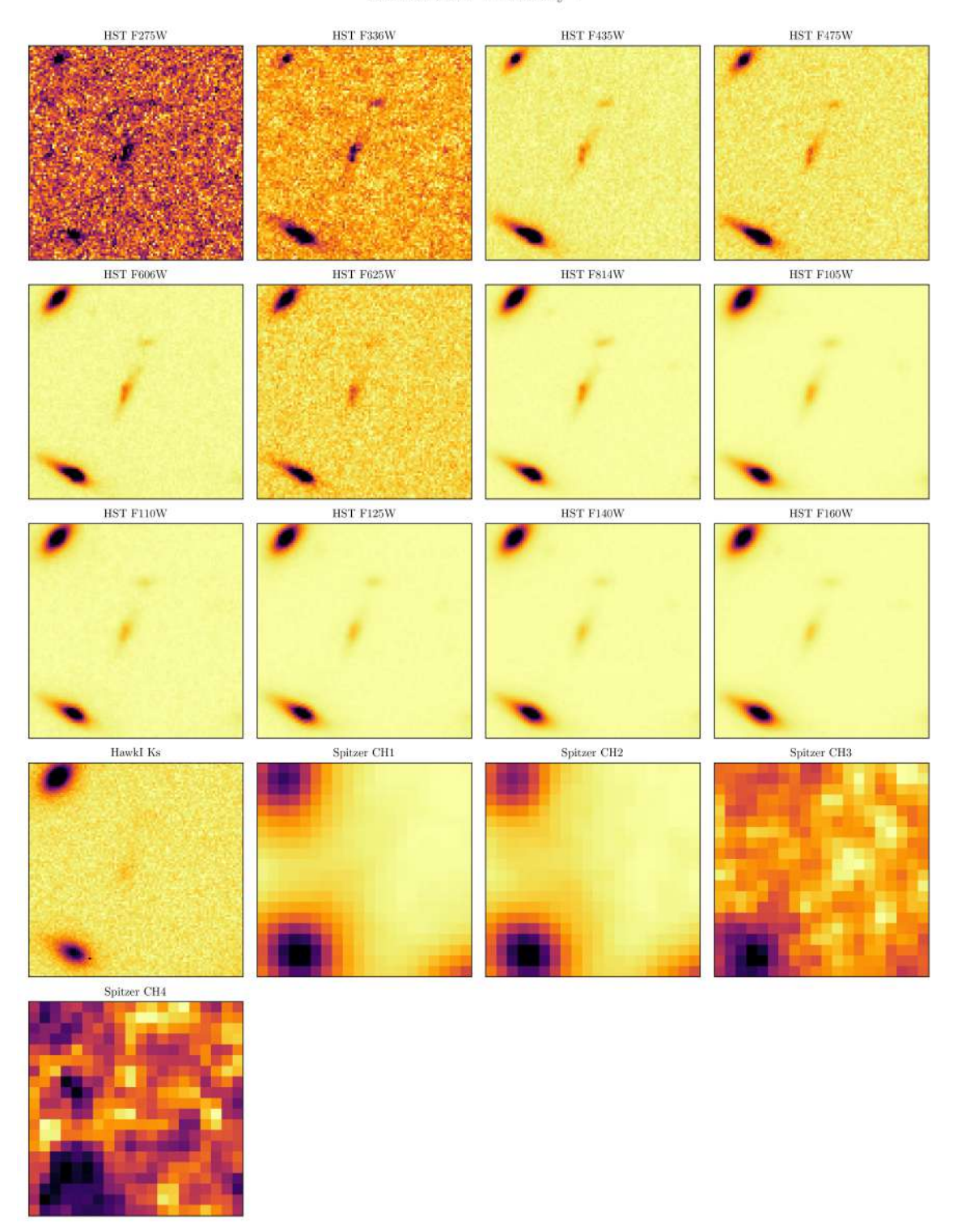


Figure B.32: HST, HAWK-I and Spitzer images of DEEPSPACE ID 1602.

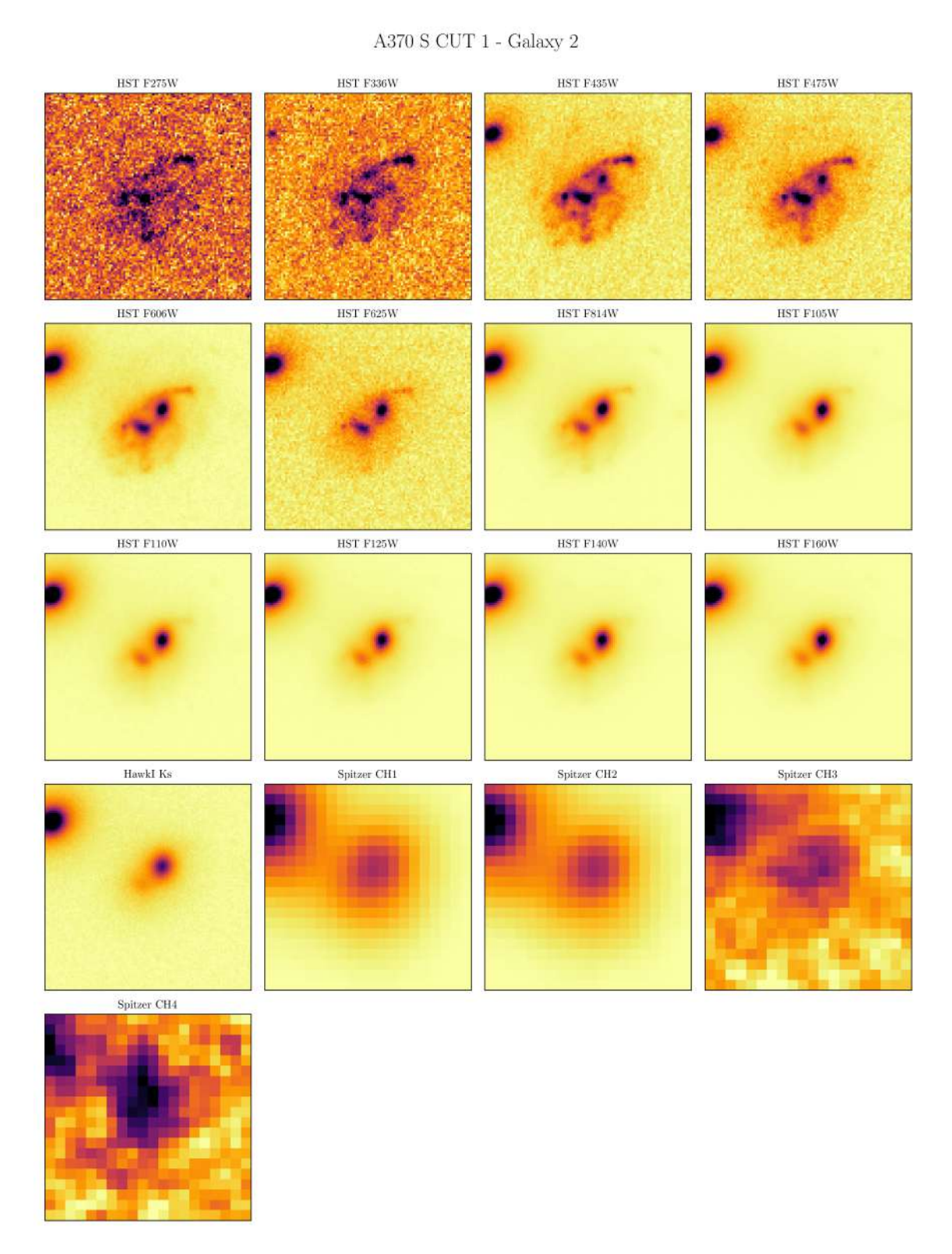


Figure B.33: HST, HAWK-I and Spitzer images of DEEPSPACE ID 2807.

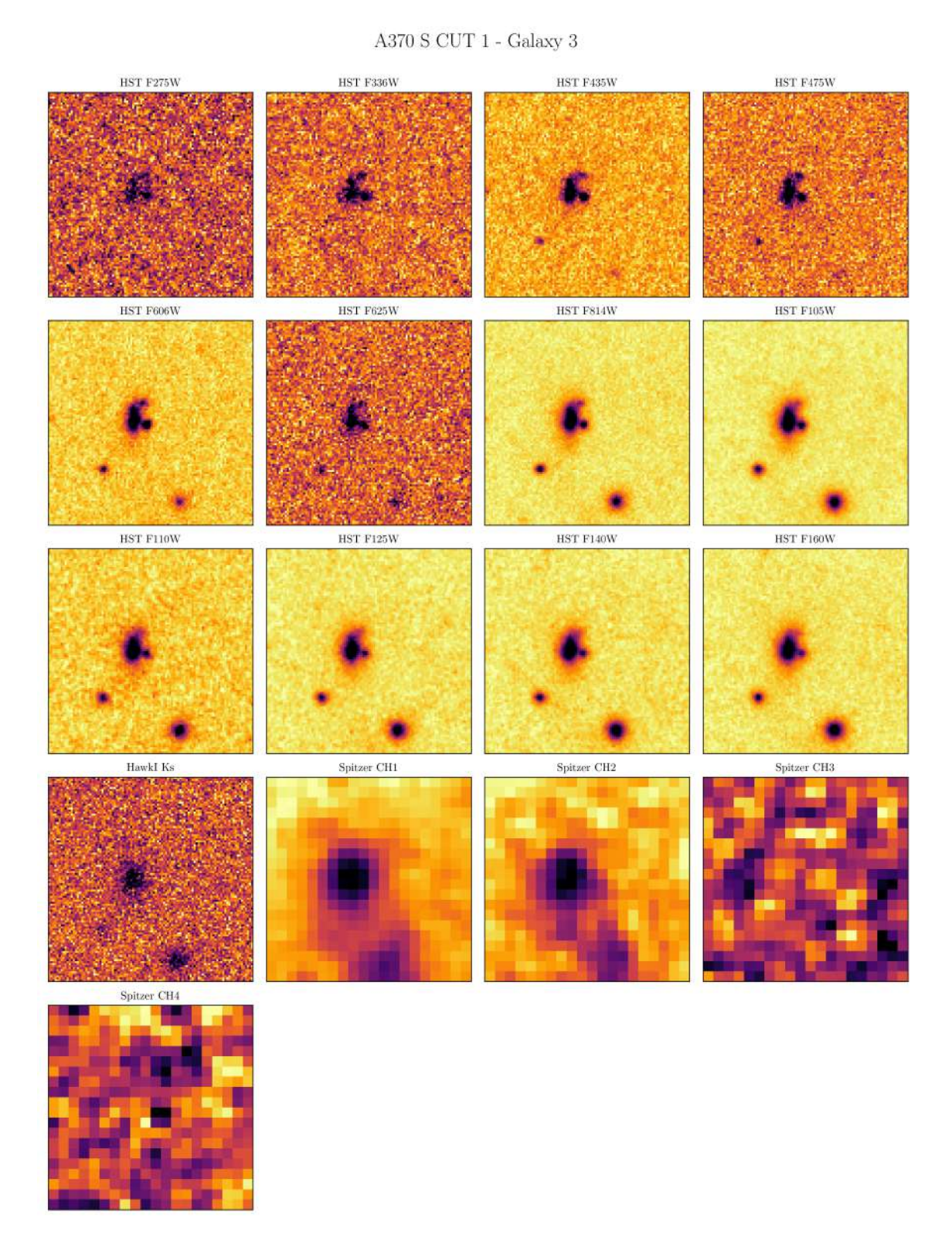


Figure B.34: HST, HAWK-I and Spitzer images of DEEPSPACE ID 2002.

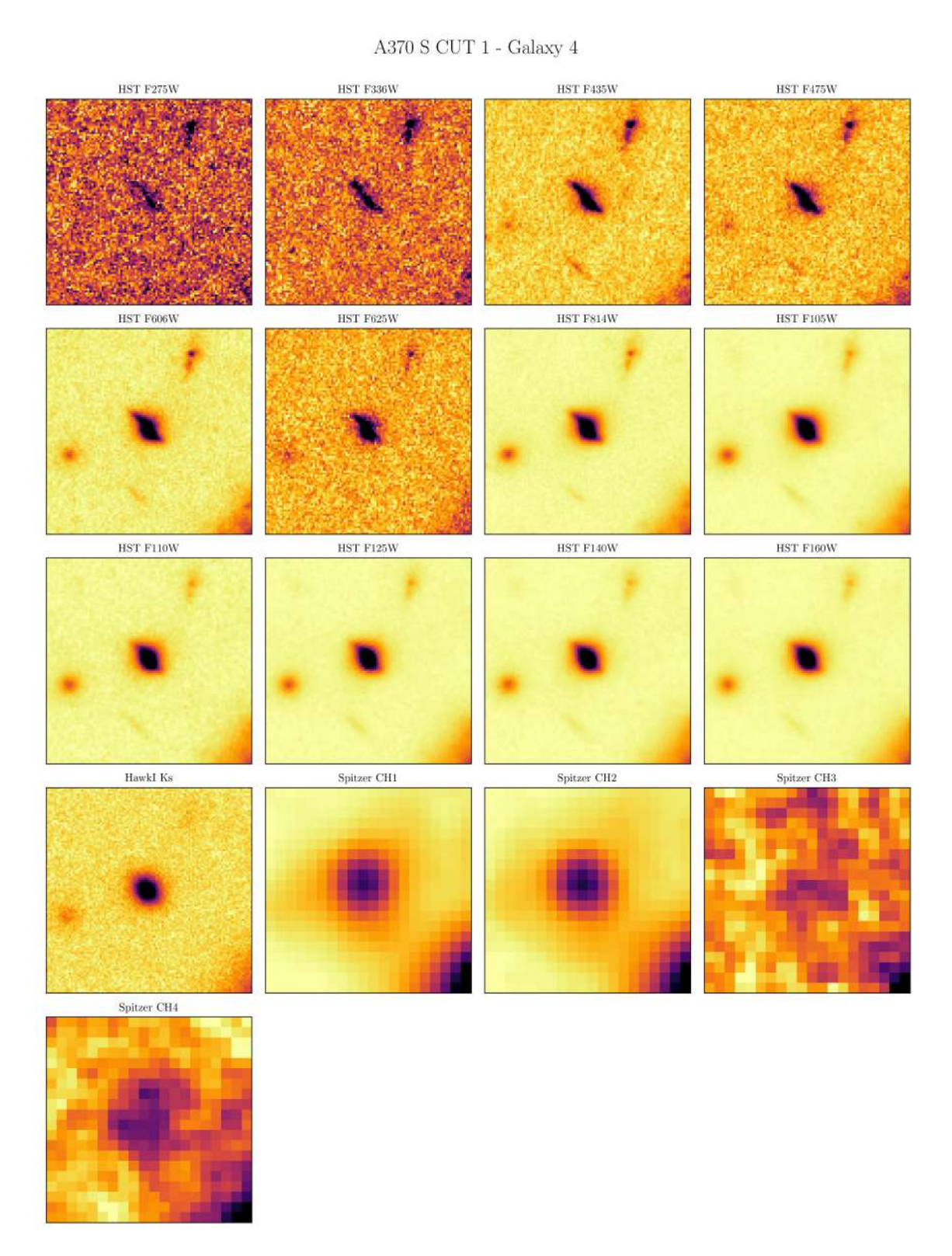
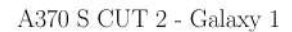


Figure B.35: HST, HAWK-I and Spitzer images of DEEPSPACE ID 2441.

### B.5 A370 S CUT 2



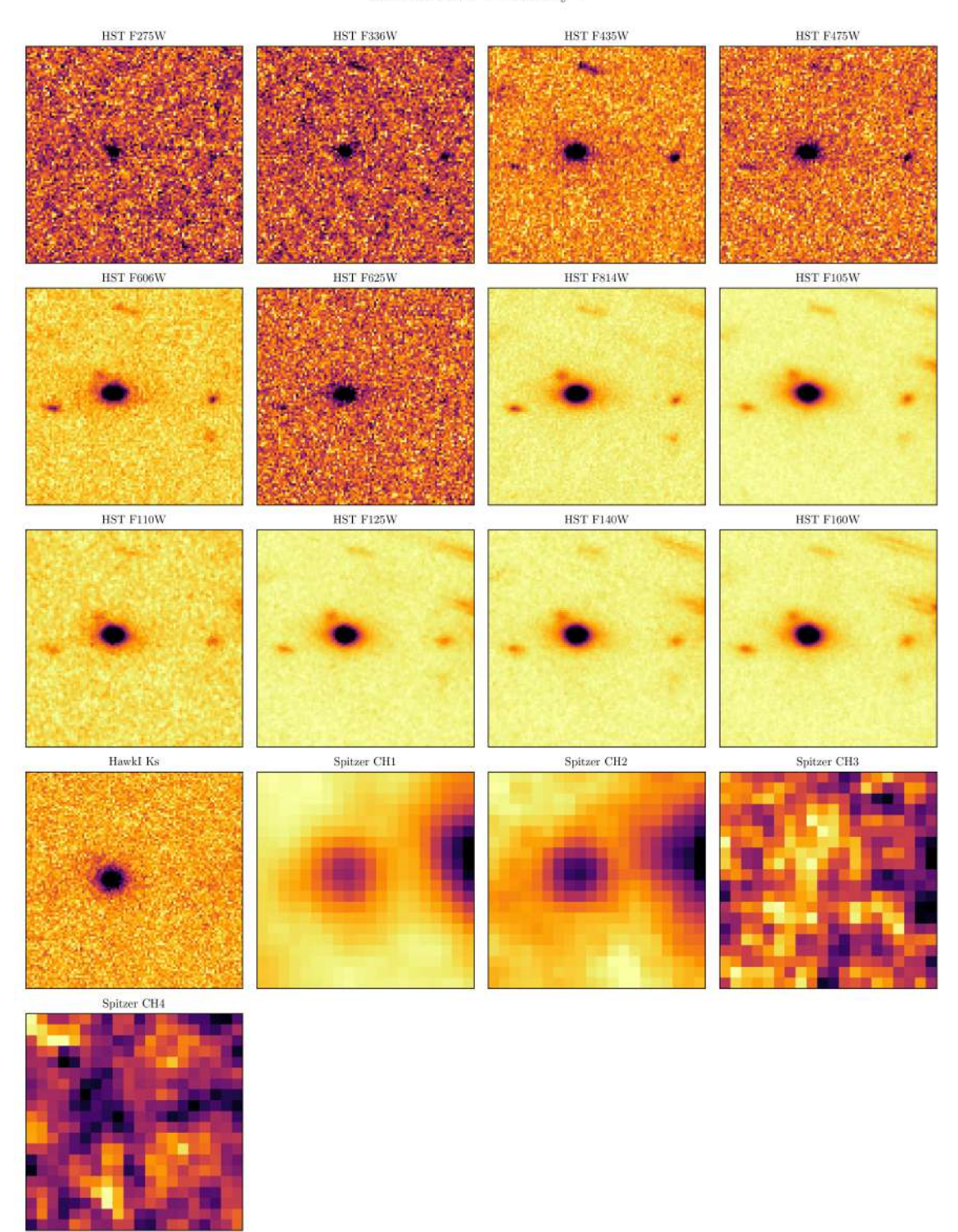


Figure B.36: HST, HAWK-I and Spitzer images of DEEPSPACE ID 998.

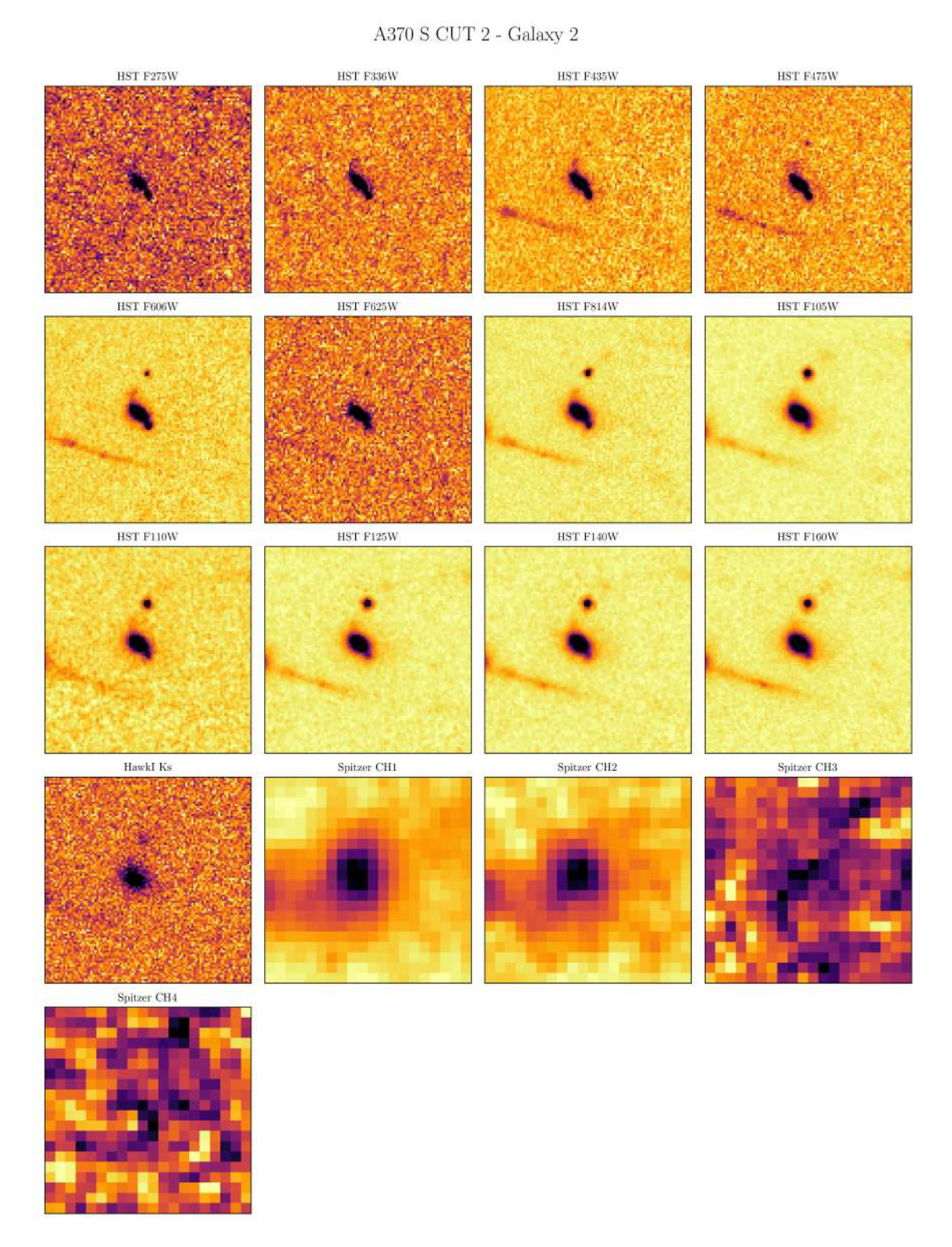


Figure B.37: HST, HAWK-I and Spitzer images of DEEPSPACE ID 1247.

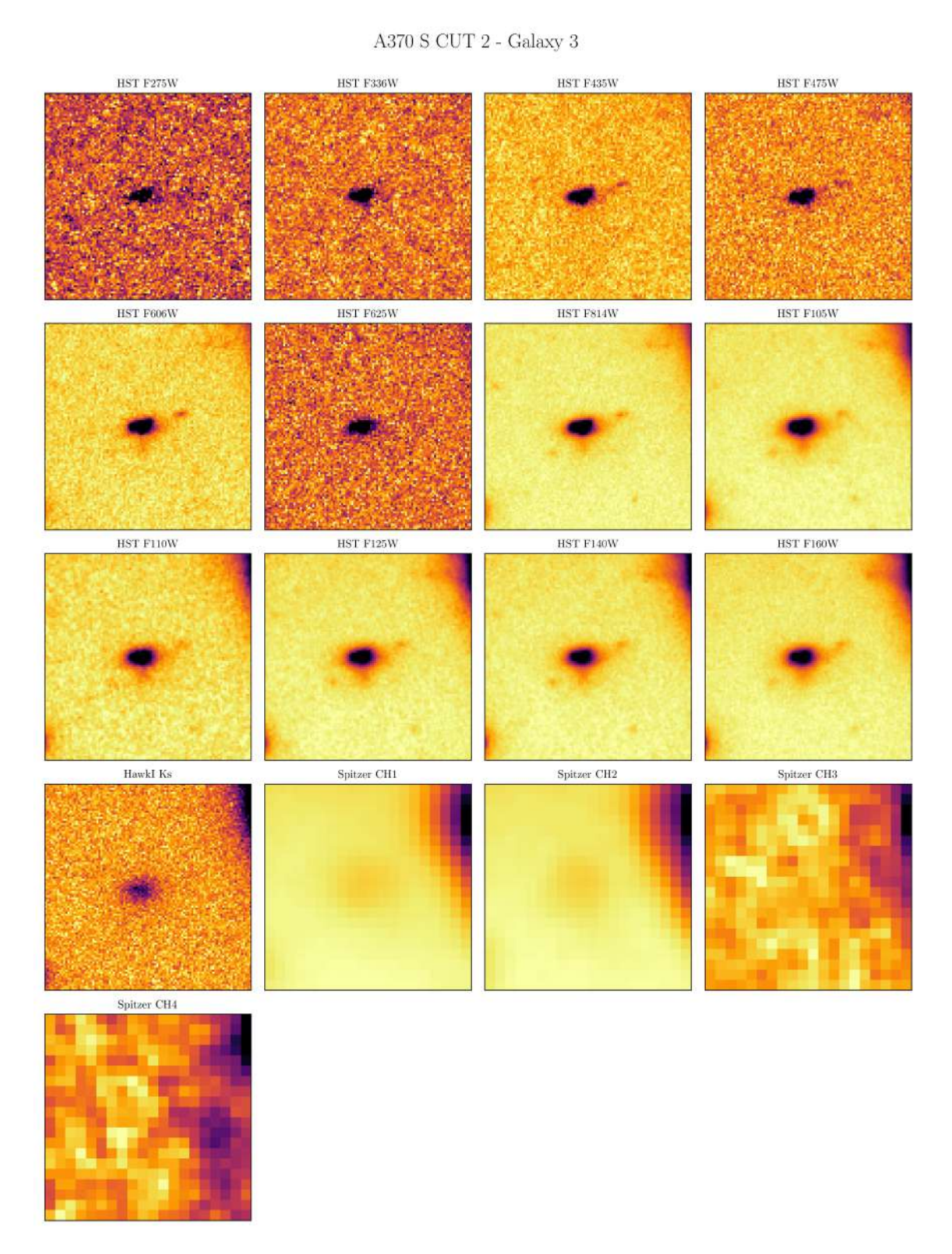


Figure B.38: HST, HAWK-I and Spitzer images of DEEPSPACE ID 1989.

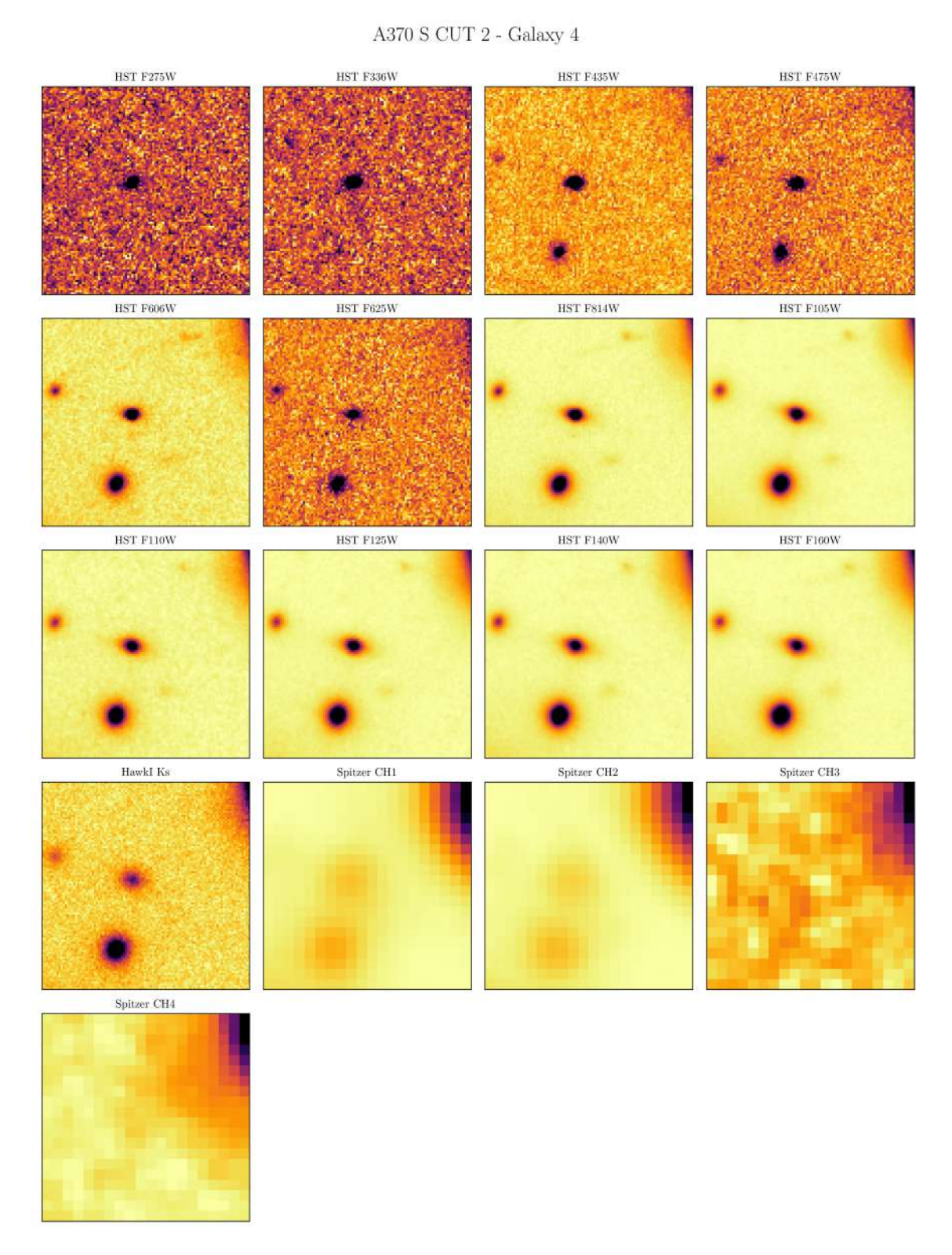


Figure B.39: HST, HAWK-I and Spitzer images of DEEPSPACE ID 1666.

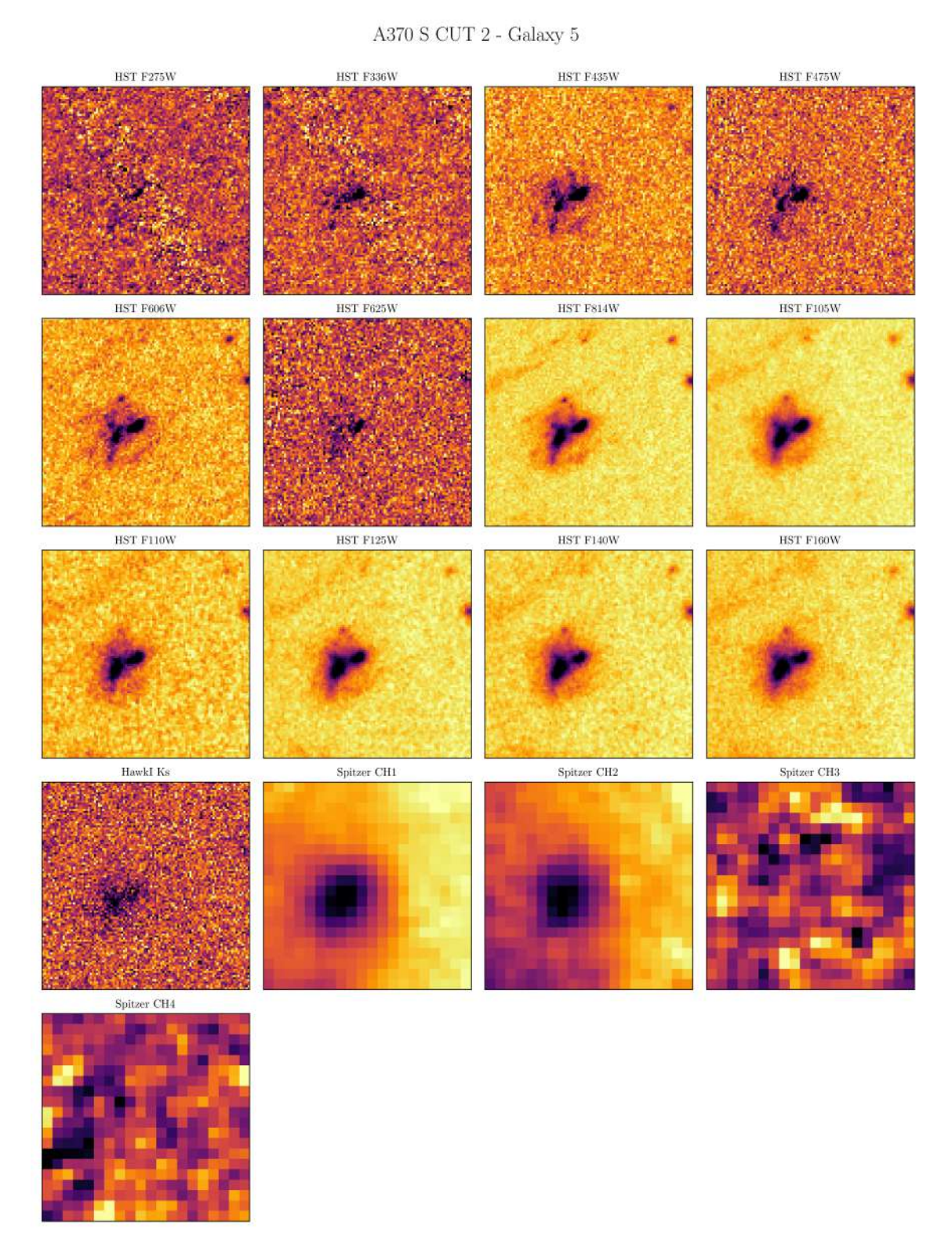


Figure B.40: HST, HAWK-I and Spitzer images of DEEPSPACE ID 1857.

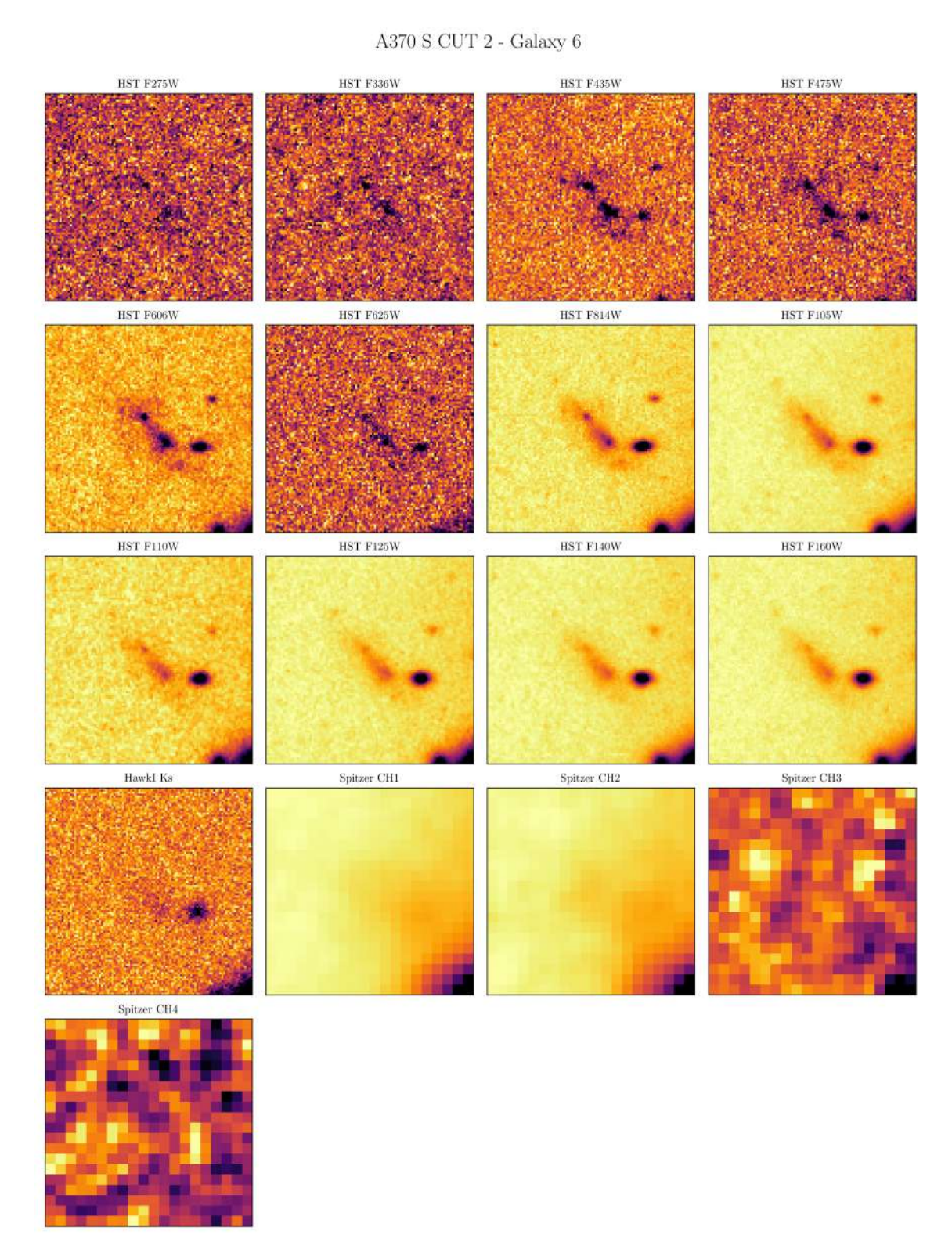


Figure B.41: HST, HAWK-I and Spitzer images of DEEPSPACE ID 2753.

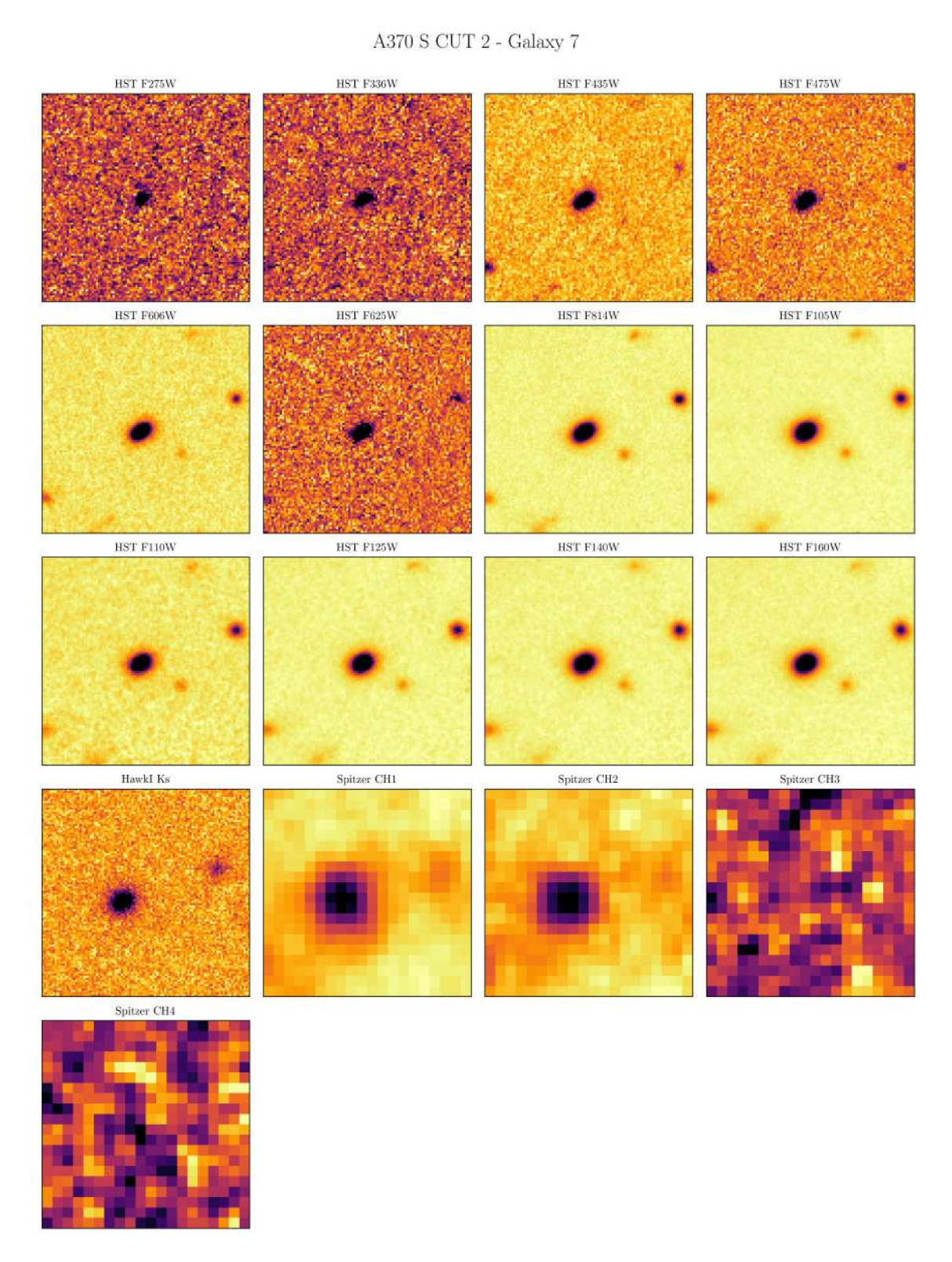


Figure B.42: HST, HAWK-I and Spitzer images of DEEPSPACE ID 1227.

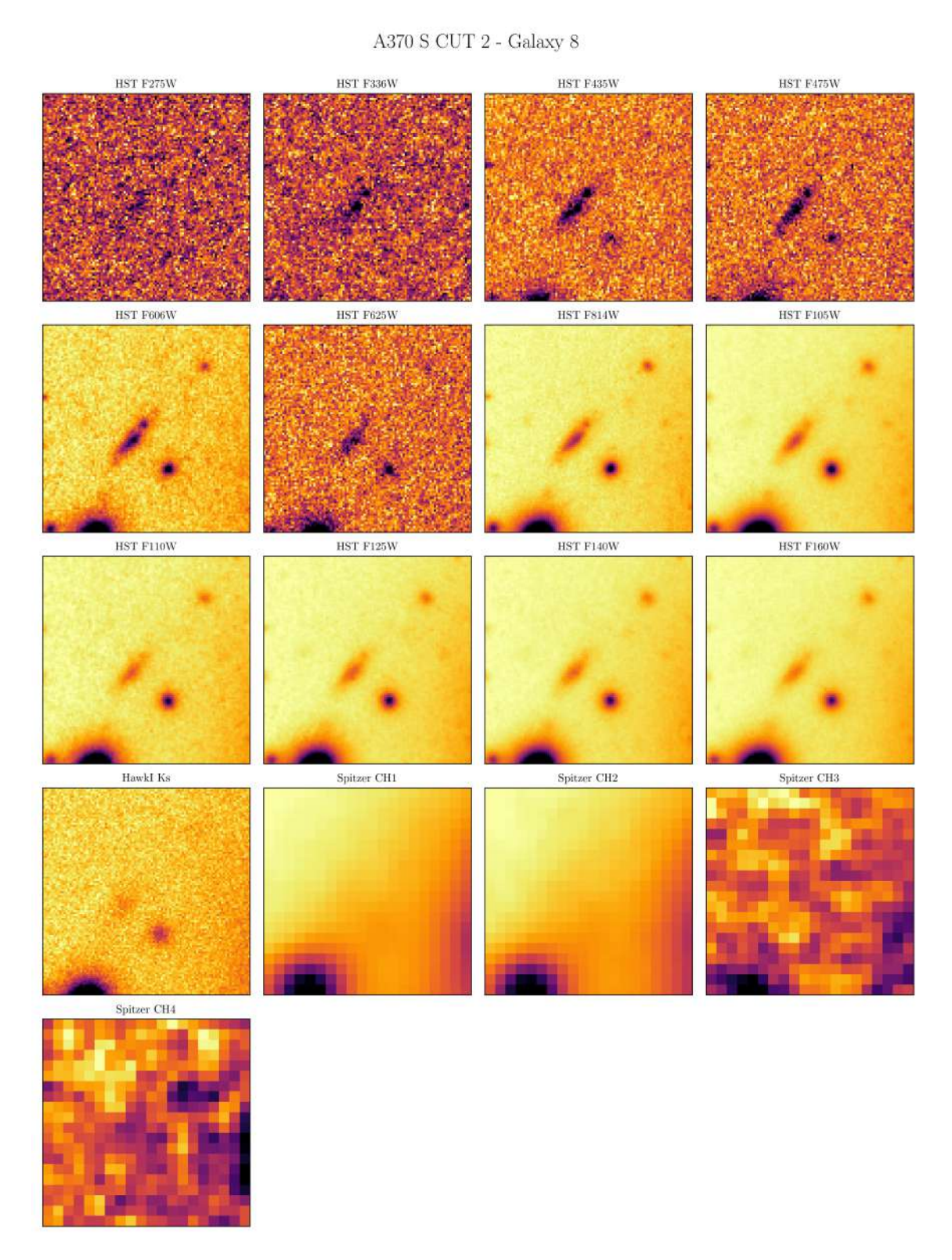


Figure B.43: HST, HAWK-I and Spitzer images of DEEPSPACE ID 3060.

### B.6 A370 S CUT 3

A370 S CUT 3 - Galaxy 1

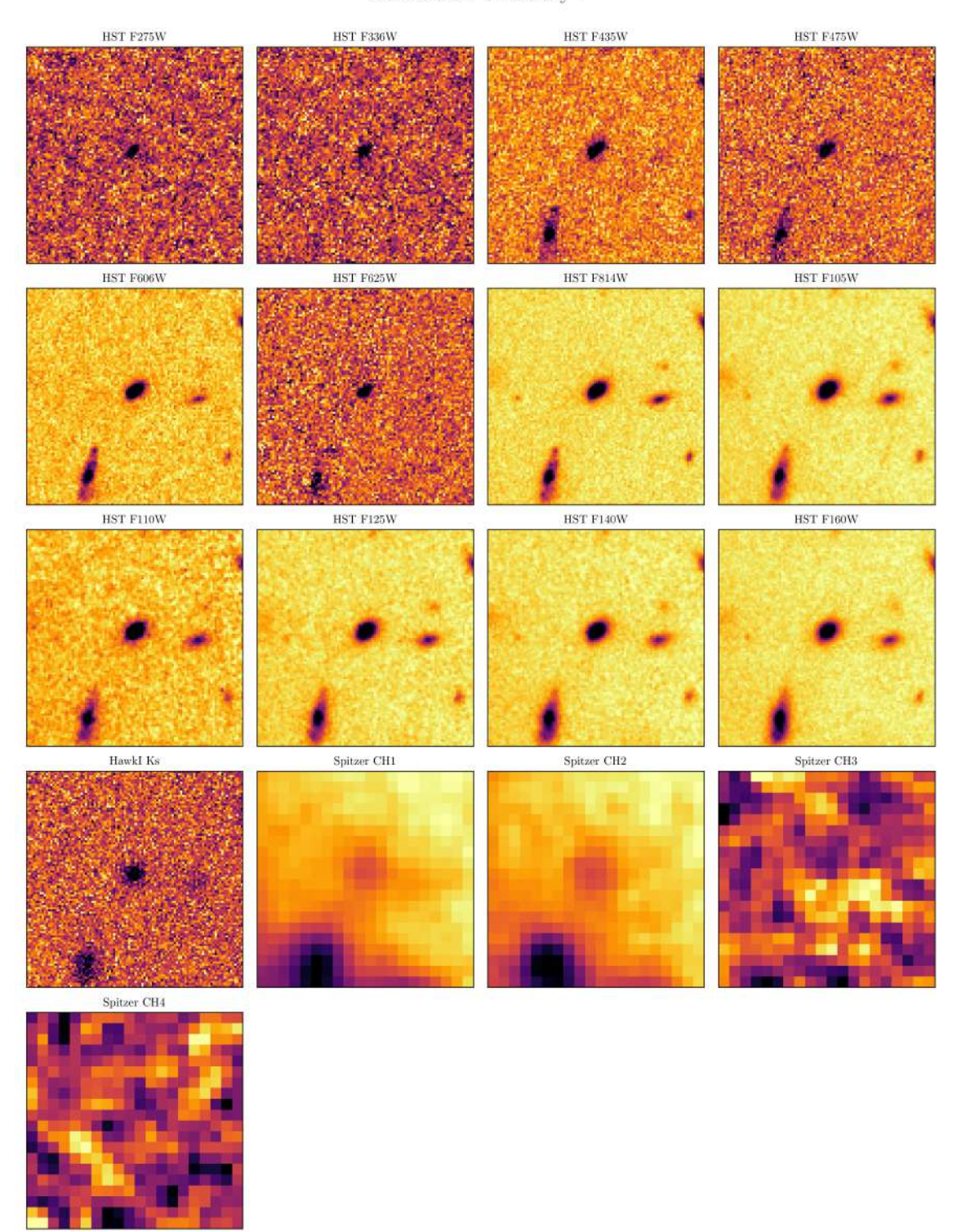


Figure B.44: HST, HAWK-I and Spitzer images of DEEPSPACE ID 2935.

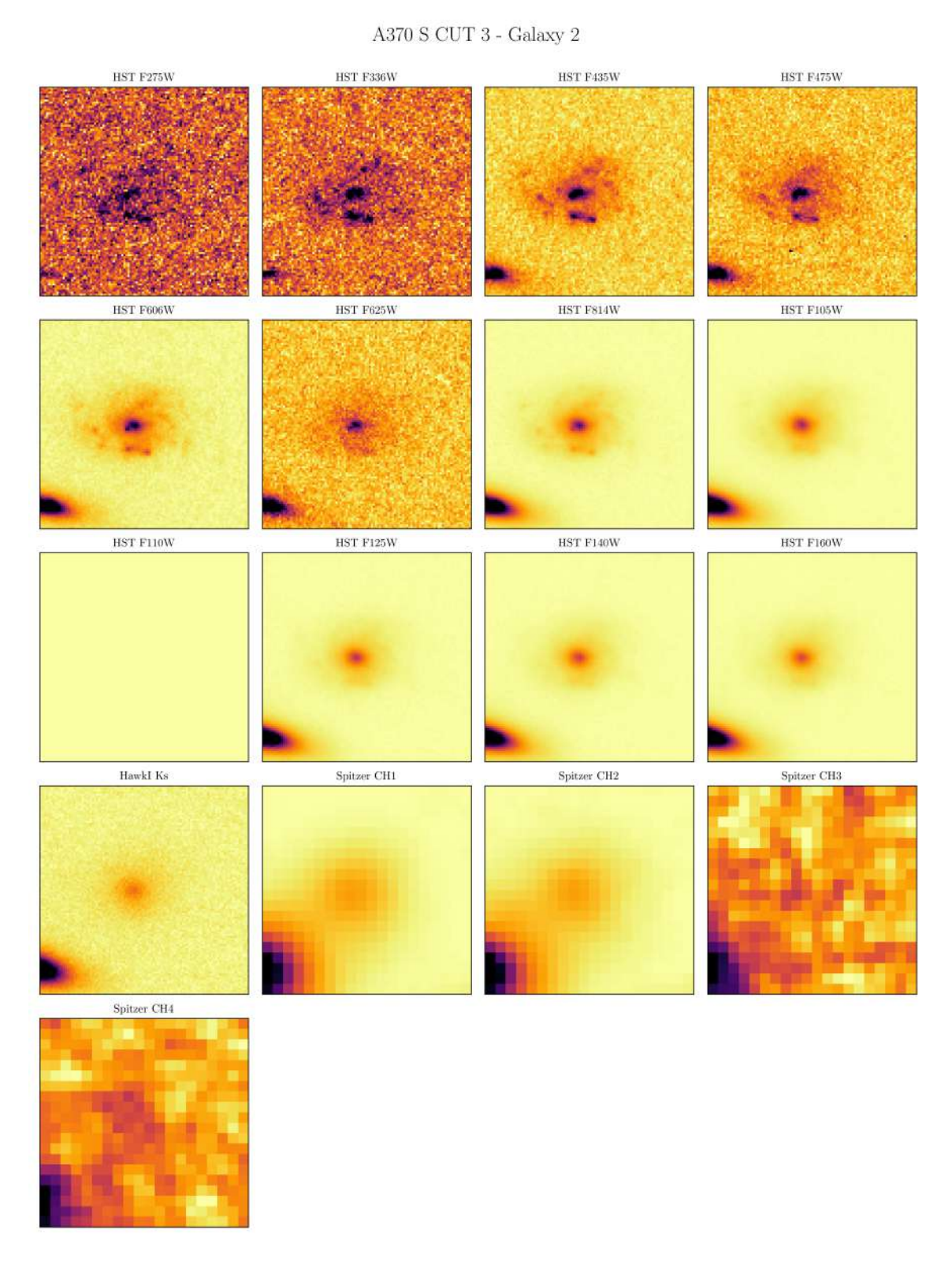


Figure B.45: HST, HAWK-I and Spitzer images of DEEPSPACE ID 3187.

# **Bibliography**

- Abazajian, K., Adelman-McCarthy, J. K., Agüeros, M. A., et al. 2003, AJ, 126, 2081, doi: 10.1086/378165
- Agertz, O., Kravtsov, A. V., Leitner, S. N., & Gnedin, N. Y. 2013, ApJ, 770, 25, doi: 10.1088/0004-637X/770/1/25
- Álvarez-Márquez, J., Crespo Gómez, A., Colina, L., et al. 2023, A&A, 671, A105, doi: 10. 1051/0004-6361/202245400
- Amorín, R., Aguerri, J. A. L., Muñoz-Tuñón, C., & Cairós, L. M. 2009, A&A, 501, 75, doi: 10.1051/0004-6361/200809591
- Amorín, R., Pérez-Montero, E., Vílchez, J. M., & Papaderos, P. 2012, ApJ, 749, 185, doi: 10.1088/0004-637X/749/2/185
- Amorín, R., Pérez-Montero, E., Contini, T., et al. 2015, A&A, 578, A105, doi: 10.1051/0004-6361/201322786
- Amorín, R. O., Muñoz-Tuñón, C., Aguerri, J. A. L., Cairós, L. M., & Caon, N. 2007, A&A, 467, 541, doi: 10.1051/0004-6361:20066152
- Amorín, R. O., Pérez-Montero, E., & Vílchez, J. M. 2010, ApJ, 715, L128, doi: 10.1088/2041-8205/715/2/L128
- Andrews, B. H., & Martini, P. 2013, ApJ, 765, 140, doi: 10.1088/0004-637X/765/2/140
- Arrabal Haro, P., Dickinson, M., Finkelstein, S. L., et al. 2023, Nature, 622, 707, doi: 10.1038/s41586-023-06521-7
- Asplund, M., Amarsi, A. M., & Grevesse, N. 2021, A&A, 653, A141, doi: 10.1051/0004-6361/202140445
- Bacon, R., Piqueras, L., Conseil, S., Richard, J., & Shepherd, M. 2016, MPDAF: MUSE Python Data Analysis Framework, Astrophysics Source Code Library, record ascl:1611.003. http://ascl.net/1611.003

- Bacon, R., Accardo, M., Adjali, L., et al. 2010, in Society of Photo-Optical Instrumentation Engineers (SPIE) Conference Series, Vol. 7735, Ground-based and Airborne Instrumentation for Astronomy III, ed. I. S. McLean, S. K. Ramsay, & H. Takami, 773508, doi: 10.1117/12.856027
- Baldwin, J. A., Phillips, M. M., & Terlevich, R. 1981, PASP, 93, 5, doi: 10.1086/130766
- Bertin, E., & Arnouts, S. 1996, A&AS, 117, 393, doi: 10.1051/aas:1996164
- Besla, G., Patton, D. R., Stierwalt, S., et al. 2018, MNRAS, 480, 3376, doi: 10.1093/mnras/sty2041
- Bian, F., Kewley, L. J., & Dopita, M. A. 2018, ApJ, 859, 175, doi: 10.3847/1538-4357/aabd74
- Blanc, G. A., Kewley, L., Vogt, F. P. A., & Dopita, M. A. 2015, ApJ, 798, 99, doi: 10. 1088/0004-637X/798/2/99
- Blumenthal, G., Faber, S., Primack, J., & REES, M. 1985, Nature, 313, doi: 10.1038/313072a0
- Bobylev, V. V., & Baykova, A. T. 2023, Astronomy Reports, 67, 812, doi: 10.1134/ \$1063772923080024
- Boquien, M., Burgarella, D., Roehlly, Y., et al. 2019, A&A, 622, A103, doi: 10.1051/0004-6361/201834156
- Bradač, M., Huang, K.-H., Fontana, A., et al. 2019, MNRAS, 489, 99, doi: 10.1093/mnras/stz2119
- Brammer, G. B., Marchesini, D., Labbé, I., et al. 2016, ApJS, 226, 6, doi: 10.3847/0067-0049/226/1/6
- Bresolin, F., Garnett, D. R., & Kennicutt, Robert C., J. 2004, ApJ, 615, 228, doi: 10.1086/424377
- Bressan, A., Fagotto, F., Bertelli, G., & Chiosi, C. 1993, A&AS, 100, 647
- Brutti, P., Genovese, C. R., Miller, C. J., Nichol, R. C., & Wasseerman, L. H. 2005. https://api.semanticscholar.org/CorpusID:14205268
- Bruzual, G., & Charlot, S. 2003, MNRAS, 344, 1000, doi: 10.1046/j.1365-8711.2003. 06897.x
- Cairós, L. M., Caon, N., Vílchez, J. M., González-Pérez, J. N., & Muñoz-Tuñón, C. 2001, ApJS, 136, 393, doi: 10.1086/322532
- Cairós, L. M., Caon, N., Zurita, C., et al. 2010, A&A, 520, A90, doi: 10.1051/0004-6361/201014004

- Calabrò, A., Amorín, R., Fontana, A., et al. 2017, A&A, 601, A95, doi: 10.1051/0004-6361/201629762
- Calzetti, D. 2012, Star Formation Rate Indicators. https://arxiv.org/abs/1208.2997
- Calzetti, D., Armus, L., Bohlin, R. C., et al. 2000, ApJ, 533, 682, doi: 10.1086/308692
- Cardamone, C., Schawinski, K., Sarzi, M., et al. 2009, MNRAS, 399, 1191, doi: 10.1111/j.1365-2966.2009.15383.x
- Cardelli, J. A., Clayton, G. C., & Mathis, J. S. 1989, ApJ, 345, 245, doi: 10.1086/167900
- Carnall, A. C., McLure, R. J., Dunlop, J. S., & Davé, R. 2018, Monthly Notices of the Royal Astronomical Society, 480, 4379–4401, doi: 10.1093/mnras/sty2169
- Castellano, M., Amorín, R., Merlin, E., et al. 2016, A&A, 590, A31, doi: 10.1051/0004-6361/201527514
- Cole, S., Lacey, C. G., Baugh, C. M., & Frenk, C. S. 2000, MNRAS, 319, 168, doi: 10.1046/j.1365-8711.2000.03879.x
- Conroy, C. 2013, ARA&A, 51, 393, doi: 10.1146/annurev-astro-082812-141017
- Cowie, L. L., Songaila, A., Hu, E. M., & Cohen, J. G. 1996, AJ, 112, 839, doi: 10.1086/ 118058
- Curti, M., Cresci, G., Mannucci, F., et al. 2017, MNRAS, 465, 1384, doi: 10.1093/mnras/stw2766
- Curti, M., Mannucci, F., Cresci, G., & Maiolino, R. 2020, MNRAS, 491, 944, doi: 10. 1093/mnras/stz2910
- Curti, M., Maiolino, R., Curtis-Lake, E., et al. 2024, A&A, 684, A75, doi: 10.1051/ 0004-6361/202346698
- del Valle-Espinosa, M. G., Sánchez-Janssen, R., Amorín, R., et al. 2023, MNRAS, 522, 2089, doi: 10.1093/mnras/stad1087
- de Oliveira, N. O. L., Jiménez-Teja, Y., & Dupke, R. 2022, Monthly Notices of the Royal Astronomical Society, 512, 1916–1923, doi: 10.1093/mnras/stac407
- Dickinson, M., Amorin, R., Arrabal Haro, P., et al. 2024, The CANDELS-Area Prism Epoch of Reionization Survey (CAPERS), JWST Proposal. Cycle 3, ID. #6368
- Donnan, C. T., McLeod, D. J., McLure, R. J., et al. 2023, MNRAS, 520, 4554, doi: 10.1093/mnras/stad471
- Dopita, M. A., Sutherland, R. S., Nicholls, D. C., Kewley, L. J., & Vogt, F. P. A. 2013, ApJS, 208, 10, doi: 10.1088/0067-0049/208/1/10

- Duan, Q., Conselice, C. J., Li, Q., et al. 2024, MNRAS, 529, 4728, doi: 10.1093/mnras/stae872
- Eisenstein, D. J., Willott, C., Alberts, S., et al. 2023, Overview of the JWST Advanced Deep Extragalactic Survey (JADES). https://arxiv.org/abs/2306.02465
- Eldridge, J. J., Stanway, E. R., Xiao, L., et al. 2017, PASA, 34, e058, doi: 10.1017/pasa. 2017.51
- Ellison, S. L., Patton, D. R., Simard, L., & McConnachie, A. W. 2008, ApJ, 672, L107, doi: 10.1086/527296
- Erb, D. K., Shapley, A. E., Pettini, M., et al. 2006, The Astrophysical Journal, 644, 813, doi: 10.1086/503623
- Fernández, V., Amorín, R., Firpo, V., & Morisset, C. 2024, arXiv e-prints, arXiv:2405.15072, doi: 10.48550/arXiv.2405.15072
- Fernández, V., Amorín, R., Pérez-Montero, E., et al. 2022, MNRAS, 511, 2515, doi: 10. 1093/mnras/stab3150
- Feroz, F., & Hobson, M. P. 2008, Monthly Notices of the Royal Astronomical Society, 384, 449–463, doi: 10.1111/j.1365-2966.2007.12353.x
- Feroz, F., Hobson, M. P., & Bridges, M. 2009, Monthly Notices of the Royal Astronomical Society, 398, 1601–1614, doi: 10.1111/j.1365-2966.2009.14548.x
- Feroz, F., Hobson, M. P., Cameron, E., & Pettitt, A. N. 2019, The Open Journal of Astrophysics, 2, doi: 10.21105/astro.1306.2144
- Figueira, M., Pollo, A., Małek, K., et al. 2022, A&A, 667, A29, doi: 10.1051/0004-6361/202141701
- Finkelstein, S. L., Bagley, M. B., Arrabal Haro, P., et al. 2022, ApJ, 940, L55, doi: 10. 3847/2041-8213/ac966e
- Finkelstein, S. L., Bagley, M. B., Ferguson, H. C., et al. 2023, ApJ, 946, L13, doi: 10. 3847/2041-8213/acade4
- Finkelstein, S. L., Leung, G. C. K., Bagley, M. B., et al. 2024, ApJ, 969, L2, doi: 10. 3847/2041-8213/ad4495
- Fioc, M., & Rocca-Volmerange, B. 1997, A&A, 326, 950, doi: 10.48550/arXiv.astro-ph/9707017
- Gao, Y., Bao, M., Yuan, Q., et al. 2018, The Astrophysical Journal, 869, 15, doi: 10. 3847/1538-4357/aae9ef

- Gardner, J. P., Mather, J. C., Abbott, R., et al. 2023, Publications of the Astronomical Society of the Pacific, 135, 068001, doi: 10.1088/1538-3873/acd1b5
- Garg, P., Narayanan, D., Byler, N., et al. 2022, The Astrophysical Journal, 926, 80, doi: 10.3847/1538-4357/ac43b8
- Garnett, D. R. 1992, AJ, 103, 1330, doi: 10.1086/116146
- Garnett, D. R., Kennicutt, Robert C., J., & Bresolin, F. 2004, ApJ, 607, L21, doi: 10. 1086/421489
- González, R. E., & Padilla, N. D. 2016, ApJ, 829, 58, doi: 10.3847/0004-637X/829/1/58
- Guo, K., Zheng, X. Z., Wang, T., & Fu, H. 2015, ApJ, 808, L49, doi: 10.1088/2041-8205/808/2/L49
- Harikane, Y., Nakajima, K., Ouchi, M., et al. 2024, ApJ, 960, 56, doi: 10.3847/1538-4357/ad0b7e
- Izotov, Y. I., Guseva, N. G., Fricke, K. J., & Henkel, C. 2016, MNRAS, 462, 4427, doi: 10.1093/mnras/stw1973
- Janowiecki, S., Salzer, J. J., van Zee, L., Rosenberg, J. L., & Skillman, E. 2017, ApJ, 836, 128, doi: 10.3847/1538-4357/836/1/128
- Johnson, T. L., Sharon, K., Bayliss, M. B., et al. 2014, ApJ, 797, 48, doi: 10.1088/ 0004-637X/797/1/48
- Kauffmann, G., Heckman, T. M., Tremonti, C., et al. 2003, MNRAS, 346, 1055, doi: 10. 1111/j.1365-2966.2003.07154.x
- Kennicutt, R. C., J., & Keel, W. C. 1984, ApJ, 279, L5, doi: 10.1086/184243
- Kennicutt, Robert C., J. 1992, ApJS, 79, 255, doi: 10.1086/191653
- —. 1998, ARA&A, 36, 189, doi: 10.1146/annurev.astro.36.1.189
- Kewley, L. J., & Dopita, M. A. 2002, ApJS, 142, 35, doi: 10.1086/341326
- Kewley, L. J., Dopita, M. A., Sutherland, R. S., Heisler, C. A., & Trevena, J. 2001, ApJ, 556, 121, doi: 10.1086/321545
- Kewley, L. J., & Ellison, S. L. 2008, ApJ, 681, 1183, doi: 10.1086/587500
- Kewley, L. J., Maier, C., Yabe, K., et al. 2013, ApJ, 774, L10, doi: 10.1088/2041-8205/774/1/L10
- Kewley, L. J., Nicholls, D. C., & Sutherland, R. S. 2019, ARA&A, 57, 511, doi: 10.1146/annurev-astro-081817-051832

- Khostovan, A. A., Malhotra, S., Rhoads, J. E., et al. 2021, Monthly Notices of the Royal Astronomical Society, 503, 5115–5133, doi: 10.1093/mnras/stab778
- Kobulnicky, H. A., & Kewley, L. J. 2004, ApJ, 617, 240, doi: 10.1086/425299
- Koekemoer, A. M., Faber, S. M., Ferguson, H. C., et al. 2011, ApJS, 197, 36, doi: 10. 1088/0067-0049/197/2/36
- Kroupa, P., & Boily, C. M. 2002, MNRAS, 336, 1188, doi: 10.1046/j.1365-8711.2002.05848.x
- Kunth, D., & Östlin, G. 2000, A&ARv, 10, 1, doi: 10.1007/s001590000005
- Lagattuta, D. J., Richard, J., Clément, B., et al. 2017, MNRAS, 469, 3946, doi: 10.1093/mnras/stx1079
- Lagattuta, D. J., Richard, J., Bauer, F. E., et al. 2019, Monthly Notices of the Royal Astronomical Society, doi: 10.1093/mnras/stz620
- Lagattuta, D. J., Richard, J., Bauer, F. E., et al. 2022, MNRAS, 514, 497, doi: 10.1093/mnras/stac418
- Lamareille, F. 2010, A&A, 509, A53, doi: 10.1051/0004-6361/200913168
- Lamareille, F., Mouhcine, M., Contini, T., Lewis, I., & Maddox, S. 2004, in SF2A-2004: Semaine de l'Astrophysique Française, ed. F. Combes, D. Barret, T. Contini, F. Meynadier, & L. Pagani, 609
- Lara-López, M. A., Cepa, J., Bongiovanni, A., et al. 2010, A&A, 521, L53, doi: 10.1051/ 0004-6361/201014803
- Lara-Lopez, M. A., Hopkins, A. M., Lopez-Sanchez, A. R., et al. 2013, MNRAS, 433, L35, doi: 10.1093/mnrasl/slt054
- Le Fèvre, O., Tasca, L. A. M., Cassata, P., et al. 2015, A&A, 576, A79, doi: 10.1051/0004-6361/201423829
- Leitherer, C., Schaerer, D., Goldader, J. D., et al. 1999, ApJS, 123, 3, doi: 10.1086/313233
- Lequeux, J., Peimbert, M., Rayo, J. F., Serrano, A., & Torres-Peimbert, S. 1979, A&A, 80, 155
- Llerena, M., Amorín, R., Pentericci, L., et al. 2024, arXiv e-prints, arXiv:2403.05362, doi: 10.48550/arXiv.2403.05362
- Lotz, J. M., Koekemoer, A., Coe, D., et al. 2017, ApJ, 837, 97, doi: 10.3847/1538-4357/837/1/97

- Luridiana, V., Morisset, C., & Shaw, R. A. 2015, A&A, 573, A42, doi: 10.1051/0004-6361/201323152
- Ly, C., Malhotra, S., Malkan, M. A., et al. 2016a, ApJS, 226, 5, doi: 10.3847/0067-0049/226/1/5
- Ly, C., Malkan, M. A., Rigby, J. R., & Nagao, T. 2016b, ApJ, 828, 67, doi: 10.3847/ 0004-637X/828/2/67
- Madau, P., & Dickinson, M. 2014, Annual Review of Astronomy and Astrophysics, 52, 415–486, doi: 10.1146/annurev-astro-081811-125615
- Maiolino, R., & Mannucci, F. 2019, The Astronomy and Astrophysics Review, 27, doi: 10. 1007/s00159-018-0112-2
- Maiolino, R., Nagao, T., Grazian, A., et al. 2008, A&A, 488, 463, doi: 10.1051/0004-6361:200809678
- Mannucci, F., Cresci, G., Maiolino, R., Marconi, A., & Gnerucci, A. 2010, Monthly Notices of the Royal Astronomical Society, 408, 2115, doi: 10.1111/j.1365-2966.2010.17291.
- Martin, D. C., Fanson, J., Schiminovich, D., et al. 2005, ApJ, 619, L1, doi: 10.1086/ 426387
- McGaugh, S. S. 1991, ApJ, 380, 140, doi: 10.1086/170569
- McLure, R. J., Pentericci, L., Cimatti, A., et al. 2018, MNRAS, 479, 25, doi: 10.1093/mnras/sty1213
- McQuinn, K. B. W., Skillman, E. D., Cannon, J. M., et al. 2010, ApJ, 724, 49, doi: 10.1088/0004-637X/724/1/49
- Merlin, E., Fontana, A., Ferguson, H. C., et al. 2015, A&A, 582, A15, doi: 10.1051/0004-6361/201526471
- Merlin, E., Amorín, R., Castellano, M., et al. 2016, A&A, 590, A30, doi: 10.1051/0004-6361/201527513
- Mouri, H., & Taniguchi, Y. 2006, A&A, 459, 371, doi: 10.1051/0004-6361:20065604
- Moustakas, J., Zaritsky, D., Brown, M., et al. 2011, Evolution of the Stellar Mass-Metallicity Relation Since z=0.75. https://arxiv.org/abs/1112.3300
- Nagao, T., Maiolino, R., & Marconi, A. 2006, A&A, 459, 85, doi: 10.1051/0004-6361: 20065216

- Naidu, R. P., Oesch, P. A., Setton, D. J., et al. 2022, Schrodinger's Galaxy Candidate: Puzzlingly Luminous at  $z\approx 17$ , or Dusty/Quenched at  $z\approx 5$ ? https://arxiv.org/abs/2208.02794
- Nakajima, K., & Ouchi, M. 2014, MNRAS, 442, 900, doi: 10.1093/mnras/stu902
- Nakajima, K., Ouchi, M., Xu, Y., et al. 2022, ApJS, 262, 3, doi: 10.3847/1538-4365/ac7710
- Neistein, E., van den Bosch, F. C., & Dekel, A. 2006, MNRAS, 372, 933, doi: 10.1111/j.1365-2966.2006.10918.x
- Niemiec, A., Jauzac, M., Eckert, D., et al. 2023, MNRAS, 524, 2883, doi: 10.1093/mnras/stad1999
- Oesch, P. A., Brammer, G., Naidu, R. P., et al. 2023, MNRAS, 525, 2864, doi: 10.1093/mnras/stad2411
- Osterbrock, D., & Ferland, G. 2006, The Astrophysics of Gaseous Nebulae and Active Galactic Nuclei, doi: 10.1007/978-94-009-0963-2
- Ott, T. 2012, QFitsView: FITS file viewer, Astrophysics Source Code Library, record ascl:1210.019. http://ascl.net/1210.019
- Paalvast, M., Verhamme, A., Straka, L. A., et al. 2018, Astronomy &; Astrophysics, 618, A40, doi: 10.1051/0004-6361/201832866
- Pagel, B. E. J., Edmunds, M. G., Blackwell, D. E., Chun, M. S., & Smith, G. 1979, MNRAS, 189, 95, doi: 10.1093/mnras/189.1.95
- Papaderos, P., Loose, H. H., Fricke, K. J., & Thuan, T. X. 1996, A&A, 314, 59
- Pearson, W. J., Wang, L., Alpaslan, M., et al. 2019, A&A, 631, A51, doi: 10.1051/0004-6361/201936337
- Peimbert, M., Peimbert, A., & Delgado-Inglada, G. 2017, PASP, 129, 082001, doi: 10.1088/1538-3873/aa72c3
- Pérez-Montero, E. 2014, MNRAS, 441, 2663, doi: 10.1093/mnras/stu753
- —. 2017, PASP, 129, 043001, doi: 10.1088/1538-3873/aa5abb
- Pérez-Montero, E., Amorín, R., Sánchez Almeida, J., et al. 2021, MNRAS, 504, 1237, doi: 10.1093/mnras/stab862
- Richard, J., Kneib, J.-P., Limousin, M., Edge, A., & Jullo, E. 2010, Monthly Notices of the Royal Astronomical Society: Letters, 402, L44–L48, doi: 10.1111/j.1745-3933. 2009.00796.x

- Roberts-Borsani, G., Treu, T., Shapley, A., et al. 2024, arXiv e-prints, arXiv:2403.07103, doi: 10.48550/arXiv.2403.07103
- Robertson, B. E. 2022, ARA&A, 60, 121, doi: 10.1146/annurev-astro-120221-044656
- Sanders, R. L., Shapley, A. E., Jones, T., et al. 2021, ApJ, 914, 19, doi: 10.3847/1538-4357/abf4c1
- Schaller, G., Schaerer, D., Meynet, G., & Maeder, A. 1992, A&AS, 96, 269
- Schawinski, K., Thomas, D., Sarzi, M., et al. 2007, MNRAS, 382, 1415, doi: 10.1111/j. 1365-2966.2007.12487.x
- Scoville, N., Abraham, R. G., Aussel, H., et al. 2007, ApJS, 172, 38, doi: 10.1086/516580
- Searle, L., & Sargent, W. L. W. 1972, ApJ, 173, 25, doi: 10.1086/151398
- Shapley, A. E., Reddy, N. A., Kriek, M., et al. 2015, ApJ, 801, 88, doi: 10.1088/0004-637X/801/2/88
- Shi, W.-B., Liang, Y.-C., Shao, X., et al. 2014, Research in Astronomy and Astrophysics, 14, 875, doi: 10.1088/1674-4527/14/7/010
- Shipley, H. V., Lange-Vagle, D., Marchesini, D., et al. 2018, ApJS, 235, 14, doi: 10.3847/1538-4365/aaacce
- Smith, H. E. 1975, ApJ, 199, 591, doi: 10.1086/153727
- Soto, K. T., Lilly, S. J., Bacon, R., Richard, J., & Conseil, S. 2016, MNRAS, 458, 3210, doi: 10.1093/mnras/stw474
- Soucail, G., Fort, B., Mellier, Y., & Picat, J. P. 1987, A&A, 172, L14
- Spitoni, E., Calura, F., Mignoli, M., et al. 2020, A&A, 642, A113, doi: 10.1051/ 0004-6361/202037879
- Steidel, C. C., Rudie, G. C., Strom, A. L., et al. 2014, ApJ, 795, 165, doi: 10.1088/0004-637X/795/2/165
- Stierwalt, S., Besla, G., Patton, D., et al. 2015, ApJ, 805, 2, doi: 10.1088/0004-637X/805/1/2
- Storchi-Bergmann, T., Calzetti, D., & Kinney, A. L. 1994, ApJ, 429, 572, doi: 10.1086/ 174345
- Strom, A. L., Steidel, C. C., Rudie, G. C., et al. 2017, ApJ, 836, 164, doi: 10.3847/1538-4357/836/2/164
- Sullivan, M., Treyer, M. A., Ellis, R. S., et al. 2000, MNRAS, 312, 442, doi: 10.1046/j.1365-8711.2000.03140.x

- Tang, M., Stark, D. P., Chevallard, J., & Charlot, S. 2019, MNRAS, 489, 2572, doi: 10.1093/mnras/stz2236
- Taylor, M. B. 2005, in Astronomical Society of the Pacific Conference Series, Vol. 347, Astronomical Data Analysis Software and Systems XIV, ed. P. Shopbell, M. Britton, & R. Ebert, 29
- Terlevich, R., Melnick, J., Masegosa, J., Moles, M., & Copetti, M. V. F. 1991, A&AS, 91, 285
- Thuan, T. X., & Martin, G. E. 1981, ApJ, 247, 823, doi: 10.1086/159094
- Tody, D. 1986, in Society of Photo-Optical Instrumentation Engineers (SPIE) Conference Series, Vol. 627, Instrumentation in astronomy VI, ed. D. L. Crawford, 733, doi: 10. 1117/12.968154
- Tortora, C., Hunt, L. K., & Ginolfi, M. 2021, Astronomy &; Astrophysics, 657, A19, doi: 10.1051/0004-6361/202140414
- Tremonti, C. A., Heckman, T. M., Kauffmann, G., et al. 2004, ApJ, 613, 898, doi: 10. 1086/423264
- Treu, T., Roberts-Borsani, G., Bradac, M., et al. 2022, ApJ, 935, 110, doi: 10.3847/1538-4357/ac8158
- Troncoso, P., Maiolino, R., Sommariva, V., et al. 2014, A&A, 563, A58, doi: 10.1051/0004-6361/201322099
- Trump, J. R., Arrabal Haro, P., Simons, R. C., et al. 2023, ApJ, 945, 35, doi: 10.3847/1538-4357/acba8a
- Tumlinson, J., Peeples, M. S., & Werk, J. K. 2017, Annual Review of Astronomy and Astrophysics, 55, 389–432, doi: 10.1146/annurev-astro-091916-055240
- Veilleux, S., & Osterbrock, D. E. 1987, ApJS, 63, 295, doi: 10.1086/191166
- Vilchez, J. M., & Esteban, C. 1996, MNRAS, 280, 720, doi: 10.1093/mnras/280.3.720
- Vogelsberger, M., Marinacci, F., Torrey, P., & Puchwein, E. 2020, Nature Reviews Physics, 2, 42, doi: 10.1038/s42254-019-0127-2
- Walcher, J., Groves, B., Budavári, T., & Dale, D. 2010, Astrophysics and Space Science, 331, 1–51, doi: 10.1007/s10509-010-0458-z
- Weilbacher, P. M., Streicher, O., Urrutia, T., et al. 2012, in Society of Photo-Optical Instrumentation Engineers (SPIE) Conference Series, Vol. 8451, Software and Cyberinfrastructure for Astronomy II, ed. N. M. Radziwill & G. Chiozzi, 84510B, doi: 10.1117/12.925114

- Weilbacher, P. M., Streicher, O., Urrutia, T., et al. 2014, in Astronomical Society of the Pacific Conference Series, Vol. 485, Astronomical Data Analysis Software and Systems XXIII, ed. N. Manset & P. Forshay, 451, doi: 10.48550/arXiv.1507.00034
- Whitaker, K. E., Franx, M., Leja, J., et al. 2014, ApJ, 795, 104, doi: 10.1088/0004-637X/795/2/104
- White, S. D. M., & Rees, M. J. 1978, MNRAS, 183, 341, doi: 10.1093/mnras/183.3.341
- Wise, J. H. 2019, Contemporary Physics, 60, 145–163, doi: 10.1080/00107514.2019. 1631548
- Wright, E. L., Eisenhardt, P. R. M., Mainzer, A. K., et al. 2010, The Astronomical Journal, 140, 1868–1881, doi: 10.1088/0004-6256/140/6/1868
- York, D. G., Adelman, J., Anderson, John E., J., et al. 2000, AJ, 120, 1579, doi: 10.1086/ 301513
- Zahid, H. J., Dima, G. I., Kudritzki, R.-P., et al. 2014, ApJ, 791, 130, doi: 10.1088/0004-637X/791/2/130
- Zamora, S., Díaz, Á. I., Terlevich, E., & Fernández, V. 2022, MNRAS, 516, 749, doi: 10. 1093/mnras/stac2201